

<https://doi.org/10.15388/vu.thesis.712>

<https://orcid.org/0000-0002-8446-4819>

VILNIUS UNIVERSITY

CENTER FOR PHYSICAL SCIENCES AND TECHNOLOGY

Viktorija Liustrovaitė

# Application of Conducting Polymers in Composite Materials and Structures Applied in Sensor Technologies

**DOCTORAL DISSERTATION**

Natural Sciences,  
Chemistry (N 003)

VILNIUS 2024

The dissertation was prepared between 2020 and 2024 at Vilnius University, Faculty of Chemistry and Geosciences, Institute of Chemistry. The research was supported by Research Council of Lithuania.

**Academic supervisor – Prof. Habil. Dr. Arūnas Ramanavičius**  
(Vilnius University, Natural Sciences, Chemistry – N 003).

This doctoral dissertation will be defended in a public meeting of the Dissertation Defence Panel:

**Chairman** – Prof. Habil. Dr. Rimantas Ramanauskas (State Research Institute Center for Physical Sciences and Technology, Natural Sciences, Chemistry – N 003).

**Members:**

Assoc. Prof. Dr. Renata Butkutė (State Research Institute Center for Physical Sciences and Technology, Natural Sciences, Material Engineering – T 008),

Assoc. Prof. Dr. Lina Mikoliūnaitė (Vilnius University, Natural Sciences, Chemistry – N 003),

Dr. Germanas Peleckis (Wollongong university, Natural Sciences, Chemistry – N 003),

Prof. Dr. Vida Vičkačkaitė (Vilnius University, Natural Sciences, Chemistry – N 003).

The dissertation shall be defended at a public meeting of the Dissertation Defence Panel at 15:00 on the 10<sup>th</sup> of January 2025 in the Inorganic chemistry auditorium of Vilnius University, the Faculty of Chemistry and Geosciences. Address: Naugarduko st. 24, 141(NChA), Vilnius, Lithuania. Tel. +370 5 219 3105; e-mail: [info@chgf.vu.lt](mailto:info@chgf.vu.lt)

The text of this dissertation can be accessed at the libraries of Vilnius University, and the library of Center for Physical sciences and Technology, as well as on the website of Vilnius University:

[www.vu.lt/lt/naujienos/ivykiu-kalendorius](http://www.vu.lt/lt/naujienos/ivykiu-kalendorius)

<https://doi.org/10.15388/vu.thesis.712>

<https://orcid.org/0000-0002-8446-4819>

VILNIAUS UNIVERSITETAS  
FIZINIŲ IR TECHNOLOGIJOS MOKLSŲ CENTRAS

Viktorija Liustrovaitė

# Elektrai laidžių polimerų taikymas kompozitinėse medžiagose ir struktūrose skirtose jutiklių technologijoms

**DAKTARO DISERTACIJA**

Gamtos mokslai,  
Chemija (N 003)

VILNIUS 2024

Disertacija rengta 2020 – 2024 metais Vilniaus universitete.  
Mokslinius tyrimus rėmė Lietuvos mokslo taryba.

**Mokslinis vadovas – Prof. habil. dr. Arūnas Ramanavičius** (Vilniaus universitetas, gamtos mokslai, chemija – N 003).

Gynimo taryba:

**Pirmininkas** – prof. habil. dr. Rimantas Ramanauskas (Valstybinis mokslinių tyrimų institutas Fizinių ir technologijos mokslų centras, gamtos mokslai, chemija – N 003).

**Nariai:**

Doc. dr. Renata Butkutė (Valstybinis mokslinių tyrimų institutas Fizinių ir technologijos mokslų centras, gamtos mokslai, medžiagų inžinerija – T 008),  
Doc. dr. Lina Mikoliūnaitė (Vilniaus universitetas, gamtos mokslai, chemija – N 003),

Dr. Germanas Peleckis (Wollongong universitetas, gamtos mokslai, chemija – N 003),

Prof. dr. Vida Vičkačkaitė (Vilniaus universitetas, gamtos mokslai, chemija – N 003).

Disertacija ginama viešame Gynimo tarybos posėdyje 2025 m. sausio mėn. 10 d. 15 val. Vilniaus universiteto, chemijos ir geomokslų fakulteto, neorganinės chemijos auditorijoje. Adresas: Naugarduko g. 24, 141(NChA), Vilnius, Lietuva. tel. +370 5 219 3105; el. paštas [info@chgf.vu.lt](mailto:info@chgf.vu.lt)

Disertaciją galima peržiūrėti Vilniaus universiteto, Fizinių ir technologijos mokslų centro bibliotekose ir VU interneto svetainėje adresu: <https://www.vu.lt/naujienos/ivykiu-kalendorius>

## ACKNOWLEDGMENTS

I want to express my gratitude to everyone who contributed to this dissertation and supported me along the way.

I am deeply thankful to my lab mates, whose collaboration and encouragement created a supportive and stimulating environment. Your insights, dedication, and willingness to share knowledge were invaluable. I would also like to extend my appreciation to the scientific group “NanoTechnas”, whose collaborative spirit and innovative ideas significantly enriched the research and broadened its scope.

A special thanks to my advisor, Arūnas Ramanavičius, for your guidance, patience, and honest feedback throughout this process.

To my family and friends, thank you for standing by me, encouraging me, and reminding me of what truly matters. This journey has been difficult, but your belief in me has made it possible.

## LIST OF INCLUDED PUBLICATIONS

- Paper 1** V. **Liustrovaite**, M. Pogorielov, R. Boguzaitė, V. Ratautaite, A. Ramanaviciene, G. Pilvenyte, V. Holubnycha, V. Korniienko, K. Diedkova, R. Viter, A. Ramanavicius. Towards electrochemical sensor based on molecularly imprinted polypyrrole for the detection of bacteria—*Listeria monocytogenes*, *Polymers*, 15(7), (2023), 1597.  
<https://doi.org/10.3390/polym15071597>
- Paper 2** V. **Liustrovaite**, A. Valiuniene, G. Valincius, A. Ramanavicius. Electrochemical impedance spectroscopy based evaluation of chlorophyll a reconstitution within tethered bilayer lipid membrane, *Journal of The Electrochemical Society*, 168 (6), (2021), 066506.  
<https://doi.org/10.1149/1945-7111/ac0262>
- Paper 3** M. Drobysh, V. **Liustrovaite**, A. Baradoke, A. Rucinskiene, A. Ramanaviciene, V. Ratautaite, R. Viter, C.F. Chen, I. Plikusiene, U. Samukaite-Bubniene, R. Slibinskas, E. Ciplys, M. Simanavicius, A. Zvirbliene, I. Kucinskaite-Kodze, A. Ramanavicius. Electrochemical determination of interaction between SARS-CoV-2 Spike protein and specific antibodies, *International Journal of Molecular Sciences*, 23(12), (2022), 6768.  
<https://doi.org/10.3390/ijms23126768>
- Paper 4** V. **Liustrovaite**, M. Drobysh, A. Rucinskiene, A. Baradoke, A. Ramanaviciene, I. Plikusiene, U. Samukaite-Bubniene, R. Viter, C.F. Chen, A. Ramanavicius. Towards an electrochemical immunosensor for the detection of antibodies against SARS-CoV-2 Spike protein, *Journal of The Electrochemical Society*, 169(3), (2022), 037523.  
<https://doi.org/10.1149/1945-7111/ac5d91>
- Paper 5** V. **Liustrovaite**, V. Ratautaite, A. Ramanaviciene, A. Ramanavicius. Detection of the SARS-CoV-2 nucleoprotein by electrochemical biosensor based on molecularly imprinted polypyrrole formed on self-assembled monolayer. **Revisions submitted following the reviewers' feedback**
- Paper 6** V. **Liustrovaite**, V. Ratautaite, A. Ramanaviciene, I. Plikusiene, U. Malinovskis, D. Ertis, J. Sarvutiene, A. Ramanavicius. Electrochemical sensor for vascular endothelial growth factor based on self-assembling DNA aptamer structure, *Science of the Total Environment*, 955, (2024), 177151.  
<https://doi.org/10.1016/j.scitotenv.2024.177151>

## CONTRIBUTION TO INCLUDED PUBLICATIONS

- Paper 1** Carried out formal analysis and played a central role in organising the study, including data management. Contributed to the initial draft and was actively involved in writing, reviewing, and editing, as well as managing the visualisation aspects of the article.
- Paper 2** Performed electrochemical impedance spectroscopy and fluorescence microscopy analysis of samples containing chlorophyll a embedded in a bilayer phospholipid membrane on a gold surface. Analysed the data obtained during the research and visualised the obtained data. Contributed to the initial manuscript writing and editing.
- Paper 3** Performed electrochemical impedance spectroscopy measurements and analysed the data to detect antibodies against SARS-CoV-2 spike proteins. This process involved covalently immobilising proteins on a gold electrode surface modified with a self-assembled monolayer of 11-mercaptoundecanoic acid. Contributed to writing and editing the initial manuscript.
- Paper 4** Conducted studies using electrochemical impedance spectroscopy and cyclic voltammetry to detect antibodies against SARS-CoV-2 spike proteins. Proteins were covalently immobilised on a gold electrode surface modified with a composite self-assembled monolayer of 11-mercaptodecanoic acid and 6-mercapto-1-hexanol. Contributed to writing and editing the initial manuscript.
- Paper 5** Developed a sensor for the detection of SARS-CoV-2 nucleocapsid protein using a composite made from a self-assembled monolayer-based under-layer and a molecularly imprinted polypyrrole-based upper-layer. Contributions included investigation, formal analysis, visualisation, original draft writing, review and editing.
- Paper 6** Designed an electrochemical sensor for the detection of vascular endothelial growth factor (VEGF) by introducing a self-assembling DNA aptamer structure into a polypyrrole matrix to enhance sensitivity. Contributions included investigation, formal analysis, visualisation, original draft writing, review and editing.

## TABLE OF CONTENTS

|  |    |
|--|----|
| ACKNOWLEDGMENTS.....   | 5  |
| LIST OF INCLUDED PUBLICATIONS .....  | 6  |
| CONTRIBUTION TO INCLUDED PUBLICATIONS .....  | 7  |
| TABLE OF CONTENTS .....  | 8  |
| LIST OF ABBREVIATIONS .....  | 11 |
| INTRODUCTION.....  | 12 |
| 1. LITERATURE REVIEW .....   | 15 |
| 1.1. Conducting polymers .....   | 15 |
| 1.1.1. The mechanism of polypyrrole synthesis.....   | 15 |
| 1.2. The formation and application of molecularly imprinted polymers... 18   |    |
| 1.2.1. The formation of polymer underlayer .....   | 20 |
| 1.2.2. The formation of a self-assembled monolayer on the gold surface ... 20  |    |
| 1.2.3. The formation of MIPs-aptamer.....  | 23 |
| 1.3. The selected analytes .....   | 24 |
| 1.3.1. <i>Listeria monocytogenes</i> bacteria.....   | 24 |
| 1.3.2. Severe acute respiratory syndrome coronavirus 2.....  | 25 |
| 1.3.3. The vascular endothelial growth factor.....   | 27 |
| 2. EXPERIMENTAL SECTION.....   | 29 |
| 2.1. The analytical system used in MIP-based biosensors dedicated to bacteria sensing .....  | 29 |
| 2.2. The analytical system used for the development of SAM-based biosensor for the detection of antibodies against rS protein..... | 30 |
| 2.2.1.The preparation and modification of square gold electrode – Au(s) .....  | 31 |
| 2.2.2. The preparation and modification of microscope glass slides coated with gold (Au(MS)).....                                  | 32 |
| 2.2.3. The electrochemical assessment of Au(s) and Au(MS) electrodes....   | 32 |
| 2.3. The analytical system used for the development of SAM-supported MIP biosensor for the detection of rN protein.....            | 33 |



|   |    |
|---|----|
| 2.3.1. The formation of a SAM.....  | 34 |
| 2.3.2. Electrochemical modification of SAM-modified electrodes by Ppy and formation of MIP-based layer .....              | 34 |
| 2.3.3. The evaluation of electrodes covered by MIP layer.....   | 34 |
| 2.4. The analytical system used for the development of an aptamer-based biosensor for the detection of VEGF protein ..... | 35 |
| 3. RESULTS AND DISCUSSION.....  | 38 |
| 3.1. The detection of <i>Listeria Monocytogenes</i> bacteria using MIP-based electrochemical sensor .....                 | 38 |
| 3.1.1. The electrodeposition of MIP and extraction of imprinted bacteria ..   | 39 |
| 3.1.2. Electrochemical characterisation for bacteria-imprinted MIP layer ..   | 43 |
| 3.1.3. Determination of the limit of detection, the limit of quantification and the imprinting factor.....                | 44 |
| 3.2. Detection of antibodies against SARS-CoV-2 rS using SAM-based detection method .....                                 | 46 |
| 3.2.1. Electrochemical impedance spectroscopy-based evaluation of SAM and tethered bilayer lipid membranes layers .....   | 46 |
| 3.2.2. The electrochemical characterisation of a modified gold electrode surface .....                                    | 49 |
| 3.2.3. The analytical characterisation of immunosensor dedicated for anti-rS detection .....                              | 52 |
| 3.3. The detection of the SARS-CoV-2 nucleoprotein using the SAM-supported MIP detection method .....                     | 54 |
| 3.3.1. Electrochemical characterisation of Au(SPE) surface modified by SAMs.....  | 54 |
| 3.3.2. Electrodeposition of MIP- and NIP-based layers.....  | 55 |
| 3.3.3. Electrochemical characterisation and detection of the rN protein .....   | 58 |
| 3.3.4. Specificity test.....  | 60 |
| 3.4. The determination of the VEGF protein using a self-assembling aptamer-based electrochemical sensor .....             | 61 |
| 3.4.1. The electrodeposition of polypyrrole-based VEGF aptamer .....  | 61 |
| 3.4.2. Electrochemical characterisation of polypyrrole-based aptamer layer and VEGF detection.....                        | 62 |

|   |     |
|---|-----|
| 3.4.3. The evaluation of analytical parameters. Adapted Langmuir isotherm ..... | 64  |
| 3.4.4. Adaptation of integrated Cottrell equation.....                          | 67  |
| 3.4.5. The determination of the limit of detection.....                         | 70  |
| CONCLUSIONS.....  | 71  |
| FUTURE OUTLOOK.....   | 72  |
| REFERENCES.....   | 73  |
| SANTRAUKA .....   | 86  |
| CURRICULUM VITAE .....  | 105 |
| PARTICIPATION IN CONFERENCES .....  | 106 |
| CO-AUTHORED SCIENTIFIC PUBLICATIONS.....  | 107 |
| COPIES OF PUBLICATIONS .....  | 109 |

## LIST OF ABBREVIATIONS

|            |   |
|------------|---|
| 11-MUA     | 11-mercaptoundecanoic acid                      |
| 6-MCOH     | 6-mercapto-1-hexanol                            |
| Au(MS)     | Microscope glass slides coated with gold        |
| Au(s)      | Square gold electrode                           |
| Au(SPE)    | Screen-printed gold electrodes                  |
| BSA        | Bovine serum albumin                            |
| EIS        | Electrochemical impedance spectroscopy          |
| EDC        | 1-ethyl-3-(3-dimethylaminopropyl) carbodiimide  |
| LOD        | Limit of detection                              |
| LOQ        | Limit of quantification                         |
| MIP        | Molecularly imprinted polymer                   |
| NHS        | N-hydroxysuccinimide                            |
| NIP        | Non-imprinted polymer                           |
| PAD        | Pulsed amperometric detection                   |
| Ppy        | Polypyrrole                                     |
| PUT        | 11-(1H-pyrrol-1-yl)-undecane-1-thiol            |
| rN         | SARS-CoV-2 nucleocapsid protein                 |
| rS         | SARS-CoV-2 spike protein                        |
| SAM        | Self-assembled monolayer                        |
| SAMmix     | Mixture of self-assembled monolayers            |
| SARS-CoV-2 | Severe acute respiratory syndrome coronavirus 2 |
| SPCE       | Screen-printed carbon electrodes                |
| SPE        | Screen-printed electrode                        |
| SWV        | Square wave voltammetry                         |

## INTRODUCTION

Electrochemical sensor technologies have evolved in recent decades, revolutionising various fields such as food safety and healthcare. As the complexity and scale of these applications increase, so does the demand for analytical systems that are precise, dependable, cost-effective, and capable of providing real-time data. This growing need for better sensors requires the development of new materials and innovative techniques that can enhance the sensitivity, stability, and selectivity of the analysis. Among the materials explored, conductive polymers and their composites have emerged as critical components in next-generation sensor design, offering unique electrochemical properties that are well-suited to address these challenges.

The development of sensors, which meet the increasingly strict requirements of modern applications, is a complex task beyond simply selecting the suitable materials. It also involves integrating these materials into composite systems that deliver enhanced performance. For example, it is possible to create composite structures with superior characteristics by combining conductive polymers with other functional materials, such as underlayers, self-assembled monolayers (SAM) or aptamers.

Electrochemical methods such as electrochemical impedance spectroscopy (EIS), square wave voltammetry (SWV), and pulsed amperometric detection (PAD) have become indispensable tools in the advancement of sensor technologies. EIS is a versatile technique used to analyse the electrical properties of sensor surfaces. By measuring the electrochemical impedance of a system over a range of frequencies, EIS provides detailed information about the changes on the electrode surface, allowing the analysis of the formation of SAM or molecularly imprinted polymer (MIP). This technique is particularly valuable for assessing the stability of these modifications, as well as for detecting changes at the sensor interface when an analyte is present. SWV is another advanced technique used in sensor development and is known for its high sensitivity and resolution, making it ideal for detecting low concentrations of analytes. PAD plays a crucial role in the electropolymerisation of polymers on the sensor surface by using controlled pulses to form the conductive polymer layer. Additionally, PAD is used for the detailed characterisation of the electrode, assessing its response to analytes and optimising sensor functionality.

These electrochemical techniques – EIS, SWV, and PAD – are robust and reliable methods for analysing and quantifying surface modifications and target analytes. Integrating these methods enables the development of highly sensitive and selective diagnostic tools.

**The aim of the study** is to apply advanced conducting polymer composite production techniques for the development of molecularly imprinted polymer-based sensors and immunosensors.

**The objectives of the study:**

1. To design a sensor based on screen-printed carbon electrode modified by molecularly imprinted polypyrrole for the detection of *Listeria monocytogenes* bacteria.
2. To apply gold electrodes modified with different self-assembled monolayers for the development of an immunosensor for the detection of antibodies against the SARS-CoV-2 spike protein.
3. To develop a sensor for the detection of SARS-CoV-2 nucleocapsid protein using a composite made from a self-assembled monolayer-based underlayer and a molecularly imprinted polypyrrole-based upper-layer.
4. To develop a sensor designed to detect vascular endothelial growth factor (VEGF) using aptamers embedded in a conductive polypyrrole matrix.

**Scientific novelty**

The research presented in the dissertation is based on the application of polypyrrole, a conducting polymer known for its high conductivity, electrocatalytic activity, and biocompatibility. The study advances the field by incorporating three distinct materials to enhance sensor performance: underlayers, SAMs, and embedded aptamers.

The research presented in the dissertation employs MIPs, which are synthesised by polymerising monomers around a target molecule. This creates specific binding sites within the polymer matrix, enabling highly selective and sensitive detection of analytes. Firstly, the dissertation explores creating an underlayer beneath the MIP layer during sensor formation in order to address challenges related to analyte diffusion and adsorption to the electrode surface. Secondly, SAMs were used to reduce non-specific interactions and improve biomolecule immobilisation efficiency. Specifically, combining SAM and polypyrrole MIP composites could achieve improvements in the sensitivity and selectivity of the sensor. This layer formation-based methodology ensures the design of a more sensitive structure, while the MIP provides specific binding sites for the target analytes. Lastly, the incorporation of aptamers into the polymer matrix was explored. This allowed the creation of a polymer-stabilised sensing surface.

In this dissertation, the presented techniques were successfully employed for the development of MIP-based sensors to detect *Listeria monocytogenes*

bacteria, a leading cause of foodborne illness-related deaths. These sensors were designed by using the molecular imprinting technique to create specific binding sites for the target bacteria, enabling rapid and precise detection. Similarly, for infectious disease diagnostics, conductive polymer composites have been employed to create electrochemical immunosensors for detecting severe acute respiratory syndrome coronavirus 2 (SARS-CoV-2).

Overall, this research contributes to advancing sensor technologies by demonstrating how developed conductive polymer composites can perform in the design of selective and sensitive sensors. The continued innovation in this area is expected to drive further progress in sensor technologies, addressing the growing demand for efficient and reliable analytical devices across various fields.

#### **Statements for defence:**

1. A polypyrrole-based underlayer formed by using the pulsed amperometric technique can be incorporated in the design of a molecularly imprinted sensor employed for the detection of *Listeria monocytogenes* bacteria.
2. A gold electrode modified with a mixed self-assembled monolayer can be applied for the development of a label-free immunosensor used to detect antibodies against the SARS-CoV-2 spike protein.
3. A composite made of a self-assembled monolayer underlayer and molecularly imprinted polypyrrole upper-layer can be used for the development of SARS-CoV-2 nucleocapsid protein sensor.
4. Conductive polypyrrole matrix with embedded DNA aptamers can be employed for the development of a sensor used to detect VEGF.

# 1. LITERATURE REVIEW

## 1.1. Conducting polymers

Conducting polymers have received a lot of attention due to their unique combination of organic polymer properties and semiconductor-like electronic characteristics. The synthesis of these polymers dates back to 1862 when the English chemist H. Letheby performed the first known anodic oxidation of aniline in a dilute sulphuric acid solution and obtained dark blue/black colour, water-insoluble particles [1]. The modern development of conducting polymer research began with the discovery of electrical conductivity by Shirakawa et al. in 1977 [2]. Since then, these materials have been extensively studied for their unique electrical properties.

Conducting polymers are  $\pi$ - $\pi$  conjugated polymers that can conduct electricity by means of doping [3].  $\pi$ - $\pi$  conjugated polymers are organic macromolecules with a backbone chain composed of alternating double and single bonds. Spatial  $\pi$ - $\pi$  conjugation in their chains allows electrons to delocalise throughout the molecule, allowing multiple atoms to share them. Delocalised electrons can move throughout the molecule and become charge carriers, making it conductive. However, because the polymers are covalently bonded, the material must be doped for the continuous electron flow to occur. Doping involves the addition or removal of electrons from a polymer structure [4]. After the doping,  $\pi$ -orbital electrons can freely move through the polymer chain, creating an electrical current. Furthermore, the chemical and physical properties of polymers can be tailored by combining different monomers, changing polymerisation conditions, and creating polymeric composites. Polymers and their composites are increasingly being used in the development of sensing devices. Because of their distinct electronic, magnetic, and optical properties, conducting polymers are extremely important in scientific and technological applications [5–7]. The most frequently used conducting polymers are polyaniline, polypyrrole, polyacetylene, poly(3,4-ethylenedioxythiophene), and polythiophene.

### 1.1.1. The mechanism of polypyrrole synthesis

Among the various conducting polymers, polypyrrole (Ppy) is notable for its ease of synthesis, environmental stability, and promising electrical properties. Polypyrrole, derived from the pyrrole monomer, a five-membered heterocyclic ring containing a nitrogen atom, was discovered to be a conducting polymer in 1968. Ppy was initially synthesised chemically [8], but

later research demonstrated that it can also be developed electrochemically. While both chemical and electrochemical synthesis methods rely on oxidative polymerisation, alternative techniques such as photochemically initiated [9] and enzyme-catalysed polymerisation [10] exist but will not be discussed further.

Electrochemical synthesis of conducting polymers has advantages, such as the targeted formation of a polymer layer at the anode and the elimination of oxidising agents. This direct electrochemical oxidation process simplifies the synthesis pathway, enhances the purity of the resulting polymer, and allows more precise control over the polymerisation conditions. Furthermore, the polypyrrole is deposited on the electrode, allowing for additional electrochemical analysis to be performed. Given its widespread use in theoretical and practical contexts, the following discussion will concentrate on the principles of electrochemical synthesis. Some properties of electrochemically obtained conducting polymers are determined by the employed electrochemical polymerisation technique. These techniques are generally divided into two categories: galvanostatic and potentiostatic.

The galvanostatic technique creates a conducting polymer by maintaining a constant current density during polymerisation. The resulting polymer film is doped and conductive because dopant ions from the electrolyte are incorporated into the polymer matrix as it forms [11]. This technique allows to control the thickness of the polymer film by adjusting the duration of the polymerisation process [12]. Because of its simplicity, the galvanostatic technique is common for practical applications [13]. However, choosing the appropriate polymerisation current density is critical because the potential of the electrode increases during polymerisation as the polymer film grows due to an increase in resistance. This rise in potential can promote side reactions, lowering polymerisation efficiency [14]. Thus, this method is not chosen in certain applications because managing the increasing resistance and the potential side reactions is difficult, which can compromise the overall efficiency of the polymerisation process.

The potentiostatic polymerisation technique, which applies a constant positive potential for oxidative polymerisation, ensures the production of a high-quality polymer film. Maintaining a potential that is sufficiently high for effective polymerisation yet low enough to prevent undesirable secondary reactions and polymer over-oxidation is crucial for achieving this quality [15,16]. The modified pulse potentiostatic technique further improves the film's properties by alternating between anodic pulses (+950 mV vs. Ag/AgCl for 1 s) and cathodic pulses (0 mV for 30 s). This method initiates the reaction and then allows time for the pyrrole concentration near the electrode to



replenish, reducing the likelihood of side reactions. By applying at least 10 potential pulses with a rectangular profile, this approach minimises side reactions and significantly enhances the uniformity, stability, and overall quality of the polymer film [15] making it a promising method for further study in this dissertation.

Understanding how the synthesis techniques lead to polypyrrole formation is a complex but essential aspect. To delve into this, it is crucial to first examine the underlying electrochemical polymerisation mechanism. This process, which begins with the formation of the primary radical cation, is illustrated in Figure 1.

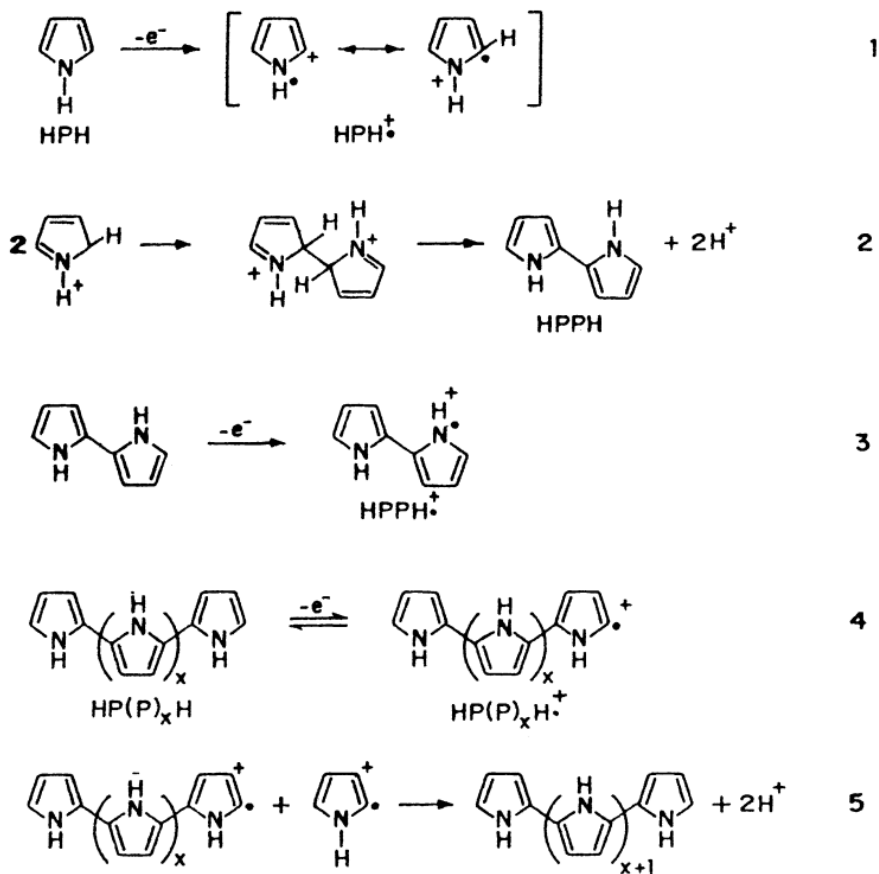


**Figure 1.** Mechanism of polypyrrole electrochemical synthesis. Reprinted with permission from [16].

The unpaired electron and positive charge are delocalized, and quantum mechanical calculations indicate that the electron spin density is highest at the ortho positions. As a result, radical coupling occurs primarily at these

positions [16–18]. When two primary radical cations combine, a positively charged dimer is produced. The presence of two protons in this dimer distorts the conjugation, causing rearomatisation via deprotonation and the formation of a more energetically favourable neutral dimer. In the following steps, the neutral dimer is oxidised at the anode, producing a new radical cation. This oxidation process occurs at a lower potential than for the neutral pyrrole. The next steps involve the coupling of dimer radical cations (and later oligomer radical cations) with primary radical cations, followed by proton release and rearomatisation. This cycle of oxidation, coupling, and rearomatisation continues, resulting in the formation of polypyrrole. Although electron spin density is highest at the ortho-position, as conjugation length increases, the spin density spreads throughout the conjugated system. This can lead to radicals coupling at different positions, disrupting linearity and causing branching [19].

## 1.2. The formation and application of molecularly imprinted polymers

Having discussed the fundamentals of polypyrrole synthesis, the focus will shift to molecularly imprinted polymers (MIP). This next chapter will examine how molecular imprinting techniques are applied using polypyrrole to create polymers with specific molecular recognition properties, enhancing their functionality and application.

MIPs are formed through molecular imprinting, where molecular recognition sites are formed within a polymer matrix by synthesising the polymer in the presence of a target template. During polymerisation, the complementary interactions between the functional monomers and the template molecule are maintained in their spatial arrangement [20]. Molecular imprinting involves several key steps, illustrated in Figure 2. First, a target molecule, known as the template, is selected. This template is the specific molecule or analyte that the polymer will be designed to recognise. Second, the functional monomers, which have a chemical affinity for the template are mixed with the template molecules, allowing them to interact through various forces such as hydrogen bonding or ionic interactions. Third, the polymerisation process is initiated, linking the functional monomers and forming a polymer network around the template. Finally, after polymerisation, the template molecule is removed, typically by washing with a solvent, leaving behind specific cavities or imprints in the polymer that are complementary in shape and chemical functionality to the original template [21].

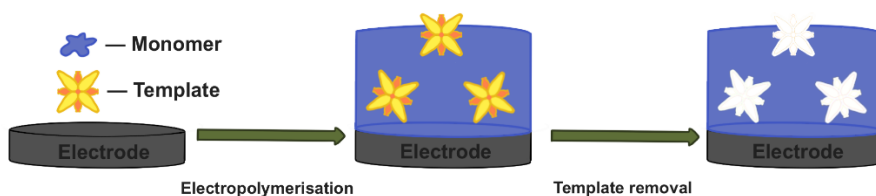


**Figure 2.** Molecular imprinting process for MIP formation: template selection, polymerisation and template removal.

The resulting MIP has these imprinted sites that allow it to selectively recognise and bind the target molecule. Thus, MIPs offer significant potential in various fields, including biotechnology and environmental monitoring. A notable application of MIPs is in protein-based affinity sensors, where they are used to imprint target proteins within polymer matrices. These sensors selectively recognise target analytes, such as specific proteins or polypeptides, and generate measurable signals through integrated transducers [22]. Molecular imprinting enhances selectivity by creating binding sites that are complementary to the imprinted analytes [23,24]. Protein-imprinted MIPs offer a promising alternative to traditional sensors, which employ antibodies and receptors and often face long-term stability challenges [25,26]. Although achieving proper protein orientation within the polymer matrix and maintaining correct protein conformation is challenging [27,28], the development of protein-imprinted MIPs represents a significant advancement in bioanalytical chemistry [29–31]. Additionally, MIP technology can be extended to imprint larger entities, such as bacteria and viruses, for diagnostic applications [32,33].

Understanding the interaction of analytes with electrochemical sensor surfaces is crucial in the development of MIP-based sensors. Accurate control over these interactions is key to enhancing the sensitivity, selectivity, and overall analytical performance of the sensor. If not properly managed, analytes may adsorb non-specifically on the surface rather than binding to the intended imprints, leading to compromised results. Several strategies have been systematically investigated to address the challenges posed by unwanted analyte-surface interactions. One prominent approach involves the sequential deposition of a non-imprinted polymer (NIP) underlayer, effectively insulating the electrode surface from the effects of analyte adsorption. Another approach of considerable interest is the integration of a self-assembled monolayer (SAM) as an interfacial layer between the gold substrate and the electrochemically deposited MIP. This SAM underlayer mitigates non-specific interactions, thereby enhancing the specificity of the sensor.

Additionally, an alternative strategy employs aptamers embedded within the polymer matrix to function as selective recognition elements instead of the MIP itself. These polymers with integrated aptamers are engineered to selectively bind target proteins, thereby illustrating the adaptability and potential of this approach in a wide array of biosensing applications. Further details on these methodologies will be discussed in the following sections.

#### 1.2.1. The formation of polymer underlayer

This approach involves the formation of a thin NIP underlayer, which serves as a foundational layer before the synthesis of the MIP layer is performed. This methodology has been effectively demonstrated for the detection of flumequine using a surface acoustic wave (SAW) signal transduction system [34]. According to experimental data and density functional theory (DFT) calculations, flumequine molecules tend to interact with the gold surface, thereby obstructing its electrochemical activity. A thin NIP underlayer is deposited to mitigate this interference and improve the adhesion of the MIP layer. This approach not only alleviates potential interference but also enhances the overall efficacy of the MIP layer formation. In this dissertation, a similar technique was employed, where incorporating an NIP underlayer was crucial in improving the performance and reliability of the MIP layer.

#### 1.2.2. The formation of a self-assembled monolayer on the gold surface

Another strategy involves using SAM as an interfacial layer in sensor development. It offers a convenient, adaptable, and straightforward method to customise the surface properties of metals, metal oxides, and semiconductors. SAMs are organic layers formed by the absorption of molecular components from either solution or the gas phase onto solid surfaces or in organised arrays on the surface of liquids. These adsorbed molecules spontaneously arrange, sometimes epitaxially, into crystalline or semicrystalline structures [35].

The molecules or ligands constituting SAMs possess a chemical functional group, often called the "headgroup," which exhibits a specific affinity for the substrate. The headgroup usually demonstrates a strong affinity for the surface, displacing previously adsorbed organic materials. Various headgroups selectively bind to metals, metal oxides, and semiconductors. SAM is typically formed on a metal surface, where they establish chemical bonds [36].

The process by which n-alkanethiols form SAMs on gold has been extensively studied, particularly on single crystals of Au(111) in ultra-high vacuum (UHV) [37,38]. However, the most accessible and common method involves the adsorption of alkanethiols from an ethanolic solution onto polycrystalline gold surfaces prepared by vapour phase deposition (Figure 3). When gold films are transferred from an evaporator to a solution without maintaining a vacuum, atmospheric contaminants quickly adsorb onto the gold surface. The thiols must then displace these adsorbed materials and any solvent from the surface.

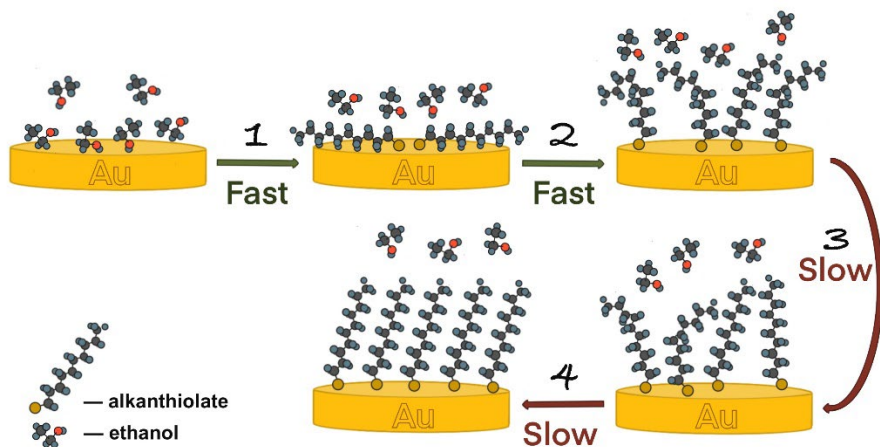


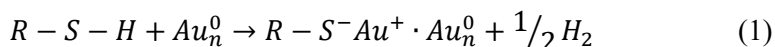
**Figure 3.** Sequential stages of self-assembled monolayer (SAM) formation on gold substrate.

Initially, most of the thiols that form the SAM adsorb quickly, creating a low mass coverage striped layer followed by a denser, upright layer within 5-6 minutes, covering approximately 90% of the surface (Figure 3, Step 1) [39]. The chemisorption of the thiol onto the gold substrate causes two main effects: (a) it induces local strain on the gold surface, which is relieved by releasing gold atoms to form pits or "vacancy islands," and (b) it increases the mobility of the gold-thiolate complex on the surface. During SAM formation, vacancy islands coalesce, and gold adatoms move to the step edges, resulting in a surface rougher than the original gold surface [37,38].

The alkanethiolate-gold complexes nucleate small crystalline regions of the monolayer, which grow as additional thiols adsorb (Figure 3, Step 2). The next phase involves the unfolding of alkane chains into their all-trans configuration, a process 3-4 times slower than the initial coverage phase (Figure 3, Step 3). This reordering maximises van der Waals interactions between molecules. Further adsorption of alkanethiols completes the well-packed monolayer (Figure 3, Step 4). Over a period of up to 7 hours, most

gauche defects in tail groups disappear, leaving a surface with steps in the gold, various grain boundaries, and other defects, but with the majority of alkanethiolate molecules present in the crystalline grains [40].

The formation of such monolayers is based on the strong adsorption of disulfides (R-S-S-R), sulphides (R-S-R), and thiols (R-SH) onto the Au surface. The sulphur donor atoms coordinate strongly with the gold surface, while van der Waals forces between the methylene groups orient and stabilise the monolayer into an orderly structure [41]. Voltammetric studies have shown that during adsorption, thiol groups undergo deprotonation [42]. The assumed equation for the formation of SAM is:



Porter et al. demonstrated that alkanethiols with long chains (consisting of more than 10 methylene groups) assemble in a manner reminiscent of crystalline structures. Shortening the chain length results in less organised structures [43]. However, alkanethiols such as 11-mercaptoundecanoic acid (11-MUA) or 11-(1H-pyrrol-1-yl)-undecane-1-thiol (PUT) form dense and stable films, which facilitate the observation of mediated electron transfer kinetics. SAMs can create a chemical environment that attracts or binds specific molecules by functionalising the end groups of alkanethiols (e.g., with carboxyl, amine, or pyrrole groups). These bound molecules might participate in electron transfer processes, effectively acting as intermediaries between the analyte and the electrode.

When dealing with  $\omega$ -functionalized thiols, various chemical moieties can be strongly bound at the solid-liquid interface, enabling the design of materials with new surface properties for biomolecule binding [44,45]. Mixed SAMs, formed by the co-adsorption of two thiols, have been shown to prevent denaturation and improve the bioactivity of immobilised proteins compared to pure SAMs [46–48]. Typically, mixed SAMs consist of one thiolate with a desired functional group (e.g., a carboxylic acid) at a low fraction and another "diluting" thiolate containing inert functional groups at a high fraction. This configuration reduces the surface concentration of functional groups, minimising steric hindrance, partial protein denaturation [46] and non-specific interactions that can cause interference signals [47].

The nature of functional groups on thiols plays a crucial role in their interactions with biomolecules. Grazing incidence infrared spectroscopy reveals that alkane thiols with functional groups like  $NH_2$  or  $OH$  are tightly packed, highly oriented, and well-ordered. The monolayer's orientation remains unaffected when these end groups are small (less than 5 Å). However,

larger groups like COOH reduce packing density and order [49]. In mixed monolayers of  $\omega$ -substituted thiols and shorter alkanethiols, the thiols adsorb in the same proportion as in solution without phase separation, indicating random ordering [50,51]. This allows for blending  $\omega$ -substituted alkanethiols with shorter non-substituted thiols to ensure anchor groups are available for immobilisation, potentially reducing steric hindrance [52,53]. The SAM mixture (SAMmix) presented in this dissertation, consisting of 6-mercapto-1-hexanol (6-MCOH) and 11-MUA, provides a precise method for surface modification with desired functional groups in order to facilitate covalent biomolecule immobilisation. It also reduces non-specific protein adsorption on the working electrode surface [54].

For example, during the development of MIP-based glyphosate sensors, Balciunas et al. [55] investigated the dispersion of glyphosate and its direct adsorption on the gold surface of the electrochemical surface plasmon resonance (ESPR) sensor. They suggested a method involving the creation of a SAM underlayer between the gold and the electrochemically produced MIP layer in response to the template molecule's strong interaction with the gold electrode. However, it's noteworthy that the insulating properties of SAM-based underlayers can negatively affect the electrodeposition rate of Ppy, necessitating careful consideration during sensor development.

### 1.2.3. The formation of MIPs-aptamer

The use of MIPs as recognition elements has attracted a lot of attention among the different approaches used in biosensor design with specially designed binding sites that can precisely and selectively bind target molecules of interest. You et al. [56] have introduced a novel approach to biosensor development, demonstrating the preparation of MIP on a glassy carbon electrode (GCE). In this innovative method, the MIP layer is formed in the presence of an amyloid- $\beta$  oligomers (A $\beta$ O) template molecule, which acts as an artificial antibody with high specificity for sample matrices. A $\beta$ O molecules within the samples can be selectively captured, and non-specifically bound entities can be eliminated by forming a sandwich structure in conjunction with aptamers. This MIPs-aptamer sandwich biosensor, under optimal conditions, exhibits exceptional specificity and sensitivity. With the use of appropriate MIPs and aptamers, this technique can be extended to detect additional protein biomarkers, thereby presenting a new perspective on MIPs and aptamers as alternatives to antibodies in biomarker detection [57].

Another innovative approach to biosensor development involves embedding aptamers in the polymer matrix to act as selective recognition

elements. These polymers with embedded aptamers are specifically formulated to capture target proteins not by the MIP but rather by the aptamer embedded in the polymer structure, demonstrating the adaptability and versatility of this methodology in diverse biosensing applications. This dissertation also examines such an approach.

### 1.3. The selected analytes

The formation of MIPs using Ppy has led to the development of advanced biosensor systems that combine the conductive properties of Ppy with the selective recognition capabilities of MIPs. This enhances biosensor performance, allowing for more sensitive and selective detection of various analytes. The following subsections provide information about the analytes studied in the dissertation. The analyte properties and the electrochemical detection methods are reviewed.

#### 1.3.1. *Listeria monocytogenes* bacteria

*Listeria monocytogenes* is a Gram-positive, rod-shaped bacterium that thrives at an optimum temperature of 37°C [58], and is a leading cause of foodborne illness-related mortality [59]. This bacterium is primarily an environmental contaminant found in soil and can be carried by various animals, including ruminants, birds, marine life, insects, ticks, and crustaceans [60]. *Listeria monocytogenes* can infiltrate the food supply chain, contaminating a wide range of products, such as meat, raw and unpasteurised milk and cheeses, ice cream, raw or processed vegetables and fruits, undercooked poultry, sausages, hot dogs, deli meats, and raw or smoked fish and seafood [61].

One severe form of illness caused by *Listeria monocytogenes* can lead to septicaemia and meningitis, with a case-fatality rate of 20–30% [62]. Another form is a non-invasive gastrointestinal illness that typically does not have severe consequences. Despite the relatively low incidence of listeriosis in the general population, it remains a significant and deadly foodborne disease, with a hospitalisation rate exceeding 95% [63]. The primary concern is that *Listeria monocytogenes* disproportionately affect vulnerable groups, including the elderly, pregnant women, unborn babies, and immunocompromised individuals (such as those with cancer or AIDS or those who have undergone organ transplants) [64]. Pregnant women, for example, have a 17-fold increased risk of contracting invasive listeriosis [65], and the infection accounts for 22% of fatalities among immunocompromised adults [61].



Detecting *Listeria monocytogenes* is critical for healthcare and the food industry [66]. The minimal infectious dose for listeriosis is 100 colony-forming units per gram (CFU/g) of food. Most countries enforce a zero-tolerance policy for the presence of *Listeria monocytogenes* in food. According to the European Regulation on Microbiological Criteria for Foodstuffs, the presence of *Listeria monocytogenes* is not permitted in foods intended for infants and certain medical purposes [67]. However, other foods are allowed to contain up to 100 CFU/g of the bacterium during their shelf life [68].

The application of MIPs for detecting *Listeria monocytogenes* bacteria has shown potential benefits. However, it is noteworthy that only a few studies have explored the use of electrochemical techniques for this purpose, suggesting that the field of MIP-based sensors for *Listeria monocytogenes* detection is still relatively underdeveloped. For instance, a gold disk electrode combined with recombinase-assisted amplification-based CRISPR/Cas12a (RAA-based E-CRISPR) used square wave voltammetry (SWV), achieving a limit of detection (LOD) of 26 CFU/mL and a linear range from  $2.6 \times 10^1$  to  $2.6 \times 10^9$  CFU/mL [69]. Another study employed a gold electrode with a sandwich assay using cyclic voltammetry (CV) and electrochemical impedance spectroscopy (EIS), achieving a linear range from  $10^2$  to  $10^6$  CFU/mL [70]. Multiwalled carbon nanotube electrodes used in an immunoassay with CV realised a LOD of  $1.07 \times 10^2$  CFU/mL and a linear range from  $10^2$  to  $10^5$  CFU/mL [71]. Additionally, an aluminium disc electrode used in an immunoassay with EIS had a 1.3 log CFU/mL LOD and a linear range from 1.3 to 4.3 log CFU/mL [72]. Typically, lysozyme was used as the enzyme for template extraction during MIP-based sensor development.

### 1.3.2. Severe acute respiratory syndrome coronavirus 2

The global health crisis caused by severe acute respiratory syndrome coronavirus 2 (SARS-CoV-2) has necessitated an urgent response from public health authorities. The World Health Organization (WHO) officially declared COVID-19 a pandemic on March 12, 2020, following its initial outbreak in Wuhan, China [73,74]. Since then, numerous virus variants have emerged, complicating disease management strategies.

SARS-CoV-2 is a linear, single-stranded, positive-sense RNA virus with a genome of approximately 29.9 kb, making it one of the longest among RNA viruses [75]. The virus is characterised by its crown-like spikes on the outer surface, which are crucial for its ability to infect host cells [76]. The genome of SARS-CoV-2 encodes four structural proteins: spike (rS), envelope (E),

membrane (M), and nucleocapsid (rN) proteins [75]. The E-protein, the smallest structural protein, is involved in virus formation and maturation. The M-protein maintains the shape of the viral shell and connects with other structural proteins [77]. The rN protein is essential for viral replication and immune modulation, playing a significant role in the virus's life cycle [78]. It is expressed abundantly in host cells and is less frequently mutated than other structural proteins, making it a reliable marker for diagnosis and a target for understanding COVID-19-related inflammation due to its immunogenicity and role in cytokine storms [79]. The rS protein, a homotrimer, facilitates viral entry into host cells by binding to angiotensin-converting enzyme 2 (ACE2) receptors via its S1 subunit and mediating membrane fusion through its S2 subunit. The rS protein is a primary focus for diagnostic tools and vaccine development because of its essential role in viral entry and its high mutation rate in new variants [80–83].

Initially, the detection of SARS-CoV-2 focused on identifying antibodies against the rS protein, as the immune response to infection leads to the production of specific antibodies [84]. Most patients do not develop an antibody response until the second week following the onset of symptoms, often allowing for diagnosis based on antibody detection only during the recovery phase [85]. The rS protein can act as a biorecognition element in immunosensors by triggering an immune response that leads to the production of specific antibodies. These antibodies can then be targeted and detected by the immunosensor, making the rS protein a valuable component for this purpose [84]. Currently, serologic tests for the presence of antibodies against SARS-CoV-2 virus proteins are mainly based on standard approaches such as the enzyme-linked immunosorbent assay (ELISA) [85] and the lateral flow immunoassay (LFIA) [86]. Despite their widespread use, immunoanalytical methods like ELISA and LFIA have notable drawbacks: ELISA is time-consuming, and LFIA is not fully automated. As a result, there is a clear need for rapid, easy-to-use, and precise testing methods that also allow for quantitative analysis. Various physical techniques can detect analytical signals from affinity sensors, including surface plasmon resonance [87], scanning electrochemical microscopy [88], quartz crystal microbalance [89] and total internal reflection ellipsometry [90]. Among these, electrochemical immunosensors stand out due to their advantages of low cost, robustness, and simplicity in both detection procedures and data interpretation [91]. These sensors enable the detection of both antibodies against SARS-CoV-2 and the nucleocapsid (rN) protein, which plays a crucial role in virus identification. As SARS-CoV-2 began to mutate, the spike (rS) protein underwent significant changes, complicating the detection of antibodies due to variations in protein

affinity. In response, the focus can shift to the detection of the rN protein, which is more abundantly expressed in host cells and less prone to mutations compared to the rS protein [92,93].

Immunosensors, which had already proven vital due to their sensitivity, selectivity, and cost-effectiveness, were adapted to detect the rN protein. This shift enhanced the reliability of viral diagnostics despite the ongoing mutations of SARS-CoV-2.

### 1.3.3. The vascular endothelial growth factor

Vascular endothelial growth factor (VEGF) is a protein activated in response to low oxygen levels (hypoxia). It is critical for blood vessel development during embryogenesis (vasculogenesis) and for the formation of new blood vessels from existing ones (angiogenesis), processes often associated with cancer [94]. In mammals, the VEGF family includes five members: A, B, C, D [95] and placenta growth factor (PLGF) [96]. The most studied member, VEGFA (commonly referred to as VEGF), has nine proangiogenic isoforms produced by alternative exon splicing [97], with VEGF<sub>165</sub> being the most common and associated with the growth and metastasis of various human cancers [98].

Identifying and quantifying disease-related proteins like VEGF are essential for clinical diagnosis, biological applications, and medical research. Early detection of VEGF protein biomarkers significantly simplifies cancer diagnosis and is vital for monitoring the effectiveness of treatment interventions [99]. Additionally, VEGF has been linked to several human disorders through blood biomarker analysis, including rheumatoid arthritis [100], psoriasis [101], and Alzheimer's disease [102]. VEGF detection has been achieved using various methods, each employing different electrode materials, polymers, and detection techniques. One approach involves flexible silk protein matrices combined with a conducting ink containing poly(3,4-ethylenedioxythiophene) and polystyrene sulfonate, creating a biocompatible platform suitable for antibody immobilisation. This method demonstrates a moderate LOD of 1.03 pg/mL and a wide linear range from 1 pg/mL to 1 µg/mL [103]. Another method uses a gold screen-printed electrode (SPE) functionalised with a MIP, synthesised with acrylamide and N,N'-methylenebis(acrylamide) as the monomer and crosslinker, polymerised around EGFR and VEGF templates. This technique shows a LOD of 0.005 pg/mL and a wide linear range from 0.01 pg/mL to 7000 pg/mL [104]. Additionally, this biosensor underscores the value of multidisciplinary approaches in protein detection by combining MIP technology, antibody-

conjugated nanoliposomes, and electrochemical detection for the sensitive and selective determination of VEGF. Another method employs poly(o-phenylenediamine) as the polymer matrix on a glassy carbon electrode modified with graphene nanoribbons (GNRs) and gold nanoparticles (AuNPs). Using differential pulse voltammetry (DPV), this approach achieves a linear range from 0.5 ng/mL to 500 ng/mL and an LOD of 300 pg/mL [105]. Accurate detection of VEGF is crucial for understanding its role in disease progression and developing targeted therapeutic strategies, offering significant implications for improving clinical outcomes across various conditions, including cancer and chronic inflammatory diseases.

## 2. EXPERIMENTAL SECTION

This section details the methodologies employed in developing four distinct biosensors: (i) a MIP-based biosensor for *Listeria monocytogenes* bacteria sensing; (ii) a SAM-based biosensor for detecting antibodies against the rS protein; (iii) a biosensor integrating SAM-supported MIP for rN protein detection; and (iv) an DNR-aptamer biosensor for the detection of VEGF protein. Each biosensor employs a unique strategy for target detection, using electrochemical techniques to achieve precise and reliable measurements.

### 2.1. The analytical system used in MIP-based biosensors dedicated to bacteria sensing

A potential cycling strategy was used to clean the screen-printed carbon electrodes (SPCE) electrochemically. The electrodes were cleaned in 0.5 M sulphuric acid using 20 potential cycles in a potential range from  $-0.1$  V to  $+1.2$  V vs. Ag/AgCl with a potential sweep rate of  $0.1$  V·s<sup>-1</sup>. Bacteria – *Listeria monocytogenes* – were acquired from Sumy State University's Bacteria Collection (Sumy, Ukraine). To eradicate virulence while maintaining the antigenic structure on the *Listeria monocytogenes* membrane,  $10^9$  CFU/mL of the bacteria were submerged in 70% ethanol and exposed to UV light for a full day. This process makes it possible to destroy bacterial DNA while having little effect on the shape and cell wall, both of which are essential for the development of MIP.

For the MIP deposition, several steps were followed: (i) electrochemically depositing the Ppy underlayer from a polymerisation solution with 0.5 M pyrrole using a sequence of 5 potential pulses ( $+950$  mV for 1 s and 0 V for 30 s), (ii) adding  $10^9$  CFU/mL of *Listeria monocytogenes* bacteria into the same polymerisation bulk solution during the deposition of the second layer and repeating the pulse sequence, and (iii) incubating the electrodes in different extraction solutions (0.05 M sulphuric acid, 10% acetic acid, 0.1% L-lysine, 10 U/mL trypsin) at 37°C for 30 minutes to remove imprinted bacteria and form the MIP. The NIP-based layer was formed similarly to MIP without the addition of bacteria, acting as a control surface. Pulsed amperometric detection was then employed, using a sequence of 10 potential pulses of  $+600$  mV vs. Ag/AgCl for 2 s, followed by 0 V vs. Ag/AgCl for 2 s, to assess the MIP and NIP-modified electrodes.

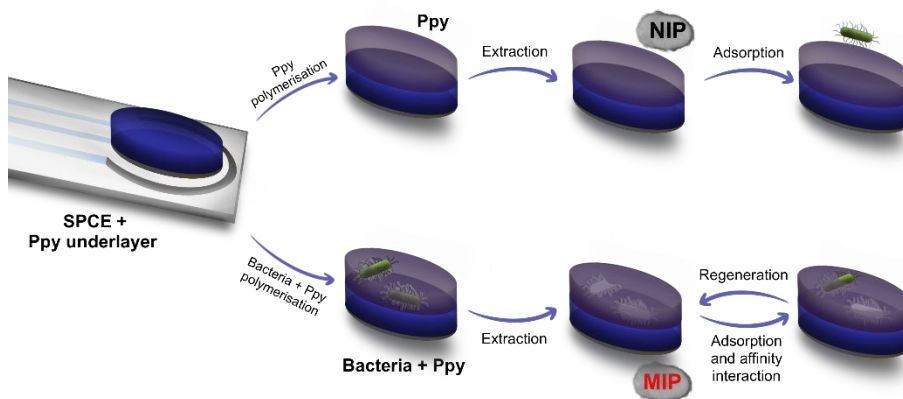


**Figure 4.** Schematic representation of electrode modification for MIP-based biosensor.

The limit of detection (LOD) and limit of quantification (LOQ) were calculated according to Equations (2) and (3):

$$LOD = \frac{3.3 \cdot SD}{slope} \quad (2)$$

$$LOQ = \frac{10 \cdot SD}{slope} \quad (3)$$

where SD is the standard deviation of the linear relationship on the calibration plot.

## 2.2. The analytical system used for the development of SAM-based biosensor for the detection of antibodies against rS protein

Developing a SAM-based biosensor for detecting antibodies against the SARS-CoV-2 rS protein necessitates the use of well-prepared electrode surfaces. The two primary types of electrodes used in this study, the square gold electrode (Au(s)) and gold-coated microscope glass slides (Au(MS)), are prepared with specific procedures to ensure their optimal performance for biosensor applications. The following subsections provide detailed methodologies of the preparation, functionalisation, and electrochemical characterisation of these electrodes. This includes the formation of SAMs, the activation of surface groups for protein immobilisation, and the assessment of electrode performance using electrochemical techniques.

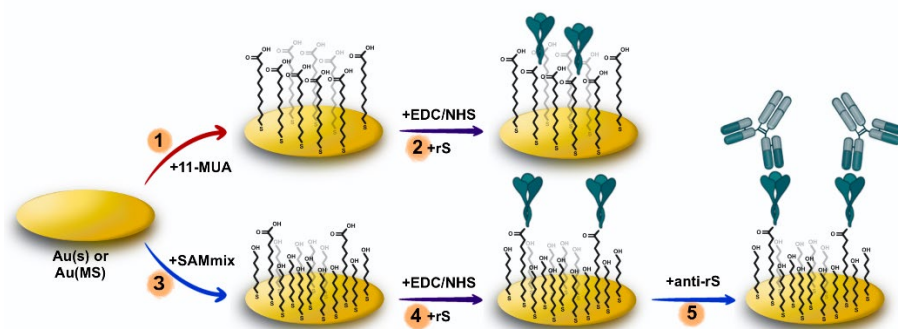


**Figure 5.** Schematic representation of experimental stages for the SAM-based biosensor.

### 2.2.1. The preparation and modification of square gold electrode – Au(s)

The square gold electrode (Au(s)), made of 99.9% chemically pure gold, had a geometrical area of 2 cm<sup>2</sup>. To prepare the Au(s) surface, it was first mechanically polished using an alumina suspension. After polishing, the electrode was cleaned in an ultrasonic bath (EMAG Emmi-40 HC, Germany) for 10 min. Following this, the electrode was treated in a 0.5 M NaBH<sub>4</sub> solution (H<sub>2</sub>O/MeOH, v/v, 1:1) [106] for 10 minutes. The Au(s) electrode was reused after each experiment by repeating this same preparation procedure. The Au(s) electrode was then used for the formation of an 11-MUA monolayer (Figure 5, Step 1). The electrode was incubated at 24°C in a 1 mM ethanolic solution of 11-MUA for 18 hours, then rinsed with ethanol and dried under a nitrogen flow to create the Au(s)/11-MUA layer. To activate the 11-MUA monolayer on the Au(s)/11MUA surface, the electrode was treated with a mixture of 0.04 M N-(3-dimethylaminopropyl)-N'-ethyl-carbodiimide hydrochloride (EDC) and 0.01 M N-hydroxysuccinimide (NHS) in 10 mM PBS solution for 15 minutes, forming the Au(s)/11-MUA/EDC-NHS layer. Next, the electrodes were incubated with 1 mL of a 50 µg/mL solution of the rS protein in 10 mM PBS solution at room temperature for 45 minutes. This prolonged exposure allowed the rS protein to covalently bind to the activated Au(s)/11-MUA/EDC-NHS layer through its primary amine groups, forming the Au(s)/11-MUA/EDC-NHS/rS structure (Figure 5, Step 2). The higher volume and concentration of the protein solution used on the Au(s) electrode with 11-MUA were chosen to ensure thorough and effective protein binding to the surface-modified layer.

### 2.2.2. The preparation and modification of microscope glass slides coated with gold (Au(MS))

The 20 x 30 mm microscope slides were cleaned with 2-propanol and then ultrasonically cleaned using an ultrasonic bath. After ultrasonic cleaning, the slides were submerged in H<sub>2</sub>SO<sub>4</sub> solution for 30 min. Once removed from the acid, the slides were dried with a stream of N<sub>2</sub> gas (99.99% purity). The dried slides were placed inside a vacuum magnetron chamber manufactured by VST Services Ltd. (Israel). Film deposition did not commence until a vacuum of at least 7·10<sup>-8</sup> Torr was achieved. A thin layer of titanium, approximately 10 nm, was first applied to enhance the adhesion of gold to the glass surface. This was followed by the application of a 100 nm layer of gold (Au(MS)). The working electrode geometric area was 0.179 cm<sup>2</sup>.

Au(MS) electrodes were incubated at 24°C for 4 hours in a 1 mM solution of 6-mercapto-1-hexanol (6-MCOH) and 11-mercaptoundecanoic acid (11-MUA) in ethanol, using a molar ratio of 9:1, respectively, to form a mixed self-assembled monolayer (SAMmix) (Figure 5, Step 3). After incubation, the electrodes were rinsed with ethanol to remove any excess of SAMmix and then dried with a flow of nitrogen gas, forming the Au(MS)/SAMmix layer on the gold-coated slides. The SAMmix layer on Au(MS) was activated using a mixture of 0.004 M EDC and 0.001 M NHS in 10 mM PBS solution at room temperature for 15 minutes, resulting in the Au(MS)/SAMmix/EDC-NHS layer. Following the activation step, the electrodes were treated with 70 µL of 100 µg/mL of rS protein in 10 mM PBS solution at room temperature for 30 minutes, forming the Au(MS)/SAMmix/EDC-NHS/rS structure (Figure 5, Step 4). The electrodes were treated with a 0.5% bovine serum albumin (BSA) solution for 30 minutes to deactivate any remaining reactive esters. Following this, 100 µL of an anti-rS antibody solution in 10 mM PBS solution was added to the electrode at concentrations ranging from 30 to 150 nM for 45 minutes at room temperature, forming the Au(MS)/SAMmix/EDC-NHS/rS/anti-rS complex (Figure 5, Step 5). After each step of the incubation process, the electrodes were rinsed with 10 mM PBS solution to remove any unbound materials.

### 2.2.3. The electrochemical assessment of Au(s) and Au(MS) electrodes

Electrochemical characterisation of the Au(s) and Au(MS) electrodes was conducted using the µAUTOLAB TYPE III potentiostat (Metrohm, Netherlands), controlled by FRA2-EIS software from ECO-Chemie (Utrecht, Netherlands). All experiments were performed in a three-electrode



electrochemical cell. All experiments, before and after each incubation step, were carried out in 10 mM PBS, pH 7.4, with the addition of 2 mM  $[\text{Fe}_3(\text{CN})_6]$  and 2 mM  $[\text{Fe}_4(\text{CN})_6]$  as a redox probe ( $[\text{Fe}(\text{CN})_6]^{3-/4-}$ ). The three-electrode system comprised the Au-based electrode (Au(s) or Au(MS)) as the working electrode, platinum (Pt) wire as the counter electrode, and Ag/AgCl in saturated KCl (Ag/AgCl<sub>(KCl<sub>sat</sub>)</sub>) microelectrode (ISAG/AGCL.AQ.RE) as the reference electrode (ItalSens, The Netherlands).

Electrochemical characterisation of Au(s) and Au(MS) electrodes at different modification steps was performed using CV and EIS methods. CV measurements were conducted in the potential range from  $-0.2$  to  $+0.6$  V for Au(MS) electrode and  $0$  to  $+0.4$  V for Au(s) vs Ag/AgCl<sub>(KCl<sub>sat</sub>)</sub> at a scan rate of  $50 \text{ mV}\cdot\text{s}^{-1}$ . EIS spectra were recorded over a frequency range from  $0.1$  Hz to  $100$  kHz with a perturbation amplitude of  $10$  mV and a potential of  $0.2$  V vs Ag/AgCl<sub>(KCl<sub>sat</sub>)</sub> for both electrodes. Randles equivalent circuit was applied for the evaluation of EIS data, where  $R_s$  represents the dynamic solution resistance,  $C_{dl}$ —represents the double layer capacitance measured between the electrode and the electrolyte solution,  $R_{ct}$ —represents the charge transfer resistance of the immobilised recognition layer and  $Z_w$  representing the Warburg diffusion element.

### 2.3. The analytical system used for the development of SAM-supported MIP biosensor for the detection of rN protein

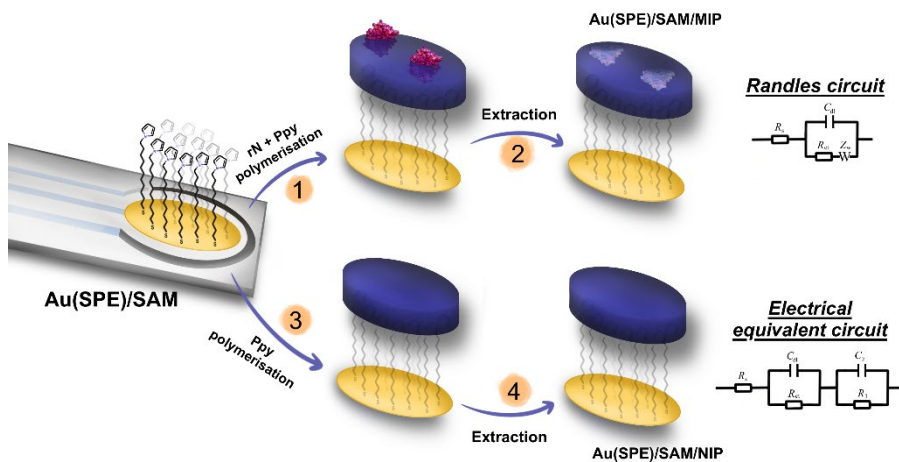


**Figure 6.** Schematic representation of electrode modification steps for SAM-supported molecularly imprinted polymer (MIP) formation, including applied electrical equivalent circuits.

### 2.3.1. The formation of a SAM

Screen-printed gold electrodes (Au(SPE)) were incubated at 20 °C for 2 hours in an ethanolic solution containing 10 mM of PUT to form a SAM (Au(SPE)/SAM) on the working surface. Following incubation, the Au(SPE)/SAM electrodes were rinsed with deionised water and dried under a nitrogen flow.

### 2.3.2. Electrochemical modification of SAM-modified electrodes by Ppy and formation of MIP-based layer

Ppy was electrodeposited onto Au(SPE)/SAM electrodes using a polymerisation solution containing 25 mM pyrrole and 25  $\mu\text{g}\cdot\text{mL}^{-1}$  rN protein, following a sequence of ten potential pulses (at +950 mV for 1 s followed by 0 V for 30 s). As described previously in Chapter 2.1., the MIP-based biosensor for bacteria sensing used a higher concentration of Ppy (0.5 M) to account for the larger size of bacteria, while a concentration of 25 mM was chosen to accommodate the smaller size of the rN protein. The resulting polymer immediately after deposition is denoted as Au(SPE)/SAM/(Ppy+rN) (Figure 6, Step 1), wherein the rN protein remains embedded within the polypyrrole structure.

Subsequently, similar to the procedures used for the detecting bacteria, the Au(SPE)/SAM/(Ppy+rN) electrodes underwent a washing step to remove the rN protein, resulting in the formation of a MIP structure with complementary cavities to the original template (Figure 6, Step 2). The imprinted rN proteins were extracted from the Ppy layer by incubating the electrodes in a 0.1 M  $\text{H}_2\text{SO}_4$  extraction solution for 10 minutes. The final MIP structure containing the polymer is marked as Au(SPE)/SAM/MIP. Similarly, a polymer layer was formed on Au(SPE)/SAM electrodes without the addition of rN protein, marked as Au(SPE)/SAM/Ppy (Figure 6, Step 3). After incubation of the SPE/SAM/Ppy electrodes in a 0.1 M  $\text{H}_2\text{SO}_4$  extraction solution for 10 minutes, the resulting non-imprinted polymer Au(SPE)/SAM/NIP (Figure 6, Step 4) was used as a control surface.

### 2.3.3. The evaluation of electrodes covered by MIP layer

The following experimental protocol was conducted to evaluate the biosensor ability to detect the rN protein: Au(SPE)/SAM/MIP electrodes were exposed to rN protein concentrations ranging from 0 to 35 nM for 5 minutes. The electrodes were immersed in a pH 7.4 PBS solution containing the rN

protein and a redox probe throughout this incubation period. For electrochemical measurements, 2.5 mM  $[\text{Fe}(\text{CN})_6]^{3-/4-}$  was added to a 0.1 M PBS solution at pH 7.4. The working electrode underwent electrochemical characterisation using EIS and square wave voltammetry (SWV) at various stages of modification. EIS measurements were recorded at open circuit potential (OCP) with a 10 mV amplitude over a frequency range from 100 kHz to 0.1 Hz. Experiments with SWV were conducted with a step size of 4 mV, square wave frequency of 20 Hz, and a pulse height of 50 mV in the potential range from  $-0.4$  V to  $+0.6$  V vs. Ag/AgCl. All experiments were performed at room temperature ( $20$  °C). Two different systems were employed to evaluate the EIS data. Initially, the Randles equivalent circuit was used with  $R_s$  representing dynamic solution resistance,  $C_{dl}$  representing double layer capacitance between electrode and electrolyte solution,  $R_{ct}$  representing charge transfer resistance, and  $Z_w$  representing the Warburg diffusion element (Figure 6). The second system was employed using EEC ( $R_s + C_{dl}/R_{ct} + C_2/R_3$ ), which is composed of three components connected in series (Figure 6). The first component,  $R_s$ , expresses electrolyte resistance. The parallel elements  $C_{dl}$  and  $R_{ct}$ , associated with the first Nyquist semi-circle, correspond to the constant phase element (CPE) and the charge transfer resistance. For the second Nyquist semi-circle, the parallel elements  $C_2$  and  $R_3$  represent CPE and charge transfer resistance, respectively.

#### 2.4. The analytical system used for the development of an aptamer-based biosensor for the detection of VEGF protein

The hybridisation of oligonucleotides, specifically the anti-VEGF aptamer, involves several steps to assemble the desired structure. The anti-VEGFA SL2B aptamer sequence, highlighted in Table 1, is critical for this process. Additional DNA sequences are designed to form a stem (stalk) structure following oligonucleotide hybridisation (Figure 7). Initially, the thiol-modified oligonucleotide (stalkGTG) undergoes reduction before aptamer assembly. This reduction involves treating the disulfide bond of the 3'-thiol modifier using a standard protocol. The thiol-modified oligonucleotide is first dissolved in 125  $\mu\text{L}$  of dithiothreitol solution (100 mM DTT in 10 mM sodium phosphate buffer, pH 8.3) and incubated at room temperature for 1 hour. After incubation, any by-products are removed using a Sephadex® G-25 column (NAP-10, 'Cytiva'). Once reduced, hybridisation of the oligonucleotides occurs, assembling the aptamer by mixing equal volumes of normalised oligonucleotide solutions (combSL2B, stalkGTG, and  $r\_stalkGTG$ ) at a concentration of 30 pM/ $\mu\text{L}$  in PBS buffer. This mixture is then boiled in a water bath for 5 minutes before being slowly cooled to room temperature.

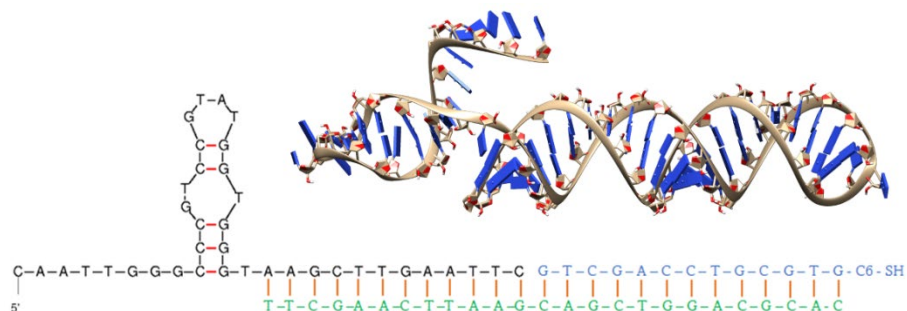


**Figure 7.** Self-assembling anti-VEGF aptamer based on three oligonucleotides. Black letters - combS12B oligonucleotide, blue letters - stalkGTG oligonucleotide and green letters - r\_stalkGTG oligonucleotide.

**Table 1.** DNA nucleotides.

| <i>Oligomer</i> | <i>Sequence (5'-3')</i>                                      | <i>Modification</i>                                  | <i>Ln</i> | <i>MW</i> |
|-----------------|--|--|-----------|-----------|
| combS12B        | <u>CAATTGGGCCCGT</u><br><u>CCGTATGGTGGGT</u><br>AAGCTTGAATTC |  | 38        | 11744     |
| stalkGTG        | GTCGACCTGCGTG/<br>[ThiC6]                                    | [ThiC6] - 3' Thiol<br>modifier C6 S-S -<br>on 3' end | 13        | 6763      |
| r_stalkGTG      | CACGCAGGTCGAC<br>GAATTCAAGCTT                                |  | 25        | 7655      |

For the electrochemical modification and measurement, the experiments were conducted using a potentiostat/galvanostat AUTOLAB TYPE III (ECO-Chemie/Metrohm, Barendrecht, The Netherlands) controlled by FRA2-EIS software (ECO-Chemie/Metrohm, Utrecht, The Netherlands). Before modification with a polymer layer, the SPCE electrodes underwent electrochemical cleaning through cyclic voltammetry. This involved immersing the electrodes in a 0.5 M sulfuric acid solution and cycling the potential for 20 cycles at a sweep rate of 0.1 V/s within a potential range of -0.1 V to +1.2 V vs. Ag/AgCl. The polymer layer was deposited using a two-step electrochemical polymerisation procedure (Figure 8). In the first step, a Ppy underlayer was electrochemically deposited from a solution containing 0.1 M pyrrole in 10 mM PBS, pH 7.4, by applying a sequence of 5 potential pulses (+0.95 V for 1 s followed by 0 V for 30 s). In the second step, the anti-VEGF aptamer was added to the same polymerisation solution, and the sequence of 5 potential pulses was repeated. This process embeds the anti-

VEGF aptamer within the Ppy structure, enhancing the stability and support of the aptamer molecule. Pulsed Amperometric Detection (PAD) was employed to evaluate the Ppy-modified DNR-aptamer electrodes. The detection sequence consisted of 10 potential pulses of +600 mV vs Ag/AgCl for 2 seconds, followed by 0 V vs Ag/AgCl for 2 seconds.

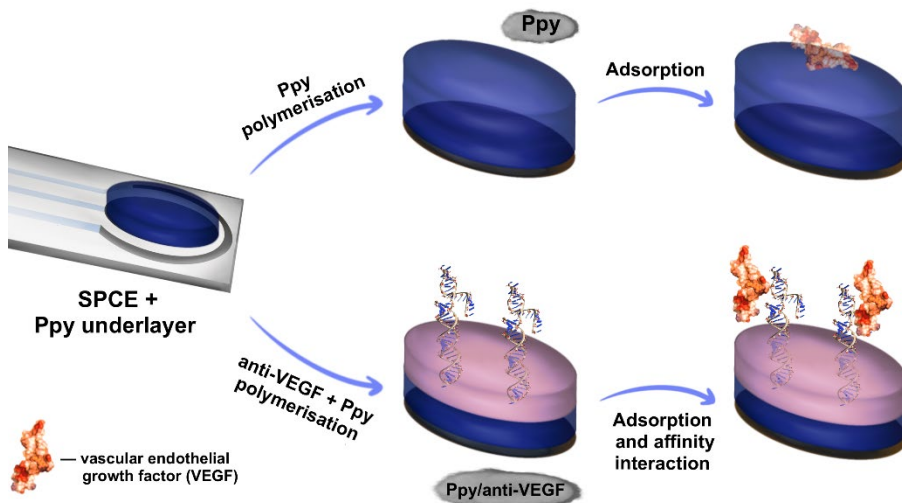


**Figure 8.** Schematic representation of two experimental setups applied for assessment of developed aptamer-based sensor.

### 3. RESULTS AND DISCUSSION

The results and discussion section is divided into 4 main subsections. Subsection 3.1., based on **Paper 1**, describes the electrodeposition process of MIP and NIP layers on SPCE electrodes using potential pulses, emphasising the crucial role of the Ppy-based underlayer in facilitating the formation of a robust MIP sensing layer. This underlayer reduces direct interaction with *Listeria monocytogenes* and allows precise entrapment of bacteria within the polymer matrix, improving detection sensitivity. Subsection 3.2., based on **Paper 2, Paper 3 and Paper 4**, presents the electrochemical characterisation of SAM-modified gold electrodes, detailing the effects of different SAMs on electron transfer properties and their impact on immunosensor performance. Subsection 3.3, based on **Paper 5**, demonstrates the implementation of a SAM-supported MIP detection method for SARS-CoV-2 nucleoprotein. This approach combines the MIP technique introduced in Section 3.1 with the use of a SAM underlayer discussed in Section 3.2, resulting in a composite structure. The SAM underlayer played a pivotal role in enhancing the formation and stability of the MIP sensing layer on electrodes, creating a controlled and optimised surface. This composite methodology significantly improved the sensor's performance, achieving enhanced sensitivity and specificity in detecting the SARS-CoV-2 nucleoprotein when compared to NIP-modified electrodes. Finally, Subsection 3.4, based on **Paper 6**, outlines the electrodeposition of a Ppy/anti-VEGF aptamer-based sensing layer on SPCE electrodes. The composite was formed by embedding the anti-VEGF aptamer within the Ppy matrix, creating a robust and functional sensing layer. Initially, a Ppy-based underlayer was deposited to ensure strong adhesion of the sensing layer and to minimise direct interaction between VEGF and the electrode surface.

#### 3.1. The detection of *Listeria Monocytogenes* bacteria using MIP-based electrochemical sensor

This section explores the application of MIPs for the electrochemical detection of *Listeria monocytogenes* bacteria, detailing the process from electrode modification to sensor evaluation. The methodology involves the electrochemical deposition of Ppy and Ppy+bacteria layers and the subsequent extraction of imprinted bacteria, followed by detailed electrochemical characterisation to assess the performance and sensitivity of the developed MIP sensor.

### 3.1.1. The electrodeposition of MIP and extraction of imprinted bacteria

The Ppy and Ppy+bacteria layers were electrochemically deposited onto SPCE electrodes using a series of potential pulses (Figure 9). Figures 9 A and D illustrate the potential pulse series profiles for the deposition of the Ppy layer on SPCE electrodes. The electrochemical formation of the Ppy+bacteria layer on SPCE electrodes was conducted in multiple steps, as detailed in the experimental section (Figure 4). Initially, a Ppy-based underlayer was electrodeposited to support and cover the electrode, reducing the direct interaction of *Listeria monocytogenes* bacteria with the electrode surface before forming the Ppy+bacteria sensing layer. This thin Ppy underlayer facilitated the subsequent formation of the Ppy+bacteria sensing layer. During the second step, *Listeria monocytogenes* bacteria were entrapped as templates within an upper Ppy layer (sensing layer), which, after bacteria removal, constituted the MIP layer. The electrochemical deposition of Ppy enabled precise control over the thickness of the formed layers and effective entrapment of *Listeria monocytogenes* bacteria within the electropolymerised matrix.

The entrapped bacteria were removed from the Ppy+bacteria layer by incubating the electrodes in various extraction solutions, resulting in the final MIP imprint. The first extraction method involved incubating Ppy and Ppy+bacteria electrodes with an acetic acid solution, as shown in Figures 10 A and B. Scanning electron microscopy (SEM) images of this process reveal the effectiveness of acetic acid in removing the bacteria. Acetic acid, a weak organic acid toxic to most bacteria even at concentrations as low as 0.5 wt%, disrupts bacterial cells by lowering intracellular pH and interfering with metabolic processes through its anion [107]. The SEM images vividly demonstrate the efficacy of acetic acid, which creates holes in the bacterial cell membranes, allowing cytosol and organelles to leak out. This results in rough, uneven pits on the cell surfaces, confirming the high effectiveness of this method. In contrast, when Ppy and Ppy+bacteria electrodes were incubated in a sulfuric acid solution, the surfaces of the electrodes remained unchanged, as depicted in Figures 10 C and D.

The third method investigated for extracting the *Listeria monocytogenes* bacterial template from the Ppy+bacteria involved using a trypsin enzyme solution. Trypsin, a well-known pancreatic enzyme, functions by hydrolysing peptide bonds, specifically at the C-terminal of arginine (Arg) and lysine (Lys) residues, leading to the breakdown of proteins into peptides [108].

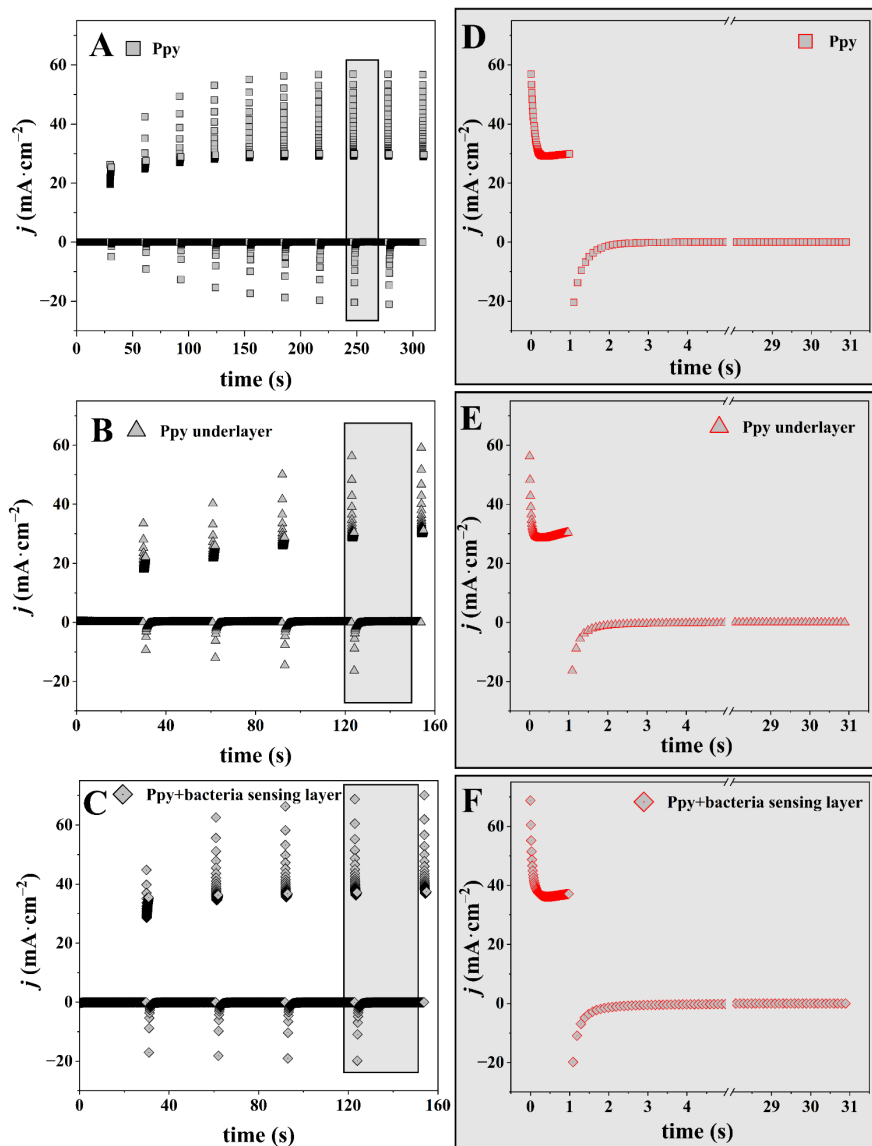


**Figure 9.** Electrochemical deposition of Ppy and Ppy+bacteria layers. The current profiles shown for the deposition of the Ppy layer on SPCE electrodes demonstrate the changes in current during the formation of the Ppy layer from a polymerisation solution that does not contain bacteria (A). Current profiles were registered during the electrochemical deposition of Ppy layers, Ppy underlayer (B), and Ppy+bacteria sensing layer with entrapped *Listeria monocytogenes* bacteria on SPCE electrodes (C). Insets (D – F) display an extended current profile during the indicated potential pulse.



In this study, trypsin effectively hydrolysed cell wall proteins, aiding in the removal of bacterial cells from the Ppy-based matrices. Notably, trypsin only targets specific areas of the cell wall and does not affect the Ppy layer, making it an ideal candidate for the selective removal of bacteria without damaging the underlying polymer structure. This characteristic is particularly useful for developing MIP-based sensor platforms. Comparative results (Figure 10 F) indicated that the trypsin-based extraction method was more efficient than other methods tested. Previous studies have highlighted the role of proteolytic enzymes like trypsin in bacterial lysis, with increased enzyme activity observed in inflammatory sites. For example, Grenier demonstrated that Gram-positive bacteria in the oral cavity exhibit greater resistance to lysis than Gram-negative bacteria [109]. Zhou et al. further showed that a concentration of 2 mg/mL trypsin had similar effects on both bacterial types, including biofilm formation [110]. The research revealed that a 10 U/mL trypsin solution is the most efficient method for removing *Listeria monocytogenes* cells from the Ppy layer and forming MIP. Notably, trypsin only targets specific areas of the cell wall and does not affect the Ppy layer, making it particularly useful for eliminating bacteria-based templates and creating MIP-based sensor platforms.

L-lysine, a zwitterionic amino acid, was also tested for its ability to dissociate and remove bacteria from Ppy-based matrices. As an amino acid and a zwitterion at pH = 7.0, L-lysine is expected to be more effective than trypsin in dissociating or removing certain compounds from polymeric structures. A comparison of the results (Figure 10 H) indicated that the trypsin-based extraction method was more effective than the L-lysine extraction method. Additionally, L-lysine plays a role in protein synthesis and is found in the peptidoglycan layer of Gram-positive cell walls of bacteria, aiding cell metabolism. This property highlights its significance in bacterial structure and function, although, in this context, the trypsin method proved superior for removing *Listeria monocytogenes* from the Ppy layer.

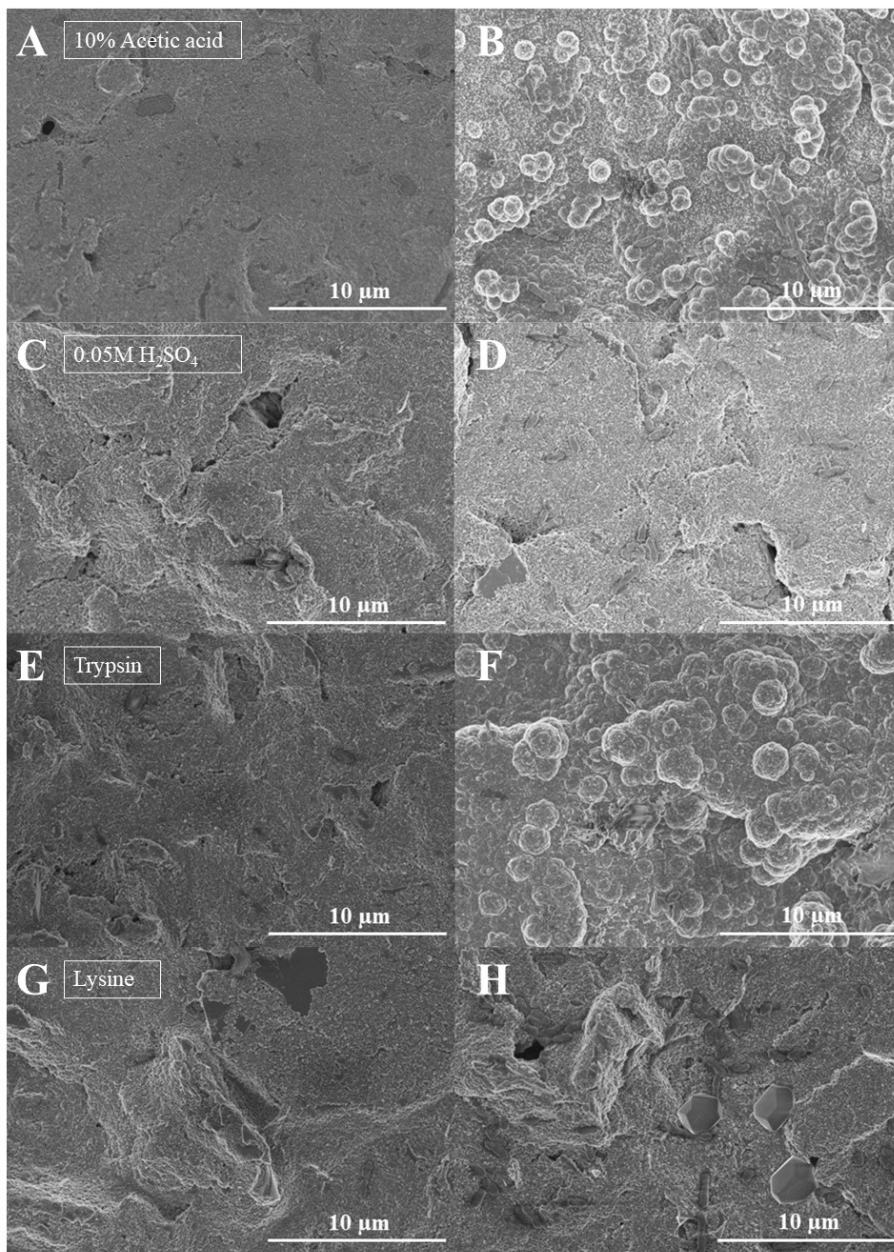


**Figure 10.** SEM images of NIP (A, C, E, G) and MIP (B, D, F, H) electrodes after incubation in different template extraction solutions: 10% acetic acid (A, B), 0.05 M sulphuric acid (C, D), 10 U/mL trypsin (E, F) and 0.1% L-lysine at 37°C for 30 min (G, H).

### 3.1.2. Electrochemical characterisation for bacteria-imprinted MIP layer

The NIP and MIP sensors were evaluated using pulsed amperometric detection, which measures current density in a series of 10 potential pulses of +600 mV for 2 s and 0 mV for 2 s. *Listeria monocytogenes* bacteria at concentrations ranging from  $3.4 \times 10^6$  to  $1.0 \times 10^8$  CFU/mL were incubated in a pH 7.4 PBS solution using SPCE electrodes modified with MIP and NIP. As the bacteria concentration increased, the amperometric response decreased, a common trend for redox-inactive analytes [111].

The effectiveness of various extraction solutions was assessed, including 10% acetic acid (Figure 11 A), 0.05 M sulfuric acid (Figure 11 B), 10 U/mL trypsin (Figure 11 C), and 0.1% L-lysine (Figure 11 D). For acetic acid, the current density of MIP was at least 12 times higher than that of NIP, indicating that it was highly effective, as shown in Figure 10. The current density barely changed when using the sulfuric acid solution. However, *Listeria monocytogenes* bacteria have an acid tolerance, a predicted molecular response that keeps the cells alive in an unfavourable environment. Morphological techniques confirmed the increased intracellular survival and the development of acid-adapted *Listeria monocytogenes* cells in the cytoplasm and vacuoles [112]. Various strategies were employed to address the *Listeria monocytogenes* bacteria acid-tolerance response. One approach involved using the enzyme trypsin to enhance the extraction process. Using this technique, the *Listeria monocytogenes* bacteria were effectively removed from the NIP and MIP layers (Figure 11 C). Finally, L-lysine (Figure 11 D) solutions were also tested. Trypsin-treated MIP exhibited a current density approximately three times higher than NIP, while L-lysine-treated MIP showed no change in current density. Electrochemical results indicated that electrical capacitance varied after removing the imprinted bacteria, with trypsin and acetic acid proving to be the most effective solution for releasing trapped *Listeria monocytogenes* bacteria and forming the MIP.

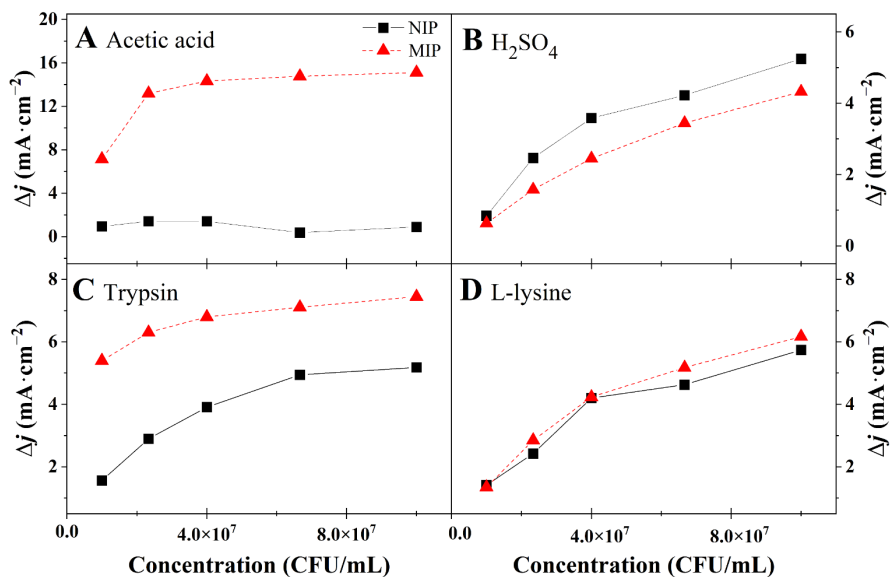


**Figure 11.** The current density of electrodes of NIP (solid black lines) and MIP (dashed red lines) was registered using PAD after incubation in solutions containing varying concentrations of *Listeria monocytogenes* bacteria. The bacteria were extracted using different solutions: 10% acetic acid (A), 0.05 M H<sub>2</sub>SO<sub>4</sub> (B), 10 U/mL trypsin (C), and 0.1% L-lysine (D).

### 3.1.3. Determination of the limit of detection, the limit of quantification and the imprinting factor

The efficiency of trypsin solution in extracting entrapped *Listeria monocytogenes* bacteria from the Ppy-based layer to form MIP was confirmed. Although both acetic acid and trypsin were effective extraction solutions, trypsin was ultimately preferred due to the acid tolerance of *Listeria monocytogenes*, which could diminish the effectiveness of acetic acid for application in real world diagnostics, where acid tolerant bacteria can be found. Electrochemical measurements based on PAD were performed to determine the LOD and LOQ (Equations 2 and 3). Analytical signals were represented by  $\Delta I$  values for NIP and MIP, respectively. Figure 12 illustrates *Listeria monocytogenes* bacteria concentration calibration curves plotted against  $\Delta I$  ( $\mu\text{A}$ ). The slope of the change in current ( $\Delta I$ ,  $\mu\text{A}$ ) versus the concentration of *Listeria monocytogenes* bacteria (expressed in CFU/mL) recorded by the NIP electrode was 0.016  $\mu\text{A}/(\text{CFU}/\text{mL})$ , with an  $R^2$  value of 0.98. Conversely, the linear regression slope for the *Listeria monocytogenes* bacteria-imprinted MIP was 0.063  $\mu\text{A}/(\text{CFU}/\text{mL})$ , with an  $R^2$  value of 0.97.

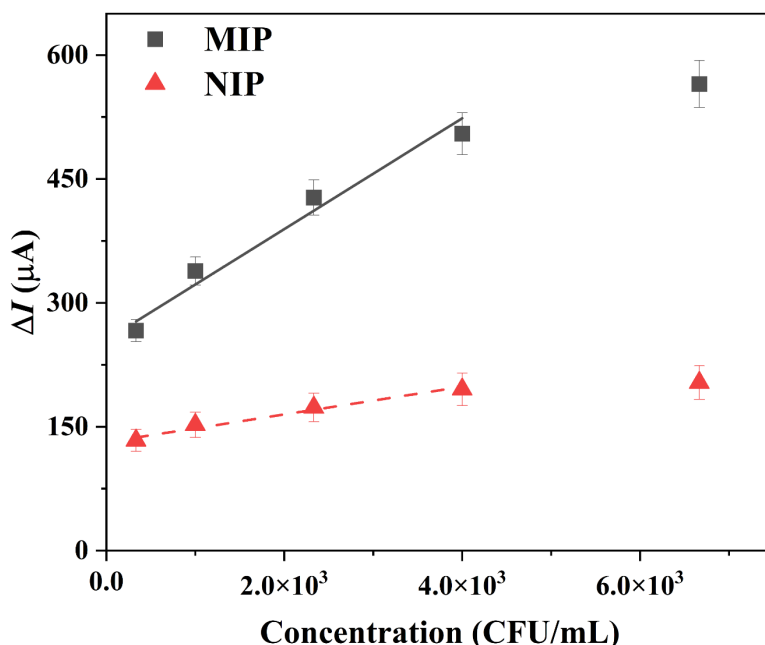


**Figure 12.** Calibration curve  $\Delta I$  registered by MIP (black line) and NIP (red line) vs. *Listeria monocytogenes* concentration. Error bars are expressed as the standard deviation of the sample.

Molecular imprinting is ranked according to the relationship between the MIP and the NIP, which is obtained according to Equation (4) [113,114]:

$$IF = \frac{I_{MIP}}{I_{NIP}} \quad (4)$$

Usually,  $IF$  is called an imprinting factor, whereas Ayerdurai et al. [115] argued that an *apparent imprinting factor* is a more correct term for  $IF$ . The results showed that, compared to the NIP electrode, the MIP had an *apparent imprinting factor* towards the *Listeria monocytogenes* bacteria that was roughly 3.93. If the value of  $IF$  exceeds 1, it indicates a high degree of molecular imprinting and strong specificity for the target analyte [113]. The LOD and the LOQ were calculated according to Equations (2) and (3). It was evaluated that the LOD and LOQ for the MIP were 70 CFU/mL and 210 CFU/mL, respectively, in the linear range from 300 to 6700 CFU/mL.

### 3.2. Detection of antibodies against SARS-CoV-2 rS using SAM-based detection method

This section explores the use of SAM to modify gold electrodes in order to enable the construction of a biosensor used for detecting antibodies against the SARS-CoV-2 rS protein. The study builds on the principles of EIS and CV to evaluate the performance of these SAM-based systems. The approach involves understanding how SAMs, particularly mixed SAMs (SAMmix), influence the surface properties and electron transfer characteristics of electrode surfaces.

The section is divided into two main parts. First, **subsection 3.2.1** discusses the evaluation of SAM layers using EIS, including the use of tethered bilayer lipid membranes (tBLMs) as model systems to assess SAM stability, defect density, and electron transfer properties. This foundational analysis provides insights into how SAM and mixed SAM systems behave in terms of surface modification and electrochemical performance.

In **subsection 3.2.2**, the focus shifts to the direct functionalisation and electrochemical characterisation of modified gold electrode surfaces. Gold electrodes, including square gold electrodes (Au(s)) and gold-coated microscopic slides (Au(MS)), are modified with SAMs and SAMmix systems. The electrochemical behaviour of these modified electrodes is characterised before and after surface treatments, providing detailed insights into their role in enhancing sensor detection capabilities.

#### 3.2.1. Electrochemical impedance spectroscopy-based evaluation of SAM and tethered bilayer lipid membranes layers

While the formation and characteristics of these monolayers have been widely studied on various substrates, including gold electrodes, the present study also includes the use of SAMmix systems. These SAMmix systems, when evaluated using tBLMs, demonstrate reduced defect density and improved stabilisation of electron transfer. This indicates that such an approach could enhance biosensing performance by ensuring better control over the structural integrity of the modified electrode surface. The detailed electrochemical analysis and impedance behaviour of both SAM and tBLM layers provide a crucial foundation for understanding the surface modifications that will be further explored in the following section for the design of a biosensor.

The Au(MS) were incubated for 3 hours in an ethanolic solution containing 0.1 mM  $\beta$ -mercaptoethanol ( $\beta$ ME) and 20-tetradecyloxy-

3,6,9,12,15,18,22-heptaohexatricontane-1-thiol (WC14) in a molar ratio of 65:35. This incubation allowed the formation of a Au(MS)/SAMmix, composed of  $\beta$ ME as a backfiller and synthetic thiolipid WC14 molecules.

Figure 13 A illustrates the typical changes in the EIS spectra following the formation of a tBLM on an anchor SAMmix. Specifically, the semicircle of the complex capacitance decreased by approximately tenfold, from  $8 \mu\text{F}\cdot\text{cm}^2$  before vesicle fusion and membrane formation to  $0.6\text{--}0.8 \mu\text{F}\cdot\text{cm}^2$  after tBLM formation. This decrease is attributed to the creation of a dielectric layer around 3 nm thick [116].

In this study, we examined two lipid compositions of tBLMs capable of incorporating chlorophyll-a. The EIS data enabled verification of tBLM integrity across different lipid ratios. The base composition consisted of DOPC and cholesterol (Chol) in a 6:4 molar ratio. Chl-a was introduced in two stages: first, replacing some DOPC to achieve a 5:4:1 molar composition of DOPC/Chol/Chl-a; then, cholesterol was replaced to create a 6:3:1 molar ratio. Across the various DOPC, Chol, and Chl-a ratios—ranging from 6:4 to 5:4:1 and 6:3:1—only slight changes in tBLM capacitance were observed, which were not statistically significant (Figure 13 C). However, if the defectiveness is analysed, the inclusion of Chl-a into DOPC/Chol tBLMs was found to be an important factor in determining the defect densities in tBLMs. The algorithm described in [117], was used to estimate the defect densities in tBLMs with and without Chl-a. The algorithm relates defect density in membranes with the position of the phase minima in the negative of impedance phase vs frequency plots. The Equation 5 was used to calculate approximate densities is:

$$\lg N_{def} \approx 0.93 \lg f_{min} - \lg k - 0.2 \lg r_0 - const \quad (5)$$

where  $N_{def}$  the defect density in  $\mu\text{m}^{-2}$ ,  $f_{min}$  the frequency of the negative of phase minimum, Hz,  $k = 1.6 \cdot 10^{-6} \text{ cm}^2 \cdot \text{s}^{-1}$ ,  $r_0 = 1 \text{ nm}$  and  $const = 1.24$ , one obtains the approximate values of defect densities in tBLMs of different composition. The calculated according to Equation 5 defect densities are  $0.87 \pm 0.09 \mu\text{m}^{-2}$  for DOPC/Chol (6:4),  $0.73 \pm 0.08 \mu\text{m}^{-2}$  for DOPC/Chol/Chl-a (6:3:1) and  $0.16 \pm 0.08 \mu\text{m}^{-2}$  for DOPC/Chol/Chl-a tBLMs.

As shown in Figure 2D, the introduction of Chl-a significantly reduced defectiveness, particularly in the 5:4:1 DOPC/Chol/Chl-a composition, where defect density was six times lower than that of the base DOPC/Chol (6:4) composition, and lower compared to the 6:3:1 mixture. This sharp reduction in defects for the 5:4:1 composition may be due to the combined destabilising

effects of cholesterol and Chl-a, as cholesterol's conical shape destabilises defects in highly curved bilayer fragments like transient pores, while Chl-a's inverted cone shape likely contributes to further destabilization. Together, these effects enhance bilayer stiffness by forming complementary pairs with cholesterol.

Interestingly, the defect density was lower in the DOPC/Chol/Chl-a (6:3:1) mixture, underscoring the importance of the total concentration of Chol and Chl-a in influencing membrane properties. Overall, Chl-a was found to induce a significant decrease in tBLM capacitance, likely due to its lower relative dielectric constant compared to the dioleoyl fragment in DOPC. However, substituting cholesterol with Chl-a did not result in a similar magnitude of decrease, suggesting that Chl-a and Chol have comparable dielectric properties. Another key effect of Chl-a incorporation was a significant reduction in membrane defectiveness, especially when the total content of Chol and Chl-a reached 50% of the membrane lipid composition.

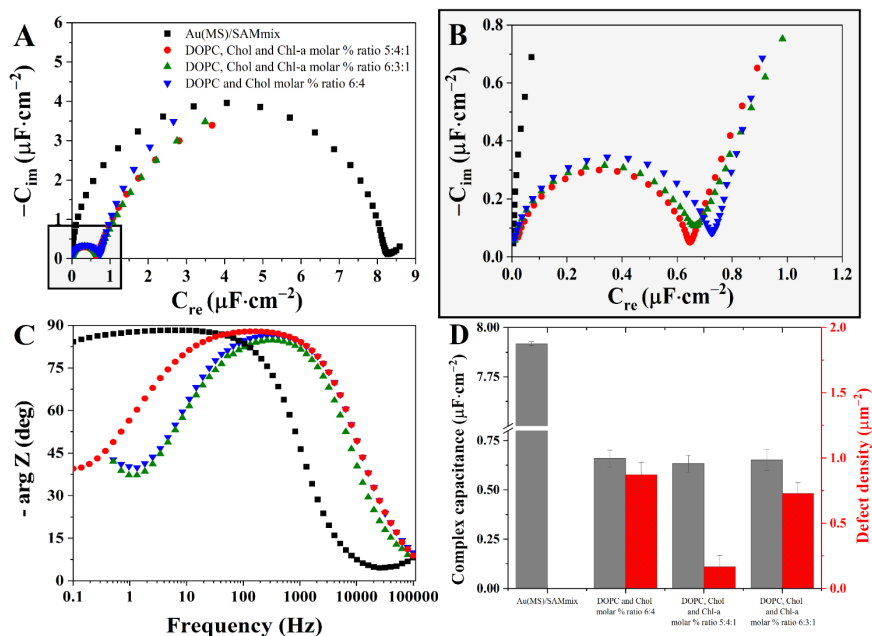


**Figure 13.** Cole-Cole plot of EIS spectra (A), (B) of (▪) a Au(MS)/SAMmix and tBLM structure formed at different molar % ratios of various components: (•) – DOPC, Chol and Chl-a at molar % ratio of 5:4:1, respectively, (▲) – DOPC, Chol and Chl-a at molar % ratio of 6:3:1, respectively, (▼) – DOPC and Chol at molar % ratio of 6:4, respectively. Bode coordinates (C) – frequency dependence on complex phase shift (frequency was applied until phase minimum was reached), complex capacitance, and defect density of



various components tBLM structures (D). Bias potential 0 V vs Ag/AgCl/NaCl<sub>sat</sub>.

However, in the subsequent stages of this study, the focus shifts away from the use of tBLMs as the investigation moves towards the application of different SAM systems for direct functionalisation of gold electrodes. These SAMs, particularly the SAMmix on Au(MS), will be evaluated independently using electrochemical techniques, allowing for a more focused examination of their role in enhancing detection capabilities in biosensing platforms. The detailed characterisation of these SAM layers is key to understanding the modifications and their direct impact on electrode performance, as presented in the next section.

### 3.2.2. The electrochemical characterisation of a modified gold electrode surface

Building upon these insights, the following study employs similar SAM-based approaches, applying them to gold electrodes enabling the creation of immunosensor used for the detection of antibodies against the SARS-CoV-2 rS protein. Electrochemical techniques, including CV and EIS, were used to probe the modifications and their impact on the electrode surfaces. Both square gold electrodes (Au(s)) and gold-coated microscopic slides (Au(MS)) were characterised before and after surface treatments.

Initially, the Au(s) electrode was modified with an 11-MUA, forming a SAM. The  $[\text{Fe}(\text{CN})_6]^{3-/4-}$  redox couple was used to probe the influence of these modifications on electrode conductivity through changes in oxidation and reduction peaks in the cyclic voltammogram. The formation of the 11-MUA SAM resulted in a stable and well-organised monolayer, acting as an ionic insulator on the gold electrode. This SAM, characterised by a low defect rate and high fractional coverage, obstructed the electron transfer pathway, leading to a substantial reduction in the current response, as shown in Figure 14 A.

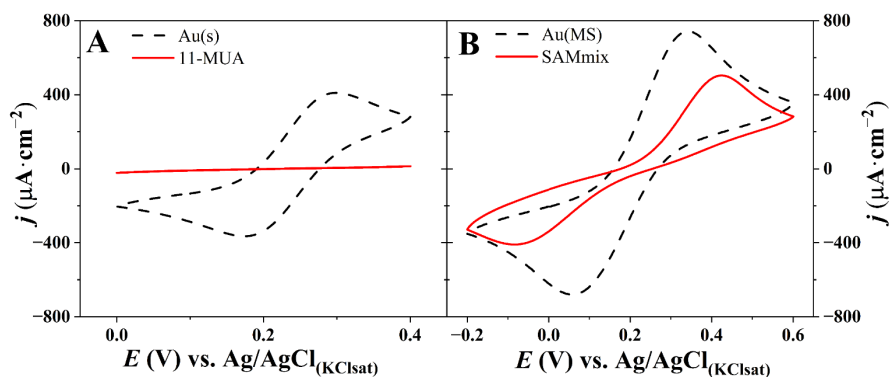


**Figure 14.** Cyclic voltammograms of the Au(s) electrode (A) and Au(MS) electrode (B). Potential scans range from 0 to +0.4 V (A) and from -0.2 to +0.6 V (B) at  $50 \text{ mV}\cdot\text{s}^{-1}$  vs  $\text{Ag}/\text{AgCl}(\text{KCl}_{\text{sat}})$ .

For the Au(MS) electrode, a mixed SAM (SAMmix) consisting of 6-MCOH and 11-MUA was applied. The SAMmix was designed to maintain stability while allowing redox mediator access to the electrode surface, reducing pinholes and structural defects. The cyclic voltammogram for the unmodified Au (MS) electrode (Figure 14 B) showed typical redox behaviour with a peak current density of  $712.4 \pm 5.9 \mu\text{A}\cdot\text{cm}^{-2}$ . After the formation of the SAMmix, the peak current density decreased to  $504.6 \pm 19.3 \mu\text{A}\cdot\text{cm}^{-2}$ , indicating restricted electron transfer due to the mixed SAM layer. EDC-NHS activation of the terminal carboxyl groups caused a slight increase in current density to  $513.1 \pm 6.6 \mu\text{A}\cdot\text{cm}^{-2}$ , suggesting enhanced electron transfer. However, the subsequent immobilisation of rS protein led to a further decrease in current density to  $459.6 \pm 9.3 \mu\text{A}\cdot\text{cm}^{-2}$ , attributed to the additional barrier formed by the protein layer.

EIS measurements provided detailed insight into the changes in charge transfer resistance ( $R_{\text{ct}}$ ) associated with each modification step. As depicted in Figure 15 A, the  $R_{\text{ct}}$  of the Au(s) electrode increased significantly with the formation of the 11-MUA SAM, reaching  $10.6 \pm 0.2 \text{ k}\Omega\cdot\text{cm}^2$ . This increase is attributed to the insulating nature of the SAM, which obstructs the movement of  $[\text{Fe}(\text{CN})_6]^{3-/4-}$  ions and hinders electron transfer at the electrode interface. Activating the 11-MUA carboxyl groups with EDC and NHS resulted in a reduced  $R_{\text{ct}}$  of  $5.67 \pm 0.09 \text{ k}\Omega\cdot\text{cm}^2$ , likely due to the formation of an electrochemically active ester, facilitating electron transfer. The subsequent immobilisation of rS protein increased  $R_{\text{ct}}$  to  $12.3 \pm 0.27 \text{ k}\Omega\cdot\text{cm}^2$ , as the protein layer adds another barrier to electron transfer.

In contrast, the modifications of Au(MS) electrode showed a different pattern of  $R_{\text{ct}}$  changes, as illustrated in Figure 15B. The  $R_{\text{ct}}$  for the unmodified

Au(MS) electrode was  $98.2 \pm 1.2 \Omega \cdot \text{cm}^2$ , which increased to  $803 \pm 10 \Omega \cdot \text{cm}^2$  with the formation of the SAMmix. This increase, although significant, is lower than the  $R_{ct}$  for the Au(s) with the 11-MUA SAM, likely due to the different composition and properties of the SAMmix, which allows some electron transfer while still providing a barrier. Following activation with EDC and NHS, the  $R_{ct}$  decreased, likely due to the formation of an electrochemically active ester that facilitated electron transfer. However, the subsequent immobilisation of the rS protein caused the  $R_{ct}$  to rise again to  $1202 \pm 23 \Omega \cdot \text{cm}^2$ , as the protein layer added another barrier to electron transfer (Table 2).

It was observed that the  $R_{ct}$  of the NHS and EDC-activated either Au(s)/11-MUA or Au(MS)/SAMmix electrodes substantially decreased compared to its value before activation. The activation process involving EDC and NHS results in the formation of an intermediate electrochemically active ester due to the interaction between the terminal carboxyl (-COOH) groups and EDS and NHS. The increase in  $R_{ct}$  following the binding of rS is attributed to the poor electrical conductivity of most proteins at low frequencies, which impedes charge transfer at the electrode-solution interface. These EIS data are consistent with previous studies, which used Total Internal Reflection Ellipsometry to evaluate the interactions between SARS-CoV-2 proteins and their specific antibodies. Those studies demonstrated significant increases in protein layer thickness and changes in dielectric properties occurring at the electrode-solution interface [118].

The observed differences in  $R_{ct}$  between the Au(s) and Au(MS) systems are primarily due to the nature of the surface modifications and the specific characteristics of the SAM layers. The 11-MUA SAM on the Au (s) electrode forms a highly insulating layer with minimal defects, leading to a significant increase in  $R_{ct}$ . In contrast, the SAMmix on the Au (MS) electrode, while still increasing  $R_{ct}$ , allows for electron transfer due to its composition and structure.

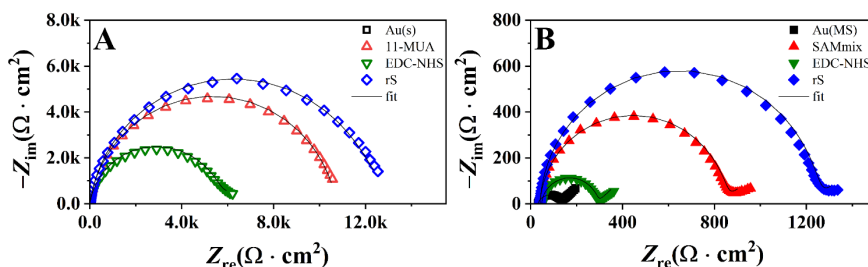


**Figure 15.** Nyquist plots of differently modified electrodes: Au (s) electrode (A) and Au (MS) electrode (B). A – Au (s) electrode ( $\square$ ), electrode after 11-MUA formation ( $\blacktriangle$ ), EDC-NHS electrode after activation of 11-MUA ( $\blacktriangledown$ ),

and rS electrode after immobilisation of SARS-CoV-2 rS protein (◆). **(B)** – Au (MS) electrode (■), electrode after SAMmix formation (▲), EDC-NHS electrode after activation of SAMmix (▼), and rS electrode after immobilisation of SARS-CoV-2 rS protein (◆). EIS measurements were performed in the PBS, pH 7.4, in the presence of 2 mM of  $[\text{Fe}(\text{CN})_6]^{3-/4-}$  at 0.2 V vs Ag/AgCl( $\text{KCl}_{\text{sat}}$ ), signal normalised to the area of the electrode,  $A = 2 \text{ cm}^2$  for Au(s) electrode **(A)** and  $A = 0.179 \text{ cm}^2$  for Au(MS) electrode **(B)**.

**Table 2.** Analytical parameters obtained from CV and EIS. Error bars are expressed as the standard deviation of the sample.

|                | $j_{\text{pa}}, \mu\text{A}\cdot\text{cm}^{-2}$ | $R_s, \Omega\cdot\text{cm}^2$ | $R_{\text{ct}}, \Omega\cdot\text{cm}^2$ | $C_{\text{dl}}, \mu\text{F}$ | $n$  |
|----------------|---|-------------------------------|---|------------------------------|------|
| <b>Au(s)</b>   | $410.4 \pm 9.6$                                 | $14.45 \pm 0.07$              | $96.2 \pm 1.2$                          | $80.1 \pm 0.4$               | 0.92 |
| <b>11-MUA</b>  | -   | $9.8 \pm 0.3$                 | $10600 \pm 200$                         | $9.7 \pm 0.1$                | 0.92 |
| <b>EDC-NHS</b> | -   | $9.8 \pm 0.2$                 | $5670 \pm 90$                           | $11.1 \pm 0.1$               | 0.91 |
| <b>rS</b>      | -   | $10.7 \pm 0.2$                | $12300 \pm 270$                         | $11.4 \pm 0.1$               | 0.92 |
| <b>Au (MS)</b> | $712.4 \pm 5.9$                                 | $32.1 \pm 0.3$                | $98.8 \pm 1.2$                          | $84.1 \pm 0.3$               | 0.83 |
| <b>SAMmix</b>  | $504.6 \pm 19.3$                                | $41.2 \pm 0.5$                | $803 \pm 10$                            | $9.1 \pm 0.5$                | 0.97 |
| <b>EDC-NHS</b> | $513.1 \pm 6.6$                                 | $48.4 \pm 0.7$                | $239 \pm 21$                            | $10.2 \pm 0.5$               | 0.96 |
| <b>rS</b>      | $459.6 \pm 9.3$                                 | $41.2 \pm 0.6$                | $1202 \pm 23$                           | $8.4 \pm 0.5$                | 0.97 |

These findings demonstrate the stepwise impact of surface modifications on the electrochemical properties of gold electrodes. The initial 11-MUA SAM provided a stable and insulating layer, while the SAMmix, EDC-NHS activation, and protein immobilisation introduced progressive changes in electron transfer characteristics. This comprehensive characterisation underscores the importance of each modification stage in tailoring the surface properties of gold electrodes for specific electrochemical applications. In later experiments targeting antibody detection against the rS protein, the 11-MUA SAM was not used due to its high  $R_{\text{ct}}$  and insulating properties, which hindered electron transfer. Instead, the SAMmix system was adopted for its balanced stability and efficient electron transmission, significantly enhancing the sensitivity and effectiveness of the antibody detection process.

### 3.2.3. The analytical characterisation of immunosensor dedicated for anti-rS detection

The affinity interaction between anti-rS antibodies and immobilised rS proteins was studied by sequentially incubating the working electrode surface with varying concentrations of anti-rS in a 10 mM PBS solution, starting at

30 nM and increasing up to 150 nM through successive dilutions of a stock solution (Figure 16). EIS measurements were performed in PBS, 7.4, containing 2 mM  $[\text{Fe}(\text{CN})_6]^{3-/4-}$ , using previously detailed parameters. As anti-rS interacts with immobilised rS, an immune complex forms, progressively insulating the electrode surface. This reduces the flow of  $[\text{Fe}(\text{CN})_6]^{3-/4-}$  to the electrode, leading to a stepwise decrease in the redox current. Notably, at lower anti-rS concentrations (0–90 nM), the current densities decrease more rapidly, whereas at higher concentrations (90–150 nM), the process approaches saturation. This is reflected in the Nyquist plots, where the semicircle radius increases with anti-rS concentration, indicating increased  $R_{ct}$ . EIS data shows a significant increase in the semicircle radius at lower concentrations (0–90 nM), which slows down at higher concentrations (90–150 nM). As the concentration of anti-rS increases, the number of unoccupied rS sites decreases, resulting in a plateau effect in  $R_{ct}$  values at higher concentrations. Table 3 summarises the signal values obtained from EIS, showing the increase in  $R_{ct}$  levels off at higher anti-rS concentrations.

**Table 3.** Analytical parameters obtained from EIS. Error bars are expressed as the standard deviation of the sample.

| <i>Anti-rS concentration</i> | $R_s, \Omega \cdot \text{cm}^2$ | $R_{ct}, \Omega \cdot \text{cm}^2$ | $C_{dl}, \mu\text{F}$ | $n$   |
|------------------------------|---------------------------------|------------------------------------|-----------------------|-------|
| 0 nM                         | 41.4±2.7                        | 1300±105                           | 8.35±0.4              | 0.976 |
| 30 nM                        | 37.9±2.5                        | 1840±165                           | 8.6±0.6               | 0.973 |
| 60 nM                        | 44.1±2.4                        | 2600±212                           | 9.1±0.6               | 0.972 |
| 90 nM                        | 40.5±2.1                        | 3360±286                           | 9.45±0.7              | 0.975 |
| 120 nM                       | 43.4±2.2                        | 3570±259                           | 9.51±0.8              | 0.973 |
| 150 nM                       | 39.4±2.3                        | 3750±319                           | 9.652±0.7             | 0.975 |

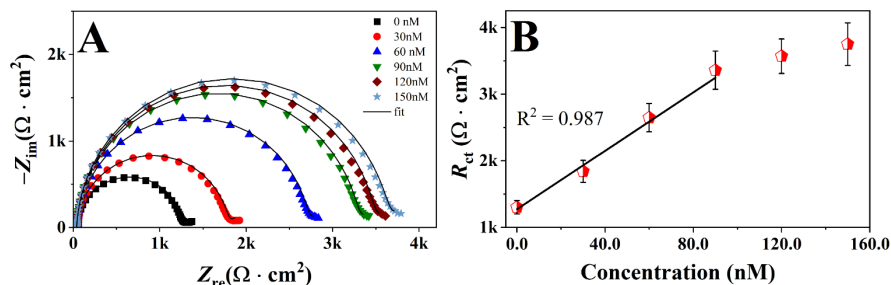


**Figure 16.** Nyquist plots of the modified Au(MS)/SAMmix/rS electrode (A) after affinity interaction with anti-rS of different concentrations (0–150 nM). Calibration curves for  $R_{ct}$  obtained from EIS are shown in relation to anti-rS

concentration (**B**). Error bars are expressed as the standard deviation of the sample. EIS measurements were performed from 100 kHz to 0.1 Hz, at 10 mV amplitude and applied potential 0.2 V vs Ag/AgCl<sub>(KCl<sub>sat</sub>)</sub> in PBS, pH 7.4, while adding 2 mM of [Fe(CN)<sub>6</sub>]<sup>3-/4-</sup>, signal normalised to the area of the electrode,  $A = 0.179 \text{ cm}^2$ .

To evaluate the analytical characteristics of the electrochemical immunosensor, LOD and LOQ for sensing anti-rS were calculated from data gathered using EIS measurements (Equations 2 and 3). As a signal, the  $R_{ct}$  value was obtained from fitting EIS data using Randles equivalent circuit. As a result, the immunosensor for anti-rS detection using EIS based on the  $R_{ct}$  value had a LOD of 2.78 nM and LOQ of 9.17 nM.

### 3.3. The detection of the SARS-CoV-2 nucleoprotein using the SAM-supported MIP detection method

In the case of of *Listeria monocytogenes* sensor, a Ppy-based underlayer was electrodeposited to minimise the direct interaction of electrode surface with the bacteria (Chapter 3.1.). This thin Ppy underlayer facilitated the subsequent formation of the MIP sensing layer. However, for this study the SAM was adopted as an underlayer because it offers enhanced performance and a more controlled surface for the sensor development. SAMs provide a robust interface between the Au(SPE) surface and the polymer layers, which is crucial for biosensor applications [119]. Particularly in biosensors, the stability of the conducting polymer layer on the electrode is critical for long-term performance. To improve the stability and interaction between the Au(SPE) surface and the Ppy layer, pyrrolyl-terminated alkanethiol (PUT) was introduced to form the SAM. Acting as a bridge, this SAM creates a transition system between the SAM and the Ppy film. Previous studies have shown that strong dipole-dipole interactions between the pyrrolyl end groups contribute to the formation of the PUT SAM [55]. The polymerisation reaction between the pyrrolyl-terminated alkanethiol in the SAM and the pyrrole molecules in the polymerisation solution was expected to enhance the stability of the Ppy film formed on the gold electrode.

#### 3.3.1. Electrochemical characterisation of Au(SPE) surface modified by SAMs

The SWV and EIS methods were used to characterise the Au(SPE) and Au(SPE)/SAM electrodes using a [Fe(CN)<sub>6</sub>]<sup>3-/4-</sup> couple as a redox probe. The

analysis of oxidation peaks in square wave voltammograms (Figure 17 A) led to research into the impact of surface modifications on the electrical conductivity of the working electrode. The Au(SPE)/SAM electrode had a significant decrease in peak current density from  $2.63 \pm 0.21$  to  $1.06 \pm 0.09 \text{ mA}\cdot\text{cm}^{-2}$  compared to the bare Au(SPE) electrode. Furthermore, the Nyquist plots were an efficient tool for monitoring impedimetric characteristics and conducting theoretical analysis of impedance properties (Figure 17 B). Using an analogous circuit provided insights into chemical transformations and processes on the conductive electrode surface. Figure 17 B shows the redox probe's response regarding imaginary impedance ( $-Z_{\text{im}}$ ) and real impedance ( $Z_{\text{re}}$ ). The Randles equivalent circuit was used to evaluate EIS data (Figure 17 B). The studied frequency range was 100 kHz to 0.1 Hz. The development of the Au(SPE)/SAM resulted in a charge transfer resistance ( $R_{\text{ct}}$ ) increase almost tenfold from  $5.48 \pm 0.07$  to  $47.5 \pm 0.9 \Omega\cdot\text{cm}^2$ .

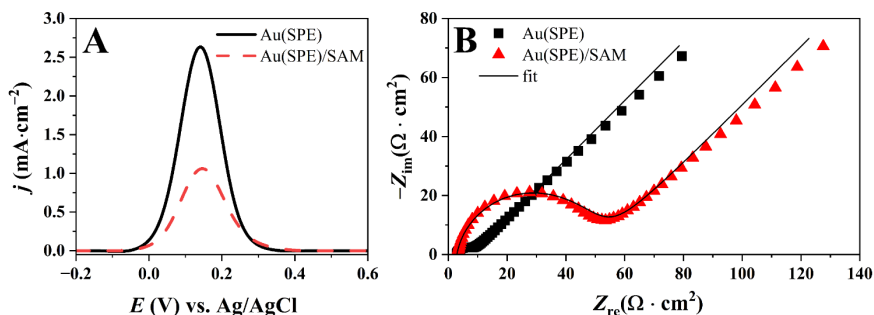


**Figure 17.** Square wave voltammograms (A) and Nyquist plot (B) of Au(SPE) and Au(SPE)/SAM electrodes. SWV and EIS measurements were performed in 10 mM PBS, pH 7.4, with 2.5 mM of  $[\text{Fe}(\text{CN})_6]^{3-/4-}$ . SWV: step size of 4 mV, frequency of 20 Hz, and a pulse height of 50 mV vs. Ag/AgCl in the potential range from  $-0.2 \text{ V}$  to  $+0.6 \text{ V}$ . EIS was registered at open circuit potential (OCP) in the frequency range from 100 kHz to 0.1 Hz, with an amplitude of 10 mV.

### 3.3.2. Electrodeposition of MIP- and NIP-based layers

SWV was used to evaluate the Au(SPE)/SAM/Ppy and Au(SPE)/SAM/(Ppy+rN) electrodes in the presence of  $[\text{Fe}(\text{CN})_6]^{3-/4-}$  as a redox probe (Figure 18 A). The SWV analysis indicated electrode features following Ppy electropolymerisation, most notably a drop in current intensity associated with oxidation peak. The square wave voltammogram for the Au(SPE)/SAM/Ppy electrode exhibited a higher peak current compared to the SPE/SAM/(Ppy+rN) electrode. This increased current is attributed to the

lower thickness of the Au(SPE)/SAM/Ppy electrode. After extracting the template from SPE/SAM/(Ppy+rN), the redox peak increased significantly ( $0.44 \pm 0.03 \text{ mA} \cdot \text{cm}^{-2}$ ), surpassing SPE/SAM/NIP ( $0.19 \pm 0.06 \text{ mA} \cdot \text{cm}^{-2}$ ), showing the presence of imprinted cavities that enhance charge transfer.

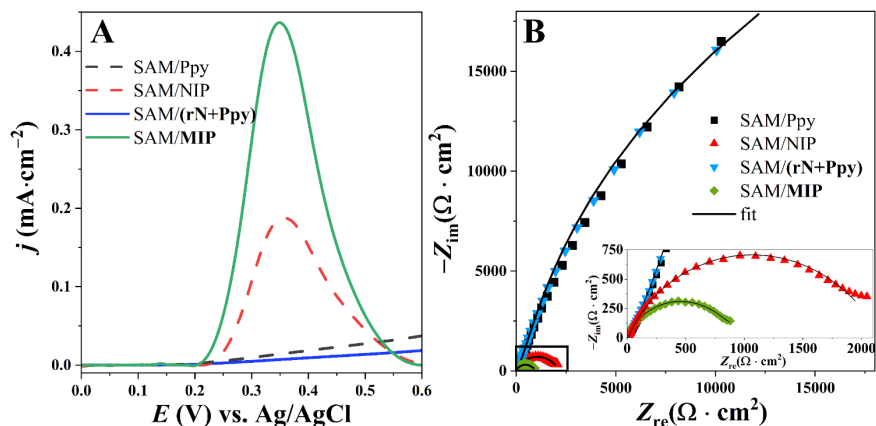


**Figure 18.** Square wave voltammograms (A) of Au(SPE)/SAM/Ppy (—), Au(SPE)/SAM/NIP (---), Au(SPE)/SAM/(Ppy+rN) (-·-) and Au(SPE)//SAM/MIP (-·-·) electrodes, Nyquist plot (B) and Inset in (B): enlarged view of the Nyquist plot for detailed analysis. SWV and EIS measurements were performed in 10 mM PBS, pH 7.4, with 2.5 mM of  $[\text{Fe}(\text{CN})_6]^{3-/4-}$ . SWV: step size of 4 mV, frequency of 20 Hz, and a pulse height of 50 mV vs. Ag/AgCl in the potential range from 0 V to +0.6 V. EIS was registered at open circuit potential (OCP) in the frequency range from 100 kHz to 0.1 Hz, with an amplitude of 10 mV.

EIS was used to further characterise the Au(SPE)/SAM/Ppy and Au(SPE)/SAM/(Ppy+rN) electrodes, using the identical redox probe ( $[\text{Fe}(\text{CN})_6]^{3-/4-}$ ) (Figure 18 B). The EIS data were fitted using an equivalent electrical circuit (EEC), and the best optimal fit was obtained with EEC ( $R_s + C_{dl}/R_{ct} + C_2/R_3$ ), which included three serial components.  $R_s$  represented electrolyte resistance, while the first Nyquist semi-circle was determined by parallel components  $C_{dl}$  and  $R_{ct}$ , which represented the constant phase element (CPE) and charge transfer resistance, respectively. The second Nyquist semi-circle included parallel parts  $C_2$  and  $R_3$ , which represented CPE and charge transfer resistance, respectively. This circuit model successfully characterises porous structures.  $C_{dl}$  and  $C_2$  are viewed as non-ideal capacitances influenced by surface features. The relation between these constant phase elements (CPE) and the impedance ( $Z$ ) is given by Equation 6:



$$Z_{CPE} = \frac{1}{Q(j\omega)^n} \quad (6)$$

where  $j$  is the imaginary number,  $\omega$  is the angular frequency and  $n$  is the correction factor ( $0 < n < 1$ ). If the value  $n$  tends to 0, the CPE becomes less capacitive [120,121]. The selection of the equivalent circuit depended upon the fitting of the Nyquist plot to produce the lowest error.

Removing the nucleocapsid template from SPE/SAM/(Ppy+rN) resulted in increased electron transport and lower impedance (Figure 14 B). This resulted in a change in the EEC from the prior model ( $R_s + C_{dl}/R_{ct} + C_2/R_3$ ) to the Randles equivalent circuit, which reflects enhanced electron transfer dynamics due to altered surface morphology. While changes in the Nyquist plot were not apparent after template removal, the Bode plot (Figure 19) provided more insight into these dynamics. The shift to the Randles circuit was more evident in the Bode plot, providing a better understanding of electron transport variations caused by cavity introduction on the electrode surface.

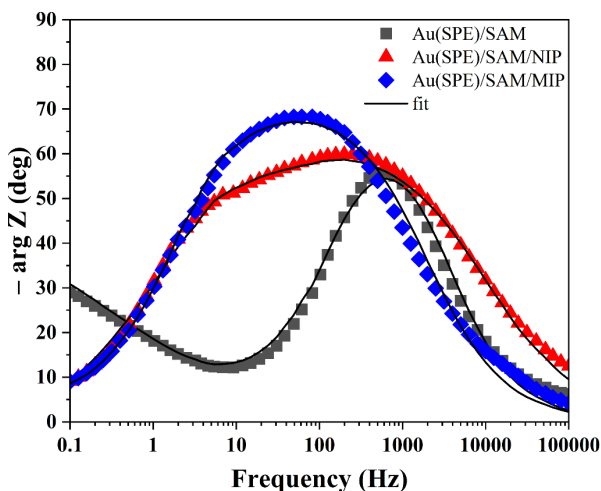


**Figure 19.** Bode plot of EIS spectra of Au(SPE)/SAM (■), Au(SPE)/SAM/NIP (▲) and the Au(SPE)/SAM/MIP (◆) — frequency dependence on complex phase shift (frequency was applied until phase minimum was reached). EIS was registered at open circuit potential (OCP) in the frequency range from 100 kHz to 0.1 Hz, with an amplitude of 10 mV. Measurements were performed in 10 mM PBS, pH 7.4, with 2.5 mM of  $[\text{Fe}(\text{CN})_6]^{3-/4-}$ .

Furthermore, comparing Au(SPE)/SAM/Ppy and Au(SPE)/SAM/(Ppy+rN) post-template extraction found that the EEC for Au(SPE)/SAM/NIP electrode remained consistent with the two-semicircle model, indicating minor changes in electrochemical properties. This emphasises the specificity of molecular imprinting in SPE/SAM/MIP and its impact on sensor surface electrochemical behaviour and selectivity. After template extraction, Au(SPE)/SAM/NIP had a greater charge transfer resistance ( $R_{ct} = 1975 \pm 9 \Omega \cdot \text{cm}^2$ ) than Au(SPE)/SAM/MIP ( $R_{ct} = 879 \pm 3 \Omega \cdot \text{cm}^2$ ) due to imprinted cavities that promote electron transfer.

The SWV and EIS results were further confirmed by SEM micrographs of the comparative surfaces of the Au(SPE) electrode and the modified Au(SPE)/SAM electrode with Ppy (Figure 20). The SEM micrograph of the bare Au(SPE) electrode (Figure 20 A) showed round bulges. In contrast, the SEM micrograph of the Au(SPE)/SAM/NIP electrode (Figure 20 B) displayed a distinctive asphalt-like appearance, indicating a transformation in surface morphology. Furthermore, the SEM micrograph of the Au(SPE)/SAM/MIP electrode (Figure 20 C) revealed the presence of cavities on the surface, indicating the successful creation of MIP and contributing to a unique and tailored topography.

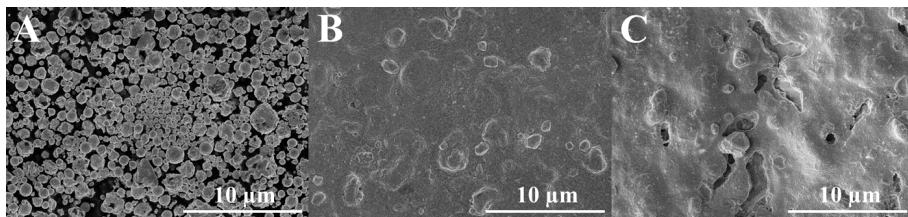


**Figure 20.** SEM micrographs of Au(SPE) electrode (A), Au(SPE)/SAM/NIP (B) and Au(SPE)/SAM/MIP (C) electrode surface.

### 3.3.3. Electrochemical characterisation and detection of the rN protein

The ability of the biosensor to detect the rN protein was tested using a series of electrochemical experiments. Au(SPE)/SAM/MIP electrodes were incubated for 5 minutes with rN protein concentrations ranging from 0 to 35 nM in a 10 mM PBS, pH 7.4, solution containing  $[\text{Fe}(\text{CN})_6]^{3-/4-}$ . Impedance responses were investigated for Au(SPE)/SAM/NIP and Au(SPE)/SAM/MIP modified electrodes. As the rN protein concentration increased, the  $R_{ct}$  for Au(SPE)/SAM/MIP electrodes also increased. In contrast, the  $R_{ct}$  for Au(SPE)/SAM/NIP electrodes remained constant, demonstrating the molecularly imprinted layer selectivity compared to its non-imprinted counterpart. Additionally, SWV measurements were performed

after the incubations. The voltammograms showed a gradual narrowing of the potential window from 0.2 V to 0.5 V, accompanied by a corresponding decrease in current density. The current density values decreased from  $0.44 \pm 0.03 \text{ mA}\cdot\text{cm}^{-2}$  in the solution with 0 nM of rN protein to  $0.278 \pm 0.063 \text{ mA}\cdot\text{cm}^{-2}$  in the solution with 35 nM (Figure 18).

SWV and EIS electrochemical measurements were used to determine the LOD and LOQ (Figure 21). SPE/SAM/NIP and SPE/SAM/MIP electrodes were analysed using  $\Delta j$  and  $R_{ct}$  values, respectively. The SWV approach was used to generate calibration curves that plot rN protein concentration against  $\Delta j$  ( $\text{mA}\cdot\text{cm}^{-2}$ ). The Au(SPE)/SAM/MIP electrode showed a linear regression slope of  $7.75 \text{ mA}\cdot\text{cm}^{-2}\cdot\text{nM}^{-1}$  ( $R^2 = 0.97$ ), while the Au(SPE)/SAM/NIP electrode had a slope of  $0.57 \text{ mA}\cdot\text{cm}^{-2}\cdot\text{nM}^{-1}$  ( $R^2 = 0.97$ ). The slope of  $R_{ct}$  ( $\Omega\cdot\text{cm}^2$ ) vs rN protein concentration for the Au(SPE)/SAM/MIP electrode was  $37.52 \Omega\cdot\text{cm}^2\cdot\text{nM}^{-1}$  ( $R^2 = 0.99$ ), while for the Au(SPE)/SAM/NIP electrode it was  $4.77 \Omega\cdot\text{cm}^2\cdot\text{nM}^{-1}$  ( $R^2 = 0.96$ ). The sensitivity derived from the calibration curves of the MIP-modified Au(SPE)/SAM electrode for rN detection was approximately 13.5 times higher for  $\Delta j$  measurements and 8 times higher for  $R_{ct}$  measurements compared to the NIP-modified Au(SPE)/SAM electrode, highlighting the superior performance of the MIP-modified electrodes. The LOD and LOQ for the developed immunosensor were calculated using EIS method (Equations 2 and 3).

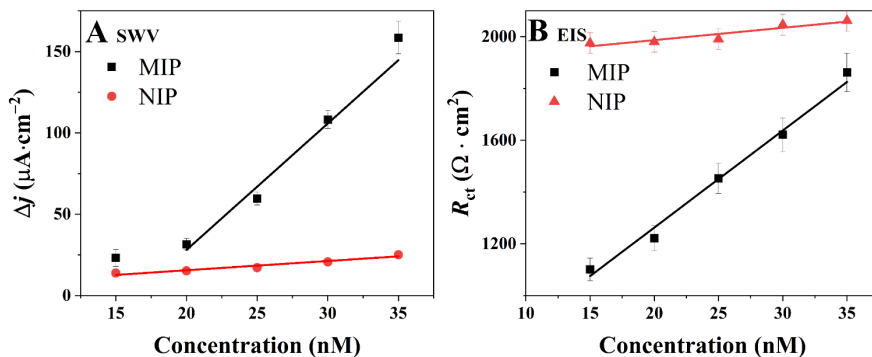


**Figure 21.** Calibration curves for  $\Delta j$  obtained from SWV (A) and  $R_{ct}$  obtained from EIS (B), respectively, vs. rN concentration. Error bars are expressed as the standard deviation of the sample.

For the SWV-based method, the LOD and LOQ were not calculated, as the data presented in Figure 21 suggest that the EIS-based method provided more reliable results. For the EIS-based method, the LOD and LOQ were determined to be 0.2 nM and 0.66 nM, respectively. These findings highlight the high sensitivity and promising potential of the MIP-modified

Au(SPE)/SAM electrodes in designing biosensors for rN protein detection. The formation of a SAM underlayer plays a crucial role in this design by providing a well-organised, stable, and functional surface that enhances the electrode's sensitivity. The SAM underlayer facilitates the effective formation of the MIP layer, ensuring a uniform and controlled distribution of specific binding sites. This not only improves the selective recognition of the rN protein but also minimises nonspecific interactions, thereby contributing to the overall performance and reliability of the biosensor.

### 3.3.4. Specificity test

The investigation of nonspecific binding on Au(SPE)/SAM/MIP involved comparing the electrochemical signal responses, as shown in Figure 22. These comparisons were based on the initial electrochemical signal responses obtained after immersing the electrodes in a 10 mM PBS, pH 7.4, solution containing a redox probe and either 35 nM rS or 35 nM BSA protein. The analysis showed that for  $\Delta j$  obtained from SWV, the relative response ( $RR$ ) percentages were  $13.0 \pm 2.5\%$  for BSA and  $6.54 \pm 0.86\%$  for rS protein. Similarly, for  $R_{ct}$  obtained from the EIS method, the  $RR$  percentages were  $15.1 \pm 2.32\%$  for BSA and  $0.93 \pm 0.09\%$  for rS protein. Overall, the sensor shows good specificity for rN protein.

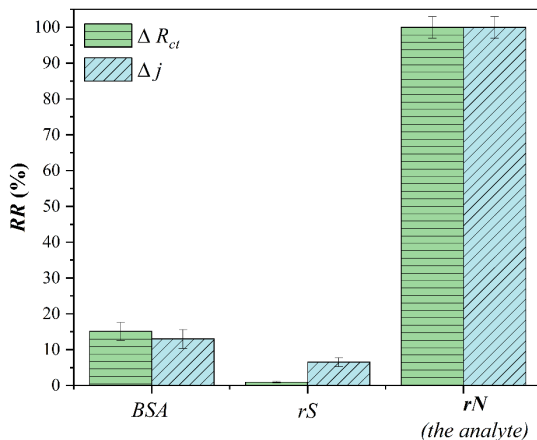


**Figure 22.** Comparison of the relative responses of 35 nM rS and 35 nM BSA, for  $\Delta j$  obtained from SWV (blue) and  $R_{ct}$  obtained from EIS (green). Error bars are expressed as the standard deviation of the sample.

### 3.4. The determination of the VEGF protein using a self-assembling aptamer-based electrochemical sensor

As mentioned in previous sections, this research employed a thin Ppy underlayer before developing the polymer-supported aptamer sensing layer. This essential step enhanced the adhesion of the sensing layer and reduced direct interaction between the target analyte and the electrode surface, thereby improving the performance of the Ppy/anti-VEGF sensing layer. Moreover, the thin Ppy-based underlayer played a crucial role in minimising direct interaction between the anti-VEGF and the electrode surface during the formation of the sensing layer, facilitating the effective creation of the Ppy/anti-VEGF-based sensing layer.

#### 3.4.1. The electrodeposition of polypyrrole-based VEGF aptamer

Using a series of potential pulses, polymer-based layers were electrochemically deposited on the surface of SPCE. The profile of the potential pulses during the application of the polypyrrole-based layer to SPCE is illustrated in Figure 23 A. Following the experimental procedures outlined in the experimental section, a polypyrrole-based VEGF aptamer (Ppy/anti-VEGF) layer was formed on SPCEs through a two-step process (Figure 23 B, C). A Ppy underlayer was electrochemically deposited in the initial step using a solution containing 0.1 M pyrrole in 10 mM PBS, pH 7.4. This was achieved by applying a series of 5 potential pulses (+0.95 V for 1 second followed by 0 V for 30 seconds). The resulting thin Ppy underlayer was designed to enhance the adhesion and performance of the sensing layer while reducing direct interactions between the electrode and the target analyte. Specifically, it minimised the direct interaction of VEGF aptamer with the electrode surface, facilitating more effective Ppy/anti-VEGF layer formation.

In the subsequent step, the anti-VEGF was introduced to the same polymerisation solution, and the sequence of 5 potential pulses was repeated. This approach allowed the anti-VEGF to be embedded within the Ppy matrix, enhancing the stability and support of the aptamer while also shielding the electrode surface. This strategy is analogous to methods used in MIPs and SAM systems. Overall, this two-step process is essential for optimising the adhesion and functional performance of the sensing layer.

### 3.4.2. Electrochemical characterisation of polypyrrole-based aptamer layer and VEGF detection

Duration selection in the PAD method is essential for obtaining precise and sensitive electrochemical measurements. In this study, 10 pulses of 0 V and 10 pulses of +0.6 V, each lasting 2 seconds, were employed (Figure 24 A), as previously used in my studies. The selection of +0.6 V for detection was guided by its effectiveness in triggering the desired electrochemical reactions and yielding an optimal signal response. Additionally, it has been reported that at +0.65 V vs Ag/AgCl (3 M KCl), unsubstituted Ppy starts to overoxidise [122].

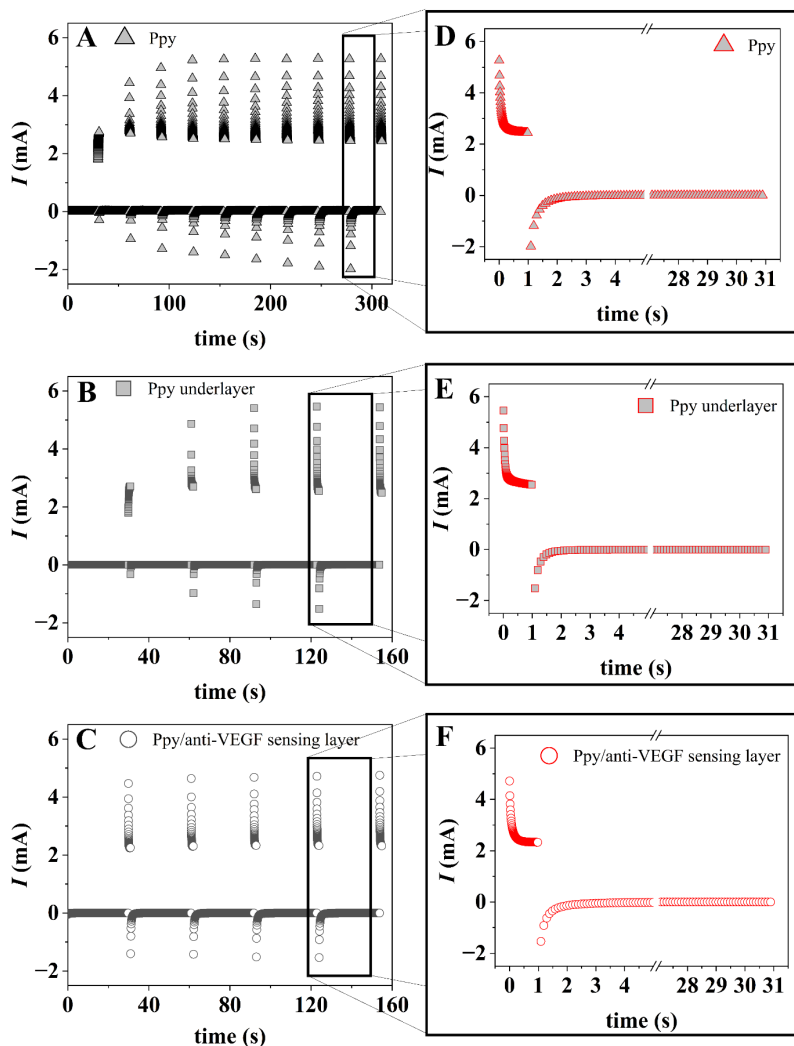


**Figure 23.** Electrochemical deposition of Ppy layers: (A) on SPCE electrodes, showing the profile of the current registered during the formation of the Ppy

layer from polymerisation solution without anti-VEGF. Ppy underlayers on SPCE electrodes (**B**) and of the Ppy layers with anti-VEGF entrapped as a sensing element of the system (**C**). **Inset (D-F)**: Potential pulse sequence for the signal analysis. Measurements were performed in 10 mM PBS solution, pH 7.4.

During the evaluation of current variations induced by potential pulses, careful analysis was conducted to monitor the current drop at specific points or intervals within the pulses of +0.6 V and 0 V. These key intervals included 0.1 s, 0.2 s, 0.4 s, 0.6 s, 0.8 s, and 2.0 s (Figure 24 B). Examining current changes at precise moments within the potential pulses enables the characterisation of distinct electrochemical processes, allowing for the identification of different redox reactions or species that exhibit varying kinetics or affinities for the electrode surface. This method provides a detailed understanding of the electrochemical system.

Figure 24 A shows a graphical representation of the PAD method, with time on the x-axis and current on the y-axis. Figure 24 B shows the two pulses applied to the electrode, one at +0.6 V and the other at 0 V. Specific time points, marked on the x-axis at the aforementioned time points, indicate the extracted current values for both potentials. These values were labelled as  $\Delta I$  0.1 s for 0.6 V and 0 V. Similarly, data points were collected at intervals of 0.1 s, 0.2 s, 0.4 s, 0.6 s, and 0.8 s, labelled as  $\Delta I$  0.1 s,  $\Delta I$  0.2 s,  $\Delta I$  0.4 s,  $\Delta I$  0.6 s, and  $\Delta I$  0.8 s, respectively. These time points correspond to different moments within the pulse duration and were used for further analysis, as detailed in the following discussion (Figure 25).

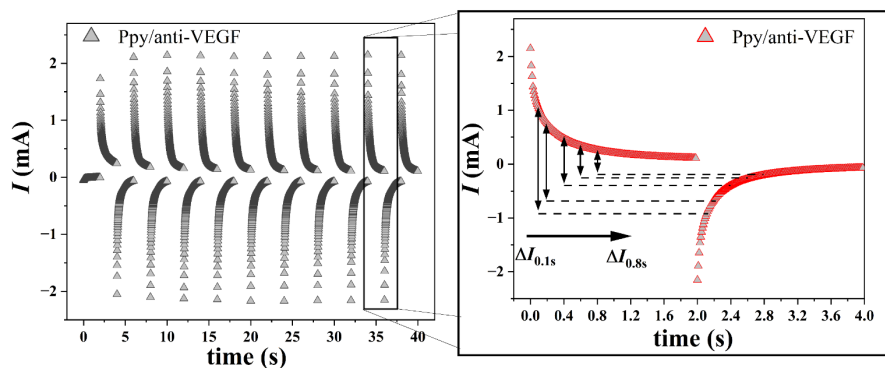


**Figure 24.** Pulsed amperometry-based evaluation of Ppy/anti-VEGF modified electrodes performed by the potential pulse sequence (0.6 V and 0 V potentials vs Ag/AgCl) (**A**). **Inset (B)**: Potential pulse sequence for the signal analysis. Measurements were performed in 10 mM PBS solution, pH 7.4.

### 3.4.3. The evaluation of analytical parameters. Adapted Langmuir isotherm

Figure 24 illustrates the current response observed during various intervals, emphasising the significance of pulse length in the PAD method. To measure VEGF across concentrations ranging from 0 to 24 nM, potential pulse values of +0.6 V and 0 V were applied. Different pulse durations were tested, including 0.1 s, 0.2 s, 0.4 s, 0.6 s and 0.8 s. Calibration curves were plotted (Figure 25) using normalised responses ( $NR \Delta I_{at Xs}$ ) from PAD measurements. These measurements were conducted after incubating Ppy/anti-VEGF and Ppy electrodes in a 10 mM PBS solution, pH 7.4, with VEGF at various concentrations. The incubation lasted 15 minutes at room temperature. After incubation, the electrodes were rinsed with PBS, pH 7.4, between different VEGF concentrations. To normalise the  $\Delta I$  signals, the response at 0 nM VEGF was set to zero (Equation 7).

$$NR \Delta I_{at Xs} = \Delta I_{at Xs}(0 \text{ nM VEGF}) - \Delta I_{at Xs} \quad (7)$$

Understanding how aptamers and proteins interact with binding sites can be challenging when using electrochemical methods. Therefore, our investigation relies significantly on mathematical analysis, specifically the Langmuir adsorption isotherm model. This approach involves fitting experimental data to the Langmuir isotherm to extract model parameters.

In a study by Gonzato et al. [123], cilostazol-extracted MIPs embedded in a polymer film were used to measure analyte binding parameters. They employed Freundlich, Langmuir, and Langmuir-Freundlich isotherms to analyse their data. The Langmuir-Freundlich isotherm provided the best fit, suggesting the presence of highly homogeneous and relatively homogeneous binding sites within the polymer matrix. Similarly, Çalık, Balcı, and Özdamar [124] performed equilibrium binding analyses for recombinant human growth hormone (rhGH) in both liquid-phase and immobilized-aptamer phases using the Langmuir-type adsorption isotherm (Equation 8). Building on this prior research, the Langmuir isotherm model was adapted for the results illustrated in Figure 25.

$$\Delta I = \Delta I_{max} \times \frac{[VEGF]}{K + [VEGF]} \quad (8)$$

where  $\Delta I_{max}$  is the maximal normalised value of current density,  $K$  – is the adapted Langmuir constant, and  $[VEGF]$  – is the concentration of VEGF.  $K$ ,  $\Delta I_{max}$ , and  $R^2$  values can be found in Table 4.



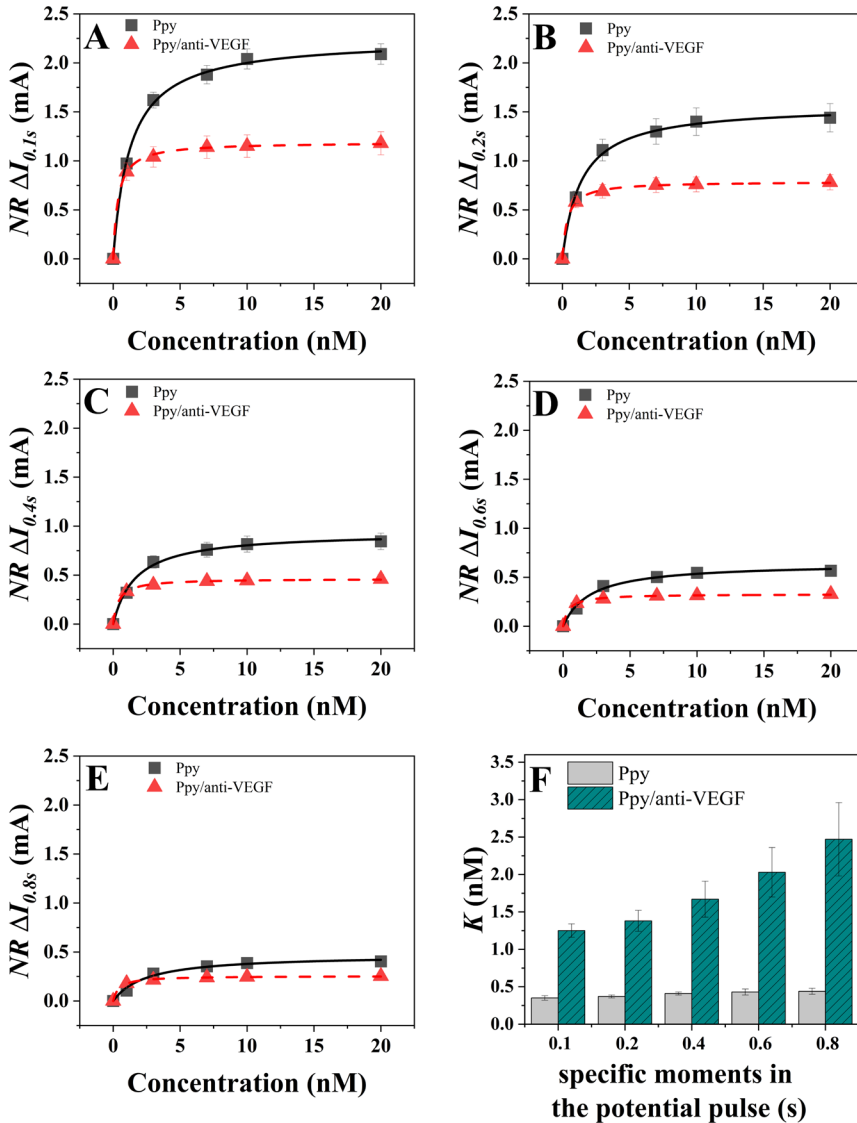


**Figure 25.** Calibration curves ( $NR \Delta I$ (at Xs) vs. VEGF protein concentration) obtained using modified electrodes of Ppy and Ppy/anti-VEGF for specific moments in the potential pulse at 0.1 s (A), 0.2 s (B), 0.4 s (C), 0.6 s (D), 0.8 s (E). The error bars were expressed as the standard deviation of the sample (n=4). The dependence of the adapted Langmuir constant of Ppy/anti-VEGF and the corresponding Ppy-modified electrodes for specific moments in potential pulse (n=4) (F).

**Table 4.**  $K$ ,  $\Delta I_{\max}$ , and  $R^2$  values were calculated for specific moments in the potential pulse of +0.6 V and 0 V potential pulses at 0.1 s, 0.2 s, 0.4 s, 0.6 s, and 0.8 s. Errors were calculated as a standard deviation.

| Specific moments in the potential pulse, s | <i>Ppy</i> |                        |       | <i>Ppy/anti-VEGF</i> |                        |       |
|--|------------|------------------------|-------|----------------------|------------------------|-------|
|  | $K$ (nM)   | $\Delta I_{\max}$ (mA) | $R^2$ | $K$ (nM)             | $\Delta I_{\max}$ (mA) | $R^2$ |
| 0.1  | 0.35±0.03  | 1.19±0.01              | 0.999 | 1.25±0.09            | 2.25±0.03              | 0.998 |
| 0.2  | 0.37±0.02  | 0.79±0.01              | 0.999 | 1.38±0.14            | 1.57±0.03              | 0.998 |
| 0.4  | 0.41±0.03  | 0.46±0.01              | 0.999 | 1.67±0.24            | 0.94±0.03              | 0.995 |
| 0.6  | 0.43±0.04  | 0.33±0.01              | 0.999 | 2.03±0.33            | 0.64±0.03              | 0.992 |
| 0.8  | 0.44±0.04  | 0.26±0.01              | 0.998 | 2.47±0.49            | 0.47±0.03              | 0.988 |

Table 4 presents a comprehensive summary of the  $K$ ,  $\Delta I_{\max}$ , and  $R^2$  values obtained from experiments conducted at specific moments during the potential pulses of +0.6 V and 0 V. These moments include 0.1 s, 0.2 s, 0.4 s, 0.6 s, and 0.8 s (Figure 25 A-E), along with their corresponding standard deviation errors. The high  $R^2$  values, close to 1, across these different time points, indicate a good fit of the experimental data to the adapted Langmuir model. This suggests that the Langmuir model is well-suited for describing the adsorption behaviour of VEGF on the sensing surface.

Figure 25 F shows how  $K$  varies with the specific moments in the potential pulse for both *Ppy/anti-VEGF* and *Ppy*-modified electrodes. Notably,  $K$  values tend to increase with longer specific moments, indicating a positive correlation between the duration of the interaction and the affinity of VEGF for the sensing material. This trend suggests that prolonged exposure to VEGF enhances binding interactions, resulting in a higher equilibrium constant. Longer specific moments likely facilitate greater adsorption of VEGF molecules onto the surface, thereby improving the sensitivity and specificity of the sensor.

The observed increase in  $K$  values from  $1.25 \pm 0.09$  nM to  $2.47 \pm 0.49$  nM with longer specific moments underscores the importance of optimising experimental conditions to achieve desired sensitivity and accuracy in VEGF detection. Optimising the duration of these specific intervals could improve VEGF binding while ensuring that the dynamic range and reliability of the sensor are maintained. Additionally, careful calibration and testing during these intervals may further enhance the accuracy and sensitivity of the sensor. It is also worth noting that the  $K$  values for the *Ppy* layer remain relatively consistent, indicating stable performance across different conditions.

Consequently,  $\Delta I_{\max}$  values for the Ppy/anti-VEGF layer are consistently lower than those for the Ppy layer with longer specific moments in the potential pulse. This suggests that fine-tuning the pulse duration could be a crucial factor in balancing the sensitivity and stability of the sensor, as longer intervals may allow for more controlled interactions but at the expense of peak signal intensity.

#### 3.4.4. Adaptation of integrated Cottrell equation

The integrated Cottrell equation (Anson plot) was employed to analyse the results further and discuss them. The relation of the cumulative charge passed and time in Ppy-based electrochemical sensors obeys the integrated Cottrell equation (Equations 9-11):

$$Q = Q_f + Q_{d.l.} + Q_{ads.} \quad (9)$$

$$Q_f = 2nFAC \sqrt{\frac{D}{\pi}} \sqrt{t} = k\sqrt{t} \quad (10)$$

$$Q_{ads.} = Fn\Gamma \quad (11)$$

where:  $Q$  – total charge (C);  $n$  – number of electrons;  $F$  – Faraday constant (96,485 C/mol);  $A$  – area of the electrode (cm<sup>2</sup>);  $C$  – concentration (M);  $D$  – diffusion coefficient (cm<sup>2</sup>/s);  $t$  – time (s);  $Q_{d.l.}$  – the charge of the electrical double layer;  $Q_{ads.}$  – charge induced by adsorbed ions.

Anson et al. [125] highlighted the effectiveness of the double potential step chronocoulometric technique for accurately quantifying adsorbed reactants. This approach provides valuable insights into electrochemical processes without requiring complex models. In the context of the integrated Cottrell equation, the total charge accumulation consists of three components: Faradaic charges ( $Q_f$ ) resulting from redox activity, charges from the charging and discharging of the electrode-electrolyte double-layer capacitance ( $Q_{d.l.}$ ), and changes in charge due to adsorbed species ( $Q_{ads.}$ ). A linear relationship is observed when plotting the total charge ( $Q$ ) against the square root of time ( $t^{1/2}$ ). The plot of  $Q$  versus  $t^{1/2}$  shows a linear correlation where the slope represents  $k$  and the intercept represents  $Q_{ads.} + Q_{d.l.}$ . The study noted that maximum adsorption generally occurs at intermediate concentrations of specific compounds, and variations in adsorption patterns indicate bonding interactions between the reactants and the electrode surface. A previous study [126] examined how electrode modifications affect the adsorption behaviour of analytes and reaction products. Unlike earlier studies using plain

electrodes, this study employed Pt electrodes modified with the conducting polymer Ppy, which were further imprinted or non-imprinted with glycoprotein. This modification added extra layers and functionalities to the electrode surface, thereby altering the electrochemical behaviour of the system. The Ppy layer could participate in charging and discharging processes during electrochemical oxidation and reduction reactions by varying the potential.

In the study presented in this dissertation, a polymer-supported aptamer layer on the electrode was used. While this complexity adds challenges to analysing amperograms, it is still possible to describe them using the framework proposed by Anson.

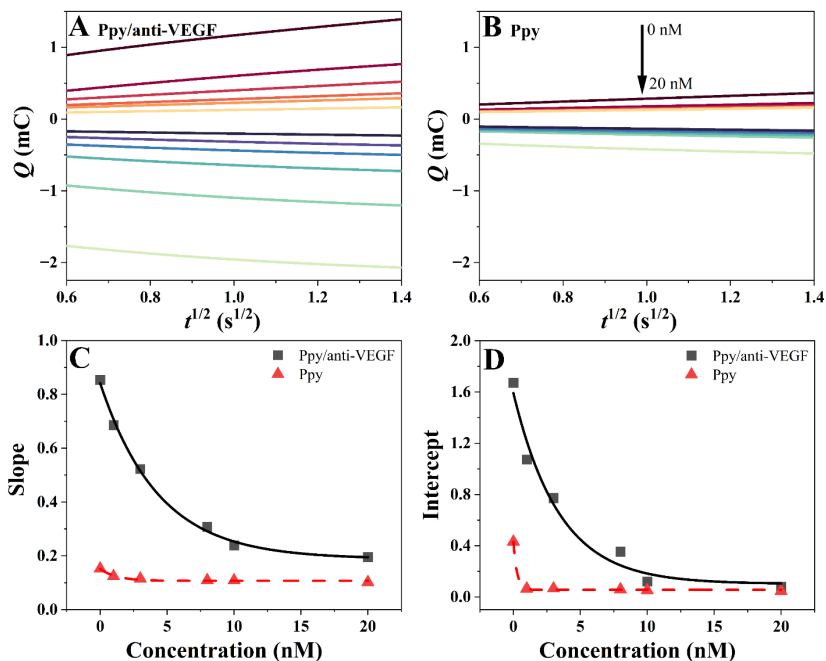


**Figure 26.** The Anson plots ( $Q$  vs.  $t^{1/2}$ ) derived from the amperometric response registered during the last (10<sup>th</sup>) potential pulse of the applied potential pulse sequence (0.6 V and 0 V) for Ppy/anti-VEGF modified electrode (A) and Ppy modified electrode (B). Slope (C) and intercept (D) values represent the linear regression equation  $y = ax + b$  (from) vs. the concentration of VEGF protein (nM).

Figure 26 provides a detailed analysis of the Anson plots for the amperogram data shown in Figure 24. Figure 26 A presents the results for Ppy/anti-VEGF, while Figure 26 B shows the results for Ppy. Linear regression was employed to fit the relationship between the total charge ( $Q$ )

and the square root of time ( $t^{1/2}$ ). The parameters of the corresponding equations are listed in Table 5, which also shows the  $R^2$  values indicating a strong linear correlation in the  $Q$  vs.  $t^{1/2}$  plots.

**Table 5.** Linear regression parameters of the Anson plot ( $Q$ , mC vs.  $t^{1/2}$ ,  $s^{1/2}$ ) derived from the Ppy/anti-VEGF and Ppy for the last (10th) pulse of the potential pulse sequence.

| $y = ax + b$<br>C, nM | Ppy/anti-VEGF |         |       | Ppy    |        |       |
|-----------------------|---------------|---------|-------|--------|--------|-------|
|                       | $a$           | $b$     | $R^2$ | $a$    | $b$    | $R^2$ |
| 0                     | 0.854         | 1.672   | 0.993 | 0.1523 | 0.4314 | 0.992 |
| 1                     | 0.6859        | 1.0719  | 0.996 | 0.1242 | 0.0651 | 0.996 |
| 3                     | 0.5226        | 0.77176 | 0.994 | 0.1152 | 0.0653 | 0.999 |
| 7                     | 0.3078        | 0.35404 | 0.995 | 0.1088 | 0.0592 | 0.999 |
| 10                    | 0.2384        | 0.1197  | 0.994 | 0.1085 | 0.0524 | 0.999 |
| 20                    | 0.1951        | 0.0782  | 0.999 | 0.1017 | 0.0461 | 0.999 |

Figures 26 C and 26 D illustrate the exponential dependence of the slope and intercept on VEGF concentration at +0.6 V. These plots reveal differences in slope and intercept values between Ppy/anti-VEGF and Ppy-modified electrodes under identical experimental conditions. Specifically, Figure 26 C shows a notable decrease in the slope of the Anson equation, calculated using equation 9, with increasing VEGF concentrations. The slope is influenced by factors including the number of electrons ( $n$ ) transferred during the electrochemical reaction, the electrochemically active area ( $A$ ), the material concentration ( $C$ ), and the diffusion coefficient ( $D$ ). These results suggest that the observed decrease in the slope with higher VEGF concentrations reflects a reduction in the electrochemically active area, assuming that electrons and  $D$  remain constant across all VEGF concentrations due to consistent solution properties (e.g., density and viscosity). Notably, this effect is more pronounced for the Ppy/anti-VEGF-modified electrode compared to the Ppy-modified electrode.

In chronocoulometric experiments, the charge accumulates proportionally with  $t^{1/2}$  as additional reactants diffuse to the electrode surface. When some of the reactant adsorbs onto the electrode/electrolyte interface at 0 V, it will be reduced almost immediately upon switching to +0.6 V, resulting in an additional charge burst. However, after this initial response, the chronocoulometric behaviour is generally unaffected by the adsorbed reactant. Consequently, the plots of  $Q$  vs.  $t^{1/2}$  will have intercepts exceeding  $Q$  by an amount equivalent to  $Q_{dl}$ , with the slope remaining unchanged by the presence of the adsorbed reactant. The values of  $Q_{ads}$  provide direct measures of the

quantity of adsorbed reactant according to Faraday's Law (Equation 10), where  $\Gamma$  represents the quantity of adsorbed reactant in moles. Figure 26 D shows intercept values corresponding to VEGF protein concentration (nM), where the intercept represents  $Q_{\text{ads}} + Q_{\text{dl}}$ . To determine  $Q_{\text{ads}}$  from the intercept in a chronocoulometric plot of  $Q$  vs.  $t^{1/2}$ , it is essential to measure or estimate  $Q_{\text{dl}}$ . This measurement is straightforward if the adsorption of the reactant does not significantly alter the interfacial capacitance, allowing the  $Q_{\text{dl}}$  value from a blank experiment (0 nM VEGF) to be applied to measurements in the presence of the adsorbing analyte [127].

### 3.4.5. The determination of the limit of detection

PAD-based electrochemical measurements were performed to determine the LOD. Intercept values, representing  $Q_{\text{ads}} + Q_{\text{dl}}$ , were obtained from Table 5. To evaluate  $Q_{\text{ads}}$ , blank experiments were conducted with 0 nM of VEGF for both Ppy and Ppy/anti-VEGF electrodes, serving as the baseline analytical signals. Figure 27 presents the linear calibration of VEGF protein concentration plotted against  $\Delta Q$  (mC). The slope for VEGF concentration (nM) measured with the Ppy electrode was 0.001 mC/nM with an  $R^2$  value of 0.96, whereas the slope for VEGF on the Ppy/anti-VEGF modified electrode was 0.1 mC/nM with an  $R^2$  value of 0.99. The LOD was calculated using Equation 2. It was evaluated that the LOD for the modified electrode Ppy/anti-VEGF was 0.21 nM.

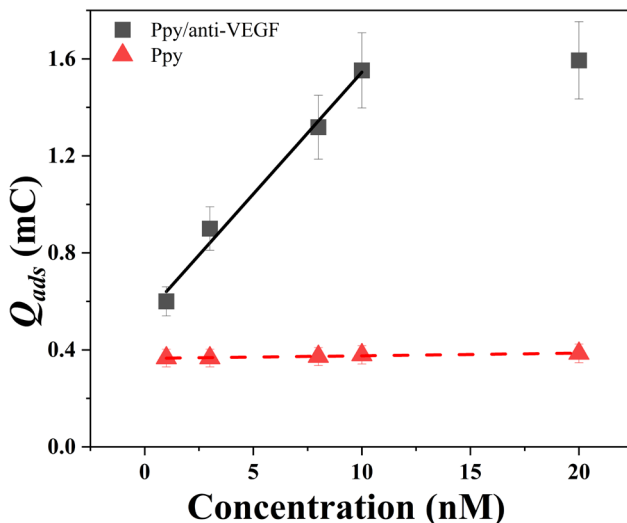


**Figure 27.** Calibration curve  $Q_{\text{ads}}$  registered by Ppy/anti-VEGF (black line) and Ppy (red line) vs. VEGF concentration. Error bars are calculated as a percentage of the standard deviation ( $n=4$ ).

## CONCLUSIONS

1. Through the application of the pulsed amperometric deposition technique, a polypyrrole-based underlayer was developed and integrated into the design of a molecularly imprinted polymer-based sensor suitable for the detection of *Listeria monocytogenes* bacteria. During the preparation process, trypsin was used to efficiently extract and remove the imprinted bacterial templates. The resulting sensor achieved a LOD of 70 CFU/mL and a LOQ of 210 CFU/mL.
2. The electrochemical properties of various SAM-modified gold electrodes were determined. The formation of an 11-mercaptopundecanoic acid self-assembled monolayer on the Au(s) electrode created an insulating layer that significantly increased charge transfer resistance. In contrast, the Au(MS) electrode modified with a self-assembled monolayer mixture (composed of 6-mercapto-1-hexanol and 11-mercaptopundecanoic acid) exhibited a lower charge transfer resistance, making it suitable for the development of a label-free immunosensor used to detect antibodies against the SARS-CoV-2 spike protein, achieving a LOD of 2.78 nM and a LOQ of 9.17 nM.
3. Sensor for the determination of SARS-CoV-2 nucleocapsid protein was designed by the formation of self-assembled monolayer under-layer on a screen-printed electrode modified by gold nanostructures, followed by deposition of molecularly imprinted polypyrrole layer. The selectivity towards the target protein was confirmed by electrochemical analysis methods. An increase in charge transfer resistance was observed with increasing concentrations of the SARS-CoV-2 nucleocapsid protein. The sensor exhibited a LOD and LOQ of 0.2 nM and 0.66 nM, respectively, using electrochemical impedance spectroscopy.
4. A self-assembling DNA aptamer was incorporated into a conducting polypyrrole matrix, supported by a polypyrrole underlayer, on a screen-printed carbon electrode. The modified electrode was used for the detection of VEGF protein, achieving a LOD of 0.21 nM. The use of the pulsed amperometric technique allowed to simplify the detection process by eliminating the application of redox mediators.

## FUTURE OUTLOOK

This dissertation opens several pathways for advancing electrochemical sensor technologies. An immediate step involves transitioning from controlled laboratory conditions to testing in more realistic settings, beginning with spiked or artificially produced blood samples. Following successful validation, the next stage would involve testing with actual clinical or environmental samples to assess the sensors' robustness, reproducibility, and practical utility. Simultaneously, the development of multiplexed sensors capable of simultaneously detecting multiple analytes should be prioritised to enhance diagnostic capabilities for complex systems. Additionally, integrating these sensors into portable, real-time platforms would revolutionise point-of-care diagnostics, particularly in resource-limited settings. Expanding the application of molecularly imprinted polymers and aptamer-embedded systems will further enable the detection of rare disease biomarkers and foodborne pathogens. By addressing these future directions sequentially, researchers can build on the advancements presented in this work to create versatile, high-performance sensors that meet the evolving demands of modern analytical technologies.



## REFERENCES

1. Letheby, H. XXIX.—On the Production of a Blue Substance by the Electrolysis of Sulphate of Aniline. *J. Chem. Soc.* **1862**, *15*, 161–163, doi:10.1039/JS8621500161.
2. Shirakawa, H.; Louis, E.J.; MacDiarmid, A.G.; Chiang, C.K.; Heeger, A.J. Synthesis of Electrically Conducting Organic Polymers: Halogen Derivatives of Polyacetylene, (CH)  $x$ . *J Chem Soc Chem Commun* **1977**, *578*, doi:10.1039/c39770000578.
3. Shea, J.J. Handbook of Conducting Polymers, 2nd Edition. *IEEE Electrical Insulation Magazine* **1999**, *15*, 37–37, doi:10.1109/MEI.1999.744595.
4. Li, C.M.; Sun, C.Q.; Chen, W.; Pan, L. Electrochemical Thin Film Deposition of Polypyrrole on Different Substrates. *Surf Coat Technol* **2005**, *198*, 474–477, doi:10.1016/j.surfcoat.2004.10.065.
5. Lange, U.; Roznyatovskaya, N. V.; Mirsky, V.M. Conducting Polymers in Chemical Sensors and Arrays. *Anal Chim Acta* **2008**, *614*.
6. Le, T.-H.; Kim, Y.; Yoon, H. Electrical and Electrochemical Properties of Conducting Polymers. *Polymers (Basel)* **2017**, *9*, 150, doi:10.3390/polym9040150.
7. Ramanavicius, S.; Ramanavicius, A. Conducting Polymers in the Design of Biosensors and Biofuel Cells. *Polymers (Basel)* **2020**, *13*, 49, doi:10.3390/polym13010049.
8. Machida, S.; Miyata, S.; Techagumpuch, A. Chemical Synthesis of Highly Electrically Conductive Polypyrrole. *Synth Met* **1989**, *31*, 311–318, doi:10.1016/0379-6779(89)90798-4.
9. Xu, Z.; Zheng, E.; Xiao, Z.; Shao, H.; Liu, Y.; Wang, J. Photo-Initiated in Situ Synthesis of Polypyrrole Fe-Coated Porous Silicon Microspheres for High-Performance Lithium-Ion Battery Anodes. *Chemical Engineering Journal* **2023**, *459*, 141543, doi:10.1016/j.cej.2023.141543.
10. Kausaitė-Minkstimiene, A.; Mazeiko, V.; Ramanaviciene, A.; Ramanavicius, A. Evaluation of Amperometric Glucose Biosensors Based on Glucose Oxidase Encapsulated within Enzymatically Synthesized Polyaniline and Polypyrrole. *Sens Actuators B Chem* **2011**, *158*, 278–285, doi:10.1016/j.snb.2011.06.019.
11. Heinze, J.; Frontana-Urbe, B.A.; Ludwigs, S. Electrochemistry of Conducting Polymers—Persistent Models and New Concepts. *Chem Rev* **2010**, *110*, 4724–4771, doi:10.1021/cr900226k.

12. Uang, Y.-M.; Chou, T.-C. Criteria for Designing a Polypyrrole Glucose Biosensor by Galvanostatic Electropolymerization. *Electroanalysis* **2002**, *14*, 1564–1570, doi:10.1002/1521-4109(200211)14:22<1564::AID-ELAN1564>3.0.CO;2-H.
13. Zhang, J.; Kong, L.-B.; Li, H.; Luo, Y.-C.; Kang, L. Synthesis of Polypyrrole Film by Pulse Galvanostatic Method and Its Application as Supercapacitor Electrode Materials. *J Mater Sci* **2010**, *45*, 1947–1954, doi:10.1007/s10853-009-4186-0.
14. Chen, S.; Zhitomirsky, I. Capacitive Behaviour of Polypyrrole, Prepared by Electrochemical and Chemical Methods. *Mater Lett* **2014**, *125*, 92–95, doi:10.1016/j.matlet.2014.03.124.
15. Schuhmann, W.; Kranz, C.; Wohlschläger, H.; Strohmeier, J. Pulse Technique for the Electrochemical Deposition of Polymer Films on Electrode Surfaces. *Biosens Bioelectron* **1997**, *12*, 1157–1167, doi:10.1016/S0956-5663(97)00086-9.
16. Somani, P.R.; Radhakrishnan, S. Electrochromic Materials and Devices: Present and Future. *Mater Chem Phys* **2003**, *77*, 117–133, doi:10.1016/S0254-0584(01)00575-2.
17. Kupila, E.-L.; Kankare, J. Electropolymerization of Pyrrole: Effects of PH and Anions on the Conductivity and Growth Kinetics of Polypyrrole. *Synth Met* **1993**, *55*, 1402–1405, doi:10.1016/0379-6779(93)90258-X.
18. *Handbook of Radical Polymerization*; Matyjaszewski, K., Davis, T.P., Eds.; John Wiley & Sons, 2002; ISBN 9780471392743.
19. Gvozdenovic, M.; Jugovic, B.; Stevanovic, J.; Grgur, B. Electrochemical Synthesis of Electroconducting Polymers. *Hem Ind* **2014**, *68*, 673–684, doi:10.2298/HEMIND131122008G.
20. Ahmad, O.S.; Bedwell, T.S.; Esen, C.; Garcia-Cruz, A.; Piletsky, S.A. Molecularly Imprinted Polymers in Electrochemical and Optical Sensors. *Trends Biotechnol* **2019**, *37*, 294–309, doi:10.1016/j.tibtech.2018.08.009.
21. Vasapollo, G.; Sole, R. Del; Mergola, L.; Lazzoi, M.R.; Scardino, A.; Scorrano, S.; Mele, G. Molecularly Imprinted Polymers: Present and Future Prospective. *Int J Mol Sci* **2011**, *12*, 5908–5945, doi:10.3390/ijms12095908.
22. Mollarasouli, F.; Kurbanoglu, S.; Ozkan, S.A. The Role of Electrochemical Immunosensors in Clinical Analysis. *Biosensors (Basel)* **2019**, *9*, 86, doi:10.3390/bios9030086.
23. Gurudatt, N.G.; Chung, S.; Kim, J.-M.; Kim, M.-H.; Jung, D.-K.; Han, J.-Y.; Shim, Y.-B. Separation Detection of Different Circulating

- Tumor Cells in the Blood Using an Electrochemical Microfluidic Channel Modified with a Lipid-Bonded Conducting Polymer. *Biosens Bioelectron* **2019**, *146*, 111746, doi:10.1016/j.bios.2019.111746.
24. Rattanarat, P.; Suea-Ngam, A.; Ruecha, N.; Siangproh, W.; Henry, C.S.; Srisa-Art, M.; Chailapakul, O. Graphene-Polyaniline Modified Electrochemical Droplet-Based Microfluidic Sensor for High-Throughput Determination of 4-Aminophenol. *Anal Chim Acta* **2016**, *925*, 51–60, doi:10.1016/j.aca.2016.03.010.
  25. Refaat, D.; Aggour, M.G.; Farghali, A.A.; Mahajan, R.; Wiklander, J.G.; Nicholls, I.A.; Piletsky, S.A. Strategies for Molecular Imprinting and the Evolution of MIP Nanoparticles as Plastic Antibodies—Synthesis and Applications. *Int J Mol Sci* **2019**, *20*, 6304, doi:10.3390/ijms20246304.
  26. He, Y.; Lin, Z. Recent Advances in Protein-Imprinted Polymers: Synthesis, Applications and Challenges. *J Mater Chem B* **2022**, *10*, 6571–6589, doi:10.1039/D2TB00273F.
  27. Menaker, A.; Syritski, V.; Reut, J.; Öpik, A.; Horváth, V.; Gyurcsányi, R.E. Electrosynthesized Surface-Imprinted Conducting Polymer Microrods for Selective Protein Recognition. *Advanced Materials* **2009**, *21*, 2271–2275, doi:10.1002/adma.200803597.
  28. Gajos, K.; Awsiuk, K.; Budkowski, A. Controlling Orientation, Conformation, and Biorecognition of Proteins on Silane Monolayers, Conjugate Polymers, and Thermo-Responsive Polymer Brushes: Investigations Using TOF-SIMS and Principal Component Analysis. *Colloid Polym Sci* **2021**, *299*, 385–405, doi:10.1007/s00396-020-04711-7.
  29. Ramanaviciene, A.; Ramanavicius, A. Molecularly Imprinted Polypyrrole-Based Synthetic Receptor for Direct Detection of Bovine Leukemia Virus Glycoproteins. *Biosens Bioelectron* **2004**, *20*, 1076–1082, doi:10.1016/j.bios.2004.05.014.
  30. Takeuchi, T.; Hishiya, T. Molecular Imprinting of Proteins Emerging as a Tool for Protein Recognition. *Org Biomol Chem* **2008**, *6*, 2459, doi:10.1039/b715737c.
  31. Erdőssy, J.; Horváth, V.; Yarman, A.; Scheller, F.W.; Gyurcsányi, R.E. Electrosynthesized Molecularly Imprinted Polymers for Protein Recognition. *TrAC Trends in Analytical Chemistry* **2016**, *79*, 179–190, doi:10.1016/j.trac.2015.12.018.
  32. Hayden, O.; Lieberzeit, P.A.; Blaas, D.; Dickert, F.L. Artificial Antibodies for Bioanalyte Detection—Sensing Viruses and Proteins. *Adv Funct Mater* **2006**, *16*, 1269–1278, doi:10.1002/adfm.200500626.

33. Iskierko, Z.; Sharma, P.S.; Bartold, K.; Pietrzyk-Le, A.; Noworyta, K.; Kutner, W. Molecularly Imprinted Polymers for Separating and Sensing of Macromolecular Compounds and Microorganisms. *Biotechnol Adv* **2016**, *34*, 30–46, doi:10.1016/j.biotechadv.2015.12.002.
34. Ktari, N.; Fourati, N.; Zerrouki, C.; Ruan, M.; Seydou, M.; Barbaut, F.; Nal, F.; Yaakoubi, N.; Chehimi, M.M.; Kalfat, R. Design of a Polypyrrole MIP-SAW Sensor for Selective Detection of Flumequine in Aqueous Media. Correlation between Experimental Results and DFT Calculations. *RSC Adv* **2015**, *5*, 88666–88674, doi:10.1039/C5RA16237H.
35. Ulman, A. Formation and Structure of Self-Assembled Monolayers. *Chem Rev* **1996**, *96*, 1533–1554, doi:10.1021/cr9502357.
36. Chaki, N.K.; Aslam, M.; Sharma, J.; Vijayamohanam, K. Applications of Self-Assembled Monolayers in Materials Chemistry. *Journal of Chemical Sciences* **2001**, *113*, 659–670, doi:10.1007/BF02708798.
37. Poirier, G.E.; Pylant, E.D. The Self-Assembly Mechanism of Alkanethiols on Au(111). *Science (1979)* **1996**, *272*, 1145–1148, doi:10.1126/science.272.5265.1145.
38. Biener, M.M.; Biener, J.; Friend, C.M. Revisiting the S–Au(111) Interaction: Static or Dynamic? *Langmuir* **2005**, *21*, 1668–1671, doi:10.1021/la047387u.
39. Yamada, R.; Uosaki, K. Two-Dimensional Crystals of Alkanes Formed on Au(111) Surface in Neat Liquid: Structural Investigation by Scanning Tunneling Microscopy. *J Phys Chem B* **2000**, *104*, 6021–6027, doi:10.1021/jp994061z.
40. Dubois, L.H.; Nuzzo, R.G. Synthesis, Structure, and Properties of Model Organic Surfaces. *Annu Rev Phys Chem* **1992**, *43*, 437–463, doi:10.1146/annurev.pc.43.100192.002253.
41. Wink, Th.; van Zuilen, S.J.; Bult, A.; van Bennekom, W.P. Self-Assembled Monolayers for Biosensors. *Analyst* **1997**, *122*, 43R–50R, doi:10.1039/a606964i.
42. Widrig, C.A.; Chung, C.; Porter, M.D. The Electrochemical Desorption of N-Alkanethiol Monolayers from Polycrystalline Au and Ag Electrodes. *J Electroanal Chem Interfacial Electrochem* **1991**, *310*, 335–359, doi:10.1016/0022-0728(91)85271-P.
43. Christopher Love, J.; Wolfe, D.B.; Haasch, R.; Chabynyc, M.L.; Paul, K.E.; Whitesides, G.M.; Nuzzo, R.G. Formation and Structure of Self-Assembled Monolayers of Alkanethiolates on Palladium. *J Am Chem Soc* **2003**, *125*, doi:10.1021/ja028692+.

44. Su, X.-L.; Li, Y. A Self-Assembled Monolayer-Based Piezoelectric Immunosensor for Rapid Detection of Escherichia Coli O157:H7. *Biosens Bioelectron* **2004**, *19*, 563–574, doi:10.1016/S0956-5663(03)00254-9.
45. Lahiri, J.; Isaacs, L.; Tien, J.; Whitesides, G.M. A Strategy for the Generation of Surfaces Presenting Ligands for Studies of Binding Based on an Active Ester as a Common Reactive Intermediate: A Surface Plasmon Resonance Study. *Anal Chem* **1999**, *71*, 777–790, doi:10.1021/ac980959t.
46. Guiomar, A.J.; Guthrie, J.T.; Evans, S.D. Use of Mixed Self-Assembled Monolayers in a Study of the Effect of the Microenvironment on Immobilized Glucose Oxidase. *Langmuir* **1999**, *15*, doi:10.1021/la980974t.
47. Ge, B.; Lisdat, F. Superoxide Sensor Based on Cytochrome c Immobilized on Mixed-Thiol SAM with a New Calibration Method. *Anal Chim Acta* **2002**, *454*, doi:10.1016/S0003-2670(01)01545-8.
48. Frederix, F.; Bonroy, K.; Laureyn, W.; Reekmans, G.; Campitelli, A.; Dehaen, W.; Maes, G. Enhanced Performance of an Affinity Biosensor Interface Based on Mixed Self-Assembled Monolayers of Thiols on Gold. *Langmuir* **2003**, *19*, doi:10.1021/la026908f.
49. Bhushan, B. Self-Assembled Monolayers (Sams) for Controlling Adhesion, Friction, and Wear. In *Nanotribology and Nanomechanics (Second Edition): An Introduction*; 2008.
50. Michałowska, A.; Gajda, A.; Kowalczyk, A.; Weyher, J.L.; Nowicka, A.M.; Kudelski, A. Surface-Enhanced Raman Scattering Used to Study the Structure of Layers Formed on Metal Surfaces from Single-Stranded DNA and 6-Mercaptohexan-1-ol: Influence of Hybridization with the Complementary DNA and Influence of the Metal Substrate. *RSC Adv* **2022**, *12*, doi:10.1039/d2ra05318g.
51. Alloway, D.M.; Graham, A.L.; Yang, X.; Mudalige, A.; Colorado, R.; Wysocki, V.H.; Pemberton, J.E.; Lee, T.R.; Wysocki, R.J.; Armstrong, N.R. Tuning the Effective Work Function of Gold and Silver Using  $\omega$ -Functionalized Alkanethiols: Varying Surface Composition through Dilution and Choice of Terminal Groups. *Journal of Physical Chemistry C* **2009**, *113*, doi:10.1021/jp909494r.
52. Lacour, V.; Moumanis, K.; Hassen, W.M.; Elie-Caille, C.; Leblois, T.; Dubowski, J.J. Formation Kinetics of Mixed Self-Assembled Monolayers of Alkanethiols on GaAs(100). *Langmuir* **2019**, *35*, doi:10.1021/acs.langmuir.7b00929.

53. Comenge, J.; Puentes, V.F. The Role of PEG Conformation in Mixed Layers: From Protein Corona Substrate to Steric Stabilization Avoiding Protein Adsorption. *ScienceOpen Res* **2015**, *0*, doi:10.14293/s2199-1006.1.sor-matsci.a0z6om.v1.
54. Kausaite-Minkstimiene, A.; Ramanaviciene, A.; Kirlyte, J.; Ramanavicius, A. Comparative Study of Random and Oriented Antibody Immobilization Techniques on the Binding Capacity of Immunosensor. *Anal Chem* **2010**, *82*, 6401–6408, doi:10.1021/ac100468k.
55. Balciunas, D.; Plausinaitis, D.; Ratautaite, V.; Ramanaviciene, A.; Ramanavicius, A. Towards Electrochemical Surface Plasmon Resonance Sensor Based on the Molecularly Imprinted Polypyrrole for Glyphosate Sensing. *Talanta* **2022**, *241*, 123252, doi:10.1016/j.talanta.2022.123252.
56. You, M.; Yang, S.; An, Y.; Zhang, F.; He, P. A Novel Electrochemical Biosensor with Molecularly Imprinted Polymers and Aptamer-Based Sandwich Assay for Determining Amyloid- $\beta$  Oligomer. *Journal of Electroanalytical Chemistry* **2020**, *862*, doi:10.1016/j.jelechem.2020.114017.
57. Yoo, H.; Jo, H.; Oh, S.S. Detection and beyond: Challenges and Advances in Aptamer-Based Biosensors. *Mater Adv* **2020**, *1*.
58. Vizzini, P.; Braidot, M.; Vidic, J.; Manzano, M. Electrochemical and Optical Biosensors for the Detection of *Campylobacter* and *Listeria*: An Update Look. *Micromachines (Basel)* **2019**, *10*.
59. Eallonardo, S.J.; Wang, Y.; Freitag, N.E. *Listeria Monocytogenes*. In *Molecular Medical Microbiology*; Elsevier, **2024**; pp. 1249–1267.
60. Matle, I.; Mbatha, K.R.; Madoroba, E. A Review of *Listeria Monocytogenes* from Meat and Meat Products: Epidemiology, Virulence Factors, Antimicrobial Resistance and Diagnosis. *Onderstepoort Journal of Veterinary Research* **2020**, *87*, doi:10.4102/ojvr.v87i1.1869.
61. Lepe, J.A. Aspectos Actuales de La Listeriosis. *Med Clin (Barc)* **2020**, *154*, 453–458, doi:10.1016/j.medcli.2020.02.001.
62. Choi, M.H.; Park, Y.J.; Kim, M.; Seo, Y.H.; Kim, Y.A.; Choi, J.Y.; Yong, D.; Jeong, S.H.; Lee, K. Increasing Incidence of Listeriosis and Infection-Associated Clinical Outcomes. *Ann Lab Med* **2018**, *38*, doi:10.3343/alm.2018.38.2.102.
63. Valenti, M.; Ranganathan, N.; Moore, L.S.P.; Hughes, S. *Listeria Monocytogenes* Infections: Presentation, Diagnosis and Treatment. *Br J Hosp Med* **2021**, *82*, doi:10.12968/hmed.2021.0107.

64. Freitag, I.G.R.; Pereira, R. de C.L.; Machado, E.S.; Hofer, E.; Vallim, D.C.; Hofer, C.B. Seroprevalence of *Listeria Monocytogenes* in HIV Infected Pregnant Women from Brazil. *Brazilian Journal of Infectious Diseases* **2021**, *25*, doi:10.1016/j.bjid.2021.101635.
65. Craig, A.M.; Dotters-Katz, S.; Kuller, J.A.; Thompson, J.L. Listeriosis in Pregnancy: A Review. *Obstet Gynecol Surv* **2019**, *74*, 362–368, doi:10.1097/OGX.0000000000000683.
66. Soni, D.K.; Ahmad, R.; Dubey, S.K. Biosensor for the Detection of *Listeria Monocytogenes* : Emerging Trends. *Crit Rev Microbiol* **2018**, *44*, 590–608, doi:10.1080/1040841X.2018.1473331.
67. Ricci, A.; Allende, A.; Bolton, D.; Chemaly, M.; Davies, R.; Fernández Escámez, P.S.; Girones, R.; Herman, L.; Koutsoumanis, K.; Nørrung, B.; et al. *Listeria Monocytogenes* Contamination of Ready-to-Eat Foods and the Risk for Human Health in the EU. *EFSA Journal* **2018**, *16*, doi:10.2903/j.efsa.2018.5134.
68. Jadhav, S.; Bhave, M.; Palombo, E.A. Methods Used for the Detection and Subtyping of *Listeria Monocytogenes*. *J Microbiol Methods* **2012**, *88*, 327–341, doi:10.1016/j.mimet.2012.01.002.
69. Li, F.; Ye, Q.; Chen, M.; Zhou, B.; Zhang, J.; Pang, R.; Xue, L.; Wang, J.; Zeng, H.; Wu, S.; et al. An Ultrasensitive CRISPR/Cas12a Based Electrochemical Biosensor for *Listeria Monocytogenes* Detection. *Biosens Bioelectron* **2021**, *179*, doi:10.1016/j.bios.2021.113073.
70. Cheng, C.; Peng, Y.; Bai, J.; Zhang, X.; Liu, Y.; Fan, X.; Ning, B.; Gao, Z. Rapid Detection of *Listeria Monocytogenes* in Milk by Self-Assembled Electrochemical Immunosensor. *Sens Actuators B Chem* **2014**, *190*, doi:10.1016/j.snb.2013.09.041.
71. Lu, Y.; Liu, Y.; Zhao, Y.; Li, W.; Qiu, L.; Li, L. A Novel and Disposable Enzyme-Labeled Amperometric Immunosensor Based on MWCNT Fibers for *Listeria Monocytogenes* Detection. *J Nanomater* **2016**, *2016*, doi:10.1155/2016/3895920.
72. Chai, C.; Lee, J.; Oh, S.W.; Takhistov, P. Impedimetric Characterization of Adsorption of *Listeria Monocytogenes* on the Surface of an Aluminum-Based Immunosensor. *J Food Sci* **2014**, *79*, doi:10.1111/1750-3841.12663.
73. Raziq, A.; Kidakova, A.; Boroznjak, R.; Reut, J.; Öpik, A.; Syritski, V. Development of a Portable MIP-Based Electrochemical Sensor for Detection of SARS-CoV-2 Antigen. *Biosens Bioelectron* **2021**, doi:10.1016/j.bios.2021.113029.
74. Organization, W.H. Coronavirus Disease 2019 (COVID-19): Situation Report, 73. **2020**.

75. Khailany, R.A.; Safdar, M.; Ozaslan, M. Genomic Characterization of a Novel SARS-CoV-2. *Gene Rep* **2020**, *19*, doi:10.1016/j.genrep.2020.100682.
76. Laue, M.; Kauter, A.; Hoffmann, T.; Michel, J.; Nitsche, A. Morphometry of SARS-CoV and SARS-CoV-2 Particles in Ultrathin Plastic Sections of Infected Vero Cell Cultures (Preprint). *bioRxiv* **2020**, *4*, 2020.08.20.259531, doi:10.1101/2020.08.20.259531.
77. Astuti, I.; Ysrafil Severe Acute Respiratory Syndrome Coronavirus 2 (SARS-CoV-2): An Overview of Viral Structure and Host Response. *Diabetes and Metabolic Syndrome: Clinical Research and Reviews* **2020**, *14*, doi:10.1016/j.dsx.2020.04.020.
78. Peng, Y.; Du, N.; Lei, Y.; Dorje, S.; Qi, J.; Luo, T.; Gao, G.F.; Song, H. Structures of the SARS -CoV-2 Nucleocapsid and Their Perspectives for Drug Design . *EMBO J* **2020**, *39*, doi:10.15252/embj.2020105938.
79. Burbelo, P.D.; Riedo, F.X.; Morishima, C.; Rawlings, S.; Smith, D.; Das, S.; Strich, J.R.; Chertow, D.S.; Davey, R.T.; Cohen, J.I. Sensitivity in Detection of Antibodies to Nucleocapsid and Spike Proteins of Severe Acute Respiratory Syndrome Coronavirus 2 in Patients with Coronavirus Disease 2019. *Journal of Infectious Diseases* **2020**, *222*, doi:10.1093/infdis/jiaa273.
80. Walls, A.C.; Park, Y.J.; Tortorici, M.A.; Wall, A.; McGuire, A.T.; Velesler, D. Structure, Function, and Antigenicity of the SARS-CoV-2 Spike Glycoprotein. *Cell* **2020**, *181*, 281-292.e6, doi:10.1016/j.cell.2020.02.058.
81. Hoffmann, M.; Kleine-Weber, H.; Schroeder, S.; Krüger, N.; Herrler, T.; Erichsen, S.; Schiergens, T.S.; Herrler, G.; Wu, N.H.; Nitsche, A.; et al. SARS-CoV-2 Cell Entry Depends on ACE2 and TMPRSS2 and Is Blocked by a Clinically Proven Protease Inhibitor. *Cell* **2020**, *181*, doi:10.1016/j.cell.2020.02.052.
82. Shang, J.; Ye, G.; Shi, K.; Wan, Y.; Luo, C.; Aihara, H.; Geng, Q.; Auerbach, A.; Li, F. Structural Basis of Receptor Recognition by SARS-CoV-2. *Nature* **2020**, *581*, doi:10.1038/s41586-020-2179-y.
83. Wrapp, D.; Wang, N.; Corbett, K.S.; Goldsmith, J.A.; Hsieh, C.L.; Abiona, O.; Graham, B.S.; McLellan, J.S. Cryo-EM Structure of the 2019-NCoV Spike in the Prefusion Conformation. *Science (1979)* **2020**, *367*, doi:10.1126/science.aax0902.
84. Post, N.; Eddy, D.; Huntley, C.; van Schalkwyk, M.C.I.; Shrotri, M.; Leeman, D.; Rigby, S.; Williams, S. V; Bermingham, W.H.; Kellam,



- P.; et al. Antibody Response to SARS-CoV-2 Infection in Humans: A Systematic Review. *PLoS One* **2021**, *15*, e0244126.
85. Dhamad, A.E.; Abdal Rhida, M.A. COVID-19: Molecular and Serological Detection Methods. *PeerJ* **2020**, *8*, doi:10.7717/peerj.10180.
86. Li, Z.; Yi, Y.; Luo, X.; Xiong, N.; Liu, Y.; Li, S.; Sun, R.; Wang, Y.; Hu, B.; Chen, W.; et al. Development and Clinical Application of a Rapid IgM-IgG Combined Antibody Test for SARS-CoV-2 Infection Diagnosis. *J Med Virol* **2020**, *92*, 1518–1524, doi:10.1002/jmv.25727.
87. Kausaite-Minkstimiene, A.; Ramanavicius, A.; Ruksnaite, J.; Ramanaviciene, A. A Surface Plasmon Resonance Immunosensor for Human Growth Hormone Based on Fragmented Antibodies. *Analytical Methods* **2013**, *5*, 4757–4763, doi:10.1039/c3ay40614h.
88. Morkvenaite-Vilkonciene, I.; Ramanaviciene, A.; Kisieliute, A.; Bucinskas, V.; Ramanavicius, A. Scanning Electrochemical Microscopy in the Development of Enzymatic Sensors and Immunosensors. *Biosens Bioelectron* **2019**, *141*, doi:10.1016/j.bios.2019.111411.
89. Plausinaitis, D.; Sinkevicius, L.; Samukaite-Bubniene, U.; Ratautaite, V.; Ramanavicius, A. Evaluation of Electrochemical Quartz Crystal Microbalance Based Sensor Modified by Uric Acid-Imprinted Polypyrrole. *Talanta* **2020**, *220*, doi:10.1016/j.talanta.2020.121414.
90. Balevicius, Z.; Ramanaviciene, A.; Baleviciute, I.; Makaraviciute, A.; Mikoliunaite, L.; Ramanavicius, A. Evaluation of Intact- and Fragmented-Antibody Based Immunosensors by Total Internal Reflection Ellipsometry. *Sens Actuators B Chem* **2011**, *160*, 555–562, doi:10.1016/j.snb.2011.08.029.
91. Cui, F.; Zhou, H.S. Diagnostic Methods and Potential Portable Biosensors for Coronavirus Disease 2019. *Biosens Bioelectron* **2020**, *165*, 112349, doi:10.1016/j.bios.2020.112349.
92. Carabelli, A.M.; Peacock, T.P.; Thorne, L.G.; Harvey, W.T.; Hughes, J.; de Silva, T.I.; Peacock, S.J.; Barclay, W.S.; de Silva, T.I.; Towers, G.J.; et al. SARS-CoV-2 Variant Biology: Immune Escape, Transmission and Fitness. *Nat Rev Microbiol* **2023**, *21*, doi:10.1038/s41579-022-00841-7.
93. Rahman, M.S.; Islam, M.R.; Alam, A.S.M.R.U.; Islam, I.; Hoque, M.N.; Akter, S.; Rahaman, M.M.; Sultana, M.; Hossain, M.A. Evolutionary Dynamics of SARS-CoV-2 Nucleocapsid Protein and Its Consequences. *J Med Virol* **2021**, *93*, doi:10.1002/jmv.26626.

94. Adair, T.H. An Emerging Role for Adenosine in Angiogenesis. *Hypertension* **2004**, *44*, 618–620, doi:10.1161/01.HYP.0000144802.18301.2f.
95. Goel, H.L.; Mercurio, A.M. VEGF Targets the Tumour Cell. *Nat Rev Cancer* **2013**, *13*, 871–882, doi:10.1038/nrc3627.
96. Simons, M.; Gordon, E.; Claesson-Welsh, L. Mechanisms and Regulation of Endothelial VEGF Receptor Signalling. *Nat Rev Mol Cell Biol* **2016**, *17*, 611–625, doi:10.1038/nrm.2016.87.
97. Guyot, M.; Pagès, G. VEGF Splicing and the Role of VEGF Splice Variants: From Physiological-Pathological Conditions to Specific Pre-mRNA Splicing. In *Methods in Molecular Biology*; 2015; Vol. 1332, pp. 3–23.
98. Ferrara, N.; Gerber, H.-P.; Lecouter, J. The Biology of VEGF and Its Receptors. *Nat Med* **2003**, *9*, 669–676, doi:10.1038/nm0603-669.
99. Kwon, Y.W.; Jo, H.-S.; Bae, S.; Seo, Y.; Song, P.; Song, M.; Yoon, J.H. Application of Proteomics in Cancer: Recent Trends and Approaches for Biomarkers Discovery. *Front Med (Lausanne)* **2021**, *8*, doi:10.3389/fmed.2021.747333.
100. Di Stasi, R.; De Rosa, L.; D’Andrea, L.D. Structure-Based Design of Peptides Targeting VEGF/VEGFRs. *Pharmaceuticals* **2023**, *16*, 851, doi:10.3390/ph16060851.
101. Mao, Y.; Ge, H.; Chen, W.; Wang, Y.R.; Liu, H.; Li, Z.; Bai, Y.; Wang, D.; Yu, Y.; Zhen, Q.; et al. RasGRP1 Influences Imiquimod-Induced Psoriatic Inflammation via T-Cell Activation in Mice. *Int Immunopharmacol* **2023**, *122*, doi:10.1016/j.intimp.2023.110590.
102. Shamsipour, S.; Sharifi, G.; Taghian, F. An 8-Week Administration of Bifidobacterium Bifidum and Lactobacillus Plantarum Combined with Exercise Training Alleviates Neurotoxicity of A $\beta$  and Spatial Learning via Acetylcholine in Alzheimer Rat Model. *Journal of Molecular Neuroscience* **2021**, *71*, doi:10.1007/s12031-021-01812-y.
103. Xu, M.; Yadavalli, V.K. Flexible Biosensors for the Impedimetric Detection of Protein Targets Using Silk-Conductive Polymer Biocomposites. *ACS Sens* **2019**, *4*, doi:10.1021/acssensors.9b00230.
104. Johari-Ahar, M.; Karami, P.; Ghanei, M.; Afkhami, A.; Bagheri, H. Development of a Molecularly Imprinted Polymer Tailored on Disposable Screen-Printed Electrodes for Dual Detection of EGFR and VEGF Using Nano-Liposomal Amplification Strategy. *Biosens Bioelectron* **2018**, *107*, doi:10.1016/j.bios.2018.02.005.
105. He, M.; Luo, P.; Xie, Y.; He, Y.; Wang, X.; Tan, L. Electrochemical Determination of Vascular Endothelial Growth Factor Using

- Functional Metal-Polymer Nanocomposites. *Colloids Surf A Physicochem Eng Asp* **2023**, 677, doi:10.1016/j.colsurfa.2023.132380.
106. Yuan, M.; Zhan, S.; Zhou, X.; Liu, Y.; Feng, L.; Lin, Y.; Zhang, Z.; Hu, J. A Method for Removing Self-Assembled Monolayers on Gold. *Langmuir* **2008**, 24, 8707–8710, doi:10.1021/la800287e.
107. Trček, J.; Mira, N.P.; Jarboe, L.R. Adaptation and Tolerance of Bacteria against Acetic Acid. *Appl Microbiol Biotechnol* **2015**, 99, 6215–6229, doi:10.1007/s00253-015-6762-3.
108. Miura, C.; Ohta, T.; Ozaki, Y.; Tanaka, H.; Miura, T. Trypsin Is a Multifunctional Factor in Spermatogenesis. *Proc Natl Acad Sci U S A* **2009**, 106, doi:10.1073/pnas.0907631106.
109. Grenier, D. Effect of Proteolytic Enzymes on the Lysis and Growth of Oral Bacteria. *Oral Microbiol Immunol* **1994**, 9, doi:10.1111/j.1399-302X.1994.tb00062.x.
110. Zhou, J.; Meng, X.; Han, Q.; Huang, Y.; Huo, L.; Lei, Y. An in Vitro Study on the Degradation of Multispecies Biofilm of Periodontitis-Related Microorganisms by Bovine Trypsin. *Front Microbiol* **2022**, 13, doi:10.3389/fmicb.2022.951291.
111. Yarman, A.; Scheller, F.W. How Reliable Is the Electrochemical Readout of MIP Sensors? *Sensors* **2020**, 20, 2677, doi:10.3390/s20092677.
112. Conte, M.P.; Petrone, G.; Di Biase, A.M.; Longhi, C.; Penta, M.; Tinari, A.; Superti, F.; Fabozzi, G.; Visca, P.; Seganti, L. Effect of Acid Adaptation on the Fate of *Listeria Monocytogenes* in THP-1 Human Macrophages Activated by Gamma Interferon. *Infect Immun* **2002**, 70, doi:10.1128/IAI.70.8.4369-4378.2002.
113. Mustafa, Y.L.; Keirouz, A.; Leese, H.S. Molecularly Imprinted Polymers in Diagnostics: Accessing Analytes in Biofluids. *J Mater Chem B* **2022**, 10, 7418–7449, doi:10.1039/D2TB00703G.
114. Ratautaite, V.; Brazys, E.; Ramanaviciene, A.; Ramanavicius, A. Electrochemical Sensors Based on L-Tryptophan Molecularly Imprinted Polypyrrole and Polyaniline. *Journal of Electroanalytical Chemistry* **2022**, 917, doi:10.1016/j.jelechem.2022.116389.
115. Ayerdurai, V.; Cieplak, M.; Kutner, W. Molecularly Imprinted Polymer-Based Electrochemical Sensors for Food Contaminants Determination. *TrAC Trends in Analytical Chemistry* **2023**, 158, 116830, doi:10.1016/j.trac.2022.116830.
116. Budvytyte, R.; Valincius, G.; Niaura, G.; Voiciuk, V.; Mickevicius, M.; Chapman, H.; Goh, H.Z.; Shekhar, P.; Heinrich, F.; Shenoy, S.; et al. Structure and Properties of Tethered Bilayer Lipid Membranes with

- Unsaturated Anchor Molecules. *Langmuir* **2013**, *29*, 8645–8656, doi:10.1021/la401132c.
117. Valincius, G.; Meškauskas, T.; Ivanauskas, F. Electrochemical Impedance Spectroscopy of Tethered Bilayer Membranes. *Langmuir* **2012**, *28*, 977–990, doi:10.1021/la204054g.
  118. Plikusiene, I.; Maciulis, V.; Ramanaviciene, A.; Balevicius, Z.; Buzavaite-Verteliene, E.; Ciplys, E.; Slibinskas, R.; Simanavicius, M.; Zvirbliene, A.; Ramanavicius, A. Evaluation of Kinetics and Thermodynamics of Interaction between Immobilized SARS-CoV-2 Nucleoprotein and Specific Antibodies by Total Internal Reflection Ellipsometry. *J Colloid Interface Sci* **2021**, *594*, 195–203, doi:10.1016/J.JCIS.2021.02.100.
  119. Ratautaite, V.; Ramanaviciene, A.; Oztekin, Y.; Voronovic, J.; Balevicius, Z.; Mikoliunaite, L.; Ramanavicius, A. Electrochemical Stability and Repulsion of Polypyrrole Film. *Colloids Surf A Physicochem Eng Asp* **2013**, *418*, doi:10.1016/j.colsurfa.2012.10.052.
  120. Zouaoui, F.; Bourouina-Bacha, S.; Bourouina, M.; Alcacer, A.; Bausells, J.; Jaffrezic-Renault, N.; Zine, N.; Errachid, A. Electrochemical Impedance Spectroscopy Microsensor Based on Molecularly Imprinted Chitosan Film Grafted on a 4-Aminophenylacetic Acid (CMA) Modified Gold Electrode, for the Sensitive Detection of Glyphosate. *Front Chem* **2021**, *9*, doi:10.3389/fchem.2021.621057.
  121. Ebdelli, R.; Rouis, A.; Mlika, R.; Bonnamour, I.; Jaffrezic-Renault, N.; Ben Ouada, H.; Davenas, J. Electrochemical Impedance Detection of Hg<sup>2+</sup>, Ni<sup>2+</sup> and Eu<sup>3+</sup> Ions by a New Azo-Calix[4]Arene Membrane. *Journal of Electroanalytical Chemistry* **2011**, *661*, doi:10.1016/j.jelechem.2011.07.007.
  122. Lewis, T.W.; Wallace, G.G.; Kim, C.Y.; Kim, D.Y. Studies of the Overoxidation of Polypyrrole. *Synth Met* **1997**, *84*, doi:10.1016/s0379-6779(97)80803-x.
  123. Jyoti; Gonzato, C.; Żołek, T.; Maciejewska, D.; Kutner, A.; Merlier, F.; Haupt, K.; Sharma, P.S.; Noworyta, K.R.; Kutner, W. Molecularly Imprinted Polymer Nanoparticles-Based Electrochemical Chemosensors for Selective Determination of Cilostazol and Its Pharmacologically Active Primary Metabolite in Human Plasma. *Biosens Bioelectron* **2021**, *193*, 113542, doi:10.1016/j.bios.2021.113542.
  124. Çalik, P.; Balci, O.; Özdamar, T.H. Human Growth Hormone-Specific Aptamer Identification Using Improved Oligonucleotide Ligand

- Evolution Method. *Protein Expr Purif* **2010**, *69*, doi:10.1016/j.pep.2009.05.015.
125. Anson, Fred.C.; Christie, J.H.; Osteryoung, R.A. A Study of the Adsorption of Cadmium(II) on Mercury from Thiocyanate Solutions by Double Potential-Step Chronocoulometry. *J Electroanal Chem Interfacial Electrochem* **1967**, *13*, 343–353, doi:10.1016/0022-0728(67)80037-8.
126. Ratautaite, V.; Boguzaitė, R.; Brazys, E.; Plausinaitis, D.; Ramanavicius, S.; Samukaite-Bubniene, U.; Bechelany, M.; Ramanavicius, A. Evaluation of the Interaction between SARS-CoV-2 Spike Glycoproteins and the Molecularly Imprinted Polypyrrole. *Talanta* **2023**, *253*, doi:10.1016/j.talanta.2022.123981.
127. Anson, F.C.; Osteryoung, R.A. Chronocoulometry: A Convenient, Rapid and Reliable Technique for Detection and Determination of Adsorbed Reactants. *J Chem Educ* **1983**, *60*, doi:10.1021/ed060p293.

## SANTRAUKA

### SANTRUMPOS

|            |  |
|------------|--|
| 11-MUA     | 11-merkaptoundekano rūgštis                          |
| 6-MCOH     | 6-merkapto-1-heksanolis                              |
| Au(MS)     | Auksu dengti mikroskopiniai stikleliai               |
| Au(s)      | Kvadratinis aukso elektrodas                         |
| Au(SPE)    | Spausdinto montažo aukso elektrodas                  |
| EIS        | Elektrocheminio impedanso spektroskopija             |
| KBV        | Kvadratinės bangos voltamperometrija                 |
| MIP        | Molekuliniu būdu išpausti polimerai                  |
| NIP        | Neišpausti polimerai                                 |
| PAD        | Impulsinė amperometrija                              |
| Ppy        | Polipirolas  |
| PUT        | 11-(1H-pirol-1-yl)-undekano-1-tiolis                 |
| rN         | SARS-CoV-2 nukleokapsidės baltymas                   |
| rS         | SARS-CoV-2 spyglio baltymas                          |
| SAM        | Savitvarkiai monosluoksniai                          |
| SAMmix     | Savitvarkių monosluoksnių mišinys                    |
| SARS-CoV-2 | Sunkaus ūminio respiracinio sindromo koronavirusas 2 |
| SPCE       | Spausdinto montažo anglies elektrodai                |
| SPE        | Spausdinto montažo elektrodas                        |
| VEGF       | Kraujagyslių endotelio augimo faktorius              |

### ĮVADAS

Per pastaruosius dešimtmečius elektrocheminių jutiklių technologijos ženkliai patobulėjo ir yra taikomos tokiose srityse kaip maisto sauga ir sveikatos priežiūra. Pastoviai didėja šių analizinių technologijų sudėtingumas ir taikymo mastai. Todėl, siekiant pagerinti jutiklių jautrumą, stabilumą ir selektyvumą tenka kurti naujas šiose analizinėse sistemose taikomas medžiagas ir novatoriškus analizės metodus. Tarp įvairių analizinėse sistemose taikomų medžiagų yra ir unikaliomis elektrocheminėmis savybėmis pasižymintys elektrai laidūs polimerai bei jų kompozitai, kurie yra dažnai naudojami kaip svarbūs naujos kartos jutiklių komponentai. Sukurti jutiklius, kurie atitiktų vis griežtesnius šiuolaikinių taikomųjų programų reikalavimus, yra sudėtinga užduotis, apimanti ne tik tinkamų medžiagų pasirinkimą, bet ir jų integravimą į sudėtingas sistemas, užtikrinančias didesnę analizės našumą. Siekiant šių tikslų, derinant elektrai laidžius polimerus su kitomis funkcinėmis

medžiagomis tokiomis kaip savitvarčiai monosluoksniai (SAM) arba DNR-aptamerai, galima sukurti atrankesnes kompozitines struktūras.

Elektrocheminiai metodai, tokie kaip elektrocheminė impedanso spektroskopija (EIS), kvadratinės bangos voltamperometrija (KBV) ir impulsinė amperometrija (PAD), tapo esminėmis priemonėmis tobulinant jutiklių technologijas. EIS yra universalus metodas, skirtas analizuoti jutiklio paviršiaus elektrines savybes. Matuojant sistemos varžą, sistemą žadinant įvairių dažnių kintama elektros srovę, taikant EIS metodą galima gauti išsamią informaciją apie elektrodo paviršiaus pokyčius, tokius kaip SAM arba molekulinio būdu įspaustų polimerų (MIP) susiformavimą. Šis metodas ypač naudingas vertinant įvairių elektrodo modifikacijų stabilumą ir nustatant jutiklio paviršiaus pokyčius po sąveikos su analitėmis. KBV yra pažangus metodas, pasižymintis dideliu jautrumu ir skiriamąja geba, todėl puikiai tinka mažoms nustatomų medžiagų koncentracijoms aptikti. PAD yra dažnai naudojamas elektrocheminės polimerizacijos metu ant jutiklio paviršiaus susidariusių polimerų sluoksnių storiui įvertinti. Keičiant elektrodui užduodamų impulsų potencialus bei trukmę, galima suformuoti įvairios struktūros ir įvairaus storio polimerų sluoksnius.. Be to, PAD taip pat gali būti naudojamas analizinio signalo įvertinimui.

Visi minėti elektrocheminiai metodai (EIS, KBV ir PAD) įgalina įvairiais aspektais įvertinti elektrodo paviršiaus modifikavimo efektyvumą, bei atlikti tiek kokybinį, tiek kiekybinį įvairių analičių nustatymą. Šiuos metodus taikant jutikliuose, kuriuose selektyvaus analitės atpažinimo funkciją atlieka struktūros grįstos elektrai laidžių polimerų panaudojimu, galima ženkliai padidinti jų jautrį ir selektyvumą.

### **Darbo tikslas:**

Pritaikyti pažangias laidžiųjų polimerų kompozitų gamybos technologijas molekulinio būdu įspaustų jutiklių ir imuninių jutiklių kūrimui.

### **Darbo uždaviniai:**

1. Spausdinto montažo anglies elektroda, padengti polipirolo sluoksniu modifikuotu bakterijų *Listeria monocytogenes* paviršinių struktūrų įspaudais, ir pritaikyti bakterijų *Listeria monocytogenes* aptikimui.
2. Skirtingais savitvarčiais monosluoksniais modifikuotus aukso elektrodus pritaikyti imuninio jutiklio, skirto antikūnams prieš SARS-CoV-2 spyglio baltymą aptikti, kūrimui.
3. Sukurti jutiklį, skirtą SARS-CoV-2 nukleokapsidės baltymui aptikti, suformuojant kompozitinę struktūrą sudarytą iš savitvarkio

monosluoksnio pasluoksnio ir SARS-CoV-2 nukleokapsidės baltymo molekulių įspaudais modifikuoto polipirolo sluoksnio.

4. Sukurti jutiklį, skirtą kraujagyslių endotelio augimo faktoriui (angl. *vascular endothelial growth factor* VEGF) aptikti, panaudojant aptamerus, įterptus į elektrai laidus polipirolo matricą.

### **Mokslinis naujumas**

Daugelyje disertacijoje aprašytų tyrimų yra taikomas elektrai laidus polimeras – polipirolas. Šis elektrai laidus polimeras pasižymi geru biologiniu suderinamumu. Disertacijoje aptariamos šio polimero pritaikymo jutikliuose galimybės, panaudojant kelis skirtingus kompozitinių struktūrų formavimo metodus: (1) polipirolo sluoksnyje suformuojant molekulių įspaudus, (2) formuojant molekulinio būdu įspautus polipirolo sluoksnius ant savitvarkių monosluoksnių (SAM) pasluoksnių, (3) į Ppy sluoksnį įterpiant DNR-aptamerus.

Pirmuose tyrimo etapuose buvo formuojami MIP, kurie buvo suformuoti polimerizuojant polipirolo sluoksnį su įterptomis ląstelėmis arba SARS-CoV-2 viruso baltymų molekulėmis. Po įterptos ląstelės arba baltymo molekulės pašalinimo polimero matricoje susidaro įspautai struktūrai komplementarios ertmės, įgalinančios selektyviai ir jautriai aptikti įspautąją struktūrą. Disertacijoje aprašytuose tyrimuose buvo taikomas papildomas SAM pasluoksnio formavimas, kuris buvo atliekamas prieš MIP sluoksnio formavimą. Tai įgalina orientuoti analitės molekulę, suformuoti plonesnį polipirolo sluoksnį ant elektrodo, pagerinti analitės difuziją ir sąveiką su MIP. Todėl taikant SAM pasluoksnį galima pagerinti jutiklio jautrumą ir selektyvumą. Dar viena tyrimu kryptis nagrinėjama šioje disertacijoje buvo skirta kompozitų sudarytų iš DNR-aptamerų ir Ppy taikymui jutikliuose. Aptamero įterpimas į polimero matricą, įgalina sukurti struktūrą tinkamą aptamerui komplementarios analitės nustatymui.

Šioje disertacijoje aprašyti tyrimo metodai buvo pritaikyti jutikliuose, kuriuose pritaikyti MIP sluoksniai. Viena iš tirtų tyrimams pasirinktų analizių yra *Listeria monocytogenes* bakterijos, kurios sukelia maistu plintančias ligas ir yra viena pagrindinių su šių ligų komplikacijomis susijusių mirčių priežasčių. Šiai analizei aptikti buvo kuriamas jutiklis, naudojant molekulių įspaudų technologiją. Polimero matricoje buvo suformuotos specifinės vietos, komplementarios bakterijos išorinėms struktūroms, taip užtikrinant greitą ir tikslų *Listeria monocytogenes* bakterijų aptikimą. Kita tirtų analizių buvo SARS-CoV-2 viruso nukleokapsidės baltymas. Šis baltymas buvo įterptas į Ppy sluoksnį, suformuotą ant SAM pasluoksnio. Pašalinus baltymą iš Ppy struktūros, susidarė ertmės, kurios yra komplementarios SARS-CoV-2 viruso



nukleokapsidės baltymui, užtikrinant tikslių jo atpažinimą. Trečioji analizė buvo VEGF, kuris yra svarbus nustatant navikų augimą, metastazes ir kraujagyslių susidarymo procesus. VEGF aptikimui buvo sukurtas jutiklis, iš trijų atskirų DNR fragmentų suformuotą DNR-aptamerą, įterpiančią polipirolo sluoksnį, suformuotą ant spausdinto montažo būdu pagaminto grafito elektrodo modifikuoto papildomai suformuotu Ppy pasluoksniu.

Disertacijoje pateikiami tyrimai skirti jutiklių technologijų tobulinimui ir skatina jutiklių technologijų pažangą.

### **Ginamieji teiginiai:**

1. *Listeria monocytogenes* bakterijų išorinių struktūrų išspaudais modifikuotas polipirolo sluoksnis gali būti suformuotas ant spausdinto montažo būdu pagaminto grafito elektrodo, panaudojant elektrinio potencialo impulsus. Taip modifikuotas elektrodas buvo tinkamas bakterijų *Listeria monocytogenes* aptikimui.
2. Mišriu savitvarkiu monosluoksniu modifikuotas aukso elektrodas gali būti pritaikytas imuninio jutiklio, skirto antikūnų prieš SARS-CoV-2 spyglio baltymą aptikimui netaikant elektrocheminių žymenų, kūrimui.
3. Kompozitas, sudarytas iš savitvarkio monosluoksniu pasluoksniu ir molekulių išspaudais modifikuoto polipirolo sluoksniu, gali būti panaudotas jutiklio kūrimui, skirto SARS-CoV-2 nukleokapsidės baltymui aptikti.
4. Elektrai laidaus polipirolo matrica modifikuota DNR aptamerais gali būti panaudota kuriant jutiklį, skirtą kraujagyslių endotelio augimo faktoriaus aptikimui.

### **Elektrai laidūs polimerai**

Elektrai laidžių polimerų taikymo sritys sparčiai plėtėsi, dėl unikalių jų puslaidininkinių savybių. Elektrai laidžių polimerų tyrimai prasidėjo po to, kai 1977 m. Shirakawa ir kt. [2] pastebėjo šių medžiagų elektrinį laidumą. Šie elektrai laidūs polimerai yra  $\pi$ - $\pi$  konjuguoti, o tai leidžia elektronų delokalizaciją, kuri suteikia jiems elektrinį laidumą, kai jie yra legiruojami tinkamomis medžiagomis. Šios medžiagos įveda arba pašalina elektronus į  $\pi$ - $\pi$  konjuguotą sistemą, todėl  $\pi$ -elektronai gali laisvai judėti polimero grandinėje, taip pagerinanant elektrinį laidumą. Elektrai laidūs polimerai yra itin svarbūs dėl savo unikalių elektrinių, magnetinių ir optinių savybių. Dažniausiai praktiniams tikslams taikomi elektrai laidūs polimerai yra polianilinas, polipirolas ir politiofenas.

### **Polipirolas savybės ir sintezės metodai**

Polipirolas (angl. *polypyrrole*, toliau – Ppy) yra laidus polimeras, pasižymintis lengva sinteze, stabilumu ir daug žadančiomis elektrinėmis savybėmis. Iš pradžių Ppy buvo gaunamas naudojant cheminę sintezę [8], tačiau dabar jis taip pat gali būti susintetinamas elektrocheminiu būdu, pasitelkiant oksidacinės polimerizacijos metodą. Elektrocheminė sintezė, kurios metu monomeras tiesiogiai oksiduojamas prie anodo, turi keletą privalumų: procesas yra paprastesnis, leidžia pasiekti didesnę galutinio produkto grynumą ir tiksliau kontroliuoti polimerizacijos sąlygas. Šiai sintezei dažniausiai yra naudojami galvanostatinis (pastovios srovės) arba potenciostatinis (nuolatinio potencialo) metodai.

Galvanostatinis metodas palaiko pastovų srovės stiprį, todėl galima tiksliai kontroliuoti susidarančio polimero sluoksnio storį. Tačiau, didėjant polimero sluoksniui, jo elektrinė varža taip pat didėja, dėl ko gali atsirasti nepageidaujamų šalutinių reakcijų [11, 12, 13, 14]. Potenciostatinis metodas palaiko pastovų elektrinį potencialą (įtampą) per visą sintezės procesą. Tai reiškia, kad reakcija vyksta esant nustatytam įtampos lygiui, o ne pastoviai srovei, kaip naudojant galvanostatinį metodą. Šis metodas leidžia tiksliau kontroliuoti polimerinio sluoksnio augimą, todėl galima išvengti nepageidaujamų šalutinių reakcijų, kurios gali atsirasti, jei sintezės sąlygos yra pernelyg agresyvios. Pastovaus potencialo palaikymas taip pat apsaugo nuo per didelės monomerų oksidacijos, užtikrinamas geresnę polimero sluoksnio kokybę [15, 16]. Be to, modifikuota impulsų potenciostatinė technika, kuri keičia anodinius ir katodinius impulsus, dar labiau pagerina polimero sluoksnio kokybę. Ši technika periodiškai keičia srovės kryptį, dėl

ko keičiasi elektrodo paviršiaus įkrova. Dėl to monomerai gali lengviau difunduoti link elektrodo paviršiaus, nuolat pasipildydami šalia jo. Tai padeda išlaikyti tolygų polimerizacijos procesą, sumažina šalutinių reakcijų tikimybę ir užtikrina vienodesnį bei kokybiškesnį polimero sluoksnį [17, 18].

### **Molekuliniu būdu įspaustų polimerų (MIP) kūrimas ir taikymas**

Molekulinių įspaudų technologija remiasi analitės (šablono) ir funkcinio monomero sąveika. Polimerizacijos metu, esant dideliame monomero kiekiui, susidaro trimatis polimero tinklelis su įterpta analite. Po polimerizacijos analitės šablonas yra pašalinamas iš polimero struktūros ir jo vietoje lieka analitei specifinės ertmės, kurios atitinka šablono formą, dydį ir cheminį funkcionalumą. Šios ertmės yra skirtos tikslinei analitei nustatyti. Molekulinio atpažinimo procesą lemia komplementarios sąveikos, tokios kaip vandeniliniai ryšiai, dipolio-dipolio sąveikos ir joninės sąveikos tarp šablono molekulės ir polimero matricos funkcinų grupių. Dėl šių sąveikų polimeras tampa selektyvus ir specifškai atpažįsta nustatomą molekulės šabloną [19].

Pagrindinis molekulinių įspaudų polimerų privalumas yra didelis jų selektyvumas ir stiprus giminingumas įspausitai molekulei. Vis dėlto, vienas didžiausių iššūkių, su kuriuo susiduria MIP tyrėjai, yra efektyvus šablono sukūrimas, leidžiantis tiksliai atpažinti norimą analitę. Nepaisant šio iššūkio, MIP turi didelį potencialą įvairiose biotechnologijų ir aplinkosaugos srityse [21, 22]. MIP dažnai naudojami afininėse jutiklių sistemose, kai polimero matrica leidžia selektyviai atpažinti konkrečias molekules, baltymus, virusus, bakterijas ar cheminius junginius. Tokie jutikliai selektyviai atpažįsta tikslines analites ir generuoja išmatuojamus signalus [20]. Molekuliniu būdu įspausti polimerai yra perspektyvi alternatyva tradiciniams jutikliams, kurie naudoja antikūnus ar receptorius, nes MIP dažnai pasižymi geresniu stabilumu ir patikimumu nei tradicinės sistemos [23, 24].

Norint efektyviai valdyti analičių ir jutiklių paviršių sąveiką, svarbu taikyti įvairius būdus, kurie galėtų padidinti specifiškumą. Vienas iš sprendimų galėtų būti polimerų pasluoksnio naudojimas, kuris sumažintų nepageidaujamą adsorbciją. Kitas panaudojimo būdas galėtų būti savitvarčių monosluoksnių (SAM) pasluoksnių integravimas, siekiant sumažinti nespecifinę sąveiką tarp analitės ir elektrodo paviršiaus. Be to, į polimero matricą galima įterpti DNR aptamerus, kurie būtų panaudoti kaip selektyvūs atpažinimo elementai. Šių metodų taikymas suteikia galimybę plėsti MIP naudojimą biologiniuose jutikliuose.

## **Polimerinio pasluoksnio formavimas**

Šis metodas apima plono polipirolo pasluoksnio formavimą, kuris sumažina sąveiką tarp analitės ir elektrodo paviršiaus. Ant šio pasluoksnio galima suformuoti MIP sluoksnį, leidžiantį jutikliui tiksliai atpažinti norimą analitę. Pavyzdžiui, Ktari ir kt. aprašė, kad flumekvinas gali būti aptinkamas naudojant paviršinių akustinių bangų (angl. *surface acoustic waves* – SAW) signalų perdavimo sistemą [32]. Tyrimuose buvo nurodyta, kad flumekvino molekulės gali sąveikauti su aukso paviršiumi, sutrikdydamos jo elektrocheminį aktyvumą, kas gali turėti neigiamos įtakos jutiklių veikimui. Mano tyrime buvo pasirinktas polipirolo pasluoksnio formavimas, siekiant sumažinti šiuos trukdžius. Šis metodas, neleidžia analitėms adsorbuotis ant elektrodo paviršiaus, taip sumažindamas galimus trukdžius ir užtikrindamas patikimesnius matavimo rezultatus. Taigi, šiame darbe buvo taikyta panaši technika, kur Ppy pasluoksnio suformavimas buvo itin svarbus MIP sluoksnio formavimui ir jutiklio patikimumo gerinimui.

## **Savitvarkių monosluoksnių struktūra, formavimosi procesai ir taikymas jutiklių paviršių modifikavimui**

Kita strategija apima SAM naudojimą jutiklių kūrimui. Tai patogus būdas keisti metalų, metalų oksidų ir puslaidininkių paviršiaus savybes. SAM – tai organiniai sluoksniai, susidarantys absorbuojant molekules iš tirpalo arba dujų fazės ant kietų paviršių. Adsorbuotos molekulės dažnai išsidėsto į kristalines arba pusiau kristalines struktūras [33].

Savitvarkius monosluoksnius sudarančios molekulės turi tris pagrindines dalis: galinę grupę, pradinę grupę ir pagrindinę grandinę. Pagrindinė grandinė jungia dvi grupes ir padeda sukurti tvarkingą struktūrą. SAM formavimosi metu molekulės su galine grupe (angl. *head group*), pasižyminčia stipriu afinitetu substratui, jungiasi prie paviršiaus ir išstumia anksčiau adsorbuotas organines medžiagas. Skirtingos galinės grupės selektyviai jungiasi su metalais, metalų oksidais ir puslaidininkiais, sudarydamos stiprius cheminius ryšius ant paviršiaus [34]. Dažniausias metodas – alkanotiolių adsorbicija iš etanolio tirpalo ant polikristalinio aukso paviršiaus. Kai pradinę grupę (angl. *terminal group*) atsiranda SAM paviršiuje, ji lemia savitvarkio monosluoksnio fizines ir chemines savybes, tokias kaip hidrofilišės ar hidrofobinės savybės. Alkanotiolatų ir aukso kompleksai sudaro mažus kristalinius monosluoksnio regionus, kurie toliau auga, adsorbuojantis papildomoms tiolio molekulėms. Molekulių persitvarkymas sustiprina van der Waals sąveiką tarp jų, todėl susidaro tankus ir tvarkingas monosluoksnis [38].

SAM formavimas pagrįstas stipria disulfidų, sulfidų ir tiolių adsorbicija ant aukso paviršiaus, kurią stabilizuoja van der Waals jėgos [39].

Voltametriniai tyrimai parodė, kad adsorbcijos metu tiolio grupės deprotonuojasi [40]. Naudojant  $\omega$ -funkcionalizuotus tiolius, prie SAM galima stipriai prijungti įvairias chemines grupes, leidžiančias sukurti naujas paviršiaus savybes, reikalingas biomolekulių surišimui [42, 43]. Mišrūs SAM, sudaryti iš dviejų skirtingų tiolių, gali sumažinti baltymų denatūraciją ir pagerinti imobilizuotų baltymų bioaktyvumą [44–46]. Tokie SAM paprastai turi vieną tiolatą su funkicine grupe ir kitą – inertišką, taip sumažindami sterinę kliūtį ir nespecifines sąveikas [45]. Tiolių funkcinų grupių pobūdis lemia jų sąveiką su biomolekulėmis. Mažos pradinės grupės, tokios kaip  $\text{NH}_2$  ar  $\text{OH}$ , padeda išlaikyti glaudžią ir tvarkingą monosluoksnio struktūrą, o didesnės, pavyzdžiui,  $\text{COOH}$ , sumažina sluoksnio tankumą ir tvarką [47]. Mišriuose monosluoksnuose  $\omega$ -pakeisti tioliai ir trumpesni alkanotioliai adsorbuojasi proporcingai jų kiekiui tirpale, o tai leidžia sumažinti sterinę kliūtį ir pagerinti paviršiaus savybes [50, 51]. SAM mišinys, sudarytas iš 6-merkaptio-1-heksanolio (6-MCOH) ir 11-merkaptoundekano rūgšties (11-MUA), užtikrina tikslių paviršiaus modifikavimą, palengvina biomolekulių imobilizavimą ir sumažina nespecifinę baltymų adsorbciją [52].

### **DNR aptamerų įterpimas į polimero matricą**

DNR aptamerai, veikiantys kaip selektyvūs atpažinimo elementai, gali būti efektyviai integruoti į polimero matricą, siekiant sukurti pažangius biojutiklius. Šis procesas leidžia aptamerams išlaikyti savo struktūrinį stabilumą ir funkcionalumą, o polimero matrica užtikrina tinkamą aplinką, kurioje aptamerai gali sąveikauti su analitėmis, tokiomis kaip baltymai ar kitomis biologinėmis molekulėmis. You ir kt. [54] pristatė naują biojutiklio kūrimo metodą, kuriame MIP sluoksnis suformuojamas ant stiklinio anglies elektrodo (angl. *glassy carbon electrode* – GCE) dalyvaujant amiloido- $\beta$  oligomerų ( $\text{A}\beta\text{O}$ ) šabloninėms molekulėms, kurios veikia kaip dirbtiniai antikūnai, pasižymintys dideliu specifiškumu mėginių matricoms.  $\text{A}\beta\text{O}$  molekulės gali būti selektyviai užregistruotos mėginiuose, o nespecifiniai junginiai pašalinami, formuojant „sumuštinio“ struktūrą kartu su aptamerais. Šis MIP-aptamero „sumuštinio“ tipo biojutiklis, optimaliomis sąlygomis, pasižymi itin dideliu specifiškumu ir jautrumu. Naudojant tinkamus MIP ir aptamerus, šį metodą galima pritaikyti kitų biologinių baltymų žymenų aptikimui, kas atveria naujas galimybes naudoti MIP ir aptamerus kaip antikūnų alternatyvas [55]. Šie aptamerai pagrįsti polimerai yra sukurti taip, kad selektyviai atpažintų tikslinius baltymus, kai aptameras yra integruotas į polimero struktūrą. Šioje disertacijoje taip pat nagrinėjamas šio metodo taikymas, kuriame aptamerai buvo integruoti į polimero matricą. Šie DNR

aptameriais pagrįsti polimerai buvo sukurti taip, kad efektyviai atpažintų kraujagyslių endotelio augimo faktorių.

### ***Listeria monocytogenes* bakterijos**

*Listeria monocytogenes* yra gramteigiamos lazdelės formos bakterijos, kurios geriausiai vystosi 37°C temperatūroje [56]. Šios bakterijos dažniausiai aptinkamos dirvožemyje ir gali būti pernešamos tokių gyvūnų kaip atrajotojai, paukščiai, jūrų gyvūnai ir vabzdžiai [58]. Jos gali užkrėsti įvairius maisto produktus, įskaitant mėsą, nepasterizuotą pieną, daržoves ir jūros gėrybes [59].

Šios bakterijos sukelta liga yra vadinama listeriozė, ir ji gali sukelti infekcijas bei kitas sunkias ligas, tokias kaip septicemija ir meningitas, kurių mirtingumas siekia 20–30% [60]. Ypač pažeidžiamos yra rizikos grupės, tokios kaip vyresni žmonės, nėščios moterys ir asmenys su silpnu imunitetu. Nepaisant mažo bendro sergamumo, nėščioms moterims infekcijų rizika yra 17 kartų didesnė, o listeriozės hospitalizavimo dažnis viršija 95% [61]. *Listeria monocytogenes* bakterijų aptikimas yra labai svarbus tiek sveikatos apsaugai, tiek maisto saugai, nes daugelis šalių taiko griežtą nulinės tolerancijos principą. Bakterijų buvimas kūdikių maiste ir medicininės paskirties produktuose yra visiškai neleistinas, o kituose maisto produktuose galiojimo laikotarpiu leidžiama ne daugiau kaip 100 KFV/g [66].

Elektrocheminiai jutikliai, pagrįsti molekulių išspaudų būdu, tampa veiksminga priemone listeriozei aptikti. Pavyzdžiui, naudojant auksinį elektrodą kartu su CRISPR/Cas12a sistema, buvo pasiekta 26 KFV/ml aptikimo riba [67].

### **SARS-CoV-2 viruso struktūriniai baltymai**

Sunkaus ūminio respiracinio sindromo koronavirusas 2 (SARS-CoV-2) sukėlė pasaulinę sveikatos krizę, todėl Pasaulio sveikatos organizacija (PSO) 2020 m. kovo 12 d. paskelbė COVID-19 pandemija po pirminio protrūkio Uhane, Kinijoje [71, 72]. SARS-CoV-2 yra vienos grandinės RNR virusas, kurio genomai yra apie 29,9 kb, todėl jis yra vienas ilgiausių tarp RNR virusų [73]. Virusui būdingi karūnos formos spygliai, kurie yra būtini užkrėsti šeiminingo ląstelės [74]. Virusas koduoja keturis struktūrinius baltymus: spyglio (rS), apvalkalo (E), membranos (M) ir nukleokapsidės (rN) baltymus [73]. Iš pradžių dėmesys buvo sutelktas į antikūnų prieš rS baltymą aptikimą, tačiau antikūnai paprastai susiformuoja tik antrąją infekcijos savaitę [82, 83]. Serologiniai tyrimai, tokie kaip imunofermentinė analizė (angl. *enzyme-linked immunosorbent assay* – ELISA) ir šoninio srauto imunologinis tyrimas (angl. *lateral flow immunoassay* – LFIA), turi tam tikrų apribojimų –

jie gali užtrukti ilgai arba būti nevisiškai automatizuoti [83, 84]. Elektrocheminiai imuniniai jutikliai, dėl savo mažų sąnaudų ir paprasto naudojimo, suteikia pranašumų diagnostikoje [89]. Šie jutikliai leidžia nustatyti tiek antikūnus prieš SARS-CoV-2, tiek ir patį nukleokapsidės baltymą, kuris yra svarbus viruso identifikavimui. Kadangi nukleokapsidės baltymas mažiau linkęs mutacijoms nei spyglio baltymas, jo nustatymas gali užtikrinti patikimesnius diagnostikos rezultatus [90, 91].

### **Kraujagyslių endotelio augimo faktorius**

Kraujagyslių endotelio augimo faktorius (angl. *vascular endothelial growth factor*, toliau – VEGF) yra baltymas, kuris suaktyvėja reaguodamas į deguonies trūkumą (hipoksiją). Jis būtinas kraujagyslių formavimuisi (vaskulogenezei) ir naujų kraujagyslių augimui iš esamų (angiogenezei), o šie procesai dažnai susiję su vėžio vystymusi [92]. VEGF šeimą sudaro penki nariai: VEGF-A, VEGF-B, VEGF-C, VEGF-D ir placentos augimo faktorius (PLGF) [94], iš kurių VEGF-A yra tyrinėtas išsamiausiai. Šis baltymas turi devynias proangiogenines izoformas, o dažniausiai randama yra VEGF<sub>165</sub>, kuri glaudžiai siejama su vėžio augimu ir metastazių susidarymu [96].

VEGF aptikimas ir kiekybinis nustatymas yra itin svarbūs klinikinei diagnostikai bei gydymo efektyvumo stebėsenai. Ankstyvas šio biožymens identifikavimas padeda diagnozuoti vėžį ir yra susijęs su įvairiomis ligomis, tokiomis kaip reumatoidinis artritas [98], psoriazė [99] ir Alzheimerio liga [100]. VEGF aptikimui buvo sukurta daugybė metodų, pasitelkiant skirtingas elektrodų medžiagas ir technologijas. Viena iš metodikų apjungia lanksčias šilko baltymų matricas su laidžiais rašalais ir pasiekia aptikimo ribą – 1,03 pg/mL, o tiesinis diapazonas svyruoja nuo 1 pg/mL iki 1 μg/mL [101]. Kitas metodas naudoja spausdinto montažo auksinį elektrodą, funkcionalizuotą molekulinio būdu išpaustu polimeru, kuris pasiekia ypač žemą aptikimo ribą, kuri yra 0,005 pg/mL tiesiniame diapazone nuo 0,01 pg/mL iki 7000 pg/mL [102]. Šis metodas išryškina MIP technologijos derinimo su antikūnais konjuguotomis nanoliposomomis veiksmingumą, leidžiantį itin jautriai aptikti VEGF. Kita technika, naudojanti poli(o-fenilendiaminą) ant grafeno nanojuostų ir aukso nanodalelėmis modifikuotą stiklinį anglies elektrodą. Pasiektas tiesinis diapazonas buvo nuo 0,5 ng/mL iki 500 ng/mL, su aptikimo riba – 300 pg/mL [103]. Tikslus VEGF aptikimas yra labai svarbus siekiant geriau suprasti jo vaidmenį ligų progresavime ir kuriant tikslines terapijas, kurios galėtų reikšmingai pagerinti klinikinius tyrimus, ypač gydant vėžį ir lėtines uždegimines ligas.

### **MIP pagrindu veikiančių jutiklių analizinė sistema bakterijoms aptikti**

Jutikliams kurti buvo naudojami spausdinto montažo grafito elektrodai (angl. *screen-printed carbon electrodes*, toliau – SPCE). Prieš suformuojant Ppy sluoksnį, elektrodai buvo elektrochemiškai valomi naudojant 0,5 M sieros rūgštį, atliekant 20 ciklų, kurių metu buvo suteiktas potencialas nuo  $-0,1$  V iki  $+1,2$  V, o skleidimo greitis buvo  $0,1$  V/s. Norint sumažinti *Listeria monocytogenes* bakterijų virulentiškumą ir išlaikyti jų struktūrą,  $10^9$  KfV/ml bakterijų suspensija buvo paveikta 70% etanolio tirpalu ir 24 valandas veikama UV spinduliuote. Šis apdorojimo procesas sunaikino bakterijų DNR, tačiau minimaliai paveikė jų formą ir ląstelės sienelės. Išlaikyta bakterijų formos struktūra yra labai svarbi molekulinio būdu įspaustų polimerų kūrimui.

MIP sluoksnio formavimas vyko keliais etapais. Visų pirma, polipirolo pasluoksnis buvo suformuotas naudojant 0,5 M pirolo tirpalą, suteikiant sistemai penkių pulsų seką ( $+950$  mV 1 sekundę,  $0$  V 30 sekundžių). Tuomet į tą patį pirolo tirpalą buvo pridėta  $10^9$  KfV/ml *Listeria monocytogenes* bakterijų, ir ta pati pulsų seka buvo naudojama antrajam sluoksniui suformuoti. Vėliau, elektrodai buvo inkubuojami skirtinguose ekstrahavimo tirpaluose: 0,05 M sieros rūgštyje, 10% acto rūgštyje, 0,1% L-lizino tirpale ir 10 V/ml tripsino tirpale,  $37$  °C temperatūroje 30 minučių, kad būtų pašalintos įspaustos bakterijos ir užbaigtas MIP sluoksnio formavimas. Kontrolinis neįspausto polimero (NIP) sluoksnis buvo formuojamas analogiškai, tik nepridedant bakterijų į pirolo tirpalą. Po sluoksnių formavimo MIP ir NIP modifikuoti elektrodai buvo analizuojami naudojant impulsinę amperometriją, suteikiant sistemai 10 pulsų seką ( $+600$  mV ir  $0$  V (po 2 sekundes kiekvienam impulsui)).

### **SAM pagrindu veikiančių imuninių jutiklių analizinė sistema antikūnų prieš rS baltymą aptikti**

Siekiant sukurti SAM pagrindu veikiančius imuninius jutiklius, skirtus aptikti antikūnus prieš SARS-CoV-2 spyglio baltymą (rS), buvo būtina kruopščiai paruošti elektrodų paviršius. Tam buvo pasirinkti du elektrodų tipai: kvadratinis aukso elektrodas (Au(s)) ir auksu dengti mikroskopiniai stikleliai (Au(MS)). Abu pasirinkti elektrodai buvo specialiai apdoroti, funkcionalizuoti ir apibūdinti naudojant elektrocheminius metodus.

Kvadratiniai aukso elektrodai (Au(s)), kurių paviršiaus plotas buvo  $2$  cm<sup>2</sup> ir pagaminti iš 99,9% gryno aukso, buvo poliruojami ir valomi NaBH<sub>4</sub> tirpalu. Po kiekvieno eksperimento jie buvo pakartotinai naudojami, atliekant tą patį paruošimo procesą. Ant jų paviršiaus buvo suformuotas 11-MUA



monosluoksnis, pamerkiant elektrodą 18-ai valandų į 1 mM 11-MUA metanolio tirpalą. Po to elektrodas buvo plaunamas dejonizuotu vandeniu. Toliau elektrodas pamerkiamas į 20 mM 1-etil-3-(3-dimetilaminopropil) karbodiimido (EDC) ir 5 mM N-hidroksisukcinimido (NHS) tirpalų mišinį, ir laikomas 20 min. Elektrodas nuplaunamas dejonizuotu vandeniu, pamerkiamas į 50  $\mu\text{g}\cdot\text{mL}^{-1}$  rS tirpalą ir laikomas 45 min.

Mikroskopiniai, 20 x 30 mm dydžio stikleliai prieš naudojimą buvo valomi 2-propanoliu ir panardinami į ultragarso vonelę 15 minučių. Po šio proceso, stikleliai buvo panardinti į koncentruotą  $\text{H}_2\text{SO}_4$  tirpalą 30 minučių ir vėliau išdžiovinti naudojant  $\text{N}_2$  dujų srautą (99,99% grynumo). Išdžiovinti stikleliai buvo patalpinti į vakuuminę magnetrono kamerą, kurioje dangos nusodinimas buvo pradėtas tik pasiekus bent  $7\cdot 10^{-8}$  Torr vakuumą. Pirmiausia ant stiklelių paviršiaus buvo padengtas plonas, apie 10 nm storio titano sluoksnis, kuris pagerino aukso sukibimą su stiklo paviršiumi. Po to buvo padengtas 100 nm storio aukso sluoksnis, suformuojant auksinį elektrodą (Au(MS)). Šio darbinio elektrodo geometrinis plotas – 0,179  $\text{cm}^2$ . Au(MS) elektrodai buvo inkubuojami 4 valandas mišraus 1 mM SAM tirpalu, sudarytu iš 6-MCOH ir 11-MUA (santykiu 9:1). Po to, kai Au(MS) elektrodai buvo nuplauti ir nudžiovinti, SAM sluoksnis buvo aktyvuotas EDC/NHS tirpalu. Po aktyvacijos, Au(MS) elektrodai buvo inkubuojami 45 minutes rS baltymų tirpalu. Likę aktyvūs esteriai buvo užblokuoti 0,5% jaučio serumo albumino tirpalu, o vėliau ant paviršiaus buvo imobilizuoti anti-rS antikūnai.

Au(s) ir Au(MS) elektrodai buvo elektrochemiškai charakterizuojami naudojant ciklinę voltamperometriją (CV) ir elektrocheminę impedanso spektroskopiją (EIS). Eksperimentai buvo atlikti trijų elektrodų sistemoje, naudojant redokso mediatorių (2,5 mmol/L  $\text{K}_4[\text{Fe}(\text{CN})_6]$  ir 2,5 mmol/L  $\text{K}_3[\text{Fe}(\text{CN})_6]$  10 mmol/L PBS, 7,4 pH, tirpale), siekiant įvertinti elektrodų elektrocheminį atsaką skirtinguose modifikacijos etapuose ir patikrinti elektrodų tinkamumą imuninių jutiklių taikyme.

### **Analizinės sistemos kūrimas SAM pagrindu sukurtiems MIP jutikliams rN baltymo aptikimui**

SAM sluoksnis buvo formuojamas ant spausdinto montažo aukso elektrodų (Au(SPE)), inkubuojant juos 20 °C temperatūroje 2 valandas 10 mmol/L 11-(1H-pirol-1-yl)-undekano-1-tiolio (PUT) etanolio tirpale. Po inkubacijos elektrodai buvo nuplauti dejonizuotu vandeniu ir išdžiovinti azoto srautu. Po to ant SAM modifikuotų elektrodų buvo elektrochemiškai suformuotas polipirolų sluoksnis, naudojant polimerizacijos tirpalą, sudarytą iš 25 mmol/L pirolų ir 25  $\mu\text{g}/\text{mL}$  rN baltymo. Polimerizacija buvo vykdoma naudojant dešimt potencialo pulsų (+950 mV 1 sekundę, po to 0 V 30

sekundžių), taip suformuojant struktūrą Au(SPE)/SAM/(Ppy+rN), sudarytą įterpiant rN baltymą į polipirolo sluoksnį. Norint pašalinti rN baltymą ir sukurti molekulinį būdą įspaustą polimerą, elektrodai buvo inkubuojami 10 minučių 0,1 mol/L sieros rūgšties tirpale. Šis procesas sukūrė MIP struktūrą su erdmėmis, atitinkančiomis rN baltymo formą (Au(SPE)/SAM/MIP). Kontroliniai elektrodai buvo paruošti tokiu pačiu būdu, tačiau nenaudojant rN baltymo (Au(SPE)/SAM/NIP).

Jutiklio gebėjimas aptikti rN baltymą buvo įvertintas inkubuojant 5 minutes Au(SPE)/SAM/MIP elektrodus su skirtingomis rN baltymo koncentracijomis (nuo 0 iki 35 nM), naudojant redokso mediatorių (2,5 mmol/L  $K_4[Fe(CN)_6]$  ir 2,5 mmol/L  $K_3[Fe(CN)_6]$  10 mmol/L PBS, 7,4 pH, tirpale). Elektrocheminiai matavimai buvo atliekami pasitelkiant EIS ir KBV metodus. EIS matavimai buvo vykdomi esant atviros grandinės potencialui (angl. *open circuit potential*, toliau – OCP), naudojant 10 mV amplitudę ir dažnių diapazoną nuo 100 kHz iki 0,1 Hz. KBV eksperimentai buvo atliekami 4 mV žingsniu, 20 Hz dažniu ir 50 mV impulsų dydžiu potencialų diapazone nuo -0,4 V iki +0,6 V. EIS duomenys buvo analizuojami naudojant Randles ir ekvivalentines schemas, siekiant įvertinti elektrodų elektrinį atsaką ir biologinio jutimo tinkamumą.

### **Aptameriais pagrįsto jutiklio analitinės sistemos kūrimas VEGF baltymo aptikimui**

Prieš modifikavimą polimeriniu sluoksniu, SPCE elektrodai buvo valomi elektrochemiškai, atliekant ciklinę voltamperometriją 0,5 M sieros rūgšties tirpale. Valymas vyko naudojant 20 ciklų, suteikiant 0,1 V/s greitį, potencialo diapazone nuo -0,1 V iki +1,2 V. Polimero sluoksnio formavimas buvo vykdomas naudojant dviejų etapų elektrocheminę polimerizaciją. Pirmajame etape naudojant 5 potencialų impulsų seką (+0,95 V 1 s, po to 0 V 30 s) buvo suformuotas Ppy pasluoksnis naudojant tirpalą, sudarytą iš 0,1 mol/L pirolo. Antrajame etape į polimerizacijos tirpalą buvo pridėtas anti-VEGF aptameras, ir pakartota ta pati 5 pulsų seka. Šis metodas leido integruoti anti-VEGF aptamerą į Ppy sluoksnį, taip užtikrinant jo stabilumą ir tvirtą susirišimą polimero struktūroje. Įterpti aptamerai į polimero matricą buvo charakterizuojami naudojant impulsinę amperometriją. Matavimai buvo vykdomi naudojant dešimt potencialo pulsų (+600 mV 2 sekundes, po to 0 V 2 sekundes).

## REZULTATŲ APTARIMAS

### **MIP taikymas kuriant elektrocheminius jutiklius, skirtus aptikti *Listeria monocytogenes* bakterijas**

Šiame tyrime nagrinėjamas MIP naudojimas elektrocheminiuose jutikliuose, skirtuose aptikti *Listeria monocytogenes* bakterijas. Procesas prasideda nuo MIP sluoksnių formavimo ant SPCE naudojant impulsinę amperometriją. Pirmiausia elektrodo paviršiuje elektrochemiškai suformuojamas Ppy pasluoksnis, apsaugantis nuo tiesioginio bakterijų sąlyčio su elektrodu. Vėliau jutimo sluoksnis formuojamas polipiroliu, į kurį kartu integruojami *Listeria monocytogenes* bakterijų šablonai. Pašalinus bakterijas, lieka jų įspaudai, dėl kurių susidaro selektyvus MIP sluoksnis, gebantis tiksliai atpažinti bakterijas.

Siekiant pašalinti bakterijų šablonus iš MIP sluoksnių ir užtikrinti jų tikslių veikimą, buvo išbandyti keli ekstrakcijos metodai. Pirmasis šablonų ekstrakcijos metodas buvo pagrįstas NIP ir MIP inkubavimu acto rūgšties tirpale. Acto rūgštis yra silpna organinė rūgštis, kenksminga daugumai bakterijų net esant vos 0,5 % koncentracijai. Be kitų neigiamų poveikių, acto rūgštis anijonas sukelia viduląstelinio pH sumažėjimą ir trikdo tam tikras metaboles grandines [105]. Dėl to ląstelės membranoje susidaro skylės, pro kurias išteka citoplazma ir ląsteliniai organoidai. Skenuojančios elektroninės mikroskopijos (SEM) vaizdai parodė, kad bakterijų ląstelių paviršiuje atsirado nelygios, šiurkščios duobutės, kas patvirtino, jog ekstrakcija naudojant acto rūgštį buvo itin veiksminga (10 pav., 43 psl.). Vis dėlto, *Listeria monocytogenes* bakterijų atsparumas rūgštims yra nuspėjamas molekulinis atsakas, užtikrinantis ląstelių išlikimą nepalankioje aplinkoje. Kitų tyrėjų morfologiniai tyrimai parodė padidėjusį bakterijų viduląstelinį išlikimą bei rūgštims prisitaikiusių *Listeria monocytogenes* ląstelių vystymąsi vakuolėse ir citoplazmoje [110]. Dėl šios priežasties tolimesniuose tyrimuose acto rūgšties nebuvo naudojama. Kitu ekstrakcijos reagentu buvo pasirinktas fermentas tripsinas, kuris selektyviai hidrolizuoja ląstelių sienelių baltymus [106] nepažeisdamas Ppy matricos. Naudojant tripsiną, MIP jutikliai pasiekė didesnę srovės tankį nei NIP (11 pav., 45 psl.), o selektyvi ekstrakcija pagerino jutiklio jautrumą ir specifiškumą, užtikrindama visišką bakterijų šablonų pašalinimą.

Elektrocheminis jutiklių charakterizavimas buvo atliktas naudojant impulsinę amperometriją. MIP modifikuoti elektrodai rodė žymiai didesnę atsaką į skirtingas *Listeria monocytogenes* koncentracijas, palyginti su NIP elektrodais. Šie MIP jutikliai pasiekė aptikimo ribą – 70 KFV/mL, o nustatymo riba buvo 210 KFV/mL (12 pav., 46 psl.). Molekulinio įspaudimo

efektyvumas buvo įvertintas naudojant įspaudimo koeficientą (IF), kuris apskaičiuojamas kaip MIP ir NIP jutiklių atsako kreivės polinkio santykis [113]. Tyrimo rezultatai parodė, kad MIP įspaudimo koeficientas buvo apie 3,93. Kadangi IF vertė, didesnė nei 1, tai gali reikšti gerą molekulinio įspaudimo kokybę ir stiprų specifiškumą tikslinei analizei [111].

Rezultatai patvirtina, kad MIP pagrįsti elektrocheminiai jutikliai turi galimybę jautriai ir selektyviai aptikti *Listeria monocytogenes* bakterijas. Naudojant tripsiną kaip ekstrakcijos reagentą, padidėja išpaustų bakterijų pašalinimo efektyvumas, kas pagerina jutiklio veikimą. Šie tyrimai rodo, jog MIP pagrįsti jutikliai yra perspektyvūs diagnostikos taikymams realiomis sąlygomis.

### **SAM modifikuotų aukso elektrodų taikymas kuriant imuninius jutiklius, skirtus aptikti antikūnus prieš SARS-CoV-2 spyglio baltymus**

Šiame tyrime analizuojamas aukso elektrodų modifikavimas, naudojant SAM, siekiant sukurti imuninį jutiklį, skirtą aptikti antikūnus prieš SARS-CoV-2 rS baltymus. Modifikavimui buvo naudojami tiek kvadratiniai aukso elektrodai (Au(s)), tiek auksu padengti mikroskopiniai stikleliai (Au(MS)), ant kurių paviršiaus buvo suformuotas SAM. Norint įvertinti šių SAM modifikacijų poveikį elektrodo laidumui ir bendrajam jutiklio veikimui, buvo taikomi elektrocheminiai metodai, tokie kaip ciklinė voltamperometrija (CV) ir elektrocheminio impedanso spektroskopija (EIS). Iš pradžių Au(s) elektrodai buvo modifikuoti 1 mM 11-merkaptoundekano rūgštimi (11-MUA), kad būtų suformuotas SAM sluoksnis, o Au(MS) elektrodai buvo modifikuojami 1 mM mišriu SAM etanoliniu tirpalu (SAMmix), sudarytu iš 6-merkapto-1-heksanolio (6-MCOH) ir 11-MUA (moliniu santykiu 1 : 9).

Ant Au(s) elektrodų susiformavęs 11-MUA SAM sluoksnis sukūrė stabilų ir gerai organizuotą monosluoksnį. Dėl to žymiai sumažėjo srovės atsakas (14 pav., 51 psl.), nes buvo blokuojamas elektronų perdavimas. Kadangi 11-MUA modifikuoti elektrodai nebeužtikrino pakankamo elektronų perdavimo, tolesniems tyrimams, taikant CV metodą, buvo pasirinkti SAMmix modifikuoti Au(MS) elektrodai. SAMmix buvo naudojamas siekiant išlaikyti stabilumą ir tuo pačiu leisti redokso mediatoriams pasiekti elektrodo paviršių, taip sumažinant struktūrinių defektų kiekį. CV matavimai parodė, kad SAMmix sumažino srovės tankį nuo  $712,4 \pm 5,9 \mu\text{A}\cdot\text{cm}^{-2}$  iki  $504,6 \pm 19,3 \mu\text{A}\cdot\text{cm}^{-2}$ , kas rodo ribotą, bet vis dar pakankamą elektronų perdavimą (14 pav., 51 psl.). Vėliau, aktyvius 11-MUA karboksi grupes naudojant EDC-NHS tirpalą, srovės tankis šiek tiek padidėjo iki  $513,1 \pm 6,6 \mu\text{A}\cdot\text{cm}^{-2}$ , kas pagerino elektronų perdavimą prieš imobilizuojant rS baltymą. Baltymo sluoksnio imobilizacija dar labiau sumažino srovės tankį

iki  $459,6 \pm 9,3 \mu\text{A}\cdot\text{cm}^{-2}$ , nes baltymų sluoksnis sukūrė papildomą barjerą. EIS matavimai suteikė išsamesnės informacijos apie krūvio pernašos varžą ( $R_{ct}$ ), susijusią su kiekvienu modifikavimo etapu (15 pav., 52 psl.). Au(s) elektrodų atveju  $R_{ct}$  padidėjo nuo  $96,2 \pm 1,2 \Omega\cdot\text{cm}^2$  iki  $10,6 \pm 0,2 \text{k}\Omega\cdot\text{cm}^2$  po SAM sluoksnio susiformavimo, pabrėžiant izoliacines 11-MUA sluoksnio savybes. Aktyvinimas SAM karboksi grupių, naudojant EDC-NHS, sumažino  $R_{ct}$  iki  $5,67 \pm 0,09 \text{k}\Omega\cdot\text{cm}^2$ , palengvindamas elektronų perdavimą, o rS baltymo imobilizavimas vėl padidino  $R_{ct}$  iki  $12,3 \pm 0,27 \text{k}\Omega\cdot\text{cm}^2$ . Priešingai, Au(MS) elektrodų  $R_{ct}$  padidėjo nedaug – nuo  $98,2 \pm 1,2 \Omega\cdot\text{cm}^2$  iki  $803 \pm 10 \Omega\cdot\text{cm}^2$  po SAMmix susidarymo ir iki  $1202 \pm 23 \Omega\cdot\text{cm}^2$  po baltymų imobilizavimo, tai rodo, kad buvo pasiektas stabilumo ir elektronų perdavimo galimybių balansas.

Imuninio jutiklio, skirto anti-rS aptikimui, analizė parodė, kad jo aptikimo riba yra 2,78 nM, o nustatymo riba siekia 9,17 nM, remiantis EIS matavimais (16 pav., 54 psl.). Šie rezultatai pabrėžia SAMmix modifikuotų Au(MS) elektrodų efektyvumą, leidžiantį tiksliai ir selektyviai aptikti antikūnus prieš SARS-CoV-2 spyglio baltymus. Paviršiaus modifikavimo procesai – nuo SAM sluoksnio susiformavimo iki baltymų imobilizavimo – buvo esminiai, tobulinant elektrodų elektrochemines savybes ir gerinant imuninio jutiklio veikimą. Tyrimas išryškina paviršiaus chemijos svarbą optimizuojant elektrodų funkcionalumą specifiniams elektrocheminiams tikslams, ypač kuriant patikimas diagnostikos priemones antikūnų prieš SARS-CoV-2 baltymų aptikimui.

### **SAM modifikuotų aukso elektrodų taikymas kuriant MIP jutiklius, siekiant aptikti SARS-CoV-2 nukleokapsidės baltymą**

SARS-CoV-2 nukleokapsidės baltymo aptikimas, naudojant SAM pagrindu veikiančią MIP metodiką, pagerino jutiklio veikimą, nes buvo sukurta stabili sąsaja tarp spausdinto montažo auksinio elektrodo (Au(SPE)) ir polimero sluoksnių. Ant Au(SPE) elektrodo suformuotas SAM sluoksnis (Au(SPE)/SAM) veikė kaip tarpinis sluoksnis tarp elektrodo ir jutimo sluoksnio. Alkantolis buvo sudarytas taip, kad jo pradinė grupė buvo modifikuota piroly (PUT). Šis SAM užtikrino stabilų polipirolo jutimo sluoksnio susidarymą, o kartu su MIP formavimu buvo sukurtas kompozitas, kuris užtikrino komplementarių vietų susidarymą SARS-CoV-2 nukleokapsidės baltymui atpažinti. Toks modifikavimas padidino jutiklio stabilumą, veiksmingai pagerino sąveiką su tikslinėmis molekulėmis ir užtikrino didesnę jautrumą bei specifiškumą, kas yra itin svarbu jutiklių veikimui.

Elektrodų Au(SPE)/SAM elektrocheminis tyrimas buvo atliktas naudojant KBV ir EIS metodus. Rezultatai parodė, kad po SAM sluoksnio susidarymo srovės tankis sumažėjo, o krūvio pernašos varža ( $R_{ct}$ ) padidėjo, kas rodo pasikeitusias elektrodo paviršiaus savybes. Nyquist diagramos (18 pav., B dalis, 57 psl.) suteikė papildomų įžvalgų apie elektrodo paviršiaus pokyčius. KBV analizė parodė, kad po Ppy elektropolimerizacijos Au(SPE)/SAM/Ppy elektrodas pasižymėjo didesne srovės amplitude, palyginti su Au(SPE)/SAM/(Ppy+rN) elektrodu (18 pav., A dalis, 57 psl.). Tai siejama su mažesniu Au(SPE)/SAM/Ppy elektrodo sluoksnio storiumi. Po šablono ekstrahavimo iš Au(SPE)/SAM/(Ppy+rN) elektrodų, srovės tankis padidėjo iki  $0,44 \pm 0,03 \text{ mA} \cdot \text{cm}^2$ , palyginus su Au(SPE)/SAM/NIP reikšme ( $0,19 \pm 0,06 \text{ mA} \cdot \text{cm}^2$ ), kas rodo, jog susidarė įspaustos ertmės, pagerinančios krūvio pernašą.

EIS tyrimas papildomai charakterizavo Au(SPE)/SAM/Ppy ir Au(SPE)/SAM/(Ppy+rN) elektrodus, naudojant tą patį redokso mediatorių  $[\text{Fe}(\text{CN})_6]^{3-/4-}$  (18 pav., B dalis, 57 psl.). Pašalinus nukleokapsidės šabloną iš Au(SPE)/SAM/(Ppy+rN), buvo pastebėta padidėjusi elektronų pernaša ir mažesnė varža. Nors Nyquist diagrama neparodė ryškių pokyčių po šablono pašalinimo, Bode diagrama (19 pav., 58 psl.) leido geriau įžvelgti šiuos dinamikos pokyčius. SEM vaizdai (20 pav., 59 psl.) taip pat patvirtino skirtumus tarp palygintų paviršių: Au(SPE) elektrodas (20 pav., A dalis) apvalios struktūros, Au(SPE)/SAM/NIP elektrodas (20 pav., B dalis) pasižymėjo asfalto tipo paviršiumi, o Au(SPE)/SAM/MIP elektrodas (20 pav., C dalis) atskleidė ertmes paviršiuje, patvirtinančias sėkmingą MIP susidarymą.

Jutiklio gebėjimas aptikti rN baltymą buvo iširtas naudojant įvairias elektrochemines eksperimentines sąlygas. KBV ir EIS matavimai buvo panaudoti siekiant nustatyti aptikimo ir nustatymo ribas. Nors KBV metodu šios ribos nebuvo apskaičiuotos dėl paskutinio taško neįtraukimo į tiesinę lygtį, EIS metodas atskleidė atitinkamas reikšmes – 0,2 nM ir 0,66 nM (21 pav., 60 psl.). Šie rezultatai rodo, kad SAM pagrindu veikianti MIP metodika prisideda prie geresnio jutiklių jautrumo ir specifiškumo, leidžiančio tiksliai aptikti rN baltymą ir pasižyminčio aukštu selektyvumu. Šie rezultatai pabrėžia MIP modifikuotų Au(SPE)/SAM elektrodų potencialą kuriant itin jautrius jutiklius.

### **VEGF baltymo nustatymas, naudojant aptamerų pagrindu veikiančią elektrocheminį jutiklį**

Šiame tyrime buvo sukurtas elektrocheminis jutiklis kraujagyslių endotelio augimo faktoriui aptikti, panaudojant aptamerus, integruotus į

polipirolu matricą (Ppy/anti-VEGF). Šis integravimas leido sukurti kompozitą, jungiantį polipirolu laidžias savybes su aptamerų specifine sąveika su VEGF. Svarbi šio jutiklio konstrukcijos dalis buvo plono Ppy pasluoksnio naudojimas, kuris padidino jutiklio stabilumą ir veikimo efektyvumą. Ppy pasluoksnis pagerino aptamerų sluoksnio sukibimą su elektrodo paviršiumi ir sumažino tiesioginę sąveiką tarp elektrodo ir aptamero. Sumažinus tokią sąveiką, Ppy sluoksnis prisidėjo prie stabilios ir atkuriamos kompozito Ppy/anti-VEGF jutiklio sistemos, kas yra itin svarbu tiksliam VEGF aptikimui.

Aptamerai įterpti į polipirolu matricą buvo suformuoti ant SPCE elektrodų, naudojant dviejų etapų elektrocheminio nusodinimo metodą. Pirmame etape buvo nusodintas Ppy pasluoksnis, skirtas padengti ir apsaugoti elektrodo paviršių. Antrame etape į Ppy matricą buvo įterpti anti-VEGF aptamerai sukuriant jutiklio sluoksnį, galintį prisijungti VEGF baltymą.

Modifikuotų elektrodų elektrocheminis charakterizavimas buvo atliktas naudojant impulsinę amperometriją. Tyrimo metu buvo registruojamos srovės pokyčių reikšmės 0,1 s, 0,2 s, 0,4 s, 0,6 s, 0,8 s ir 2,0 s laiko intervalais (24 pav., 64 psl.). Remiantis šiais matavimais, buvo sudarytos kalibracinės kreivės, kurios atskleidė stiprią sąveiką tarp VEGF baltymo ir aptameriais modifikuoto paviršiaus (25 pav., 66 psl.). Langmiur adsorbcijos izoterminis modelis leido toliau analizuoti adsorbcijos dinamiką, o rezultatai parodė, kad pusiausvyros konstanta ( $K$ ) padidėjo nuo  $1,25 \pm 0,09$  nM iki  $2,47 \pm 0,49$  nM, kas rodo ilgesnį sąveikos laiką ir jutiklio jautrumo padidėjimą esant didesnėms VEGF koncentracijoms.

PAD matavimai atskleidė, kad Ppy/anti-VEGF modifikuoti elektrodai gali aptikti VEGF koncentracijas net iki 0,21 nM. Siekiant geriau suprasti jutiklio veikimą, buvo analizuojamos Ansono diagramos, kurios padėjo įvertinti krūvio ir laiko santykį elektrocheminiuose procesuose. Šiuo tikslu buvo pritaikyta integruota Cottrell lygtis, leidžianti detaliau interpretuoti gautus rezultatus. Pasitelkiant šią lygtį, buvo apskaičiuotas adsorbuotos medžiagos krūvis MIP ir NIP elektrodams, o rezultatai atskleidė afininę sąveiką tarp aptamero ir VEGF baltymo. Be to, buvo nustatyta aptikimo riba, kuri siekė 0,21 nM, pabrėžiant jutiklio jautrumą.

## IŠVADOS

1. Naudojant elektrinio potencialo impulsus, buvo suformuotas polipirolu pasluoksnis bei molekuliniai įspaudais modifikuoto polipirolu sluoksnis, kurie buvo integruoti į elektrocheminio jutiklio skirtą aptikti *Listeria monocytogenes* bakterijas konstrukciją. Šio jutiklio aptikimo riba buvo 70 KFV/mL, o nustatymo riba – 210 /KFU/mL.
2. Įvertintos savitvariais monosluksniais modifikuotų aukso elektrodų elektrocheminės savybės, buvo nustatyta, kad 11-merkaptoundekano rūgšties savitvarkis monosluksnis suformuotas ant Au(s) elektrodo sudaro izoliacinį sluoksnį, kuris žymiai padidina krūvio pernašos varžą. Tuo tarpu ant Au(MS) elektrodo suformuotas mišrus savitvarkis monosluksnis (sudarytas iš 6-merkaptu-1-heksanolio ir 11-merkaptoundekano rūgšties), pasižymi mažesne krūvio pernašos varža, todėl yra tinkamas imuninio jutiklio, skirtą aptikti antikūnus prieš SARS-CoV-2 spyglio baltymus nenaudojant elektrocheminių žymenų, kūrimui. Sukurto jutiklio aptikimo riba – 2,78 nM ir nustatymo riba – 9,17 nM.
3. Spausdinto montažo aukso nanostruktūromis modifikuoti elektrodai gali būti modifikuojami savitvarčių monoslukšnių pasluoksniais ir molekulių įspaudais modifikuoto polipirolu sluoksniais. Tokios struktūros yra tinkamos SARS-CoV-2 viruso nukleokapsidės baltymų aptikimui. Elektrocheminiais analizės metodais buvo nustatytas krūvio pernašos varžos didėjimas tiriamajame tirpale didėjant SARS-CoV-2 viruso nukleokapsidės baltymo koncentracijai. Jutiklio aptikimo riba – 0,2 nM, naudojant elektrocheminio impedanso spektroskopiją, o nustatymo riba – 0,66 nM.
4. Spausdinto montažo anglies elektrodai gali būti modifikuojami polipirolu pasluoksniumi bei polipirolu sluoksniumi su įterptais savaime susirenkančiais DNR aptamerais, sudarytais iš trijų atskirų DNR grandinių. Buvo nustatyta, kad taip modifikuoti elektrodai yra tinkami VEGF baltymo aptikimui ir jų aptikimo riba yra 0,21 nM. Impulsinės amperometrijos metodo panaudojimas tokiuose jutikliuose supaprastina analizę, kadangi nereikia naudoti redoks tarpininkų.



## CURRICULUM VITAE

| PERSONAL INFORMATION    |   |
|-------------------------|---|
| Name, Surname           | Viktorija Liustrovaitė  |
| Email                   | viktorija.liustrovaite@chgf.vu.lt   |
| EDUCATION               |   |
| 2014-2018               | Bachelor of Chemistry, Vilnius University   |
| 2018-2020               | Master of Chemistry, Vilnius University   |
| PROFESSIONAL EXPERIENCE |   |
| 2023-02 – Present       | Faculty of Chemistry and Geosciences, Vilnius University<br>Laboratory assistant  |
| TRAINING                |   |
| 2021-08                 | Secondment to a company “Nano Prime Sp. z o. o.” in Gliwice, Poland. Training in formation of self-assembled monolayer on conducting surfaces. Scientific mentor: Dr. Oleg Mishchenko |
| 2021-10 – 2022-01       | Secondment to a company “Biosensors” in Rome, Italy. Worked and trained in biosensors development focusing on field deployment. Scientific mentor: Dr. Maria Teresa Giardi            |
| 2022-05                 | Secondment to a company “Nano Prime Sp. z o. o.” in Gliwice, Poland. Training in formation of bio-selective layer on the surface of ZnO. Scientific mentor: Dr. Wojciech Simka        |
| 2022-09 – 2022-11       | Secondment to a company “Biosensors” in Rome, Italy. Worked and trained in portable biosensor development. Scientific mentor: Dr. Maria Teresa Giardi                                 |
| 2023-07 – 2023-08       | Secondment to a company “3D STRONG SIA” in Riga, Latvia. Training in ZnO electrodeposition techniques. Scientific mentor: Dr. Raimonds Mejja  |

## PARTICIPATION IN CONFERENCES

1. **V. Liustrovaite**, A. Valiuniene, G. Valincius, A. Ramanavicius. Phospholipid bilayer formation and characterization immobilizing chlorophyll a. International Conference ‘Nanostructured Bioceramic Materials 2020’, December 1-3, 2020, Vilnius, Lithuania: abstract book. Vilnius, Vilnius University Press, 2020. p. 50.
2. **V. Liustrovaite**, A. Valiuniene, G. Valincius, A. Ramanavicius. Chlorophyll a immobilization into tethered bilayer lipid membrane. International conference ‘Open readings 2021’, March 16-19, 2021, Vilnius, Lithuania: abstract book. Vilnius, Vilnius University Press, 2021. p. 421.
3. **V. Liustrovaite**, A. Valiuniene, G. Valincius, A. Ramanavicius. Evaluation of chlorophyll a immobilization within tethered bilayer lipid membrane. International conference ‘Advanced materials and technologies 2021’, August 23-27, 2021, Palanga, Lithuania: abstract book. Kaunas University of Technology, 2021. p. 35.
4. **V. Liustrovaite**, A. Valiuniene, G. Valincius, A. Ramanavicius. Formation and characterization of chlorophyll a within tethered bilayer lipid membrane. International conference ‘Chemistry and Chemical Technology 2021’, September 24, 2021, Vilnius, Lithuania: abstract book, 2021. p. 23.
5. **V. Liustrovaite**, M. Drobysh, A. Rucinskiene, A. Baradoke, I. Ilikusienė, U. Samukaitė-Bubnienė, R. Viter, C.F. Chen, A. Ramanavičius. Study on electrochemical immunosensor for the detection of specific antibodies. International conference ‘Advanced materials and technologies 2022’, August 23-27, 2022, Palanga, Lithuania: abstract book. Kaunas University of Technology, 2022. p. 41.
6. **V. Liustrovaite**, V. Ratautaite, A. Ramanavicius. A molecularly imprinted polymer immunosensor development for the serological detection of SARS-CoV-2 protein. International conference ‘Open readings 2024’, April 23-26, 2024, Vilnius, Lithuania: abstract book. Vilnius, Vilnius University Press, 2024. p. 360.
7. **V. Liustrovaite**, M. Pogorielov, R. Boguzaitė, V. Ratautaite, A. Ramanaviciene, G. Pilvenyte, V. Holubnycha, V. Korniienko, K. Diedkova, R. Viter, A. Ramanavicius. Development of an electrochemical sensor utilising molecularly imprinted polypyrrole for the rapid detection of *Listeria monocytogenes* bacteria. International conference ‘Advanced materials and technologies 2024’, August 26-30, 2024, Palanga, Lithuania: abstract book. Kaunas University of Technology, 2024. p. 98.

## CO-AUTHORED SCIENTIFIC PUBLICATIONS

The list of co-authored scientific publications, which are not part of the dissertation:

1. M. Drobysh, **V. Liustrovaite**, A. Baradoke, R. Viter, C.F. Chen, A. Ramanavicius, A. Ramanaviciene. 'Determination of rSpike protein by specific antibodies with screen-printed carbon electrode modified by electrodeposited gold nanostructures.' *Biosensors* (12) 8, p. 593, 2022
2. U. Samukaite-Bubniene, S. Zukauskas, V. Ratautaite, M. Vilkiene, I. Mockeviciene, **V. Liustrovaite**, M. Drobysh, A. Lisauskas, S. Ramanavicius, A. Ramanavicius. 'Assessment of Cytochrome c and Chlorophyll a as natural redox mediators for enzymatic biofuel cells powered by glucose.' *Energies* 15 (18), p. 6838, 2022
3. **V. Liustrovaite**, D. Karoblis, B. Brasiunas, A. Popov, A. Katelnikovas, A. Kareiva, A. Ramanavicius, R. Viter, M.T. Giardi, D. Erts, A. Ramanaviciene. 'Electrochemical immunosensor for the determination of antibodies against prostate-specific antigen based on ZnO nanostructures.' *International Journal of Molecular Sciences*, 24 (6), p. 5803, 2023
4. V. Reinikovaite, M. Matulevicius, A. Elsakova, M. Drobysh, **V. Liustrovaite**, A. Luksa, A. Jafarov, R. Slibinskas, A. Ramanavicius, Ausra Baradoke. 'Electrochemical capacitance spectroscopy based determination of antibodies against SARS-CoV-2 virus spike protein.' *Science of The Total Environment* 903, p. 166447, 2023
5. A. Baradoke, A. Jarusaitis, V. Reinikovaite, A. Jafarov, A. Elsakova, M. Franckevicius, M. Skapas, R. Slibinskas, M. Drobysh, **V. Liustrovaite**, A. Ramanavicius. 'Detection of antibodies against SARS-CoV-2 Spike protein by screen-printed carbon electrodes modified by colloidal gold nanoparticles.' *Talanta* 268, p. 125279, 2023.
6. M. Drobysh, **V. Liustrovaite**, Y. Kanetski, B. Brasiunas, A. Zvirbliene, A. Rimkute, D. Gudas, I. Kucinskaite-Kodze, M. Simanavicius, S. Ramanavicius, R. Slibinskas, E. Ciplys, I. Plikusiene, A. Ramanavicius. 'Electrochemical biosensing based comparative study of monoclonal antibodies against SARS-CoV-2 nucleocapsid protein.' *Science of the total environment* 908, p. 168154, 2023
7. **V. Liustrovaite**, M. Drobysh, V. Ratautaite, A. Ramanaviciene, A. Rimkute, M. Simanavicius, I. Dalgediene, I. Kucinskaite-Kodze, I. Plikusiene, C.F. Chen, R. Viter, A. Ramanavicius. 'Electrochemical biosensor for the evaluation of monoclonal antibodies targeting the N

- protein of SARS-CoV-2 virus.' *Science of The Total Environment* 924, p.171042, 2024
8. R. Viter, I. Tepliakova, M. Drobysh, V. Zbolotnii, S. Rackauskas, S. Ramanavicius, K. Grundsteins, **V. Liustrovaite**, A. Ramanaviciene, V. Ratautaite, E. Brazys, C.F. Chen, U.Prentice, A. Ramanavicius. 'Photoluminescence-based biosensor for the detection of antibodies against SARS-CoV-2 virus proteins by ZnO tetrapod structure integrated within microfluidic system.' *Science of The Total Environment* 939, p. 173333, 2024

## COPIES OF PUBLICATIONS

### Paper 1

**Towards electrochemical sensor based on molecularly imprinted polypyrrole for the detection of bacteria—*Listeria monocytogenes***

**V. Liustrovaite**, M. Pogorielov, R. Boguzaitė, V. Ratautaitė,  
A. Ramanaviciene, G. Pilvenyte, V. Holubnycha, V. Korniienko,  
K. Diedkova, R. Viter, A. Ramanavicius

*Polymers*, 2023, 15(7), 1597  
[doi.org/10.3390/polym15071597](https://doi.org/10.3390/polym15071597)

Article

# Towards Electrochemical Sensor Based on Molecularly Imprinted Polypyrrole for the Detection of Bacteria—*Listeria monocytogenes*

Viktorija Liustrovaite <sup>1,†</sup>, Maksym Pogorielov <sup>2,3,\*,†</sup>, Raimonda Boguzaitė <sup>4,5</sup>, Vilma Ratautaite <sup>4,5</sup>, Almira Ramanaviciene <sup>5</sup>, Greta Pilvenyte <sup>4</sup>, Viktoriia Holubnycha <sup>2</sup>, Viktoriia Korniienko <sup>2,3</sup>, Kateryna Diedkova <sup>2,3</sup>, Roman Viter <sup>3</sup> and Arunas Ramanavicius <sup>1,4,\*</sup>

<sup>1</sup> Department of Physical Chemistry, Faculty of Chemistry and Geosciences, Vilnius University, Naugarduko Str. 24, LT-03225 Vilnius, Lithuania

<sup>2</sup> Biomedical Research Centre, Sumy State University, R-Korsakova Street, 40007 Sumy, Ukraine

<sup>3</sup> Institute of Atomic Physics and Spectroscopy, University of Latvia, Jelgavas iela 3, LV-1004 Riga, Latvia

<sup>4</sup> Department of Nanotechnology, State Research Institute Center for Physical Sciences and Technology, Saulėtekio Av. 3, LT-10257 Vilnius, Lithuania

<sup>5</sup> NanoTechnas-Center of Nanotechnology and Materials Science, Institute of Chemistry, Faculty of Chemistry and Geosciences, Vilnius University, Naugarduko Str. 24, LT-03225 Vilnius, Lithuania

\* Correspondence: maksym.pogorielov@lu.lv (M.P.); arunas.ramanavicius@chf.vu.lt (A.R.)

† These authors contributed equally to this work.



**Citation:** Liustrovaite, V.; Pogorielov, M.; Boguzaitė, R.; Ratautaite, V.; Ramanaviciene, A.; Pilvenyte, G.; Holubnycha, V.; Korniienko, V.; Diedkova, K.; Viter, R.; et al. Towards Electrochemical Sensor Based on Molecularly Imprinted Polypyrrole for the Detection of Bacteria—*Listeria monocytogenes*. *Polymers* **2023**, *15*, 1597. <https://doi.org/10.3390/polym15071597>

Academic Editor: Beom Soo Kim

Received: 29 January 2023

Revised: 16 March 2023

Accepted: 17 March 2023

Published: 23 March 2023



**Copyright:** © 2023 by the authors. Licensee MDPI, Basel, Switzerland. This article is an open access article distributed under the terms and conditions of the Creative Commons Attribution (CC BY) license (<https://creativecommons.org/licenses/by/4.0/>).

**Abstract:** Detecting bacteria—*Listeria monocytogenes*—is an essential healthcare and food industry issue. The objective of the current study was to apply platinum (Pt) and screen-printed carbon (SPCE) electrodes modified by molecularly imprinted polymer (MIP) in the design of an electrochemical sensor for the detection of *Listeria monocytogenes*. A sequence of potential pulses was used to perform the electrochemical deposition of the non-imprinted polypyrrole (NIP-Ppy) layer and *Listeria monocytogenes*-imprinted polypyrrole (MIP-Ppy) layer over SPCE and Pt electrodes. The bacteria were removed by incubating Ppy-modified electrodes in different extraction solutions (sulphuric acid, acetic acid, L-lysine, and trypsin) to determine the most efficient solution for extraction and to obtain a more sensitive and repeatable design of the sensor. The performance of MIP-Ppy- and NIP-Ppy-modified electrodes was evaluated by pulsed amperometric detection (PAD). According to the results of this research, it can be assumed that the most effective MIP-Ppy/SPCE sensor can be designed by removing bacteria with the proteolytic enzyme trypsin. The LOD and LOQ of the MIP-Ppy/SPCE were 70 CFU/mL and 210 CFU/mL, respectively, with a linear range from 300 to 6700 CFU/mL.

**Keywords:** molecularly imprinted polymer; molecularly imprinted polypyrrole; *Listeria monocytogenes*; whole-cell imprinting; pulsed amperometric detection; template extraction method; trypsin; L-lysine; acetic acid; sulphuric acid

## 1. Introduction

*Listeria monocytogenes* infections with Gram-positive, rod-shaped bacteria with an optimum growing temperature at 37 °C [1] are among the leading causes of foodborne illness-related mortality [2]. *Listeria monocytogenes* is an environmental contaminant that primarily inhabits soil. Various animals (ruminants, birds, marine life, insects, ticks, and crustaceans) are carriers of bacteria [3]. *Listeria monocytogenes* can enter the food supply chain and contaminate a wide variety of food products, including meat products; raw, unpasteurised milk and cheeses; ice cream; raw or processed vegetables; raw or processed fruits; raw or undercooked poultry, sausages, hot dogs, and deli meats; and raw or smoked fish and other seafood [4].

One type of sickness induced by *Listeria monocytogenes* is very dangerous and can result in septicemia and meningitis, with a case-fatality rate of 20–30% [5]. Another kind of disease caused by *Listeria monocytogenes* is a non-invasive gastrointestinal ailment that typically has no consequences. However, despite the low-level incidences of listeriosis in the general population, it remains a significant and deadly food-borne disease with a hospitalisation rate of over 95% [6]. The major problem is that *Listeria monocytogenes* affects vulnerable segments of populations, including the elderly, pregnant women, unborn babies, and immunocompromised people (patients with cancer or AIDS, or after organ transplantations) [7]. Thus, pregnant women have a 17-fold increased risk of contracting invasive listeriosis [8], and the mortality associated with *Listeria monocytogenes* infection is responsible for 22% of fatalities in immunocompromised adults [4].

Detecting *Listeria monocytogenes* is an essential healthcare and food industry issue [9]. The minimal infection dose for listeriosis is 100 colony-forming units per gram (CFU/g) of food. The majority of countries have zero tolerance towards the presence of *Listeria monocytogenes* in food [10]. The European Regulation on Microbiological Criteria for Foodstuffs does not allow the presence of *Listeria monocytogenes* in foods for infants and particular medical purposes. However, all food can have 100 CFU/g of the organism during its shelf life [11]. In this case, fast and precise detection of *Listeria monocytogenes* is required both for the healthcare and food industries.

Among many methods for the identification of *Listeria monocytogenes*, colony plate counting is accepted to be the ‘gold standard’ procedure [12]. The detection of *Listeria monocytogenes* has been proposed using several standard techniques, including surface plasmon resonance [13], quartz crystal microbalance [14], and enzyme-linked immunosorbent assay (ELISA) [15,16]. These methods are crucial and can essentially meet the criteria for *Listeria monocytogenes* detection. However, they often have shortcomings and are labour-intensive, time-consuming, or complicated. In ELISA, secondary antibodies connected to an enzyme are immobilised in a well to capture *Listeria* antigens. These tests are used in food testing because they are straightforward, simple to interpret, and do not require much sample handling. However, they produce results in roughly 30–50 h and are not as sensitive as molecular methods. This technique has a sensitivity range of approximately  $10^5$ – $10^6$  CFU/mL [17]. The electrochemical approach, in comparison, is straightforward, sensitive, time-saving, inexpensive, and simple to use, giving it several distinct benefits over the other methods. Many excellent electrochemical systems have been successfully built in recent years to detect *Listeria monocytogenes* [18–21], including antibody- or DNA-based methods [1,12].

The exceptional selectivity of molecularly imprinted polymers towards molecularly imprinted analytes makes them appealing. Molecular imprinting can create a binding site uniquely suited to a specific molecule [22]. The molecular imprinting approach enables the development of particular molecular recognition sites that work on the idea of complementarity between the imprinted sites and the analyte due to its many distinctive benefits, including simplicity in production, affordability, and excellent stability [23,24]. Therefore, MIPs can specifically bind the analytes of interest that serve as templates for their development [25–29]. However, due to the size, imprinting the whole cell in the polymers is exceptionally challenging [30,31]. Several studies have evaluated the suitability of MIP-based sensors for detecting *Listeria monocytogenes* bacteria [32–34]. Mainly two factors governing the recognition of *Listeria monocytogenes* bacteria should be taken into account: (i) discrimination of the bacteria by their cell shape (e.g., round or rod-shaped bacteria, namely *Staphylococcus aureus* or *Escherichia coli*) and (ii) chemical recognition due to the interaction of functional groups present in polymers with functional groups that are localised on the surface of the cell, e.g., cis-diol groups of the glycan chains [35]. Taking into account the emerging problems, Piletsky et al. [30] raised some questions related to the materials suitable for the modification of electrodes by MIP-based layers. The authors of that study concluded that “success in this area will result in new paradigms for MIP

applications that both complement existing therapeutic and disposal or reuse in field diagnostic techniques”.

The current research sought to develop a MIP-based sensor for detecting *Listeria monocytogenes*. Firstly, the goal was to test the performance of two electrodes. Pt and SPCE were modified with a polypyrrole layer made from the polymerisation solution of *Listeria monocytogenes* bacteria and pyrrole dissolved in phosphate-buffered saline (PBS), pH 7.4. A novelty of this study or a second approach was to determine the most efficient solution for extraction. Thus, *Listeria monocytogenes* bacteria from imprinted cavities were extracted using trypsin and L-lysine and compared with more conventional extraction methods such as sulphuric and acetic acids. Herein, the analytical performance of electrodes modified by a non-imprinted polypyrrole (NIP-Ppy) layer and the electrodes modified with the MIP-Ppy layer were compared. Thirdly, the sensitivity (LOD and LOQ) and repeatability criteria were effectively employed to detect *Listeria monocytogenes*.

## 2. Materials and Methods

### 2.1. Materials and Electrochemical Measurements

*Listeria monocytogenes* were obtained from the Bacteria Collection of Sumy State University (Sumy, Ukraine). To preserve the antigenic structure on the *Listeria monocytogenes* membrane but eliminate virulence,  $10^9$  CFU/mL bacteria were immersed in 70% ethanol and placed under UV light for 24 h. This procedure allows the destruction of bacterial DNA with minimal influence on the cell wall and shape, which are necessary for MIP development.

Pyrrole 98% (CAS# 109-97-7, Alfa Aesar, Kandel, Germany), phosphate-buffered saline (PBS) tablets, pH 7.4 (CAS# 7647-14-5, Sigma-Aldrich, Steinheim, Germany), sulphuric acid (96%, CAS# 7664-93-9, Lachner, Neratovice, Czech Republic), acetic acid (99.8%, CAS# 64-19-7, 99.8%, Lachner, Czech Republic), trypsin 500 U/mL (TrypZean® Solution, Sigma-Aldrich, SKU T3449-500 ML), and 0.1% (*w/v*) L-lysine solution in H<sub>2</sub>O (Sigma-Aldrich, CAS# 25988-63-0) were used as received for bacteria removal from the Ppy-matrix to form the MIP-Ppy layer. All reagents were of analytical grade and were used without additional purification. All aqueous solutions were prepared in deionised water.

Electrochemical characterisation of the working surfaces was performed using two systems. A potentiostat/galvanostat AUTOLAB TYPE III (ECO-Chemie, Utrecht, The Netherlands) operated by FRA2-EIS ECO-Chemie software (ECO-Chemie, Utrecht, The Netherlands) was used for the first electrochemical system. The first set of electrodes, DRP-110 screen-printed carbon electrodes (SPCEs), which are based on a working electrode with a geometric area of 0.126 cm<sup>2</sup>, a carbon-based counter electrode, and an Ag/AgCl-based reference electrode, was purchased from Metrohm DropSens (Oviedo, Spain).

For the second electrochemical system, the second set of electrodes was based on (i) a Pt disk with a 1 mm diameter sealed in glass as the working electrode, (ii) an Ag/AgCl in 3 M KCl solution electrode as a reference electrode (Ag/AgCl), and (iii) a Pt disk of 2 mm diameter as a counter electrode. Measurements were done in a home-made cell with a total volume of 300 µL, and electrochemical characterisation was performed using a portable potentiostat controlled by DStat interface software from Wheeler Microfluidics Lab (University of Toronto, Toronto, ON, Canada).

Scanning electron microscope (SEM) images were obtained with a scanning electron microscope (Hitachi-70 S3400 N VP-SEM).

### 2.2. Pre-Treatment of Working Electrodes

Pre-treatment of electrodes for the first electrochemical system: Before the electrochemical deposition of Ppy, the working electrodes underwent pre-treatment. A potential cycling approach was used to electrochemically clean SPCEs. The cleaning was carried out in 0.5 M sulphuric acid by 20 potential cycles in a potential range between −100 mV and +1200 mV vs. Ag/AgCl at a potential sweep rate of 100 mV/s.



Pre-treatment of electrodes for the second electrochemical system: The Pt electrode was pre-treated before electrochemical deposition following the procedure described in previous studies [36]. All solutions were thoroughly degassed just before use with a stream of nitrogen (N<sub>2</sub>). According to this procedure, the Pt electrode was rinsed with concentrated HNO<sub>3</sub> solution in an ultrasonic bath for 10 min, then rinsed with water and polished with alumina paste. Later, it was rinsed with water again and then with a solution of 10 M NaOH, then with a 5 M sulphuric acid solution in an ultrasonic bath for 5 min. Electrochemical electrode cleaning was carried out in 0.5 M sulphuric acid by cycling the potential 20 times in the range between −100 mV and +1200 mV vs. Ag/AgCl at a sweep rate of 100 mV/s. The assessment of the bare electrode surface was performed by cyclic voltammogram. To improve the adhesion of the Ppy layer to the electrode surface, a layer of ‘platinum black’ was formed over the working electrode. The deposition of ‘platinum black’ clusters was performed in a solution of 5 mM H<sub>2</sub>PtCl<sub>6</sub> containing 0.1 M of KCl by 10 potential cycles in the range between +500 mV and −400 mV vs. Ag/AgCl at a potential sweep rate of 10 mV/s.

2.3. Electrochemical Modification of Electrodes by NIP-Ppy and MIP-Ppy Layers

The polymerisation solution contained 0.5 M of pyrrole in PBS and was used to electrochemically deposit the NIP-Ppy layer [25]. The deposition of MIP-Ppy on Pt and SPCE electrodes was performed in several steps: (i) during the first step, the Ppy underlayer was electrochemically deposited from polymerisation solution containing a 0.5 M solution of pyrrole, and a sequence of 5 potential pulses (of +950 mV for 1 s and 0 V for 30 s) was applied [29,36]; (ii) during the deposition of the second layer, 10<sup>9</sup> CFU/mL of *Listeria monocytogenes* bacteria was additionally added into the same polymerisation bulk solution and again the sequence of 5 potential pulses (of +950 mV for 1 s and 0 V for 30 s) was applied; (iii) the purpose of the third step was to remove imprinted bacteria from the formed Ppy layer by incubating electrodes in different extraction solutions to form the MIP-Ppy (0.05 M sulphuric acid, 10% acetic acid, 0.1% L-lysine, 10 U/mL trypsin for at 37 °C for 30 min). The NIP-Ppy-based layer was formed similarly to MIP-Ppy (only bacteria were not added), and the abovementioned extraction solutions similarly treated the NIP-Ppy-modified electrode.

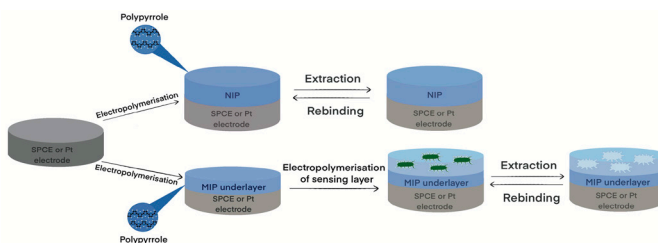
Pulsed amperometric detection was used to assess MIP-Ppy- and NIP-Ppy-modified electrodes utilising a sequence of 10 potential pulses of +600 mV vs. Ag/AgCl lasting for 2 s, and 0 V vs. Ag/AgCl for 2 s.

The limit of detection (LOD) and limit of quantification (LOQ) were calculated according to Equations (1) and (2):

$$\text{LOD} = 3.3 \sigma/S \tag{1}$$

$$\text{LOQ} = 10 \sigma/S \tag{2}$$

where  $\sigma$  is the standard deviation and  $S$  is the slope of the linear relationship on the calibration plot. A schematic representation of electrode modification is presented in Scheme 1.



Scheme 1. Schematic representation of electrode modification.

### 3. Results

#### 3.1. Electrodeposition of Molecularly Imprinted Polypyrrole

MIP-Ppy and NIP-Ppy layers were electrochemically deposited on the surface of Pt and SPCE electrodes using a series of potential pulses. Figure 1A,B depict the profile of the potential pulse series during the deposition of the NIP-Ppy layer on Pt and SPCE electrodes, respectively. The electrochemical formation of the MIP-Ppy layer on Pt and SPCE electrodes was performed in several steps as described in the experimental section, respectively (Figure 2A,B). The first step was based on the electrodeposition of the Ppy-based under-layer to support and cover the electrode. This Ppy-based under-layer decreased the direct interaction of *Listeria monocytogenes* with the electrode surface before forming the MIP-Ppy sensing layer. The deposited thin Ppy under-layer effectively favoured the formation of the MIP-Ppy-sensing layer during the second sensing-layer-formation step. The entrapped *Listeria monocytogenes* bacteria acted as a template in an upper Ppy layer (sensing layer), which, after the removal of bacteria, formed the MIP-Ppy layer. Electrochemical Ppy deposition enabled control of the thickness of formed layers and entrap the *Listeria monocytogenes* bacteria templates in the electropolymerised matrix. The entrapped *Listeria monocytogenes* bacteria templates were removed from the MIP-Ppy layer by incubation in several extraction solutions.

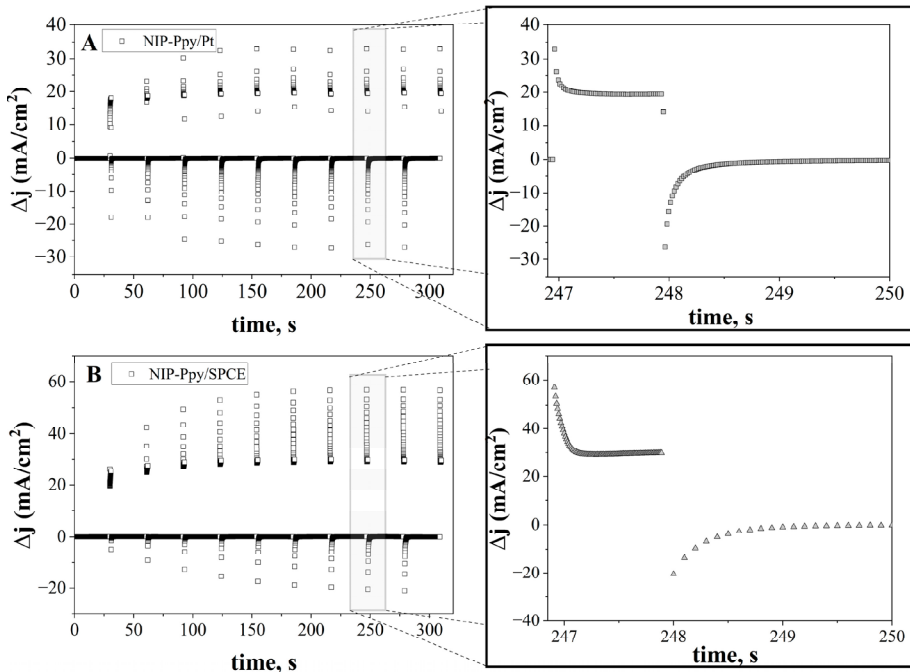


**Figure 1.** Electrochemical deposition of NIP-Ppy layers: (A) on Pt electrodes (second electrochemical system); (B) on SPCE electrodes (first electrochemical system), showing the profile of the current registered during the formation of the NIP-Ppy layer from polymerisation solution without any bacteria. Insets—extended profile of the current registered during the indicated potential pulse.

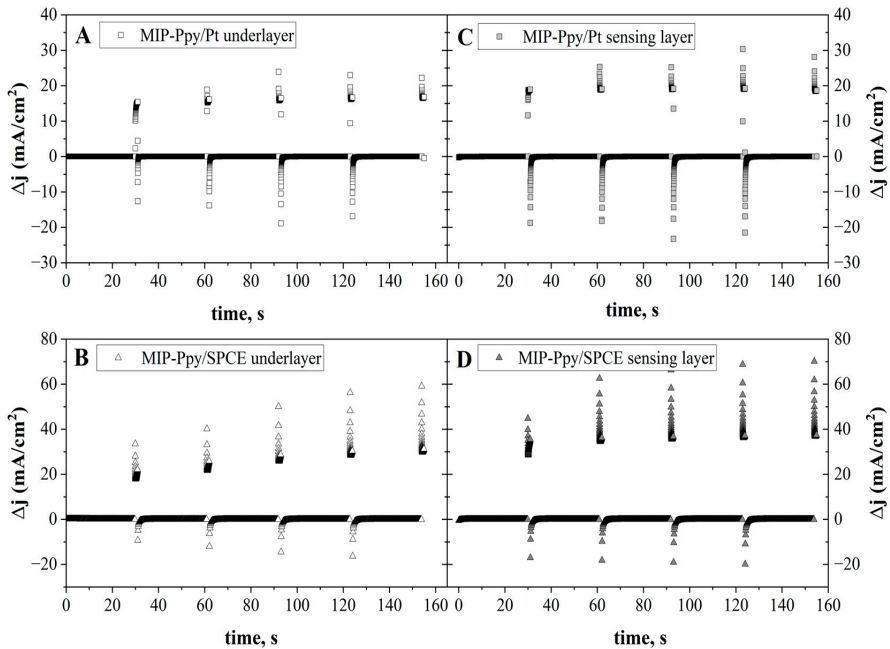


**Figure 2.** Current profiles registered during the deposition of Ppy underlayers (A) on Pt electrodes (second electrochemical system), and (B) on SPCE electrodes (first electrochemical system). Current profiles registered during electrochemical deposition of the polypyrrole layers with entrapped *Listeria monocytogenes* bacteria (C) on Pt electrodes (2nd electrochemical system), and (D) on SPCE electrodes (1st electrochemical system).

### 3.2. Extraction of Imprinted Bacteria from the MIP-Ppy Layer

Several different extraction solutions were used to remove *Listeria monocytogenes* bacteria from the MIP-Ppy layer formed on the SPCE. The first template extraction method was based on the incubation of NIP-Ppy/SPCE, and MIP-Ppy/SPCE acetic acid solution was applied. Acetic acid is a weak organic acid harmful to most bacteria, even at concentrations as low as 0.5 wt%. Acetic acid, among other harmful effects, leads to a drop in intracellular pH and the disruption of some metabolic chains by acetic acid anion [37]. Figure 3B represents the bacteria cells after incubation in acetic acid. As a result, the cell membrane develops holes that allow the cytosol and cytoplasmic organelles to leak out. The rough, uneven pits on the bacteria cell surface showed that the extraction by acetic acid was highly effective. However, the incubation of NIP-Ppy/SPCE and MIP-Ppy/SPCE in a sulphuric acid-containing solution revealed that the surface of formed NIP-Ppy and MIP-Ppy (Figure 3C,D) seem identical.

The third template extraction solution used to remove the *Listeria monocytogenes* bacteria template from MIP-Ppy/SPCE was an enzyme (trypsin) solution. Trypsin catalyses the hydrolysis of cell wall proteins to form peptides. In addition, we tried to remove *Listeria monocytogenes* bacteria from MIP-Ppy/SPCE by L-lysine, which is a zwitterion amino acid and was expected to be efficient for the dissociation and removal of bacteria from the Ppy-based matrix. However, registered results (Figure 3H) illustrate that the L-lysine-based bacteria extraction procedure was not efficient compared to that based on trypsin. Moreover, L-lysine is crucial for protein synthesis and is also present in the peptidoglycan layer on the cell walls of Gram-positive bacteria; therefore, it supports cell metabolism. Additionally,

it should be noted that trypsin has a specific target in the cell wall and does not affect the Ppy layer; this effect would be an extra advantage for the removal of bacteria-based templates and the development of MIP-Ppy-based sensor platforms. Trypsin is a well-known pancreatic enzyme that digests proteins by specifically hydrolysed peptide bonds C-terminal to the amino acid residues of lysine (Lys) and arginine (Arg) [38]. Some studies have shown increased levels of proteolytic enzymes, including trypsin in inflammatory sites, followed by bacterial lysis. For example, Grenier demonstrated that Gram-positive bacteria from the oral cavity are more resistant to lysis than Gram-negative bacteria [39]. Meanwhile, Zhou et al. showed the same effect of the enzyme on both bacteria types (including biofilm formation) in a concentration of 2 mg/mL [40].

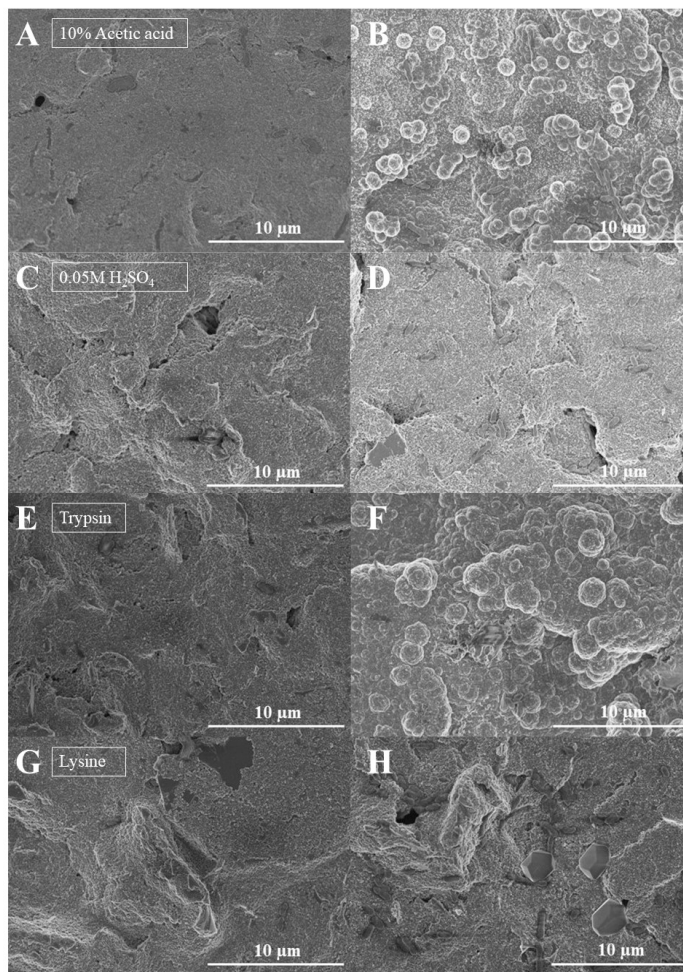


**Figure 3.** SEM images of NIP-Ppy/SPCE (A,C,E,G) and MIP-Ppy/SPCE (B,D,F,H) electrodes after incubation in different template extraction solutions: (A,B) 10% acetic acid, (C,D) 0.05 M sulphuric acid, (E,F) 10 U/mL trypsin, (G,H) 0.1% L-lysine at 37 °C for 30 min.

In contrast to trypsin, L-lysine is an amino acid that, at pH = 7.0, is a zwitterion; therefore, we expected that it can act as an efficient agent for the dissociation/removal of some compounds from polymeric structures. As demonstrated by this research, 10 U/mL trypsin solution is the most efficient for *Listeria monocytogenes* cell removal from the Ppy layer and to form MIP-Ppy.

### 3.3. Electrochemical Characterisation of Bacteria-Imprinted MIP-Ppy Layer

The formed NIP-Ppy and MIP-Ppy layers were assessed using pulsed amperometric detection to assess the current density in a sequence of 10 potential pulses of +600 mV for 2 s and 0 mV for 2 s. The determination of *Listeria monocytogenes* bacteria at several different concentrations was performed using two different electrochemical systems (Figure 4). MIP-Ppy- and NIP-Ppy-modified SPCE electrodes (Figure 4A) and MIP-Ppy- and NIP-Ppy-modified Pt electrodes (Figure 4B) were incubated in a PBS solution, pH 7.4, in a concentration range of  $3.4 \times 10^6$ – $1.0 \times 10^8$  CFU/mL *Listeria monocytogenes* bacteria. Figure 4 shows the dependence of the amperometric response. During the analysis, a decrease in the current with increasing bacteria concentration was observed, as usual in the redox-inactive analytes [41].

#### 3.3.1. Assessment of first Electrochemical System

Assessment of MIP-based sensor towards imprinted *Listeria monocytogenes* bacteria was performed in the concentration range from 0 to  $10^8$  CFU/mL. First, *Listeria monocytogenes* bacteria were eliminated from imprinted cavities using several extraction solutions, namely 10% acetic acid (Figure 5A), 0.05 M of sulphuric acid (Figure 5B), 10 U/mL of trypsin (Figure 5C), and 0.1% L-lysine (Figure 5D). As we can see from Figure 4, acetic acid was highly effective, as the current density of MIP-Ppy/SPCE was at least 12 times higher than that of NIP-Ppy/SPCE. While using the sulphuric acid solution, we observed only a slight change in the current density. However, the acid tolerance of *Listeria monocytogenes* bacteria is a predicted molecular response, which ensures cell survival in an unfavourable environment. The increased intracellular survival and the development of acid-adapted *Listeria monocytogenes* cells in the vacuoles and cytoplasm were confirmed by morphological methods [42]. To avoid the acid tolerance response in *Listeria monocytogenes* bacteria, we tried different approaches, one of which was based on applying the enzyme trypsin. Thus, trypsin was utilised to remove the *Listeria monocytogenes* bacterium template from the NIP-Ppy/SPCE and MIP-Ppy/SPCE. Accordingly, the electrodes were individually treated with solutions containing trypsin (Figure 5C) and L-lysine (Figure 5D). The current density for MIP-Ppy/SPCE, treated with trypsin, increased around three times compared with that registered for NIP-Ppy/SPCE, while MIP-Ppy/SPCE treated with L-lysine showed no changes in current density. Electrochemically registered results reveal that the electrical capacitance changed after removing imprinted bacteria; acetic-acid- and trypsin-based solutions were the most suitable for extracting entrapped *Listeria monocytogenes* bacteria and the preparation of MIP-Ppy.

#### 3.3.2. Assessment of MIP-Ppy/Pt- and NIP-Ppy/Pt-Based Electrodes

After preparation, NIP-Ppy/Pt and MIP-Ppy/Pt electrodes were incubated in solutions of *Listeria monocytogenes* bacteria of different concentrations and evaluated using pulsed amperometric detection based on 10 potential pulses of +600 mV for 2 s and 0 mV for 2 s. Figure 6A–D depict the dependence of the amperometric response of the second electrochemical system after the incubation of MIP-Ppy- and NIP-Ppy-modified platinum electrodes in PBS, pH 7.4, with a different concentration of *Listeria monocytogenes* bacteria.

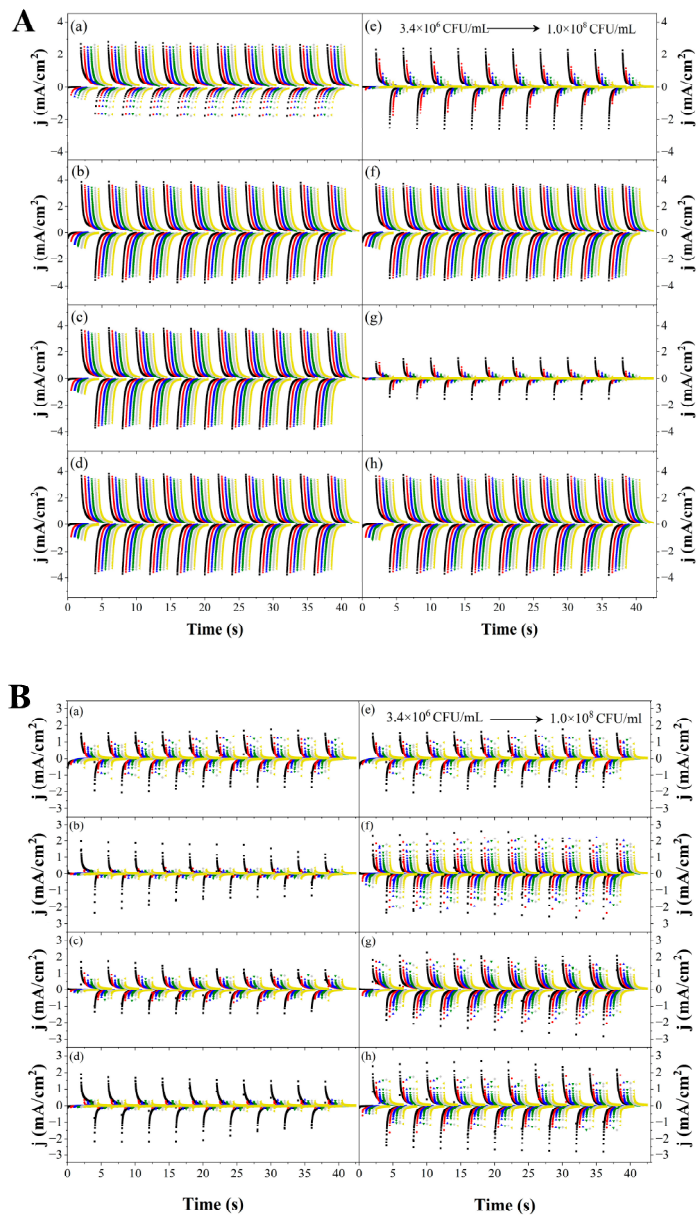


**Figure 4.** Current density vs. time determined by NIP-Ppy/SPCE (a–d), MIP-Ppy/SPCE (e–h) electrodes (A) and NIP-Ppy/Pt (a–d), MIP-Ppy/Pt (e–h) (B), with a concentration range of  $3.4 \times 10^6$ ,  $1.0 \times 10^7$ ,  $2.3 \times 10^7$ ,  $4.0 \times 10^7$ ,  $6.7 \times 10^7$ ,  $1.0 \times 10^8$  CFU/mL *Listeria monocytogenes* bacteria, prepared using different extraction solutions: 10% acetic acid (a,e), 0.05 M sulphuric acid (b,f), 10 U/mL trypsin (c,g), and 1% L-lysine (d,h) to remove *Listeria monocytogenes* bacteria from imprinted cavities.

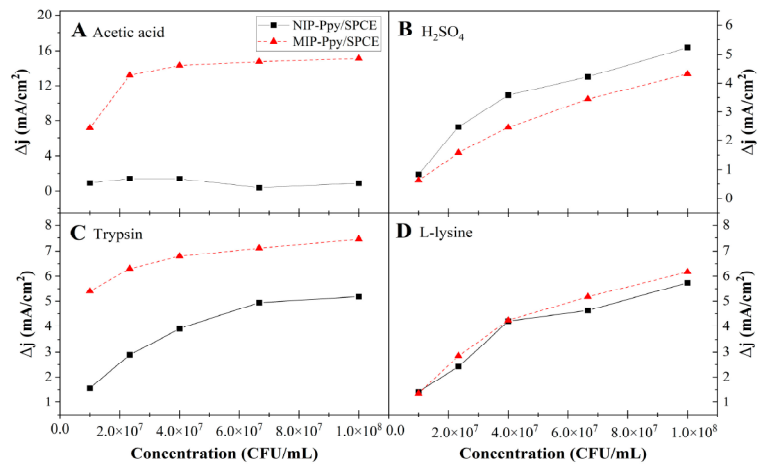


**Figure 5.** The current density of NIP-Ppy/SPCE (solid black lines) and MIP-Ppy/SPCE (dashed red lines) electrodes registered using pulsed amperometric detection after incubation in solutions containing different *Listeria monocytogenes* bacteria concentrations; *Listeria monocytogenes* from MIP-Ppy was extracted using different extraction solutions: (A) 10% acetic acid, (B) 0.05 M of sulphuric acid, (C) 10 U/mL of trypsin, (D) 0.1% L-lysine.

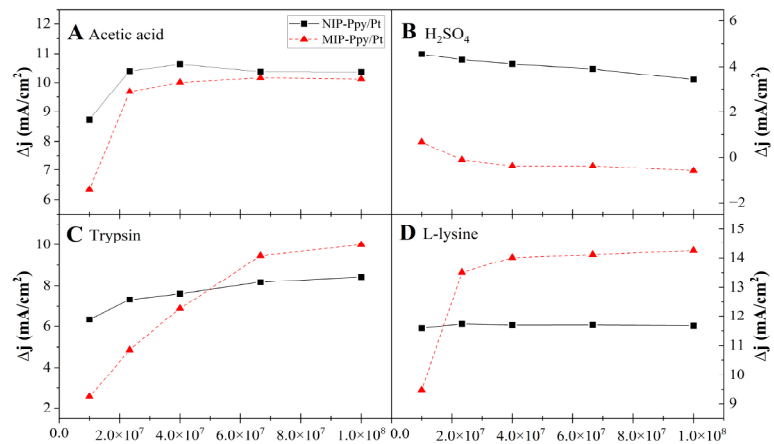


**Figure 6.** The current density of NIP-Ppy/Pt (solid black lines) and MIP-Ppy/Pt (dashed red lines) electrodes registered using pulsed amperometric detection after incubation in solutions containing different *Listeria monocytogenes* bacteria concentrations; *Listeria monocytogenes* from MIP-Ppy was extracted using different extraction solutions: (A) 10% acetic acid, (B) 0.05 M of sulphuric acid, (C) 10 U/mL of trypsin, (D) 0.1% L-lysine.

With different working electrodes, including platinum, different techniques can be used to remove the imprinted material. Various solvents are often used to remove bacteria, for instance, acetic acid, hydrochloric acid, other acids, methanol, and mixtures of those solvents [32,34,43]. Although challenging, extraction of the bacteria from the polymer

is essential for forming the MIPs [44]. During the formation of the MIP-Ppy structure within Ppy, entrapped *Listeria monocytogenes* bacteria were removed, leaving imprinted cavities using different extraction solutions, including 10% acetic acid (Figure 6A), 0.05 M of sulphuric acid (Figure 6B), 10 U/mL trypsin (Figure 6C), and 0.1% L-lysine (Figure 6D). Unlike the MIP-Ppy/SPCE electrode, a somewhat different situation was seen with the MIP-Ppy/Pt electrode. Trypsin- and L-lysine-based solutions proved to be the best for extracting *Listeria monocytogenes* bacteria from the Ppy layer. In the latter case, the current density of the MIP-Ppy/Pt electrode was twice as high compared to that registered by the NIP-Ppy/Pt electrode (Figure 6D). Trypsin proved to be effective in preparing the MIP-Ppy/Pt electrode suitable for the determination of *Listeria monocytogenes* bacteria in a broad concentration range.

#### 3.4. Determination of Limit of Detection and Limit of Quantification

As discussed, acetic acid and trypsin-based solutions were the most suitable for extracting *Listeria monocytogenes* bacteria entrapped within the Ppy-based layer and forming MIP-Ppy/SPCE. To assess the limit of detection (LOD) and limit of quantification (LOQ), pulsed amperometric detection-based electrochemical measurements were conducted.  $\Delta I$  values were employed, respectively, for NIP-Ppy/SPCE and MIP-Ppy/SPCE, as analytical signals. *Listeria monocytogenes* bacteria concentration calibration logarithmic curves plotted against  $\Delta I$  ( $\mu\text{A}$ ) are shown in Figure 7. The slope for the variations in the current ( $I$ ,  $\mu\text{A}$ ) vs. concentration of *Listeria monocytogenes* bacteria (concentration expressed in CFU/mL) registered by the NIP-Ppy/SPCE electrode was  $0.016 \mu\text{A}/(\text{CFU}/\text{mL})$ , with  $R^2 = 0.98$ , while the linear regression slope for the *Listeria monocytogenes* bacteria imprinted MIP-Ppy/SPCE was  $0.063 \mu\text{A}/(\text{CFU}/\text{mL})$ , with  $R^2 = 0.97$ .

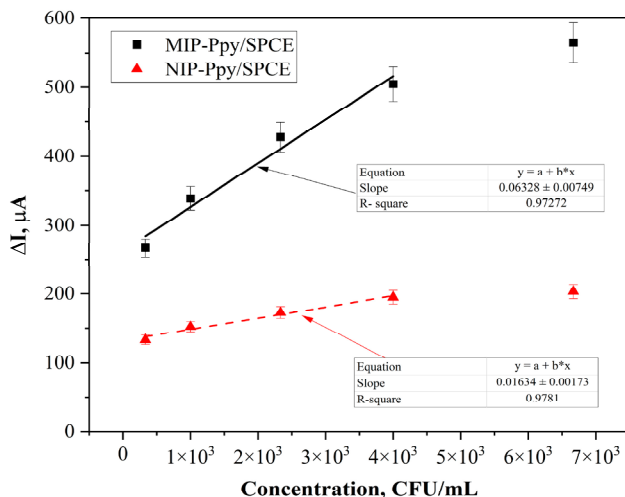


**Figure 7.** Calibration curve  $\Delta I$  registered by MIP-Ppy/SPCE (black line) and NIP-Ppy/SPCE (red line) vs. *Listeria monocytogenes* concentration. Error bars are calculated as a percentage standard error.

Molecular imprinting is ranked according to the relationship between the MIP and the non-imprinted polymer (NIP), which is obtained according to Equation (3) [45,46]:

$$IF = I_{\text{MIP}} / I_{\text{NIP}} \quad (3)$$



Usually, IF is called an imprinting factor, whereas Ayerdurai et al. [47] argued that an apparent imprinting factor is a more correct term for IF. According to the measurements, the MIP-Ppy/SPCE had an apparent imprinting factor toward the *Listeria monocytogenes* bacteria that was approximately four times higher than that registered by the NIP-Ppy/SPCE electrode. The LOD and the LOQ were calculated according to Equations (1) and (2). It was evaluated that the LOD and LOQ for the MIP-Ppy/SPCE were 70 CFU/mL and 210 CFU/mL, respectively, in the linear range from 300 to 6700 CFU/mL.

A comparison of electrochemical methods previously used to detect *Listeria monocytogenes* is shown in Table 1.

**Table 1.** Summary of the electrochemical methods previously used for the detection of *Listeria monocytogenes*.

| Electrode                             | Detection Technique             | Method Used             | LOD, LOQ and LR  | Ref. |
|---------------------------------------|---------------------------------|-------------------------|--|------|
| Gold disk                             | RAA-based E-CRISPR <sup>1</sup> | Square wave voltammetry | LOD 26 CFU/mL;<br>LR $2.6 \times 10^1$ to $2.6 \times 10^9$ CFU/mL | [48] |
| Gold electrode                        | Sandwich assay                  | CV, EIS                 | LR $10^2$ to $10^6$ CFU/ml   | [18] |
| Multiwalled carbon nanotube electrode | Immunoassay                     | CV                      | LOD $1.07 \times 10^2$ CFU/mL;<br>LR $10^2$ to $10^5$ CFU/mL       | [49] |
| Aluminium disc                        | Immunoassay                     | EIS                     | LOD 1.3 log CFU/mL<br>LR 1.3 to 4.3 log CFU/mL                     | [50] |

<sup>1</sup> RAA-based E-CRISPR—recombinase-assisted amplification-based CRISPR/Cas12a into an E-DNA biosensor platform.

The investigation of the interaction between *Listeria monocytogenes* bacteria and the MIP-Ppy-modified electrode has several advantages, but the one that stands out the most is that just two of them use electrochemical techniques (Table 2). This suggests that there were only a few studies on applying MIP-based sensors for detecting *Listeria monocytogenes* bacteria. Additionally, Table 2 summarises other MIP-based sensors for certain bacterial species, employing electrochemical and quartz crystal microbalance (QCM) approaches. The electrode, the polymer used for MIP preparation, the bacteria extraction method, the analytical method, and sensitivity (LOD and linear range) are included in Table 2. In most cases, when an enzyme was used to extract the template from the polymer during MIP-based sensor design, that enzyme was lysozyme. Meanwhile, a similar enzyme, trypsin, was employed in this study.

**Table 2.** Summary of the MIP-based sensors for *Listeria monocytogenes* and other bacteria.

| Bacteria                      | Electrode  | Polymer  | Bacteria Extraction from the Polymer         | Method Used                          | LOD, LOQ and Linear Range (LR)             | Ref. |
|-------------------------------|--|--|--|--------------------------------------|--|------|
| <i>Listeria monocytogenes</i> | -  | Acryloyl-functionalised chitosan with CdTe quantum dots          | 10% acetic acid, 1% SDS, water, and methanol | Fluorescence microscope              | LOD $10^3$ CFU/mL                          | [32] |
| <i>Listeria monocytogenes</i> | GCE  | Poly(TPA)  | SDS/AA ( <i>w/v</i> , 5%) solution           | DPV                                  | LOD 6 CFU/mL;<br>LR $10$ to $10^6$ CFU/mL  | [33] |
| <i>Listeria monocytogenes</i> | GCE with MXenes nanoribbon (Ti <sub>3</sub> C <sub>2</sub> T <sub>x</sub> R) | Poly(Th) with  | 0.5 M HCl                                    | DPV                                  | LOD 2 CFU/mL;<br>LR $10$ to $10^8$ CFU/mL  | [34] |
| <i>Klebsiella pneumoniae</i>  | SPE  | Acrylamide-based polymer with carbon or gold or rGO              | 10% acetic acid for 30 min                   | CV in PBS with a redox probe         | LOD of 0.012 CFU/mL and LOQ of 1.61 CFU/mL | [51] |
| <i>Klebsiella pneumoniae</i>  | ITO coated glass electrode   | Ppy obtained by the interfacial oxidative polymerisation process | DI and ethanol                               | DPV and CV in PBS with a redox probe | LOD of 1.352 CFU/mL                        | [52] |

Table 2. Cont.

| Bacteria  | Electrode      | Polymer                             | Bacteria Extraction from the Polymer   | Method Used  | LOD, LOQ and Linear Range (LR)  | Ref. |
|---|----------------|-------------------------------------|--|--|---|------|
| <i>Salmonella</i>   | GCE            | Ppy with MXene                      | SDS/acetic acid (5%, w/v) for 5 min and washed three times   | EIS  | LOD of 23 CFU/mL  | [53] |
| <i>Pseudomonas aeruginosa</i>                             | QCM electrode  | Overoxidised Ppy                    | With lysozyme (10 mg/mL) for 2 h at 4 °C and 10% Triton X for 80 min   | QCM  | LOD 10 <sup>3</sup> CFU/mL  | [54] |
| <i>Escherichia coli</i> and <i>Pseudomonas aeruginosa</i> | QCM electrode  | Overoxidised Ppy                    | Lysozyme (10 mg/mL) containing 10% Triton X and EDTA (200 µg/mL) for 1 day at room temperature   | QCM  | -   | [55] |
| <i>Escherichia coli</i> (serotypes O157:H7 and O26:H11)   | QCM sensor     | Overoxidised Ppy                    | Lysozyme (30 mg/mL) and 5% SDS for 48 h at 30 °C   | QCM  | -   | [56] |
| <i>Escherichia coli</i>                                   | Gold electrode | Polymer of MAH, HEMA, and EGDMA     | 10 mM sodium phosphate buffer (pH 7.4) and treated with 10 mg/mL lysozyme solution (in 10 mM Tris-HCl buffer, pH 8.0, with 1 mM EDTA) for 30 min | Capacitance measurements in a continuous flow system | LOD 70 CFU/mL, LR 1.0 × 10 <sup>2</sup> –1.0 × 10 <sup>7</sup> CFU/mL | [57] |
| <i>Escherichia coli</i> K-12                              | GCE            | Polymer of 2-APBA and ANI           | 2 h treated with 2 mg mL <sup>-1</sup> lysozyme enzyme in PBS (pH 1/4 7.4), 10% Triton X, water, and then overoxidised                           | DPV, EIS   | -   | [58] |
| <i>Saccharomyces cerevisiae</i> (Bakers' yeast)           | QCM            | Polyurethane                        | Hot water  | QCM  | LOD 1 × 10 <sup>4</sup> cells/mL                                      | [59] |
| <i>Staphylococcus epidermidis</i>                         | Gold electrode | Poly(3-APBA)                        | 30 min with fructose (20 mM), plenty of water, and phosphate solution (pH 2.2) for 20 min  | EIS  | LR 10 <sup>3</sup> –10 <sup>7</sup> CFU/mL                            | [60] |
| <i>Bacillus subtilis</i> endospore                        | GCE            | polypyrrole/poly(3-methylthiophene) | In DMSO for 10 min at room temperature   | CV and EIS   | -   | [61] |

SPE—screen-printed electrode; rGO—reduced graphene oxide; redox probe—K<sub>4</sub>[Fe(CN)<sub>6</sub>]/K<sub>3</sub>[Fe(CN)<sub>6</sub>]; ITO—indium tin oxide; DPV—differential pulse voltammetry; GCE—glassy carbon electrode; SDS—sodium dodecyl sulphate; 3-APBA—3-aminophenylboronic acid; GCE—glassy carbon electrode; MAH—N-methacryloyl-L-histidine methylester; HEMA—2-Hydroxyethyl methacrylate; EGDMA—ethyleneglycol dimethacrylate; 2-APBA—2-aminophenylboronic acid; ANI—aniline; TPA—3-thiopheneacetic acid; SDS—sodium dodecyl sulphate; AA—acetic acid; Th—thionine; GCE—glassy carbon electrode.

#### 4. Conclusions

This study involved the electrochemical modification of two types of electrodes, namely, SPCE and Pt, with different Ppy layers, i.e., not imprinted (NIP-Ppy) and bacteria *Listeria monocytogenes* imprinted (MIP-Ppy). The pulsed amperometric detection method was used to evaluate the performance of MIP-Ppy/SPCE and MIP-Ppy/Pt electrodes. MIP-Ppy/SPCE electrodes were found to be more effective in detecting *Listeria monocytogenes* in terms of the substantial changes in current density. Furthermore, the study analysed the efficiency of various template extraction solutions on the sensor's sensitivity. The results showed that the acetic acid solution was highly effective in removing imprinted bacteria from the MIP-Ppy layer. MIP-Ppy/SPCE exhibited at least 12 times higher current density than NIP-Ppy/SPCE. The current density increased around 3 times for MIP-Ppy/SPCE designed by extraction of *Listeria monocytogenes* bacteria with trypsin compared to changes in the current density registered by similarly treated NIP-Ppy/SPCE. Based on these results, it can be assumed that an efficient MIP-Ppy-based sensor can be designed by extracting bacteria using acetic acid and the proteolytic enzyme trypsin. The results showed that the limit of detection (LOD) and limit of quantification (LOQ) of the MIP-Ppy/SPCE prepared

using trypsin were 70 CFU/mL and 210 CFU/mL, respectively, within the linear range of 300 to 6700 CFU/mL.

**Author Contributions:** Conceptualisation, A.R. (Arunas Ramanavicius) and M.P.; methodology, A.R. (Arunas Ramanavicius), M.P., V.H., V.K. and V.R.; formal analysis, R.B., V.L., K.D., R.V. and V.R.; investigation, V.L., R.B., M.P. and V.R.; resources, A.R. (Arunas Ramanavicius) and M.P.; data curation, V.L., R.B., V.K. and V.R.; writing—original draft preparation, M.P., V.L., R.B., G.P. and V.R.; writing—review and editing, M.P., V.L., R.B., V.R. and A.R. (Almira Ramanaviciene); visualisation, V.L.; supervision, A.R. (Arunas Ramanavicius) and R.V.; project administration, M.P.; funding acquisition, M.P. and A.R. (Arunas Ramanavicius). All authors have read and agreed to the published version of the manuscript.

**Funding:** Research was funded under the CFLA project “Jauna fotoluminescences platforma *Listeria monocytogēnu* noteikšanai” (1.1.1.5/21/A/001). *L. monocytogenes* samples were prepared under the support from LV-UA bilateral project (Ministry of Education and Science of Ukraine) “Development of nanostructured optical sensor system for detection of *K. pneumonia*” (LV-UA/2021/2).

**Institutional Review Board Statement:** Not applicable.

**Data Availability Statement:** No additional information is available for this paper.

**Acknowledgments:** *L. monocytogenes* samples were prepared under the support from LV-UA bilateral project “Development of nanostructured optical sensor system for detection of *K. pneumonia*” (LV-UA/2021/2).

**Conflicts of Interest:** The authors declare no conflict of interest.

## References

- Vizzini, P.; Braidot, M.; Vidic, J.; Manzano, M. Electrochemical and Optical Biosensors for the Detection of *Campylobacter* and *Listeria*: An Update Look. *Micromachines* **2019**, *10*, 500. [[CrossRef](#)] [[PubMed](#)]
- Batt, C.A. LISTERIA | *Listeria monocytogenes*. In *Encyclopedia of Food Microbiology*, 2nd ed.; Batt, C.A., Tortorello, M.L., Eds.; Academic Press: Oxford, UK, 2014; pp. 490–493.
- Matle, I.; Mbatha Khanyisile, R.; Madoroba, E. A review of *Listeria monocytogenes* from meat and meat products: Epidemiology, virulence factors, antimicrobial resistance and diagnosis. *Onderstepoort J. Vet. Res.* **2020**, *87*, a1869. [[CrossRef](#)] [[PubMed](#)]
- Lepe, J.A. Current aspects of listeriosis. *Med. Clínica* **2020**, *154*, 453–458. [[CrossRef](#)] [[PubMed](#)]
- Choi, M.H.; Park, Y.J.; Kim, M.; Seo, Y.H.; Kim, Y.A.; Choi, J.Y.; Yong, D.; Jeong, S.H.; Lee, K. Increasing Incidence of Listeriosis and Infection-associated Clinical Outcomes. *Ann. Lab. Med.* **2018**, *38*, 102–109. [[CrossRef](#)] [[PubMed](#)]
- Valenti, M.; Ranganathan, N.; Moore, L.S.; Hughes, S. *Listeria monocytogenes* infections: Presentation, diagnosis and treatment. *Br. J. Hosp. Med.* **2021**, *82*, 1–6. [[CrossRef](#)]
- Freitag, I.G.R.; Pereira, R.d.C.L.; Machado, E.S.; Hofer, E.; Vallim, D.C.; Hofer, C.B. Seroprevalence of *Listeria monocytogenes* in HIV infected pregnant women from Brazil. *Braz. J. Infect. Dis.* **2021**, *25*, 101635. [[CrossRef](#)]
- Craig, A.M.; Dotters-Katz, S.; Kuller, J.A.; Thompson, J.L. Listeriosis in Pregnancy: A Review. *Obstet. Gynecol. Surv.* **2019**, *74*, 362–368. [[CrossRef](#)]
- Soni, D.K.; Ahmad, R.; Dubey, S.K. Biosensor for the detection of *Listeria monocytogenes*: Emerging trends. *Crit. Rev. Microbiol.* **2018**, *44*, 590–608. [[CrossRef](#)]
- EFSA Panel on Biological Hazards (BIOHAZ); Ricci, A.; Allende, A.; Bolton, D.; Chemaly, M.; Davies, R.; Fernández Escámez, P.S.; Girones, R.; Herman, L.; Koutsoumanis, K.; et al. *Listeria monocytogenes* contamination of ready-to-eat foods and the risk for human health in the EU. *EFSA J.* **2018**, *16*, e05134. [[CrossRef](#)]
- Jadhav, S.; Bhawe, M.; Palombo, E.A. Methods used for the detection and subtyping of *Listeria monocytogenes*. *J. Microbiol. Methods* **2012**, *88*, 327–341. [[CrossRef](#)]
- Silva, N.F.D.; Neves, M.M.P.S.; Magalhães, J.M.C.S.; Freire, C.; Delerue-Matos, C. Emerging electrochemical biosensing approaches for detection of *Listeria monocytogenes* in food samples: An overview. *Trends Food Sci. Technol.* **2020**, *99*, 621–633. [[CrossRef](#)]
- Tasbasi, B.B.; Guner, B.C.; Sudagidan, M.; Ucak, S.; Kavruk, M.; Ozalp, V.C. Label-free lateral flow assay for *Listeria monocytogenes* by aptamer-gated release of signal molecules. *Anal. Biochem.* **2019**, *587*, 113449. [[CrossRef](#)] [[PubMed](#)]
- Wachiralurpan, S.; Chansiri, K.; Lieberzeit, P.A. Direct detection of *Listeria monocytogenes* DNA amplification products with quartz crystal microbalances at elevated temperatures. *Sens. Actuat. B-Chem.* **2020**, *308*, 127678. [[CrossRef](#)]
- Jiang, X.; Ding, W.; Lv, Z.; Rao, C. Highly Sensitive Electrochemical Immunosensing for *Listeria Monocytogenes* Based on 3,4,9,10-Perylene Tetracarboxylic Acid/Graphene Ribbons as a Sensing Platform and Ferrocene/Gold Nanoparticles as an Amplifier. *Anal. Sci.* **2021**, *37*, 1701–1706. [[CrossRef](#)] [[PubMed](#)]
- Crowley, E.L.; O’Sullivan, C.K.; Guilbault, G.G. Increasing the sensitivity of *Listeria monocytogenes* assays: Evaluation using ELISA and amperometric detection. *Analyst* **1999**, *124*, 295–299. [[CrossRef](#)] [[PubMed](#)]

17. Lopes-Luz, L.; Mendonça, M.; Bernardes Fogaça, M.; Kipnis, A.; Bhunia, A.K.; Bühner-Sékula, S. *Listeria monocytogenes*: Review of pathogenesis and virulence determinants-targeted immunological assays. *Crit. Rev. Microbiol.* **2021**, *47*, 647–666. [[CrossRef](#)] [[PubMed](#)]
18. Cheng, C.; Peng, Y.; Bai, J.; Zhang, X.; Liu, Y.; Fan, X.; Ning, B.; Gao, Z. Rapid detection of *Listeria monocytogenes* in milk by self-assembled electrochemical immunosensor. *Sens. Actuata. B-Chem.* **2014**, *190*, 900–906. [[CrossRef](#)]
19. Zolti, O.; Suganthan, B.; Maynard, R.; Asadi, H.; Locklin, J.; Ramasamy, R.P. Electrochemical Biosensor for Rapid Detection of *Listeria monocytogenes*. *J. Electrochem. Soc.* **2022**, *169*, 067510. [[CrossRef](#)]
20. Lee, B.E.; Kang, T.; Jenkins, D.; Li, Y.; Wall, M.M.; Jun, S. A single-walled carbon nanotubes-based electrochemical impedance immunosensor for on-site detection of *Listeria monocytogenes*. *J. Food Sci.* **2022**, *87*, 280–288. [[CrossRef](#)]
21. Rivas-Macho, A.; Eletxigerra, U.; Diez-Ahedo, R.; Merino, S.; Sanjuan, A.; Bou-Ali, M.M.; Ruiz-Rubio, L.; del Campo, J.; Vilas-Vilela, J.L.; Goñi-de-Cerio, F.; et al. Design and 3D printing of an electrochemical sensor for *Listeria monocytogenes* detection based on loop mediated isothermal amplification. *Heliyon* **2023**, *9*, e12637. [[CrossRef](#)]
22. Mosbach, K. Molecular imprinting. *Trends Biochem. Sci.* **1994**, *19*, 9–14. [[CrossRef](#)]
23. Treťakov, A.; Syritski, V.; Reut, J.; Boroznjak, R.; Öpik, A. Molecularly imprinted polymer film interfaced with Surface Acoustic Wave technology as a sensing platform for label-free protein detection. *Anal. Chim. Acta* **2016**, *902*, 182–188. [[CrossRef](#)] [[PubMed](#)]
24. Ramanavicius, S.; Jagminas, A.; Ramanavicius, A. Advances in Molecularly Imprinted Polymers Based Affinity Sensors (Review). *Polymers* **2021**, *13*, 974. [[CrossRef](#)] [[PubMed](#)]
25. Ratautaite, V.; Boguzaitė, R.; Brazys, E.; Ramanaviciene, A.; Ciplys, E.; Juozapaitis, M.; Slibinskas, R.; Bechelany, M.; Ramanavicius, A. Molecularly Imprinted Polypyrrole based Sensor for the Detection of SARS-CoV-2 Spike Glycoprotein. *Electrochim. Acta* **2022**, *403*, 139581. [[CrossRef](#)] [[PubMed](#)]
26. Teng, Y.; Liu, F.; Kan, X. Voltammetric dopamine sensor based on three-dimensional electrosynthesized molecularly imprinted polymers and polypyrrole nanowires. *Microchim. Acta* **2017**, *184*, 2515–2522. [[CrossRef](#)]
27. Ratautaite, V.; Nesladek, M.; Ramanaviciene, A.; Baleviciute, I.; Ramanavicius, A. Evaluation of Histamine Imprinted Polypyrrole Deposited on Boron Doped Nanocrystalline Diamond. *Electroanalysis* **2014**, *26*, 2458–2464. [[CrossRef](#)]
28. Nguy, T.P.; Van Phi, T.; Tram, D.T.N.; Eersels, K.; Wagner, P.; Lien, T.T.N. Development of an impedimetric sensor for the label-free detection of the amino acid sarcosine with molecularly imprinted polymer receptors. *Sens. Actuata. B-Chem.* **2017**, *246*, 461–470. [[CrossRef](#)]
29. Ratautaite, V.; Boguzaitė, R.; Brazys, E.; Plausinaitis, D.; Ramanavicius, S.; Samukaite-Bubniene, U.; Bechelany, M.; Ramanavicius, A. Evaluation of the interaction between SARS-CoV-2 spike glycoproteins and the molecularly imprinted polypyrrole. *Talanta* **2023**, *253*, 123981. [[CrossRef](#)]
30. Piletsky, S.; Canfarotta, F.; Poma, A.; Bossi, A.M.; Piletsky, S. Molecularly Imprinted Polymers for Cell Recognition. *Trends Biotechnol.* **2020**, *38*, 368–387. [[CrossRef](#)]
31. Dar, K.K.; Shao, S.; Tan, T.; Lv, Y. Molecularly imprinted polymers for the selective recognition of microorganisms. *Biotechnol. Adv.* **2020**, *45*, 107640. [[CrossRef](#)]
32. Zhao, X.; Cui, Y.; Wang, J.; Wang, J. Preparation of Fluorescent Molecularly Imprinted Polymers via Pickering Emulsion Interfaces and the Application for Visual Sensing Analysis of *Listeria Monocytogenes*. *Polymers* **2019**, *11*, 984. [[CrossRef](#)] [[PubMed](#)]
33. Li, Q.; Guo, Z.; Qiu, X.; Lu, W.; Yang, W.; Wang, Q.; Wu, Q. Simple electrochemical detection of *Listeria monocytogenes* based on a surface-imprinted polymer-modified electrode. *Anal. Methods* **2021**, *13*, 4864–4870. [[CrossRef](#)] [[PubMed](#)]
34. Jiang, X.; Lv, Z.; Ding, W.; Zhang, Y.; Lin, F. Pathogen-Imprinted Polymer Film Integrated probe/Ti<sub>3</sub>C<sub>2</sub>T<sub>x</sub> MXenes Electrochemical Sensor for Highly Sensitive Determination of *Listeria Monocytogenes*. *J. Electrochem. Sci. Technol.* **2022**, *13*, 431–437. [[CrossRef](#)]
35. Cui, F.; Zhou, Z.; Zhou, H.S. Molecularly Imprinted Polymers and Surface Imprinted Polymers Based Electrochemical Biosensor for Infectious Diseases. *Sensors* **2020**, *20*, 996. [[CrossRef](#)]
36. Ramanavicius, A.; Oztekin, Y.; Ramanaviciene, A. Electrochemical formation of polypyrrole-based layer for immunosensor design. *Sens. Actuata. B-Chem.* **2014**, *197*, 237–243. [[CrossRef](#)]
37. Trček, J.; Mira, N.P.; Jarboe, L.R. Adaptation and tolerance of bacteria against acetic acid. *Appl. Microbiol. Biotechnol.* **2015**, *99*, 6215–6229. [[CrossRef](#)]
38. Miura, C.; Ohta, T.; Ozaki, Y.; Tanaka, H.; Miura, T. Trypsin is a multifunctional factor in spermatogenesis. *Proc. Natl. Acad. Sci. USA* **2009**, *106*, 20972–20977. [[CrossRef](#)]
39. Grenier, D. Effect of proteolytic enzymes on the lysis and growth of oral bacteria. *Oral Microbiol. Immunol.* **1994**, *9*, 224–228. [[CrossRef](#)]
40. Zhou, J.; Meng, X.; Han, Q.; Huang, Y.; Huo, L.; Lei, Y. An in vitro study on the degradation of multispecies biofilm of periodontitis-related microorganisms by bovine trypsin. *Front. Microbiol.* **2022**, *13*, 951291. [[CrossRef](#)]
41. Yarman, A.; Scheller, F.W. How Reliable Is the Electrochemical Readout of MIP Sensors? *Sensors* **2020**, *20*, 2677. [[CrossRef](#)]
42. Conte, M.P.; Petrone, G.; Biase, A.M.D.; Longhi, C.; Penta, M.; Tinari, A.; Superti, F.; Fabozzi, G.; Visca, P.; Seganti, L. Effect of Acid Adaptation on the Fate of *Listeria monocytogenes* in THP-1 Human Macrophages Activated by Gamma Interferon. *Infect. Immun.* **2002**, *70*, 4369–4378. [[CrossRef](#)] [[PubMed](#)]
43. Kamal Ahmed, R.; Saad, E.M.; Fahmy, H.M.; El Nashar, R.M. Design and application of molecularly imprinted Polypyrrole/Platinum nanoparticles modified platinum sensor for the electrochemical detection of Vardenafil. *Microchem. J.* **2021**, *171*, 106771. [[CrossRef](#)]

44. Wu, J.; Wang, R.; Lu, Y.; Jia, M.; Yan, J.; Bian, X. Facile Preparation of a Bacteria Imprinted Artificial Receptor for Highly Selective Bacterial Recognition and Label-Free Impedimetric Detection. *Anal. Chem.* **2019**, *91*, 1027–1033. [[CrossRef](#)] [[PubMed](#)]
45. Ratautaite, V.; Brazys, E.; Ramanaviciene, A.; Ramanavicius, A. Electrochemical Sensors based on L-Tryptophan Molecularly Imprinted Polypyrrole and Polyaniline. *J. Electroanal. Chem.* **2022**, *917*, 116389. [[CrossRef](#)]
46. Mustafa, Y.L.; Keirouz, A.; Leese, H.S. Molecularly imprinted polymers in diagnostics: Accessing analytes in biofluids. *J. Mater. Chem. B* **2022**, *10*, 7418–7449. [[CrossRef](#)]
47. Ayerdurai, V.; Cieplak, M.; Kutner, W. Molecularly imprinted polymer-based electrochemical sensors for food contaminants determination. *TRAC-Trends Anal. Chem.* **2023**, *158*, 116830. [[CrossRef](#)]
48. Li, F.; Ye, Q.; Chen, M.; Zhou, B.; Zhang, J.; Pang, R.; Xue, L.; Wang, J.; Zeng, H.; Wu, S.; et al. An ultrasensitive CRISPR/Cas12a based electrochemical biosensor for *Listeria monocytogenes* detection. *Biosens. Bioelectron.* **2021**, *179*, 113073. [[CrossRef](#)]
49. Lu, Y.; Liu, Y.; Zhao, Y.; Li, W.; Qiu, L.; Li, L. A Novel and Disposable Enzyme-Labeled Amperometric Immunosensor Based on MWCNT Fibers for *Listeria monocytogenes* Detection. *J. Nanomater.* **2016**, *2016*, 3895920. [[CrossRef](#)]
50. Chai, C.; Lee, J.; Oh, S.-W.; Takhistov, P. Impedimetric Characterization of Adsorption of *Listeria monocytogenes* on the Surface of an Aluminum-Based Immunosensor. *J. Food Sci.* **2014**, *79*, E2266–E2271. [[CrossRef](#)]
51. Pintavirooj, C.; Vongmanee, N.; Sukjee, W.; Sangma, C.; Visitsattapongse, S. Biosensors for *Klebsiella pneumoniae* with Molecularly Imprinted Polymer (MIP) Technique. *Sensors* **2022**, *22*, 4638. [[CrossRef](#)]
52. Sharma, R.; Lakshmi, G.B.V.S.; Kumar, A.; Solanki, P. Polypyrrole Based Molecularly Imprinted Polymer Platform for *Klebsiella pneumoniae* Detection. *ECS Sensors Plus* **2022**, *1*, 010603. [[CrossRef](#)]
53. Wang, O.; Jia, X.; Liu, J.; Sun, M.; Wu, J. Rapid and simple preparation of an MXene/polypyrrole-based bacteria imprinted sensor for ultrasensitive *Salmonella* detection. *J. Electroanal. Chem.* **2022**, *918*, 116513. [[CrossRef](#)]
54. Tokonami, S.; Nakadoi, Y.; Takahashi, M.; Ikemizu, M.; Kadoma, T.; Saimatsu, K.; Dung, L.Q.; Shiigi, H.; Nagaoka, T. Label-Free and Selective Bacteria Detection Using a Film with Transferred Bacterial Configuration. *Anal. Chem.* **2013**, *85*, 4925–4929. [[CrossRef](#)] [[PubMed](#)]
55. Tokonami, S.; Nakadoi, Y.; Nakata, H.; Takami, S.; Kadoma, T.; Shiigi, H.; Nagaoka, T. Recognition of gram-negative and gram-positive bacteria with a functionalised conducting polymer film. *Res. Chem. Intermed.* **2014**, *40*, 2327–2335. [[CrossRef](#)]
56. Tokonami, S.; Shimizu, E.; Tamura, M.; Iida, T. Mechanism in External Field-mediated Trapping of Bacteria Sensitive to Nanoscale Surface Chemical Structure. *Sci. Rep.* **2017**, *7*, 16651. [[CrossRef](#)] [[PubMed](#)]
57. Idil, N.; Hedström, M.; Denizli, A.; Mattiasson, B. Whole cell based microcontact imprinted capacitive biosensor for the detection of *Escherichia coli*. *Biosens. Bioelectron.* **2017**, *87*, 807–815. [[CrossRef](#)] [[PubMed](#)]
58. Yasmeen, N.; Etienne, M.; Sharma, P.S.; El-Kirat-Chatel, S.; Helú, M.B.; Kutner, W. Molecularly imprinted polymer as a synthetic receptor mimic for capacitive impedimetric selective recognition of *Escherichia coli* K-12. *Anal. Chim. Acta* **2021**, *1188*, 339177. [[CrossRef](#)]
59. Hayden, O.; Dickert, F.L. Selective Microorganism Detection with Cell Surface Imprinted Polymers. *Adv. Mater.* **2001**, *13*, 1480–1483. [[CrossRef](#)]
60. Golabi, M.; Kuralay, F.; Jager, E.W.H.; Beni, V.; Turner, A.P.F. Electrochemical bacterial detection using poly(3-aminophenylboronic acid)-based imprinted polymer. *Biosens. Bioelectron.* **2017**, *93*, 87–93. [[CrossRef](#)]
61. Namvar, A.; Warriner, K. Microbial imprinted polypyrrole/poly(3-methylthiophene) composite films for the detection of *Bacillus* endospores. *Biosens. Bioelectron.* **2007**, *22*, 2018–2024. [[CrossRef](#)]

**Disclaimer/Publisher's Note:** The statements, opinions and data contained in all publications are solely those of the individual author(s) and contributor(s) and not of MDPI and/or the editor(s). MDPI and/or the editor(s) disclaim responsibility for any injury to people or property resulting from any ideas, methods, instructions or products referred to in the content.

## **Paper 2**

### **Electrochemical impedance spectroscopy based evaluation of chlorophyll a reconstitution within tethered bilayer lipid membrane**

**V. Liustrovaite**, A. Valiuniene, G. Valincius, A. Ramanavicius

*Journal of The Electrochemical Society*, 2021, 168 (6), 066506  
[doi.org/10.1149/1945-7111/ac0262](https://doi.org/10.1149/1945-7111/ac0262)



# Electrochemical Impedance Spectroscopy Based Evaluation of Chlorophyll a Reconstitution within Tethered Bilayer Lipid Membrane

Viktorija Liustrovaitė,<sup>1</sup> Aušra Valiūnienė,<sup>1</sup> Gintaras Valincius,<sup>2,4</sup> and Arūnas Ramanavičius<sup>1,3,z</sup>

<sup>1</sup> Department of Physical Chemistry, Faculty of Chemistry and Geosciences, Vilnius University, LT-03225 Vilnius, Lithuania

<sup>2</sup> Life Sciences Center, Institute of Biochemistry Vilnius University, LT-10257, Vilnius, Lithuania

<sup>3</sup> Laboratory of Nanotechnology, State Research Institute Center for Physical Sciences and Technology, LT-10257, Vilnius, Lithuania

This article reports electrochemical impedance spectroscopy-based evaluation of chlorophyll a (Chl-a) reconstitution within tethered bilayer lipid membrane (tBLM), formed on a gold surface by vesicle fusion. The self-assembled monolayer (SAM) consisting of a mixture of WC14 (20-tetradecyloxy-3,6,9,12,15,18,22-heptaohexatricontane-1-thiol) and  $\beta$ -mercaptoethanol ( $\beta$ ME) mixed in a molar % ratio of 35:65 served as a molecular anchor for tBLMs. The fluorescence microscopy (FM) allowed direct observation of incorporation of Chl-a into membranes. The lipid composition consisting of 1,2-dioleoyl-sn-glycero-3-phosphocholine (DOPC) and cholesterol (Chol), was found to be highly compatible with the addition of Chl-a to the phospholipid membranes at different molar ratios. Moreover, the addition of Chl-a to DOPC yielding DOPC (50%)/Chol (40%)/Chl-a (10%) bilayers consistently decreased defect density in tBLMs, thus increasing dielectric integrity of the membranes. Also, we observed a significant structural stabilization of tBLMs subject to bias potential variation in experiments involving Chl-a containing bilayers. © 2021 The Author(s). Published on behalf of The Electrochemical Society by IOP Publishing Limited. This is an open access article distributed under the terms of the Creative Commons Attribution 4.0 License (CC BY, <http://creativecommons.org/licenses/by/4.0/>), which permits unrestricted reuse of the work in any medium, provided the original work is properly cited. [DOI: 10.1149/1945-7111/ac0262]



Manuscript submitted February 26, 2021; revised manuscript received April 28, 2021. Published June 2, 2021.

Chlorophyll (Chl-a) is a unique  $\pi$ - $\pi$ -conjugated system located across their macrocyclic skeleton, and the diversity of side groups around allows it to function as a major photoactive and structural component of all photosynthetic organisms.<sup>1</sup> Since in the natural environment Chl-a is able “to harvest light,” it is capable to capture solar photons and convert their energy into chemical form, which is well accessible to nearly all forms of life.<sup>2,3</sup> The majority of chlorophylls are situated in the thylakoid cell membrane, which may be at the spatial distance between the outer and inner cell, moreover, its composition and arrangement vary by cell type.<sup>4</sup>

Many different simplified biomimetic analogues of lipid membranes were widely used to evaluate/model structural and permeability/transport properties of more complex natural bio-membranes.<sup>5,6</sup> In some recent biophysical and biochemical studies tethered phospholipid bilayer membranes (tBLMs) attached to the gold surface are used as the model systems, which are well-mimicking properties of natural membranes. Therefore, these universal tBLM modeling platforms recently are finding a niche in the investigation of proteins, toxins, and membrane forming compounds.<sup>7–9</sup> The tBLM is a surface supporting structure attached to the surface of a solid substrate and consists of self-assembled lipid-like molecules, which anchor a phospholipid bilayer to the surface.<sup>10</sup> The properties of tBLM structure depend on a process, which usually starts from the formation of a self-assembled monolayer (SAM) containing a “lipid anchor” with a longer alkyl chain and short alkyl chain that forms the main part of the SAM,<sup>11</sup> followed by the formation of a phospholipid bilayer membrane filled with unbound lipids. In the first stage, thiol—or disulfide-groups of alkanethiols are exploited to attach synthetic lipid to the metal surface,<sup>12</sup> which in most cases is gold.<sup>13,14</sup> The second step involves one of two well-established procedures: (i) a solvent exchange procedure,<sup>15</sup> or (ii) a fusion of small liposomes.<sup>16</sup> The structure, nature, composition, and distribution of the SAM lipid anchor molecule on the substrate surface have a significant effect on the properties of tBLM.<sup>17</sup> Electrical impedance of tBLM, which contains the different number of defects, is an important characteristic, therefore, the concentration and the nature of defects, which are present in tBLMs, can be efficiently determined and/or revealed by electrochemical

impedance spectroscopy (EIS), showing structural differences of differently designed tBLMs.<sup>18</sup> The long-chain thiol compounds WC14 (20-tetradecyloxy-3,6,9,12,15,18,22-heptaohexatricontane-1-thiol) can be used in SAM formation as “anchors,” which enable the formation of stable and reproducible phospholipid bilayers.<sup>19</sup> It is recognized that tBLMs mimic to a certain extent the structure and function of cell membranes.<sup>20</sup> Specific modifications of tBLMs are suitable for the development of various biosensors by the incorporation of lipid components such as 1,2-dioleoyl-sn-glycero-3-phosphocholine (DOPC) and cholesterol (Chol), which provide additional stability.<sup>21,22</sup> In our very recent research we have demonstrated the applicability of such membranes for the modelling of cell-membrane treatment by pulsed electric field localized by scanning electrochemical microscope.<sup>23</sup> All this enables to apply these systems in the study of various properties of biological membranes.

The aim of this work was to test the possibility to incorporate photoactive compound Chl-a into tethered bilayer lipid membrane (tBLM) to create a platform, which can be used in the future for the development of tBLM photosensitive surface constructs, which could be potentially used for the development of new biosensors and biomimetic artificial leaves.

## Experimental

**Chemicals and other materials.**—20-tetradecyloxy-3,6,9,12,15,18,22-heptaohexatricontane-1-thiol was synthesized as described in Ref. 11  $\beta$ -mercaptoethanol ( $\geq 99.0\%$ , CAS Number 60–24–2), sulfuric acid (95.0%–98.0%, CAS Number 7664–93–9), chloroform ( $\geq 99\%$ , CAS Number 67–66–3), toluene ( $\geq 99.5\%$ , CAS Number 108–88–3) methanol ( $\geq 99.9\%$ , CAS Number 67–56–1) and silica gel (granules desiccant  $\sim 2 - 5$  mm, CAS Number 112926–00–8) were purchased from Sigma-Aldrich (St. Louis, MO). 1,2-dioleoyl-sn-glycero-3-phosphatidylcholine (CAS Number 4235–95–4) and cholesterol ( $\geq 99\%$ , CAS Number 57–88–5) were received from Avanti Polar Lipids (Alabaster, USA). H<sub>2</sub>O was purified in a Millipore (Billerica, MA) UHQ reagent-grade water purification system. Salts: NaCl ( $\geq 99.5\%$ , CAS Number 7647–14–5), NaH<sub>2</sub>PO<sub>4</sub> ( $\geq 99.0\%$ , CAS Number 7558–80–7), KCl ( $\geq 99.0\%$ , CAS Number 7447–40–7), KH<sub>2</sub>PO<sub>4</sub> ( $\geq 99.0\%$ , CAS Number 7778–77–0) were obtained from ReacheM (Slovakia p. a.). Glass slides of

<sup>z</sup>E-mail: [gintaras.valincius@gmc.vu.lt](mailto:gintaras.valincius@gmc.vu.lt); [arunas.ramanavicius@chf.vu.lt](mailto:arunas.ramanavicius@chf.vu.lt)

2.5 × 7.5 × 1 cm dimensions were received from ThermoFisher (UK) and glass Petri dishes were purchased from Sigma-Aldrich (St. Louis, MO).

**Extraction of chlorophyll a.**—7.2 grams of fresh spinach were bundled using porcelain mortar with pestle adding 20 ml of a toluene and methanol solution (molar ratio 8:2). The solution was filtered through a Buchner funnel. For Chl-a extraction silica gel and toluene were used to load the column up to 15 cm and then adding the filtrate. The column was washed with toluene until the yellow fraction containing carotenes was collected. The green fraction containing Chl-a was collected within 50 ml of a toluene-methanol solution mixed at a molar ratio of 8:2. The toluene and methanol solutions were separated from each other using a separator-funnel and then toluene solution (containing dissolved Chl-a) was evaporated. After the extraction Chl-a was dissolved in chloroform.

**Gold film deposition.**—Prior to the start of gold film deposition, glass slides were: (i) washed in glass Petri dishes for 30 min in sulfuric acid, then (ii) washed abundantly with deionized water after pouring the solution. The slides were blotted dry with a stream of nitrogen gas (99.99%) and placed in a PVD75 (Kurt J. Lesker Co., U.S.) vacuum magnetron chamber. Film depositions begin only when a vacuum of 7 × 10<sup>-8</sup> Torr and deeper was reached. The plates were first coated with a thin (~7 nm) layer of chromium (Cr) to improve the adhesion of gold (Au) to the surface of the glass. The thickness of the coated gold film was controlled by real-time monitoring with quartz crystal microbalance (QCM).

**Formation of self-assembled monolayer (SAM).**—The glass slides coated by 70 nm thick gold film (glass/Au) were incubated for 3 h in 0.1 mM βME and WC14 ethanolic solution, containing the materials in a molar ratio of 65:35, respectively, to form a self-assembled monolayer (SAM) consisting of backfiller βME and synthetic thiolipid WC14 molecules. After the incubation, the plates were washed with 20–30 ml of ethanol to remove excess thiols and then dried under a stream of nitrogen gas and, after this, formed glass/Au/SAMs tBLM were immediately used in all further experiments and the formation of glass/Au/SAMs/tBLM.

**Formation of tethered bilayer lipid membranes by vesicle fusion method.**—Bilayer lipid membranes were formed using the method of vesicle fusion described in previously reported researches.<sup>13,21</sup> Vesicle solutions were prepared from 1,2-dioleoyl-sn-glycero-3-phosphocholine (DOPC) (Avanti Lipids Alabaster, USA) and cholesterol (Chol) (Avanti Lipids Alabaster, USA) at a molar % ratio of 6:4 in phosphate buffer solution (PBS) containing 0.1 M of NaCl (Reachem Slovakia p. a.), 0.01 M NaH<sub>2</sub>PO<sub>4</sub> (Reachem Slovakia, p. a.), pH 4.6. In the same manner vesicle solutions were prepared from DOPC, Chol, and Chl-a at molar % ratio 5:4:1 and 6:3:1, respectively. Then, glass/Au/SAM/tBLM was exposed to the solution of vesicle for 30 min and then rinsed with phosphate buffer, pH 7.4, containing 0.137 M of NaCl, 0.01 M of NaH<sub>2</sub>PO<sub>4</sub>, 0.0027 M of KCl, and 0.0018 M of KH<sub>2</sub>PO<sub>4</sub>.

**Electrochemical impedance spectroscopy-based measurement setup.**—Electrochemical studies were performed by electrochemical impedance spectroscopy (EIS) method using the Zahner Zennium (Kronach, Germany) electrochemical workstation, controlled by the Thales z 2.0 software package. A perturbation amplitude of 10 mV was applied for the registration of EIS spectra in the frequency range within 0.1 Hz–100 kHz. A three-electrode system was used, in which the working electrode was based on glass/Au/SAM-tBLM, while the reference electrode was a silver/silver chloride in saturated NaCl [Ag/AgCl/NaCl<sub>sat</sub>] microelectrode M-401F, Microelectrodes (Bedford, NH) and the auxiliary electrode was a platinum wire (99.99% purity, Aldrich) of 0.25 mm diameter. The reference electrode was wrapped by a Pt-based auxiliary electrode. The surface area of the working electrode in a cell was 0.16 cm<sup>2</sup>.

**Measurement setup for spectrophotometric evaluation.**—The spectrophotometric evaluation was performed in cuvettes of a 1 cm length optical path. Calculation of the concentration of Chl-a was performed using Lambert-Bugger-Ber law and molar extension at optical absorbance maximum at λ<sub>max</sub> = 668 nm. The molar extinction coefficient (ε) of Chl-a in chloroform at 665.6 nm is equal to 90,411 × mol<sup>-1</sup> × cm<sup>-1</sup>.<sup>24</sup> It was determined that Chl-a concentration was 10.8 mmol l<sup>-1</sup>.

**Fluorescence microscopy-based measurement setup.**—Fluorescence microscopy (FM) was performed to examine the optical homogeneity of tBLM.<sup>25</sup> Cholesterol modified by fluorescent agent Cy5 (Cholesterol Cy5), which has replaced 0.5% of the Chol involved into vesicle, was used for the visualization and assessment of Chol concentration in the membrane. Microscopy was performed in an aqueous medium because formed membranes are tending to decompose in the air. Therefore, an immersion water lens was used for fluorescence microscopy-based measurement. The sample was illuminated with a mercury lamp light passed through a monochromatic filter with light permeability at only a wavelength of 570 nm, which corresponds to green light. The energy of this light wave is sufficient to excite the fluorescence of Cy5 molecules. Fluorescence image was monitored in real-time by spectrometers Exi Aqua Qimaging (Canada) and Qcapture Silicon Graphics (USA).

## Results and Discussion

**Spectrophotometric and fluorescence microscopy-based evaluation of tBLMs.**—The absorption spectrum of Chl-a in chloroform solvent (Fig. 1A) was evaluated spectrophotometrically. Figure 1A shows the maximum absorption of light with wavelengths of 415 nm (blue) and 667 nm (red). These absorption peaks correspond well with the works of other authors.<sup>24,26</sup>

The incorporation of Chl-a into tBLMs was followed by fluorescence microscopy (FM). For this purpose, 0.5% of cholesterol was labelled with a Cy5 fluorescently labelled cholesterol. Its excitation wavelength is 570 nm, while the emission occurs at 650–665 nm. It coincides with the absorption peak of chlorophyll. The image of tBLMs containing only DOPC and cholesterol is displayed in Fig. 1B. The average fluorescence intensity of the image was 96 ± 2 as measured in relative fluorescence units (RFU). Figures 1C and 1D display images of tBLMs containing DOPC, Chol, and Chl-a at molar % ratio of 5:4:1 and 6:3:1, respectively. In the case of 5:4:1 composition, the average fluorescence intensity was found to be 40 ± 3 RFU (Fig. 1C) while 6:3:1 composition exhibited a slightly higher average intensity of 49 ± 3 RFU. In both cases, an approximately two-fold decrease of the fluorescence intensity was observed. Such decreases can be explained by the absorption of Chl-a a light emitted Cy5 fluorophore. It is more likely that at higher concentrations of Cy5 in the composition of 5:4:1, self-quenching is more defined and more Cy5 dimers can be found causing random binding to the protein (Chl-a) surface, due to its hydrophobic interactions,<sup>27</sup> thus providing strong evidence of incorporation of chlorophyll into tBLMs.

**Electrochemical impedance spectroscopy-based evaluation of SAM and tBLM layers.**—The characteristic electrochemical impedance spectroscopy (EIS) spectra of the phospholipid bilayer membrane formation process are shown in Fig. 2. tBLMs were formed at different molar % ratios of various components: DOPC, Chol and Chl-a at molar % ratio of 5:4:1, respectively, DOPC, Chol and Chl-a at molar % ratio of 6:3:1, respectively, DOPC and Chol at molar % ratio of 6:4, respectively. The EIS spectra are presented in the Cole-Cole plots (Fig. 2 A graph: imaginary complex capacitance component *ImC* vs real complex capacitance component *ReC*). These coordinates are well suited to represent the capacitive type of impedance because of its semi-circular part of EIS spectra, which is proportional to the electrical capacitance of tBLMs.<sup>11</sup> Figure 2A



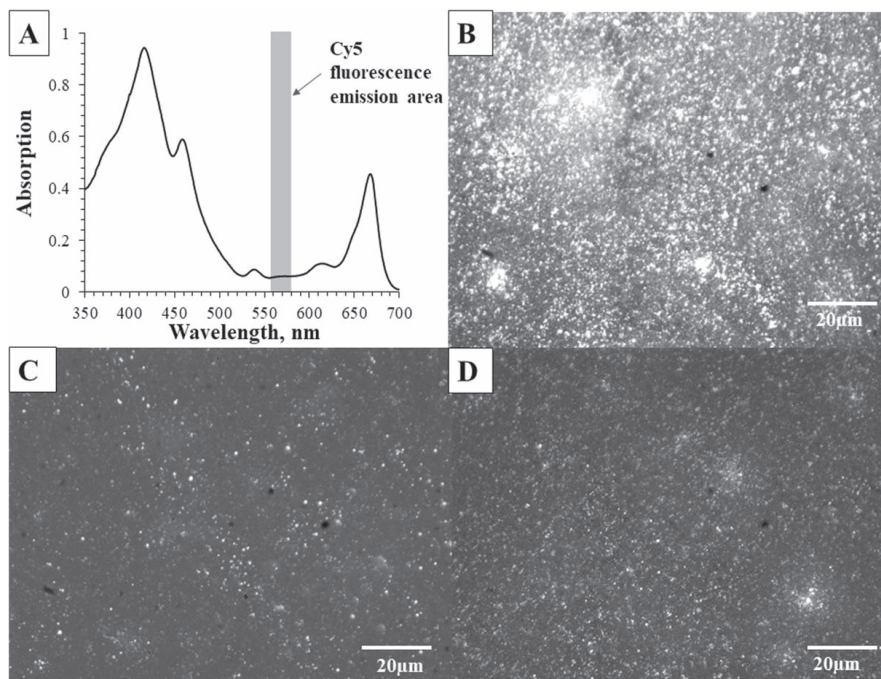


**Figure 1.** A—Optical absorption spectra of Chl-a dissolved in chloroform; Fluorescence microscopy images obtained by observing tBLM of different composition with cholesterol marked by fluorophore Cy5. B.—tBLM containing DOPC and Chol at molar % ratio of 6:4, respectively; C—tBLM containing DOPC, Chol and Chl-a at molar % ratio of 5:4:1, respectively; D—tBLM containing DOPC, Chol and Chl-a at molar % ratio of 6:3:1, respectively.

shows typical changes in EIS spectra after the formation of tBLM on an anchor SAM. Specifically, the complex capacitance semicircle decreased about 10 times, from  $8 \mu\text{F}\cdot\text{cm}^{-2}$  (before the vesicle fusion and membrane formation) to  $0.6\text{--}0.8 \mu\text{F}\cdot\text{cm}^{-2}$  (after the formation of tBLM). This effect is explained by the formation of an approximately  $3 \text{ nm}^{21}$  thick dielectric layer.

In this work, we tested two lipid compositions of tBLMs that can accommodate a certain amount of Chl-a. The EIS variation allowed verification of the integrity of tBLMs at various ratios of lipids. The base composition was DOPC and Chol at a molar % ratio of 6:4. The addition of Chl-a was performed in the following sequence: DOPC was replaced with Chl-a resulting in a molar composition of 5:4:1 (DOPC/Chol/Chl-a) and then cholesterol was replaced with DOPC resulting in a molar composition of 6:3:1, respectively.

We found that for different DOPC, Chol, and Chl-a ratios (in molar %) from 6:4 to 5:4:1 and 6:3:1, only slight variation of tBLM capacitance was observed, which in turn cannot be considered as statistically significant (Fig. 2C). However, if the defectiveness is analyzed, the inclusion of Chl-a into DOPC/Chol tBLMs was found to be an important factor in determining the defect densities in tBLMs. The algorithm described in<sup>28</sup> was used to estimate the defect densities in tBLMs with and without Chl-a. The algorithm relates defect density in membranes with the position of the phase minima in the negative of impedance phase vs frequency plots (Bode phase plot). The formula to calculate approximate densities is as follows:

$$\lg N_{def} \approx 0.93 \lg f_{min} - \lg k - 0.2 \lg r_0 - const \quad [1]$$

where  $N_{def}$  the defect density in  $\mu\text{m}^{-2}$ ,  $f_{min}$  the frequency of the negative of phase minimum, Hz,  $k = 1.6 \cdot 10^{-6} \text{ cm}^2 \cdot \text{s}^{-1}$ ,  $r_0 = 1 \text{ nm}$  and  $const = 1.24$ , one obtains the approximate values of defect

densities in tBLMs of different composition. The calculated according to Eq. 1 defect densities are  $0.87 \pm 0.09 \mu\text{m}^{-2}$  for DOPC/Chol (6:4),  $0.73 \pm 0.08 \mu\text{m}^{-2}$  for DOPC/Chol/Chl-a (6:3:1) and  $0.16 \pm 0.08 \mu\text{m}^{-2}$  for DOPC/Chol/Chl-a tBLMs.

As seen from Fig. 2D, the introduction of Chl-a into DOPC/Chol 6:4 tBLMs lowers the defectiveness, even though the decrease was found to occur in relatively narrow interval of compositions at 5:4:1 DOPC/Chol/Chl-a. In this case the defect density,  $N_{def}$  was 6-fold lower compared to basic composition DOPC/Chol (6:4) and compared to DOPC/Chol/Chl-a (6:3:1) composition as well (Fig. 2D).

Sharp decrease of  $N_{def}$  in tBLM composition DOPC/Chol/Chl-a (5:4:1) can be explained by the presence of two defect destabilizing factors: the cholesterol, which due to its geometric shape (the cone) tends to destabilize defects formed in highly curved bilayer fragments such as transient pores. The second component, Chl-a, which exhibits an effective shape of inverted cone likely destabilizes membrane defects through the concerted action of both Chol and Chl-a leading to increased stiffness of bilayer due to a formation of complementary pairs with cholesterol.<sup>29</sup>

The effect of defect density decrease is higher in DOPC/Chol/Chl-a (6:3:1) composition indicating a critical role of a total concentration of Chol and Chl-a.

Taken together we conclude that Chl-a induces a noticeable decrease of tBLM capacitance that is consistent with lower relative dielectric constant of the hydrophobic 3,7,11,15-tetramethyl-2-hexadecen molecular fragment in Chl-a molecule compared to dioleoyl fragment in DOPC. The substitution of cholesterol with Chl-a does not induce the decrease of similar magnitude, thus suggesting Chl-a and Chol exhibits similar dielectric properties. Another important change of tBLM properties is related to a

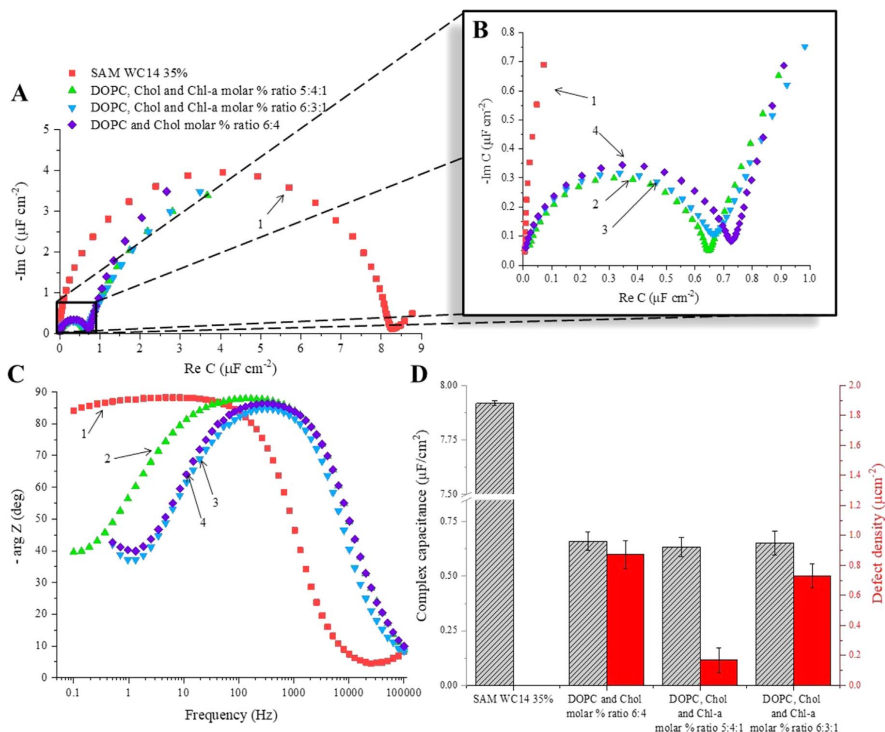


**Figure 2.** A, B—Cole-Cole plot of EIS spectra of (i) self-assembled monolayer curve 1 and (ii) tBLM structure curves 2–4 formed at different molar % ratios of various components: curve 2—DOPC, Chol and Chl-a at molar % ratio of 5:4:1, respectively, curve 3—DOPC, Chol and Chl-a at molar % ratio of 6:3:1, respectively, curve 4—DOPC and Chol at molar % ratio of 6:4, respectively. Bode coordinates: spectrum C—frequency dependence on complex phase shift (frequency was applied until phase minimum was reached), D—complex capacitance, and defect density of various components tBLM structures. Bias potential 0 V vs Ag/AgCl/NaCl<sub>sat</sub>.

significant decrease of their defectiveness, especially when the total number of Chol and Chl-a amounts to 50% of the lipid content of the membranes.

**The effect of applied electrode potential on electrochemical properties of tBLM.**—The bias potential is an important physical parameter potentially affecting both capacitance and defectiveness of tBLMs. One of the key requirements in experiments with variable bias potential is that the system should remain stable throughout the experiment. Stability is necessary because the EIS spectra recording experiments typically last between one and five minutes, depending on the frequency range chosen during which the systems under investigation must retain both functional and structural stability. In this work tBLMs of compositions involving Chl-a were tested and compared to compositions without Chl-a in the potential range between  $-0.5$  and  $0$  V vs Ag/AgCl/NaCl<sub>sat</sub>. EIS variations with potential are shown in Fig. 3.

The Cole-Cole plots (Figs. 3A–3B) indicate qualitatively similar responses to bias potential change in both chlorophyll-free and chlorophyll-loaded tBLMs. Specifically, the minimum point separating higher and lower frequency range semicircles in EIS spectra move “north and west” as the bias potential becomes less positive. Such spectral change as was shown in Kwak et al.<sup>30</sup> signals about increased defect densities, triggered by the shift of bias potential into the negative range.

Also, the comparison of the capacitive semicircular feature in Figs. 3A and 3B indicates some subtle differences. In particular, the

semicircular EIS spectra of 6:4 DOPC and Chol tBLM tend to increase with increasing negative bias potential (Fig. 3a), while, exactly this part of the spectra in Fig. 3b remained noticeably more stable for 5:3:1 DOPC, Chol, Chl-a tBLMs. These hints both at increased defectiveness as well as increased thickness of the submembrane space and the polarization of the Helmholtz layer at metal support/submembrane interface.<sup>18,30</sup> Such features are consistent with the idea of the bias potential induced membrane delamination process observed by Lipkowski et al.<sup>31</sup> Such delamination may occur due to increased hydration of the submembrane layer separating solid support and phospholipid bilayer, as well as structural rearrangement in the anchor monolayer, for example, the change of the structure from gosh to trans conformation of  $\beta$ -mercaptoethanol, which serves as a surface backfiller in anchor monolayers.<sup>32</sup> Trans conformation exhibits more loos association of the OH– group with the gold support, therefore, allowing to form more hydrogen bonds with the water molecules that are present in the reservoir and in such way increase hydration level.

The Bode EIS spectra support our conclusion about the decreased defectiveness of the Chl-a containing tBLMs. As seen from Figs. 3C and 3D in both cases the phase minima position,  $f_{min}$  which as it was shown earlier is a good indicator of a defect density in membranes,<sup>21</sup> shifts towards higher frequencies with negative polarization of tBLMs. The comparison of Figs. 3C and 3D indicates that the same extent of bias potential change (from  $0$  to  $-0.5$  V) results in different minima shifts. In the case of 6:4, DOPC/Chol tBLMs the polarization at  $-0.5$  V shifts  $f_{min}$  towards approximately

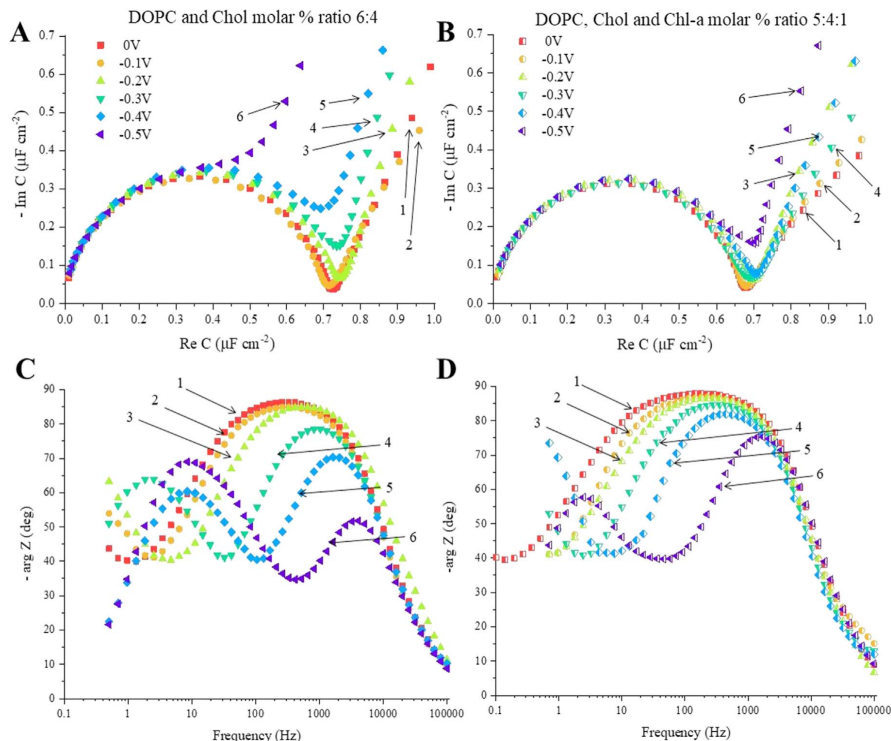


**Figure 3.** A and C—EIS spectra of the tBLM containing DOPC and Chol molar % ratio of 6:4, respectively in Cole-Cole complex capacitance and Bode coordinates at different potentials in the range from  $-0.1$  to  $-0.5$  V vs Ag/AgCl/NaCl<sub>sat</sub>. Curve 1 (squares)—at 0 V vs Ag/AgCl/NaCl<sub>sat</sub>, the curves 2–6 are marked by changing the potential from  $-0.1$  to  $-0.5$  V vs Ag/AgCl/NaCl<sub>sat</sub>, respectively. B and D—tBLM containing DOPC, Chol and Chl-a molar % ratio 5:4:1, respectively, in Cole-Cole complex and Bode coordinates at different potentials in the range from  $-0.1$  to  $-0.5$  V vs Ag/AgCl/NaCl<sub>sat</sub>. Curve 1 (squares)—at 0 V vs Ag/AgCl/NaCl<sub>sat</sub>, the curves 2–6 registered by changing the potential from  $-0.1$  to  $-0.5$  V vs Ag/AgCl/NaCl<sub>sat</sub>, respectively.

400 Hz, while the addition of Chl-a to tBLMs reduced shift to approximately 80 Hz.

These changes might suggest larger defect densities. In previous studies<sup>32,33</sup> it was demonstrated that the structural properties and the function of tethered bilayer lipid membranes (DOPC and Chol at molar % ratio 6:4) critically depend on the molecular structure of molecular anchor of the lipid bilayer. Negative electrode potential facilitates the mobility of anchor molecules on the surface by decreasing the strength of metal-adsorbate bonding. At the same time, the hydrophobic interaction between water and polymethylene chains may drive the clustering of hydrophobic molecules to minimize the energy of the system. As previously shown, clustering of molecular anchors has a detrimental effect on the integrity of tBLMs, increasing defect densities impairing the electric insulation of bilayer.<sup>33</sup>

However, the defect density is not the only factor responsible for shifts of  $f_{min}$  position, as it may be without deeper analysis inferred from Eq. 1. Equation 1 was derived for a condition of constancy of both the specific resistance  $\rho_{sub}$ , and thickness,  $d_{sub}$  of submembrane space.<sup>32</sup> If the delamination of the bilayer from the solid support occurs, then the specific resistance  $\rho_{sub}$ , decrease or thickness,  $d_{sub}$  increase, or both would trigger  $f_{min}$  shifts seen in Fig. 3. It is quite likely, that the extension of an aromatic chlorin ring structure into the submembrane space in Chl-a containing tBLMs increases hydrophobicity in this space, thus precluding the delamination and increased hydration in contrast to tBLMs void of Chl-a.

Not being able to specify the exact reason for observed shifts of  $f_{min}$  in Figs. 3D and 3C, we still may conclude that introduction of low (up to 10%, mol) amount of Chl-a into tBLMs stabilized the structural and dielectric integrity of these model bilayers, which is beneficial if light-sensitive bioelectronics devices are considered.

## Conclusions

In this study, the effect of chlorophyll a immobilization into tethered bilayer lipid membrane was evaluated. The integration of Chl-a within tBLMs was followed by fluorescence microscopy and electrochemical impedance spectroscopy. We showed that reconstitution of Chl-a is possible into tBLMs containing different amounts of cholesterol. The replacement of cholesterol with Chl-a does not cause significant changes in EIS response of tBLMs thus indicating that Chl-a and Chol possess similar dielectric properties. However, a significant decrease in membrane defectiveness was consistently observed with the introduction of Chl-a into tBLMs. We also, found that the detrimental to dielectric properties of tBLMs effects of bias negative polarization is reduced by introduction of Chl-a into tBLMs. While the exact nature of such beneficial action of Chl-a is not clear, it is rather likely that the interaction of chlorine aromatic ring with the submembrane structural elements of tBLMs may be responsible for increased hydrophobicity and consequently stability of the studied tBLM constructs. The EIS and FM data confirm the suitability of vesicular fusion and Chl-a transfer into

tBLMs thus allowing to predict the applicability of such surface constructs in the design of bioelectronic devices such as biosensors, biofuel cells, and “artificial leaves” aiming at developing light-harvesting systems.

### Acknowledgments

This research was funded by a grant (No. S-MIP-20-18) from the Lithuanian Research Council.

### ORCID

Viktorija Liustrovaitė  <https://orcid.org/0000-0002-8446-4819>  
 Aušra Valiūnienė  <https://orcid.org/0000-0003-0535-023X>  
 Gintaras Valinčius  <https://orcid.org/0000-0002-1225-0643>  
 Arūnas Ramanavičius  <https://orcid.org/0000-0002-0885-3556>

### References

1. J. Otsuki, *J. Mater. Chem. A*, **6**, 6710 (2018).
2. M. E. El-Khouly, E. El-Mohsnawy, and S. Fukuzumi, *J. Photochem. Photobiol. C Photochem. Rev.*, **31**, 36 (2017).
3. G. H. Krause and E. Weis, *Annu. Rev. Plant Physiol. Plant Mol. Biol.*, **42**, 313 (1991).
4. B. Kräutler and S. Hörtensteiner, “Chlorophyll Catabolites and the Biochemistry of Chlorophyll Breakdown.” *Chlorophylls and Bacteriochlorophylls* (Springer, New York, NY) 237 (2007).
5. M. Maccarini, E. B. Watkins, B. Stidder, J. P. Alcaraz, B. A. Cornell, and D. K. Martin, *Eur. Phys. J. E*, **39**, 123 (2016).
6. Y. xiao Shen, P. O. Saboe, I. T. Sines, M. Erbakan, and M. Kumar, *J. Memb. Sci.*, **454**, 359 (2014).
7. G. Valincius, F. Heinrich, R. Budvytyte, D. J. Vanderah, D. J. McGillivray, Y. Sokolov, J. E. Hall, and M. Lösche, *Biophys. J.*, **95**, 4845 (2008).
8. D. J. McGillivray, G. Valincius, F. Heinrich, J. W. F. Robertson, D. J. Vanderah, W. Febo-Ayala, I. Ignatjev, M. Lösche, and J. J. Kasianowicz, *Biophys. J.*, **96**, 1547 (2009).
9. T. Ragaliauskas, M. Plečkaitytė, M. Jankunec, L. Labanauskas, L. Baranauskienė, and G. Valincius, *Sci Rep.*, **9**, 11 (2019).
10. E. T. Castellana and P. S. Cremer, *Surf. Sci. Rep.*, **61**, 429 (2006).
11. D. J. McGillivray, G. Valincius, D. J. Vanderah, W. Febo-Ayala, J. T. Woodward, F. Heinrich, J. J. Kasianowicz, and M. Lösche, *Biointerphases*, **2**, 21 (2007).
12. J. A. Jackman, G. H. Zan, Z. Zhao, and N. J. Cho, *Langmuir*, **30**, 5368 (2014).
13. T. Ragaliauskas, M. Mickevicius, B. Rakovska, T. Penkauskas, D. J. Vanderah, F. Heinrich, and G. Valincius, *Biochim. Biophys. Acta - Biomembr.*, **1859**, 669 (2017).
14. H. Lang, C. Duschl, M. Grätzel, and H. Vogel, *Thin Solid Films*, **210–211**, 818 (1992).
15. A. O. Hohner, M. P. C. David, and J. O. Rädler, *Biointerphases*, **5**, 1 (2010).
16. J. Paxman, B. Hunt, D. Hallan, S. R. Zarbock, and D. J. Woodbury, *Biophys. J.*, **112**, 121 (2017).
17. A. Junghans and I. Köper, *Langmuir*, **26**, 11035 (2010).
18. G. Valincius and M. Mickevicius, “Tethered Phospholipid Bilayer Membranes. An Interpretation of the Electrochemical Impedance Response.” *Adv. Planar Lipid Bilayers Liposomes* (Science Direct) 21, 27 (2015).
19. W. Knoll et al., *Biointerphases*, **3**, 125 (2008).
20. C. G. Siontorou, G. P. Nikoleli, D. P. Nikolelis, and S. K. Karapetis, *Membranes (Basel)*, **7**, 38 (2017).
21. R. Budvytyte et al., *Langmuir*, **29**, 8645 (2013).
22. H. Alobeedallah, B. Cornell, and H. Coster, *J. Membr. Biol.*, **251**, 153 (2018).
23. A. Valiūnienė, I. Gabriunaite, M. Poderyte, and A. Ramanavicius, *Bioelectrochemistry*, **136**, 7 (2020).
24. A. R. Wellburn, *J. Plant Physiol.*, **144**, 307 (1994).
25. L. K. Tamm and H. M. McConnell, *Biophys. J.*, **47**, 105 (1985).
26. H. K. Lichtenthaler and C. Buschmann, *Handb. Food Anal. Chem.*, **21**, 153 (2005).
27. H. J. Gruber, C. D. Hahn, G. Kada, C. K. Riener, G. S. Harms, W. Ahrer, T. G. Dax, and H. G. Knaus, *Bioconjug. Chem.*, **11**, 696 (2000).
28. G. Valincius, T. Meškauskas, and F. Ivanauskas, *Langmuir*, **28**, 977 (2012).
29. S. Chakraborty et al., *Proc. Natl. Acad. Sci. U. S. A.*, **117**, 21896 (2020).
30. K. J. Kwak, G. Valincius, W. C. Liao, X. Hu, X. Wen, A. Lee, B. Yu, D. J. Vanderah, W. Lu, and L. J. Lee, *Langmuir*, **26**, 18199 (2010).
31. Z. Su, M. Shodiev, J. J. Leitch, F. Abbasi, and J. Lipkowski, *Langmuir*, **34**, 6249 (2018).
32. M. Talaikis, G. Valincius, and G. Niaura, *J. Phys. Chem. C*, **124**, 19033 (2020).
33. B. Rakovska, T. Ragaliauskas, M. Mickevicius, M. Jankunec, G. Niaura, D. J. Vanderah, and G. Valincius, *Langmuir*, **31**, 846 (2015).

### **Paper 3**

#### **Electrochemical determination of interaction between SARS-CoV-2 Spike protein and specific antibodies**

M. Drobysh, **V. Liustrovaite**, A. Baradoke, A. Rucinskiene,  
A. Ramanaviciene, V. Ratautaite, R. Viter, C.F.Chen, I. Plikusiene,  
U. Samukaite-Bubniene, R. Slibinskas, E. Ciplys, M. Simanavicius,  
A. Zvirbliene, I. Kucinskaite-Kodze, A. Ramanavicius

*International Journal of Molecular Sciences*, 2022, 23(12), 6768  
[doi.org/10.3390/ijms23126768](https://doi.org/10.3390/ijms23126768)



Communication

# Electrochemical Determination of Interaction between SARS-CoV-2 Spike Protein and Specific Antibodies

Maryia Drobysh <sup>1,2,†</sup> , Viktorija Liustrovaite <sup>1,†</sup> , Ausra Baradoke <sup>2</sup> , Alma Rucinskiene <sup>1,2</sup> , Almira Ramanaviciene <sup>1,3</sup> , Vilma Ratautaite <sup>1,2</sup> , Roman Viter <sup>4,5</sup> , Chien-Fu Chen <sup>6</sup> , Ieva Plikusiene <sup>1</sup> , Urte Samukaite-Bubniene <sup>1</sup> , Rimantas Slibinskas <sup>7</sup> , Evaldas Ciplys <sup>7</sup> , Martynas Simanavicius <sup>7</sup> , Aurelija Zvirbliene <sup>7</sup> , Indre Kucinskaite-Kodze <sup>7</sup> and Arunas Ramanavicius <sup>1,2,\*</sup>

- <sup>1</sup> NanoTechnas—Center of Nanotechnology and Materials Science, Faculty of Chemistry and Geosciences, Vilnius University, 03225 Vilnius, Lithuania; mariadrobysh@gmail.com (M.D.); viktorijaliustrovaite@gmail.com (V.L.); alma@chi.lt (A.R.); almira.ramanaviciene@chf.vu.lt (A.R.); vilma.ratautaite@ftmc.lt (V.R.); ieva.plikusiene@chgf.vu.lt (I.P.); urte.samukaite-bubniene@chf.vu.lt (U.S.-B.)
  - <sup>2</sup> State Research Institute Center for Physical and Technological Sciences, LT-10257 Vilnius, Lithuania; ausra.baradoke@ftmc.lt
  - <sup>3</sup> State Research Institute Center of Innovative Medicine, LT-08406 Vilnius, Lithuania
  - <sup>4</sup> Institute of Atomic Physics and Spectroscopy, University of Latvia, LV-1004 Riga, Latvia; roman.viter@lu.lv
  - <sup>5</sup> Center for Collective Use of Research Equipment, Sumy State University, 40000 Sumy, Ukraine
  - <sup>6</sup> Institute of Applied Mechanics, National Taiwan University, Taipei City 106, Taiwan; stevechen@iam.ntu.edu.tw
  - <sup>7</sup> Institute of Biotechnology, Life Sciences Center, Vilnius University, LT-10257 Vilnius, Lithuania; rimantas.slibinskas@bti.vu.lt (R.S.); evaldas.ciplys@bti.vu.lt (E.C.); martynas.simanavicius@bti.vu.lt (M.S.); aurelija.zvirbliene@bti.vu.lt (A.Z.); indre.kodze@bti.vu.lt (I.K.-K.)
- \* Correspondence: arunas.ramanavicius@chf.vu.lt; Tel.: +37-060-032-332  
† These authors contributed equally to this work.



**Citation:** Drobysh, M.; Liustrovaite, V.; Baradoke, A.; Rucinskiene, A.; Ramanaviciene, A.; Ratautaite, V.; Viter, R.; Chen, C.-F.; Plikusiene, I.; Samukaite-Bubniene, U.; et al. Electrochemical Determination of Interaction between SARS-CoV-2 Spike Protein and Specific Antibodies. *Int. J. Mol. Sci.* **2022**, *23*, 6768. <https://doi.org/10.3390/ijms23126768>

Academic Editor: Maciej Jarzebski

Received: 27 April 2022

Accepted: 9 June 2022

Published: 17 June 2022

**Publisher's Note:** MDPI stays neutral with regard to jurisdictional claims in published maps and institutional affiliations.



**Copyright:** © 2022 by the authors. Licensee MDPI, Basel, Switzerland. This article is an open access article distributed under the terms and conditions of the Creative Commons Attribution (CC BY) license (<https://creativecommons.org/licenses/by/4.0/>).

**Abstract:** The serologic diagnosis of coronavirus disease 2019 (COVID-19) and the evaluation of vaccination effectiveness are identified by the presence of antibodies specific to severe acute respiratory syndrome coronavirus 2 (SARS-CoV-2). In this paper, we present the electrochemical-based biosensing technique for the detection of antibodies specific to the SARS-CoV-2 proteins. Recombinant SARS-CoV-2 spike proteins (rSpike) were immobilised on the surface of a gold electrode modified by a self-assembled monolayer (SAM). This modified electrode was used as a sensitive element for the detection of polyclonal mouse antibodies against the rSpike (anti-rSpike). Electrochemical impedance spectroscopy (EIS) was used to observe the formation of immunocomplexes while cyclic voltammetry (CV) was used for additional analysis of the surface modifications. It was revealed that the impedimetric method and the elaborate experimental conditions are appropriate for the further development of electrochemical biosensors for the serological diagnosis of COVID-19 and/or the confirmation of successful vaccination against SARS-CoV-2.

**Keywords:** COVID-19; SARS-CoV-2 coronavirus; electrochemical immunosensor; electrochemical impedance spectroscopy (EIS); cyclic voltammetry (CV); self-assembled monolayer (SAM); antigen-antibody complex; spike proteins (rSpike); specific antibodies; serological diagnosis

## 1. Introduction

Biosensors have piqued the interest of many researchers in recent years, particularly in the realm of healthcare. They are distinguished by their rapid response time, ultrasensitive detection of biomolecules, and the ability to be miniaturized for a portable application while needing minimal sample processing when compared to conventional analytical procedures. The primary principle underlying biosensing devices is the conversion of biotarget detection into an analytical signal for further analysis. A variety of molecules including enzymes [1,2], proteins [3,4], antibodies [5,6], and nucleic acids [7,8] can be

used as target biomolecules, with electrochemical [5,9,10], optical [11], piezoelectric [12], surface plasmon resonance [13], and other methods being commonly used for the analytical signal registration.

Coronavirus disease 2019 (COVID-19) diagnostic techniques based on biosensors are generally classified into two categories depending on the target compounds: molecular and serological [14]. The serological type is based on the detection of the affinity interaction between antigens and specific antibodies. The determination of specific antibodies allows one to define the stage of the disease and evaluate the immune response toward severe acute respiratory syndrome coronavirus 2 (SARS-CoV-2) infection. The spike (S) protein is commonly used as the antigen in serological tests [15]. The SARS-CoV-2 structural S-protein is a transmembrane homotrimer that is required for viral adherence and penetration of a host cell [16,17].

Due to their low cost, simplicity, and availability for mass production, electrochemical biosensors are widely investigated in the biomedical applications [18–21].

However, electrochemical-based biosensors for the diagnosis of COVID-19 are still facing some challenges in order to be commercialised and further research is in high demand [22].

Recently, for electrochemical detection of SARS-CoV-2-related proteins, various electrochemical methods to evaluate analytical signals were reported [23–29]. The antibodies against SARS-CoV-2 were detected using differential pulse voltammetry [30], chronoamperometry [31], pulsed amperometric detection [4,7], square wave voltammetry [10], cyclic voltammetry (CV) [32,33], and electrochemical impedance spectroscopy (EIS) [5,9,34].

In this paper, we investigate an electrochemical-based approach for the detection of polyclonal mouse antibodies against the recombinant SARS-CoV-2 S-protein (rSpike). EIS and CV were chosen as the analytical methods for evaluating the antigen-antibody interaction taking place on the working gold electrode surface since they were both simple and straightforward. It is believed that the antigen-antibody complex produces a blocking layer in the biosensing system, which causes the electron transfer resistance to increase.

Due to the low amplitude of perturbation from steady-state, the EIS-based system allows non-destructive direct sensing of target biomolecules without employing enzyme labels [35]. CV is used for the evaluation of electrochemical properties of analyte solutions as well as the blockage of the electrode surface [36].

Because the target rSpike is detected on the working electrode's surface, it is necessary to design the surface with proper protein recognition characteristics. For this purpose, a self-assembled monolayer (SAM) is commonly used; among these, -COOH terminated SAM was shown as one of the most appropriate for specific and stable SARS-CoV-2 S-protein immobilisation [37]. 11-mercaptoundecanoic acid (11-MUA), based on alkanethiols, forms a firm and dense film and makes it possible to observe the kinetics of mediated electron passage [38]. In our previous work [29], covalent immobilization of the SARS-CoV-2 S-protein and its affinity interaction with specific antibodies against SARS-CoV-2 virus proteins in blood serum patient samples after coronavirus disease 2019 (COVID-19) (anti-rSpike) were evaluated. The anti-rSpike was quantified using CV and EIS methods, giving the limit of detection values of 2.53 nM and 1.99 nM, respectively. This research aimed to investigate the event of antigen-antibody complex formation occurring on the working electrode surface by EIS with an additional assessment of the examined surface blockage by CV. The findings of this study will serve as the foundation for the design of a biosensor powered by other electrochemical technologies.

## 2. Experimental

### 2.1. Chemicals and Other Materials

11-mercaptoundecanoic acid (11-MUA) (98%, CAS# 71310-21-9) and methanol (MeOH) ( $\geq 99\%$ , CAS# 67-56-1) were obtained from Sigma-Aldrich (Steinheim, Germany), N-hydroxysuccinimide (NHS) (98%, CAS# 6066-82-6) and N-(3-dimethylaminopropyl)-N'-ethyl-carbodiimide hydrochloride (EDC) ( $\geq 99.0\%$ , CAS# 25952-53-8) were purchased

from Alfa Aesar (Karlsruhe, Germany), alumina suspension (grain diameter 0.3  $\mu\text{m}$ ) was received from Buehler (Lake Bluff, IL, USA). Baltymas (Vilnius, Lithuania) developed the recombinant SARS-CoV-2 spike protein (rSpike). In accordance with the protocol outlined hereunder, polyclonal antibodies against rSpike (anti-rSpike) were produced. Complete Freund's adjuvant (CFA) and Incomplete Freund's adjuvant (IFA) were purchased from Thermo Fisher Scientific (USA). Ammonium sulfate (CAS# 7783-20-2, purity >99.5%) was obtained from Carl Roth (Germany).  $\text{K}_3\text{Fe}(\text{CN})_6$  ( $\geq 99.0\%$ , CAS# 13746-66-2),  $\text{K}_4\text{Fe}(\text{CN})_6$  ( $\geq 99.0\%$ , CAS# 14459-95-1),  $\text{NaBH}_4$  ( $\geq 98.0\%$ , CAS# 16940-66-2),  $\text{NaCl}$  ( $\geq 99.0\%$ , CAS# 7647-14-5),  $\text{KCl}$  ( $\geq 99.0\%$ , CAS# 7447-40-7),  $\text{NaH}_2\text{PO}_4$  ( $\geq 99.0\%$ , CAS# 7558-80-7),  $\text{K}_2\text{HPO}_4$  ( $\geq 98.0\%$ , CAS# 7758-11-4). Deionized water was used to prepare all aqueous solutions. All reagents were of analytical-reagent grade and were used as received from the producers unless otherwise noted.

All electrochemical measurements were carried out in 0.1 M phosphate buffer saline solution (PBS), pH 7.4 with the presence of 2 mM  $\text{K}_4\text{Fe}(\text{CN})_6/\text{K}_3\text{Fe}(\text{CN})_6$  ( $[\text{Fe}(\text{CN})_6]^{3-/4-}$ ). PBS was prepared by dissolving 0.137 M NaCl, 0.01 M  $\text{NaH}_2\text{PO}_4$ , 0.0027 M KCl, and 0.0018 M of  $\text{KH}_2\text{PO}_4$  in deionized water.

## 2.2. Protocol of Protein Purification

Hamster CHO cells obtained from Thermo Fisher Scientific (Waltham, MA, USA) (cat. no. A29127) were used for the secretion of rSpike protein. The gene, which encodes the SARS-CoV-2 Spike ectodomain including amino acids (aa) 1-1208, (UniProtKB sequence accession number: P0DTC2 (SPIKE\_SARS2)) was obtained from General Biosystems (USA). This gene was integrated into the expression vector pCAGGS (Creative Biogene, cat. no. VET1375) through the restriction sites NotI and XhoI, which are added at 5' and 3' ends of this gene, correspondingly. These expression constructs contain these parts: (i) full-length rSpike ectodomain (aa 1–1208) without transmembrane and cytoplasmic aa, (ii) furin cleavage site 'RRAR' mutated to "GSAS", (iii) C-terminal GSN4 trimerisation motif fused to protein sequence, (iv) thrombin cleavage site, and (v) Strep-tag II and His6-tag. Two mutations (K986P and V987P) were introduced into the rSpike sequence to stabilize the trimer in the pre-fusion conformation [39]. The rSpike protein was generated in CHO cells (cat. no. A29133) grown in ExpiCHO Expression System purchased from Thermo Fisher Scientific's (Vilnius, Lithuania). The Max Titer protocol was developed by Thermo Fisher Scientific (Vilnius, Lithuania) and was applied for protein transfection and expression procedures. Transfection lasted nine days, then cells were harvested from cultivation media and under refrigeration were centrifuged at 5000 g for 30 min. Then, supernatant was filtered using a filter that contained cavities of 0.22- $\mu\text{m}$  diameter. The supernatant was condensed and then dissolved in 50 mM PBS, pH 8.0, containing 10 mM imidazole and 300 mM NaCl through tangential ultrafiltration by TFF cassette, which was supported with 100 kDa cutoff membranes (cat. no. VF20P) from Sartorius Stedim Biotech (Göttingen, Germany). The protein solution was deposited onto Ni-NTA resin from Super Flow (Qiagen, Germantown, MD, USA). Next, non-specifically bound proteins were removed using the chromatography column using a 'Lysis' buffer with 75 mM imidazole. More tightly bound proteins were eluted by a 'gradient solution' containing 75–250 mM imidazole. The fractions containing purified rSpike glycoprotein were pooled and dialyzed against 10 mM PBS, pH 7.4, containing 3 mM of KCl and 140 mM of NaCl. Then, the solution was diluted down to 1.0 mg/mL, filtered, and separated into small samples that were stored in a frozen state before use in the experiments. SDS-PAGE electrophoresis was applied for the determination of rSpike protein purity, which was ~90%. Anti-rSpike protein was produced by BALB/c mice. Female mice were subcutaneously immunised four times (at intervals of 28 days) with 50  $\mu\text{g}$  of rSpike protein. The antigen was emulsified by complete Freund's adjuvant during the first injection and/or incomplete adjuvant during the second injection, respectively. The third and fourth immunisations were performed via antigen diluted in PBS. The mouse was sacrificed by applying cervical dislocation four days after the final immunisation. Then, whole blood samples were collected from the chest cavity.



The collected blood was centrifuged at  $300 \times g$  for 10 min, and the resulting supernatant was diluted by saturated ammonium sulfate solution at a ratio of 1:1. This solution containing polyclonal antibodies was incubated at  $4\text{ }^{\circ}\text{C}$  for 16 h. The fraction of immunoglobulin G was separated by centrifugation at  $12,000 \times g$  for 10 min. The collected precipitate was re-dissolved in 10 mM PBS, pH 7.4, and the solution was then mixed with a similar volume of saturated ammonium sulfate solution. In this solution, total protein concentration was determined spectrophotometrically. Mice used for the immunisation experiments were obtained from the breeding colony of Life Sciences Center of Vilnius University (Vilnius, Lithuania). Animal maintenance and experimental protocols were performed in accordance with FELASA guidelines and Lithuanian and European legislation. Permission No. G2-117 for the generation of polyclonal and monoclonal antibodies was issued by the State Food and Veterinary Service, Vilnius, Lithuania.

### 2.3. Preparation of Gold Electrode Surface

The geometrical area of the chemically pure (99.9%) square gold (Au) electrode was  $1\text{ cm}^2$ . The surface of the Au electrode was mechanically polished using an alumina suspension. After polishing, the Au surface was cleaned in an ultrasonic bath (EMAG Emmi-40 HC) with water for 10 min. Subsequently, the electrode was kept in 0.5 M  $\text{NaBH}_4$  solution for 10 min ( $\text{H}_2\text{O}/\text{MeOH}$ ,  $v/v$ , 1:1) [40]. The working Au electrode was reused after each experiment, going through the same steps described in this manuscript.

### 2.4. The Activation of 11-MUA Based SAM and Covalent Immobilisation of the rSpike Protein

To achieve this goal, the Au electrode was incubated in 1 mM 11-MUA solution in MeOH at  $24\text{ }^{\circ}\text{C}$  for 18 h (Figure 1, step 1). Following incubation, the electrode was rinsed with MeOH to remove the remaining 11-MUA and dried with  $\text{N}_2$ . SAM, which was formed on the Au electrode surface (Au/SAM) and activated by the EDC-NHS mixture. The reaction of 11-MUA carboxyl groups with a mixture of 0.04 M EDC and 0.01 M NHS in water resulted in functionally active NHS-esters (Figure 1, step 2). The activation procedure was performed in the dark for 20 min. After activating the carboxyl functional groups, the electrode was incubated in 1 mL of 50 g/mL rSpike in PBS solution for 45 min at room temperature. rSpike was covalently attached through primary amine functional groups (Figure 1, step 3). The remains of the active esters were deactivated with 1 mM EA solution, pH 8.5 for 10 min (Figure 1, step 4). Then, 1 mL of 50  $\mu\text{g}/\text{mL}$  anti-rSpike solution was added and the affinity interaction of antibodies specific to rSpike was performed at room temperature for 1 h. After the incubation, the formed Au/SAM/rSpike/anti-rSpike structure was washed with PBS solution and utilised for further electrochemical measurements. The formed Au/SAM, Au/SAM/EDC-NHS, and Au/SAM/rSpike electrodes were used in all subsequent electrochemical experiments. Au/SAM/rSpike electrodes were used for the detection of antibodies specific towards rSpike.

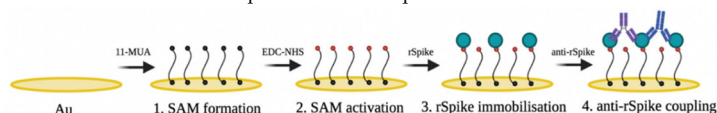


**Figure 1.** Schematic representation of experimental stages: (1) 11-MUA SAM layer formation on the Au electrode (Au/SAM); (2) SAM activation by EDC-NHS mixture; (3) rSpike immobilisation and formation of Au/SAM/rSpike sensing structure; (4) affinity interaction of anti-rSpike with immobilised rSpike.

### 2.5. Electrochemical Measurements

The bare Au electrode, Au/SAM, Au/SAM/EDC-NHS, and Au/SAM/rSpike electrodes were electrochemically characterised using the potentiostat/galvanostat AUTOLAB TYPE III (Metrohm, Netherlands) operated by FRA2-EIS ECO-Chemie software (Utrecht, Netherlands). Experiments before and after incubation stages were performed in PBS, pH 7.4, with 2 mM of  $[\text{Fe}(\text{CN})_6]^{3-/4-}$  to eliminate the impact of the electrolyte composition.

The experiments were carried out in the three-electrode electrochemical cell, which included the Au-based electrode (Au, Au/SAM, Au/SAM/EDC-NHS, and Au/SAM/rSpike) working electrode, platinum (Pt) counter electrode, and as a reference electrode, Ag/AgCl in 3M KCl (Ag/AgCl<sub>(3M KCl)</sub>) microelectrode (IS-AG/AGCL.AQ.RE) (ItalSens, Netherland) was used. CV and EIS techniques were used to characterise the electrochemical properties of bare Au, Au/SAM, Au/SAM/EDC-NHS, and Au/SAM/rSpike electrodes at diverse steps of modification. At a scan rate of 50 mV/s, CV measurements were carried out in the potential window of 0 to +0.4 V vs Ag/AgCl<sub>(3M KCl)</sub>. A perturbation amplitude of 10 mV was used to register the EIS in the frequency range between 0.1 Hz and 100 kHz.

### 3. Results and Discussion

#### Electrochemical Characterisation

CV and EIS measurements were used to characterise the Au electrode before and after 11-MUA SAM formation. Using a  $[\text{Fe}(\text{CN})_6]^{3-/4-}$  couple as a redox probe and analysing the oxidation/reduction peaks of the resulting cyclic voltammogram, the influence of each stage of the surface modification of the working electrode on conductivity was investigated. Figure 2 shows the cyclic voltammogram of the Au electrode before and after the formation of the 11-MUA monolayer. On the electrode surface, long-chain thiols ( $n = 10$ ) create a very stable and well-organised monolayer, which thus acts as an ionic insulator on a gold electrode. SAM has a lower defect rate and a higher fraction coverage rate [41]. As a result, additional 11-MUA molecules can obstruct the electron transfer pathway, considerably suppressing the current response (Figure 2b).

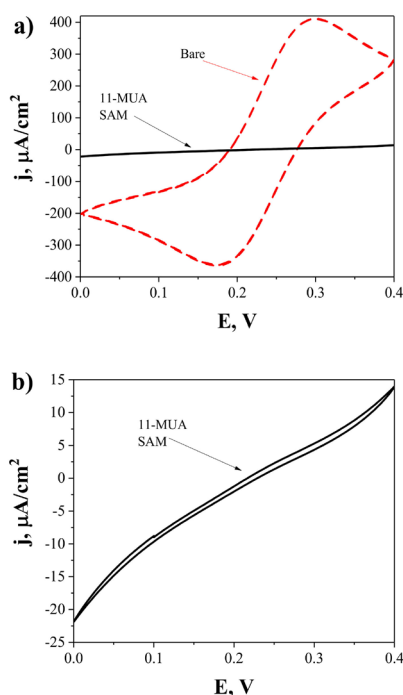


**Figure 2.** (a) Cyclic voltammograms of the bare Au electrode (dashed line) and Au/SAM electrode after the formation of 11-MUA SAM (solid line). (b) Scaled cyclic voltammogram of the Au/SAM electrode. Measurements were performed in PBS while adding 2 mM of  $[\text{Fe}(\text{CN})_6]^{3-/4-}$ . Potential scans range from 0 to +0.4 V vs Ag/AgCl<sub>(3M KCl)</sub> at 50 mV/s.

EIS was utilized to monitor impedimetric qualities based on the applied equivalent circuit, allowing chemical transformations and processes occurring on the conducting electrode surface to be perceived [42]. Figure 3a shows the impedance responses of the  $[\text{Fe}(\text{CN})_6]^{3-/4-}$  based redox probe in PBS on the Au electrode after the formation of the Au/SAM structure based on 11-MUA (Figure 3a-1), activation of SAM with EDC and NHS (Figure 3a-2), covalent immobilization of rSpike (Figure 3a-3), and affinity interaction with anti-rSpike (Figure 3a-4) in the frequency range from 0.1 Hz to 100 kHz.

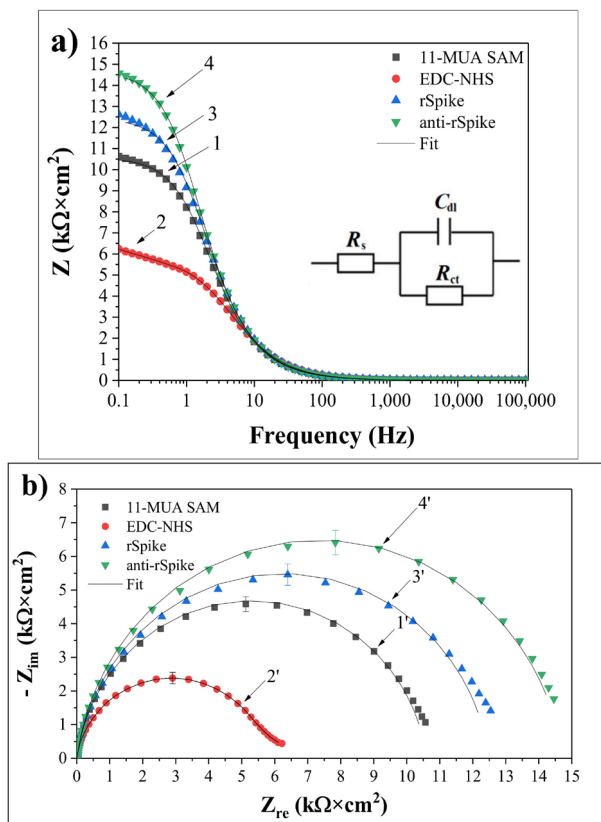


**Figure 3.** (a) Bode plots of differently modified Au electrode: (1) Au/SAM, (2) Au/SAM/EDC-NHS, (3) Au/SAM/rSpike, (4) Au/SAM/rSpike/anti-rSpike. The Randles equivalent circuit was applied for the analysis of EIS data, where  $R_s$  represents the dynamic solution resistance,  $C_{dl}$  is the double layer capacitance measured between the Au electrode and the electrolyte solution, and  $R_{ct}$  is the charge transfer resistance of the immobilised recognition layer. (b) Nyquist plots of differently modified electrodes: Au electrodes: (1') Au/SAM, (2') Au/SAM/EDC-NHS, (3') Au/SAM/rSpike, (4') Au/SAM/rSpike/anti-rSpike. EIS measurements were performed in the PBS, pH 7.4, in presence of 2 mM of  $[\text{Fe}(\text{CN})_6]^{3-/4-}$  and 0.1 M KCl at 0.2 V vs  $\text{Ag}/\text{AgCl}_{(3\text{M KCl})}$ .

No significant difference between spectra 1, 2, 3, and 4 is observed (Figure 3a) at frequencies greater than 100 Hz, suggesting that the formation of SAM based on 11-MUA, the immobilisation of rSpike, and the formation of an immunocomplex between rSpike and anti-rSpike (rSpike/anti-rSpike) on the electrode surface did not have any significant impact on the  $R_s$  value. On the contrary,  $C_{dl}$  and  $R_{ct}$  are bound to the dielectric and insulating

properties of the electrode/electrolyte interface; therefore, they are significantly affected by the changes of the Au-electrode surface. When the frequency of the EIS perturbation decreases, an imaginary component  $Z_{im} = 1/jC_{dl}$  becomes important and significantly contributes to the  $C_{dl}$  value of the equivalent circuit [43]. The double-layer capacitance ( $C_{dl}$ ) has greater impedance at lower frequencies; as a result of this effect, the current mainly passes through  $R_{ct}$  and  $R_s$ . The impedance value of  $10.6 \text{ k}\Omega\cdot\text{cm}^2$  at a given frequency (0.1 Hz) increased with the formation of the thiol monolayer (Figure 3a-1), the immobilisation of the rSpike ( $12.6 \text{ k}\Omega\cdot\text{cm}^2$ ) (Figure 3a-3), and the formation of the rSpike/anti-rSpike immunocomplex ( $14.5 \text{ k}\Omega\cdot\text{cm}^2$ ) (Figure 3a-4) on the surface of the Au electrode, compared to NHS and EDS, the activated Au/SAM/EDC-NHS electrode ( $6.2 \text{ k}\Omega\cdot\text{cm}^2$ ) (Figure 3a-2). It was observed that the  $R_{ct}$  of the Au electrode after the formation of the SAM layer increased and had very low electron transfer efficiency. However, the  $R_{ct}$  of the NHS and EDS activated Au/SAM/EDC-NHS electrode considerably decreased compared to that determined before the activation process. The EDC-NHS response involving the development of an intermediate electrochemically active ester was the result of the terminal-COOH interaction with EDS and NHS. The rise in  $R_{ct}$  following rSpike and anti-rSpike binding is due to the fact that most proteins have poor electrical conductivity at low frequencies, preventing charge transfer at the electrode-solution interface. These EIS-based data fit well with data presented in our previous investigations, which were based on the evaluation of interactions between SARS-CoV-2 proteins and specific antibodies against these proteins by Total Internal Reflection Ellipsometry, which clearly illustrate that at the interfacial electrode-solution boundary, a significant increase in protein layer thickness and changes of dielectric properties have been observed [6,44].

Despite the fact that it provides the same information as Bode graphs, Nyquist coordinates are ideally suited to depict the electrochemical impedance, especially in the 'semi-circular area' of EIS spectra (Figure 3b). As seen in the Figure 3b, the diameter of the semi-circle rises following the formation of SAM based on 11-MUA  $4.58 \pm 0.22 \text{ k}\Omega\text{cm}^2$  (Figure 3b-1'), activation of 11-MUA carboxyl groups by EDC and NHS  $2.38 \pm 0.17 \text{ k}\Omega\text{cm}^2$  (Figure 3b-2'). Progressive immobilisation of rSpike protein  $5.45 \pm 0.32 \text{ k}\Omega\text{cm}^2$  (Figure 3b-3') and affinity with anti-rSpike  $6.41 \pm 0.36 \text{ k}\Omega\text{cm}^2$  (Figure 3b-4') cause the interphase between the Au electrode and solution to become more insulating, obstructing the passage of charged  $[\text{Fe}(\text{CN})_6]^{3-/4-}$  ions and electron exchange between them. As a result, the electron transfer resistance  $R_{ct}$  increased as the Au surface was changed step by step, as shown in Figure 3a. The  $R_{ct}$  component of different modified electrodes tends to exhibit visible fluctuations, which provide the high sensitivity necessary for the EIS-based approach to detect antigen-antibody complex formation.

#### 4. Conclusions

The covalent immobilisation of rSpike and affinity interaction with anti-rSpike were investigated in this work. Cyclic voltammograms revealed that 11-MUA SAM molecules bound and blocked the surface of the Au electrode required for further electron transfer. EIS showed that the charge transfer resistance of the Au/SAM electrode after activation with EDC and NHS decreased when compared with the electrode before activation. The EIS spectra in Nyquist coordinates show distinct changes in each phase of Au electrode modification: the semicircle grows after rSpike immobilisation and the antigen-antibody complex forms after anti-rSpike interaction. This enables the use of impedimetric techniques to detect the antigen-antibody complexes and, as a result, the creation of an immunosensor for the serologic diagnosis of COVID-19 and/or the assessment of vaccination success against the SARS-CoV-2 virus.

**Author Contributions:** Conceptualization, A.R. (Almira Ramanaviciene) and A.R. (Arunas Ramanavicius); Data curation, V.L., A.B., R.V. and U.S.-B.; Formal analysis, M.D., V.L., A.B., A.R. (Alma Rucinskiene), A.R. (Almira Ramanaviciene) and A.R. (Arunas Ramanavicius); Investigation, M.D., V.L. and A.R. (Alma Rucinskiene); Methodology, M.D., C.-F.C., I.P., R.S., M.S. and I.K.-K.; Project administration, V.L., A.B. and A.R. (Alma Rucinskiene); Resources, R.S., E.C., A.Z. and A.R. (Arunas Ramanavicius);

Supervision, A.R. (Arunas Ramanavicius); Visualization, M.D.; Writing—original draft, V.L.; Writing—review & editing, M.D., A.B., A.R. (Almira Ramanaviciene), V.R., R.V., C.-F.C., I.P., U.S.-B. and A.R. (Arunas Ramanavicius). All authors have read and agreed to the published version of the manuscript.

**Funding:** This research was financially supported by Lithuania-Latvian-China (Taiwan) project and it has received funding according to agreement No S-LLT-21-3 with the Research Council of Lithuania (LMTLT).

**Institutional Review Board Statement:** Not applicable.

**Informed Consent Statement:** Not applicable.

**Data Availability Statement:** Not applicable.

**Acknowledgments:** This research was conducted under the Lithuania-Latvian-China (Taiwan) project and it has received funding according to agreement No S-LLT-21-3 with the Research Council of Lithuania (LMTLT). Schematic illustrations were created with BioRender (<https://biorender.com>).

**Conflicts of Interest:** The authors declare no conflict of interest.

## References

- German, N.; Ramanavicius, A.; Voronovic, J.; Ramanaviciene, A. Glucose biosensor based on glucose oxidase and gold nanoparticles of different sizes covered by polypyrrole layer. *Colloids Surf. A Physicochem. Eng. Asp.* **2012**, *413*, 224–230. [[CrossRef](#)]
- Morkvenaite-Vilkonciene, I.; Ramanaviciene, A.; Kisieliute, A.; Bucinskas, V.; Ramanavicius, A. Scanning electrochemical microscopy in the development of enzymatic sensors and immunosensors. *Biosens. Bioelectron.* **2019**, *141*, 111411. [[CrossRef](#)] [[PubMed](#)]
- Baradoke, A.; Hein, R.; Li, X.; Davis, J.J. Reagentless Redox Capacitive Assaying of C-Reactive Protein at a Polyaniline Interface. *Anal. Chem.* **2020**, *92*, 3508–3511. [[CrossRef](#)] [[PubMed](#)]
- Ramanavicius, A.; Oztekin, Y.; Ramanaviciene, A. Electrochemical formation of polypyrrole-based layer for immunosensor design. *Sens. Actuators B Chem.* **2014**, *197*, 237–243. [[CrossRef](#)]
- Ramanavicius, A.; Finkelsteinas, A.; Cesiulis, H.; Ramanaviciene, A. Electrochemical impedance spectroscopy of polypyrrole based electrochemical immunosensor. *Bioelectrochemistry* **2010**, *79*, 11–16. [[CrossRef](#)]
- Plikusiene, I.; Maciulis, V.; Ramanaviciene, A.; Balevicius, Z.; Buzavaite-Verteliene, E.; Ciplys, E.; Slibinskas, R.; Simanavicius, M.; Zvirbliene, A.; Ramanavicius, A. Evaluation of kinetics and thermodynamics of interaction between immobilized SARS-CoV-2 nucleoprotein and specific antibodies by total internal reflection ellipsometry. *J. Colloid Interface Sci.* **2021**, *594*, 195–203. [[CrossRef](#)]
- Ramanaviciene, A.; Ramanavicius, A. Pulsed amperometric detection of DNA with an ssDNA/polypyrrole-modified electrode. *Anal. Bioanal. Chem.* **2004**, *379*, 287–293. [[CrossRef](#)]
- Dronina, J.; Samukaite-Bubniene, U.; Ramanavicius, A. Towards application of CRISPR-Cas12a in the design of modern viral DNA detection tools (Review). *J. Nanobiotechnol.* **2022**, *20*, 41. [[CrossRef](#)]
- Ratautaite, V.; Janssens, S.D.; Haenen, K.; Nesládek, M.; Ramanaviciene, A.; Baleviciute, I.; Ramanavicius, A. Molecularly imprinted polypyrrole based impedimetric sensor for theophylline determination. *Electrochim. Acta* **2014**, *130*, 361–367. [[CrossRef](#)]
- Oztekin, Y.; Yazicigil, Z.; Ramanaviciene, A.; Ramanavicius, A. Square wave voltammetry based on determination of copper (II) ions by poly(luteolin)- and poly(kaempferol)-modified electrodes. *Talanta* **2011**, *85*, 1020–1027. [[CrossRef](#)]
- Plikusiene, I.; Balevicius, Z.; Ramanaviciene, A.; Talbot, J.; Mickiene, G.; Balevicius, S.; Stirke, A.; Tereshchenko, A.; Tamosaitis, L.; Zvirblis, G.; et al. Evaluation of affinity sensor response kinetics towards dimeric ligands linked with spacers of different rigidity: Immobilized recombinant granulocyte colony-stimulating factor based synthetic receptor binding with genetically engineered dimeric analyte d. *Biosens. Bioelectron.* **2020**, *156*, 112112. [[CrossRef](#)]
- Zuo, B.; Li, S.; Guo, Z.; Zhang, J.; Chen, C. Piezoelectric immunosensor for SARS-associated coronavirus in sputum. *Anal. Chem.* **2004**, *76*, 3536–3540. [[CrossRef](#)]
- Balciunas, D.; Plausinaitis, D.; Ratautaite, V.; Ramanaviciene, A.; Ramanavicius, A. Towards electrochemical surface plasmon resonance sensor based on the molecularly imprinted polypyrrole for glyphosate sensing. *Talanta* **2022**, *241*, 123252. [[CrossRef](#)]
- Drobysh, M.; Ramanaviciene, A.; Viter, R.; Chen, C.F.; Samukaite-Bubniene, U.; Ratautaite, V.; Ramanavicius, A. Biosensors for the Determination of SARS-CoV-2 Virus and Diagnosis of COVID-19 Infection. *Int. J. Mol. Sci.* **2022**, *23*, 666. [[CrossRef](#)]
- Pecora, N.D.; Zand, M.S. Measuring the Serologic Response to Severe Acute Respiratory Syndrome Coronavirus 2: Methods and Meaning. *Clin. Lab. Med.* **2020**, *40*, 603–614. [[CrossRef](#)]
- Song, H.C.; Seo, M.-Y.; Stadler, K.; Yoo, B.J.; Choo, Q.-L.; Coates, S.R.; Uematsu, Y.; Harada, T.; Greer, C.E.; Polo, J.M.; et al. Synthesis and Characterization of a Native, Oligomeric Form of Recombinant Severe Acute Respiratory Syndrome Coronavirus Spike Glycoprotein. *J. Virol.* **2004**, *78*, 10328–10335. [[CrossRef](#)]
- Kirchdoerfer, R.N.; Cottrell, C.A.; Wang, N.; Pallesen, J.; Yassine, H.M.; Turner, H.L.; Corbett, K.S.; Graham, B.S.; McLellan, J.S.; Ward, A.B. Pre-fusion structure of a human coronavirus spike protein. *Nature* **2016**, *531*, 118–121. [[CrossRef](#)]

18. Cui, F.; Zhou, H.S. Diagnostic methods and potential portable biosensors for coronavirus disease 2019. *Biosens. Bioelectron.* **2020**, *165*, 112349. [[CrossRef](#)]
19. Ramanaviciene, A.; Ramanavicius, A. Molecularly imprinted polypyrrole-based synthetic receptor for direct detection of bovine leukemia virus glycoproteins. *Biosens. Bioelectron.* **2004**, *20*, 1076–1082. [[CrossRef](#)]
20. Mayall, R.M.; Smith, C.A.; Hyla, A.S.; Lee, D.S.; Crudden, C.M.; Birss, V.I. Ultrasensitive and Label-Free Detection of the Measles Virus Using an N-Heterocyclic Carbene-Based Electrochemical Biosensor. *ACS Sens.* **2020**, *5*, 2747–2752. [[CrossRef](#)]
21. Kaya, S.I.; Karadurmus, L.; Ozcelikay, G.; Bakirhan, N.K.; Ozkan, S.A. Electrochemical Virus Detections with Nanobiosensors. In *Nanosensors for Smart Cities*; Elsevier: Amsterdam, The Netherlands, 2020; pp. 303–326. ISBN 9780128198704.
22. Drobys, M.; Ramanaviciene, A.; Viter, R.; Ramanavicius, A. Affinity sensors for the diagnosis of covid-19. *Micromachines* **2021**, *12*, 390. [[CrossRef](#)]
23. Yakob, A.; Pimpitak, U.; Rengpipat, S.; Hirankarn, N.; Chailapakul, O.; Chaiyo, S. Paper-based electrochemical biosensor for diagnosing COVID-19: Detection of SARS-CoV-2 antibodies and antigen. *Biosens. Bioelectron.* **2021**, *176*, 112912. [[CrossRef](#)]
24. Ali, M.A.; Hu, C.; Jahan, S.; Yuan, B.; Saleh, M.S.; Ju, E.; Gao, S.J.; Panat, R. Sensing of COVID-19 Antibodies in Seconds via Aerosol Jet Nanoprinted Reduced-Graphene-Oxide-Coated 3D Electrodes. *Adv. Mater.* **2021**, *33*, 2006647. [[CrossRef](#)]
25. Raziq, A.; Kidakova, A.; Boroznjak, R.; Reut, J.; Öpik, A.; Syritski, V. Development of a portable MIP-based electrochemical sensor for detection of SARS-CoV-2 antigen. *Biosens. Bioelectron.* **2021**, *178*, 113029. [[CrossRef](#)]
26. Ayankojo, A.G.; Boroznjak, R.; Reut, J.; Öpik, A.; Syritski, V. Molecularly imprinted polymer based electrochemical sensor for quantitative detection of SARS-CoV-2 spike protein. *Sens. Actuators B Chem.* **2022**, *353*, 131160. [[CrossRef](#)]
27. Ratautaite, V.; Boguzaitė, R.; Brazys, E.; Ramanaviciene, A.; Ciplys, E.; Juozapaitis, M.; Slibinskas, R.; Bechelany, M.; Ramanavicius, A. Molecularly Imprinted Polypyrrole based Sensor for the Detection of SARS-CoV-2 Spike Glycoprotein. *Electrochim. Acta* **2021**, *403*, 139581. [[CrossRef](#)]
28. Eissa, S.; Zourob, M. Development of a low-cost cotton-tipped electrochemical immunosensor for the detection of SARS-CoV-2. *Anal. Chem.* **2021**, *93*, 1826–1833. [[CrossRef](#)]
29. Liustrovaite, V.; Drobys, M.; Rucinskiene, A.; Baradoke, A.; Ramanaviciene, A.; Plikusiene, I.; Samukaite-Bubniene, U.; Viter, R.; Chen, C.-F.; Ramanavicius, A. Towards an Electrochemical Immunosensor for the Detection of Antibodies against SARS-CoV-2 Spike Protein. *J. Electrochem. Soc.* **2022**, *169*, 037523. [[CrossRef](#)]
30. Deshmukh, M.A.; Patil, H.K.; Bodkhe, G.A.; Yasuzawa, M.; Koinkar, P.; Ramanaviciene, A.; Shirsat, M.D.; Ramanavicius, A. EDTA-modified PANI/SWNTs nanocomposite for differential pulse voltammetry based determination of Cu(II) ions. *Sens. Actuators B Chem.* **2018**, *260*, 331–338. [[CrossRef](#)]
31. German, N.; Ramanavicius, A.; Ramanaviciene, A. Electrochemical deposition of gold nanoparticles on graphite rod for glucose biosensing. *Sens. Actuators B Chem.* **2014**, *203*, 25–34. [[CrossRef](#)]
32. Ramanavicius, S.; Ramanavicius, A. Conducting polymers in the design of biosensors and biofuel cells. *Polymers* **2021**, *13*, 49. [[CrossRef](#)] [[PubMed](#)]
33. Samukaite-Bubniene, U.; Valiūnienė, A.; Bucinskas, V.; Genys, P.; Ratautaite, V.; Ramanaviciene, A.; Aksun, E.; Tereshchenko, A.; Zeybek, B.; Ramanavicius, A. Towards supercapacitors: Cyclic voltammetry and fast Fourier transform electrochemical impedance spectroscopy based evaluation of polypyrrole electrochemically deposited on the pencil graphite electrode. *Colloids Surf. A Physicochem. Eng. Asp.* **2021**, *610*, 125750. [[CrossRef](#)]
34. Liustrovaitė, V.; Valiūnienė, A.; Valinčius, G.; Ramanavičius, A. Electrochemical Impedance Spectroscopy Based Evaluation of Chlorophyll a Reconstitution within Tethered Bilayer Lipid Membrane. *J. Electrochem. Soc.* **2021**, *168*, 066506. [[CrossRef](#)]
35. Bahadir, E.B.; Sezgingtürk, M.K. A review on impedimetric biosensors. *Artif. Cells Nanomed. Biotechnol.* **2016**, *44*, 248–262. [[CrossRef](#)]
36. Ganesh, V.; Pal, S.K.; Kumar, S.; Lakshminarayanan, V. Self-assembled monolayers (SAMs) of alkoxyphenyl thiols on gold—A study of electron transfer reaction using cyclic voltammetry and electrochemical impedance spectroscopy. *J. Colloid Interface Sci.* **2006**, *296*, 195–203. [[CrossRef](#)]
37. Pandey, L.M. Design of engineered surfaces for prospective detection of SARS-CoV-2 using quartz crystal microbalance based techniques. *Expert Rev. Proteom.* **2020**, *17*, 425–432. [[CrossRef](#)]
38. Cecchet, F.; Marcaccio, M.; Margotti, M.; Paolucci, F.; Rapino, S.; Rudolf, P. Redox mediation at 11-mercaptoundecanoic acid self-assembled monolayers on gold. *J. Phys. Chem. B* **2006**, *110*, 2241–2248. [[CrossRef](#)]
39. Loganathan, S.K.; Schleicher, K.; Malik, A.; Quevedo, R.; Langille, E.; Teng, K.; Oh, R.H.; Rathod, B.; Tsai, R.; Samavarchi-Tehrani, P.; et al. Rare driver mutations in head and neck squamous cell carcinomas converge on NOTCH signaling. *Science* **2020**, *367*, 1264–1269. [[CrossRef](#)]
40. Yuan, M.; Zhan, S.; Zhou, X.; Liu, Y.; Feng, L.; Lin, Y.; Zhang, Z.; Hu, J. A method for removing self-assembled monolayers on gold. *Langmuir* **2008**, *24*, 8707–8710. [[CrossRef](#)]
41. Ahmad, A.; Pui Kee, L.; Sheryna Jusoh, N. A comparative study of thiols self-assembled monolayers on gold electrode. *Middle-East J. Sci. Res.* **2016**, *24*, 2152–2158. [[CrossRef](#)]
42. Patolsky, F.; Filanovsky, B.; Katz, E.; Willner, I. Photoswitchable antigen-antibody interactions studied by impedance spectroscopy. *J. Phys. Chem. B* **1998**, *102*, 10359–10367. [[CrossRef](#)]

43. Kim, T.; Kang, J.; Lee, J.H.; Yoon, J. Influence of attached bacteria and biofilm on double-layer capacitance during biofilm monitoring by electrochemical impedance spectroscopy. *Water Res.* **2011**, *45*, 4615–4622. [[CrossRef](#)]
44. Plikusiene, I.; Maciulis, V.; Juciute, S.; Maciuleviciene, R.; Balevicius, S.; Ramanavicius, A.; Ramanaviciene, A. Investigation and Comparison of Specific Antibodies Affinity Interaction with SARS-CoV-2 Wild-Type, B.1.1.7, and B.1.351 Spike Protein by Total Internal Reflection Ellipsometry. *Biosensors* **2022**, *12*, 351. [[CrossRef](#)]

## **Paper 4**

### **Towards an electrochemical immunosensor for the detection of antibodies against SARS-CoV-2 Spike protein**


**V. Liustrovaite**, M. Drobysh, A. Rucinskiene, A. Baradoke,  
A. Ramanaviciene, I. Plikusiene, U. Samukaite-Bubniene, R. Viter,  
C.F. Chen, A Ramanavicius

*Journal of The Electrochemical Society*, 2022, 169(3), 037523  
[doi.org/10.1149/1945-7111/ac5d91](https://doi.org/10.1149/1945-7111/ac5d91)





## Towards an Electrochemical Immunosensor for the Detection of Antibodies against SARS-CoV-2 Spike Protein

Viktorija Liustrovaite,<sup>1,=</sup> Maryia Drobysh,<sup>1,2,=</sup> Alma Rucinskiene,<sup>1,2</sup> Austra Baradoke,<sup>2</sup> Almira Ramanaviciene,<sup>1</sup> Ieva Plikusiene,<sup>1,2</sup> Urte Samukaite-Bubniene,<sup>1</sup> Roman Viter,<sup>3</sup> Chien-Fu Chen,<sup>2</sup> and Arunas Ramanavicius<sup>1,2,\*</sup> 

<sup>1</sup>NanoTechnas—Center of Nanotechnology and Materials Science, Faculty of Chemistry and Geosciences, Vilnius University, Naugarduko str. 24, 03225 Vilnius, Lithuania

<sup>2</sup>State Research Institute Center for Physical and Technological Sciences, Sauletekio ave. 3, Vilnius, Lithuania

<sup>3</sup>Institute of Atomic Physics and Spectroscopy, University of Latvia, Jelgavas Street 3, Riga, LV-1004, Latvia

<sup>4</sup>Institute of Applied Mechanics, National Taiwan University, 1, Sec. 4, Roosevelt Rd., Da'an Dist., Taipei City 106, Taiwan

Herein we report the electrochemical system for the detection of specific antibodies against severe acute respiratory syndrome coronavirus 2 (SARS-CoV-2) proteins in blood serum patient samples after coronavirus disease 2019 (COVID-19). For this purpose, the recombinant SARS-CoV-2 spike protein (SCoV2-rS) was covalently immobilised on the surface of the gold electrode pre-modified with mixed self-assembled monolayer (SAMmix) consisting of 11-mercaptopentadecanoic acid and 6-mercapto-1-hexanol. The affinity interaction of SCoV2-rS with specific antibodies against this protein (anti-rS) was detected using two electrochemical methods: cyclic voltammetry (CV) and electrochemical impedance spectroscopy (EIS). The anti-rS was detected with a detection limit of 2.53 nM and 1.99 nM using CV and EIS methods, respectively. The developed electrochemical immunosensor is suitable for the confirmation of COVID-19 infection or immune response in humans after vaccination.

© 2022 The Author(s). Published on behalf of The Electrochemical Society by IOP Publishing Limited. This is an open access article distributed under the terms of the Creative Commons Attribution 4.0 License (CC BY, <http://creativecommons.org/licenses/by/4.0/>), which permits unrestricted reuse of the work in any medium, provided the original work is properly cited. [DOI: 10.1149/1945-7111/ac5d91]



Manuscript submitted January 21, 2022; revised manuscript received February 16, 2022. Published March 25, 2022. *This paper is part of the JES Focus Issue on Biosensors and Nanoscale Measurements: In Honor of Nonjiang Tao and Stuart Lindsay.*

The severe acute respiratory syndrome coronavirus 2 (SARS-CoV-2) induced coronavirus disease 2019 (COVID-19), is still continuously spreading worldwide. Therefore, the need for rapid and accurate detection methods, including immunosensors, remains relevant to maintain the spread of this infectious disease.<sup>1</sup> The application of immunosensors<sup>2,3</sup> and other affinity sensors<sup>1,4</sup> are of great interest in various clinical diagnostics due to their sensitivity, selectivity, and reliable cost. Antigens, which are recognised by the immune system, and antibodies expressed as the immune system response to the antigen can act as a biorecognition layer or target element in immunosensors suitable for the diagnosis of viral infections.<sup>5,6</sup>

SARS-CoV-2 contains a linear, single-stranded, positive-sense RNA with a length of approximately 29903 nucleotides<sup>7</sup>. The virus has crown-like spikes on the outer surface with a diameter of nearly 130 nm.<sup>8</sup> The genome size is 29.8–29.9 kb and its one-third consists of genes that encode structural proteins including spike (S), envelope (E), membrane (M), and nucleocapsid (N) proteins.<sup>9</sup> The E-protein is the smallest one, and it plays a role in the formation and maturation of the virus. The M-protein can connect with other structural proteins, and its function is to keep the shape of the virus shell.<sup>10</sup> The N-protein is the main structural element of the virion and it participates in viral replication and immune adjustment, it is an inherent attribute in the life cycle of the virus.<sup>11</sup> The S-protein is a homotrimer protein that protrudes from the lipid bilayer surrounding SARS-CoV-2<sup>12,13</sup> and consists of two subunits, namely, S1 and S2. S1 is responsible for binding to the host cell receptor, while S2 mediates viral fusion with the host cell membrane. The S-protein binds to the host cell via the angiotensin-converting enzyme 2 receptors.<sup>14–18</sup>

The S-protein can serve as a biorecognition element of the immunosensor. SARS-CoV-2 infection induces an immune response and the release of specific antibodies,<sup>19</sup> which might be used as a target for immunosensors. Currently, serologic tests for the presence of antibodies against SARS-CoV-2 virus proteins are mainly based on common approaches such as the enzyme-linked immunosorbent assay (ELISA)<sup>20</sup> and the lateral flow immunoassay (LFIA).<sup>21</sup>

Nonetheless, some widely used immunoanalytical methods possess several disadvantages, namely, they are time-consuming (ELISA) and/or not fully automated (LFIA). Therefore, it is necessary to develop rapid, non-laborious, and precise tests with the potential for quantitative analysis. Wherein various physical methods can be used for the determination of analytical signals generated by affinity sensors, including surface plasmon resonance,<sup>22</sup> scanning electrochemical microscopy,<sup>23</sup> electrochemical methods,<sup>24</sup> quartz crystal microbalance,<sup>25</sup> total internal reflection ellipsometry,<sup>26</sup> etc. Among all these analytical methods, electrochemical immunosensors are characterised by some advantages such as low cost, robustness, and simplicity of detection procedure and data interpretation.<sup>24,27</sup>

Only several recent studies are dedicated to the electrochemical technique-based diagnosis of COVID-19.<sup>28–30</sup> Specifically, electrochemical impedance spectroscopy (EIS)<sup>5,31,32</sup> and cyclic voltammetry (CV)<sup>33</sup> are appropriate analytical methods. The EIS is a reliable method for examining the interfacial features of events occurring on transformed surfaces. The small amplitude perturbation from the steady-state is one of the benefits of EIS, which makes it a non-destructive technique.<sup>34</sup> CV is used to acquire data concerning the redox potential and other electrochemical characteristics of analyte solutions. However, CV is also commonly used for observing the processes occurring on the surface of the sensing electrode itself.<sup>35</sup> In particular, this method is a helpful tool to assess blockage of the coated electrode surface.<sup>36</sup>

Immobilisation of the biorecognition element on the conductive surfaces of the electrode is a challenging task during the development of electrochemical affinity sensors.<sup>37</sup> One of the approaches employed for the immobilisation of biomolecules on the surface is the self-assembled monolayer (SAM) technique. Alkanethiol-based monolayers are considered as well-organised and stable interfaces with the necessary thickness and function.<sup>38</sup> Therefore, the application of SAM mixture (SAMmix) consisting of 6-mercapto-1-hexanol (6-MCOH) and 11-mercaptopentadecanoic acid (11-MUA) was used to offer an accurate approach for surface modification with desired functional groups and covalent biomolecules immobilisation. Additionally, it minimizes the adsorption of nonspecific proteins on the surface of the working electrode.<sup>39</sup>

The objectives of this study were (i) to explore the possibility to develop an immunosensor for the serologic diagnosis of COVID-19

<sup>=</sup>These authors contributed equally to this work.

\*E-mail: [Arunas.Ramanavicius@chf.vu.lt](mailto:Arunas.Ramanavicius@chf.vu.lt)

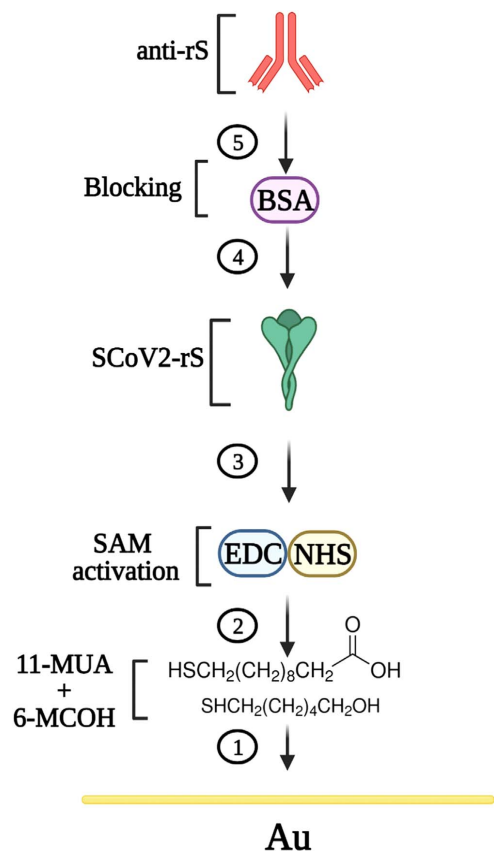


**Figure 1.** Schematic representation of experimental stages: (1) SAMmix layer formation on Au electrode (Au/SAMmix); (2) SAMmix activation by EDC-NHS mixture (Au/SAMmix/EDC-NHS); (3) SCoV2-rS immobilisation and formation of Au/SAMmix/SCoV2-rS sensing structure; (4) BSA binding of remaining activated carboxyl groups; (5) affinity interaction of anti-rS with immobilised SCoV2-rS (Au/SAMmix/SCoV2-rS/anti-rS).

based on the formation of the recombinant SARS-CoV-2 S-protein (SCoV2-rS) and specific antibodies (anti-rS) immune complex using electrochemical methods; (ii) to improve the measurement conditions and technique for effective immobilisation of SCoV2-rS on the surface of the working electrode for further use in research on other electrochemical methods.

### Experimental

**Chemicals and other materials.**—Microscope slides were obtained from Thermo Fisher Scientific (USA), 2-propanol (2-PROH), ( $\geq 99.5\%$ , CAS# 67–63–0),  $\text{H}_2\text{SO}_4$  (96%, CAS# 7664–93–9), 11-mercaptoundecanoic acid (11-MUA) (98%, CAS# 71310–21–9), 6-mercapto-1-hexanol (6-MCOH) (97%, CAS# 1633–78–9), ethanol (EtOH) (99.9%, CAS# 64–17–5), N-(3-dimethylaminopropyl)-N'-ethyl-carbodiimide hydrochloride (EDC) ( $\geq 99.0\%$ , CAS# 25952–53–8), bovine serum albumin (BSA) ( $>98.0\%$ , CAS# 90604–29–8), and phosphate buffered saline (PBS) tablets (pH 7.4) were obtained from Sigma–Aldrich (Steinheim, Germany), N-hydroxysuccinimide (NHS) (98.0%, CAS# 6066–82–6) was purchased from Alfa Aesar

(Karlsruhe, Germany). SARS-CoV-2 recombinant spike protein (SCoV2-rS) was developed by Baltymas (Vilnius, Lithuania).  $\text{K}_3\text{Fe}(\text{CN})_6$  ( $\geq 99.0\%$ , CAS# 13746–66–2),  $\text{K}_4\text{Fe}(\text{CN})_6$  ( $\geq 99.0\%$ , CAS# 14459–95–1) were obtained from Sigma–Aldrich (Steinheim, Germany). All aqueous solutions were prepared using deionised water. All chemicals were of analytical-reagent grade and were used as received from the producers unless otherwise stated. All electrochemical measurements were performed in 0.1 M PBS solution adding 2 mM  $\text{K}_3\text{Fe}(\text{CN})_6/\text{K}_4\text{Fe}(\text{CN})_6$  solution ( $[\text{Fe}(\text{CN})_6]^{3-/4-}$ ).

**Preparation and/or purification of the SCoV2-rS protein.**—The SCoV2-rS protein was generated as a secreted trimeric protein in mammalian Chinese hamster ovary (CHO) cells. To match a native conformation locked in a prefusion state, the gene encoding the SARS-CoV-2 Spike (SCoV2-S) ectodomain including amino acids (aa) 1–1208, (UniProtKB sequence accession number: P0DTC2 (SPIKE\_SARS2)) was chemically synthesised at General Biosystems (USA). The synthesised gene then was cloned into the mammalian expression vector pCAGGS (Creative Biogene, cat. no. VET1375) via NotI and XhoI restriction sites that were introduced on 5' and 3' gene ends, respectively. The whole expression construct included: full-length SCoV2-S ectodomain (aa 1–1208) w/o transmembrane and cytoplasmic aa, furin cleavage site "RRAR" mutated to "GSAS," C-terminal GSN4 trimerization motif fused to protein sequence, then follows the thrombin cleavage site, Strep-tag II and His6-tag. Two mutations (K986P and V987P) were introduced into the SCoV2-S sequence as well, to stabilize the trimer in the pre-fusion conformation.<sup>18</sup> SCoV2-rS was produced in CHO cells using ExpiCHO Expression System (Thermo Fisher Scientific, cat. no. A29133). For expression, the transfection procedures and expression conditions were applied as described in the Max Titer Protocol provided by Thermo Fisher Scientific. Following the 9th-day post-transfection, the cultivation media was harvested and centrifuged at  $5000\times g$  for 30 min in a refrigerated centrifuge. Then the supernatant was filtered through a  $0.22\ \mu\text{m}$  filter. After microfiltration, proteins were concentrated and transferred to the binding buffer (50 mM  $\text{NaH}_2\text{PO}_4$ , pH 8.0, 300 mM NaCl, 10 mM imidazole) through tangential ultrafiltration using tangential flow filtration cassette with 100 kDa cut-off membranes (SartoriusStedim Biotech, cat. no. VF20P). The protein solution was loaded onto nickel-nitrilotriacetic acid modified SuperFlow (Qiagen, USA) resin. Non-specifically bound proteins were removed by washing the column with a Lysis buffer containing 75 mM imidazole. Tightly bound proteins were eluted using 75 mM–250 mM imidazole gradient. Fractions containing purified SCoV2-S were pooled and dialysed against PBS (10 mM  $\text{Na}_2\text{HPO}_4$ , 1.8 mM  $\text{KH}_2\text{PO}_4$ , 137 mM NaCl, 2.7 mM KCl, pH 7.4), adjusted to  $1.0\ \text{mg ml}^{-1}$  concentration, filter-sterilised, aliquoted, and frozen for storage. The purity of produced SCoV2-rS was  $\sim 90\%$ , as determined by sodium dodecylsulphate polyacrylamide gel electrophoresis.

**Serum sample collection.**—A volunteer vaccinated with a single dose of the Vaxzevria (previously known as the AstraZeneca) vaccine and who after two weeks had COVID-19 was selected for the analysis. Blood was collected one month after the volunteer was positive, which was determined by reverse transcription-polymerase chain reaction for the SARS-CoV-2 virus and COVID-19 was diagnosed. Whole blood was collected in a vacuette tube containing 3.5 ml of CAT serum sep clot activator (Greiner Bio-One GmbH, Austria) in the laboratory of Tavo Klinika, LtD. (Vilnius, Lithuania). The serum was obtained after centrifugation at  $5000\times g$  for 15 min. The stock amount of binding antibodies vs SCoV2-S in the serum sample (4666 BAU  $\text{ml}^{-1}$ ) was defined using chemiluminescent microparticle immunoassay. The antibody concentration in the sample was converted from BAU  $\text{ml}^{-1}$  units to nM concentration by using the ratio as 1 BAU  $\text{ml}^{-1}$ : 20 ng  $\text{ml}^{-1}$  (the molecular weight of immunoglobulin G  $\sim 150\ \text{kDa}$ ).<sup>40–42</sup> Serum sample was stored at  $-20\ ^\circ\text{C}$  until analysis. The sample was collected in accordance with

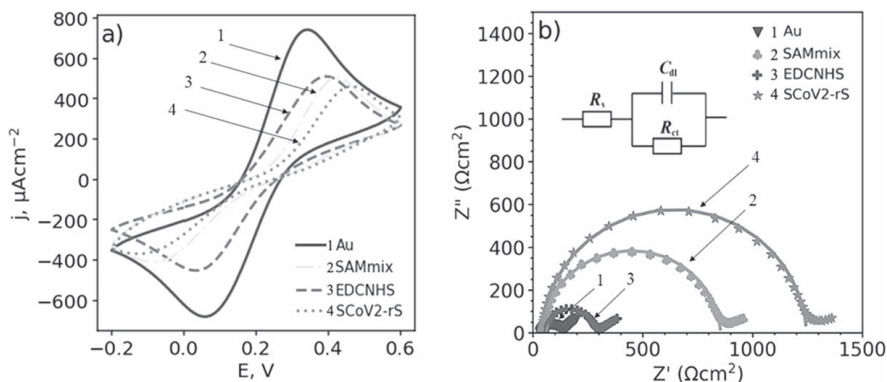


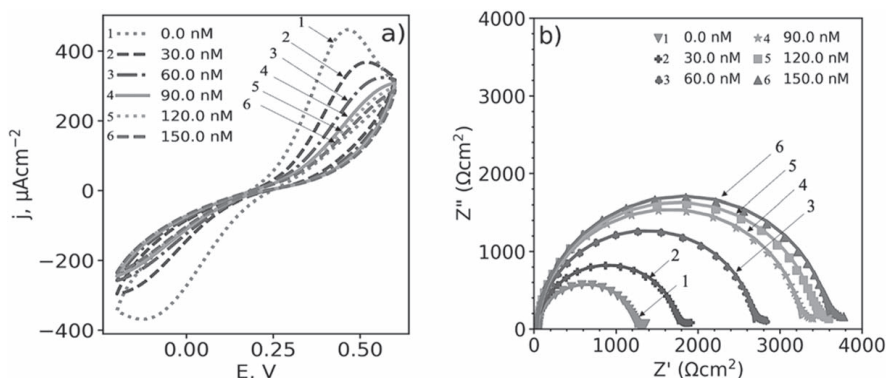
**Figure 2.** (a) Cyclic voltammograms of the Au electrode (1), Au/SAMmix electrode after formation of SAMmix (2), Au/SAMmix/EDC-NHS electrode after activation of SAMmix (3), and Au/SAMmix/SCoV2-rS electrode after immobilisation of SCoV2-rS (4). Potential scans range from  $-0.2$  to  $+0.6$  V vs Ag/AgCl(KCl<sub>sat</sub>) at  $50$  mV s<sup>-1</sup>. (b) Nyquist plots of the Au electrode (1), Au/SAMmix electrode after SAMmix formation (2), Au/SAMmix/EDC-NHS electrode after activation of SAMmix (3), and Au/SAMmix/SCoV2-rS electrode after immobilisation of SCoV2-rS (4), measured from  $100$  kHz to  $0.1$  Hz, at  $10$  mV amplitude and applied potential  $0.2$  V vs Ag/AgCl(KCl<sub>sat</sub>). Randles equivalent circuit, which was applied for the evaluation of electrochemical impedance spectroscopy data, where  $R_s$  represents the dynamic solution resistance,  $C_{dl}$ —represents the double layer capacitance measured between the Au electrode and the electrolyte solution, and  $R_{ct}$ —represents the charge transfer resistance of the immobilised recognition layer. CV and EIS measurements were performed in PBS pH 7.4 while adding  $2$  mM of  $[\text{Fe}(\text{CN})_6]^{3-/4-}$ , signal normalised to the area of the electrode,  $A = 0.179$  cm<sup>2</sup>.

the Lithuania ethics law. This study does not need the approval of the ethics committee (confirmed by the Vilnius Regional Biomedical Research Ethics Committee).

**Preparation of the gold electrode surface.**—Microscope slides  $20 \times 30$  mm were cleaned with 2-PrOH, ultrasonicated (ultrasonic bath Emmi-40 HC, EMAG, Germany) firstly with 2-PrOH, then with water and immersed in H<sub>2</sub>SO<sub>4</sub> for 30 min. The slides were dried with a stream of nitrogen (N<sub>2</sub>) gas (99.99%) and placed in a vacuum magnetron, VST services Ltd. (Israel), chamber. Film depositions begin only when a vacuum of  $7 \times 10^{-8}$  Torr and deeper was reached. The plates were first coated with a thin (10 nm) layer of titanium (Ti) to improve the adhesion of gold (Au) to the surface of the glass and then coated with a (100 nm) layer of Au.

**The activation of the SAMmix layer and covalent immobilisation of the SCoV2-rS protein.**—The glass slides coated with 100 nm

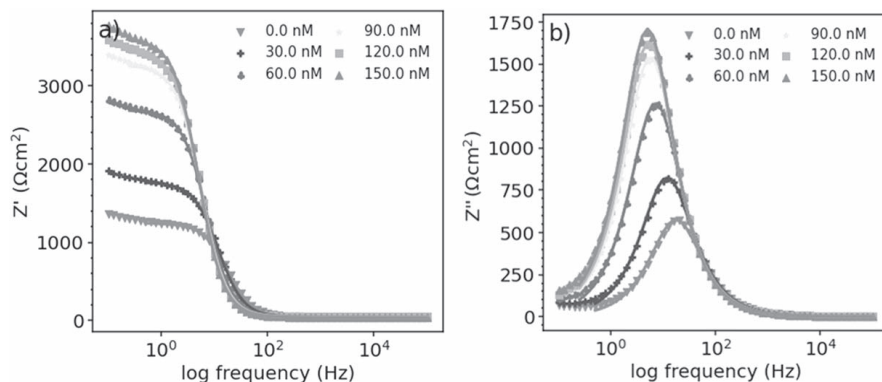
thick Au film were incubated at  $24$  °C for 4 h in 1 mM 6-MCOH and 11-MUA ethanolic solution, containing the materials in a molar ratio of 9:1, respectively, to form SAMmix (Fig. 1, step 1). After incubation, the electrode was rinsed with EtOH to remove the excess of SAMmix and then dried with N<sub>2</sub> flow. SAMmix formed on the Au electrode (Au/SAMmix) was activated by EDC-NHS mixture. During this procedure, functionally active NHS-esters were obtained by the reaction of 11-MUA carboxyl groups with a mixture of 0.004 M EDC and 0.001 M NHS in PBS (Fig. 1, step 2). The activation step was carried out for 15 min in the dark (Au/SAMmix/EDC-NHS). After activation of carboxyl functional groups, the electrode was exposed to  $70$  μg ml<sup>-1</sup> SCoV2-rS in PBS at room temperature for 30 min (Au/SAMmix/EDC-NHS/SCoV2-rS). Protein SCoV2-rS was coupled covalently via primary amine functional groups (Fig. 1, step 3). The remaining reactive esters were deactivated with 0.5% BSA, 30 min (Fig. 1, step 4). Then  $100$  μl of anti-rS in PBS was added in a concentration range



**Figure 3.** (a) Cyclic voltammograms and (b) Nyquist plots of the modified Au/SAMmix/SCoV2-rS electrode (1) after affinity interaction with anti-rS of different concentrations (0–150 nM) (respectively, from 2 to 6). Potential scans range from  $-0.2$  to  $+0.6$  V vs Ag/AgCl(KCl<sub>sat</sub>) at  $50$  mV s<sup>-1</sup>. EIS measurements were performed from  $100$  kHz to  $0.1$  Hz, at  $10$  mV amplitude and applied potential  $0.2$  V vs Ag/AgCl(KCl<sub>sat</sub>). CV and EIS measurements were performed in PBS pH 7.4, while adding  $2$  mM of  $[\text{Fe}(\text{CN})_6]^{3-/4-}$ , signal normalised to the area of the electrode,  $A = 0.179$  cm<sup>2</sup>.

**Table I.** Analytical parameters were obtained from CV and EIS. Error bars are calculated as a percentage standard error.

| Concentration anti-rS, nM | CV               |                                  | EIS             |                                  |                                 |
|---------------------------|------------------|----------------------------------|-----------------|----------------------------------|---------------------------------|
|                           | $E_{pa}$ , mV    | $j_{pa}$ , $\mu\text{A cm}^{-2}$ | $E_{pc}$ , mV   | $j_{pc}$ , $\mu\text{A cm}^{-2}$ | $R_{ct}$ , $\Omega\text{-cm}^2$ |
| 0                         | 462.6 $\pm$ 1.7  | 460.8 $\pm$ 1.6                  | 127.0 $\pm$ 0.1 | 367.9 $\pm$ 1.3                  | 1300 $\pm$ 105                  |
| 30                        | 506.6 $\pm$ 19.0 | 382.1 $\pm$ 19.3                 | 195.3 $\pm$ 6.9 | 299.8 $\pm$ 5.3                  | 1840 $\pm$ 165                  |
| 60                        | 561.5 $\pm$ 10.4 | 329.1 $\pm$ 6.6                  | 200.3 $\pm$ 0.1 | 258.7 $\pm$ 1.6                  | 2800 $\pm$ 212                  |
| 90                        | 599.4 $\pm$ 1.7  | 310.9 $\pm$ 3.5                  | 200.3 $\pm$ 0.1 | 245.7 $\pm$ 1.1                  | 3360 $\pm$ 286                  |
| 120                       | 601.1 $\pm$ 0.1  | 296.9 $\pm$ 0.6                  | 200.3 $\pm$ 0.1 | 234.6 $\pm$ 0.6                  | 3570 $\pm$ 259                  |
| 150                       | 601.1 $\pm$ 0.1  | 287.0 $\pm$ 0.8                  | 200.3 $\pm$ 0.1 | 235.7 $\pm$ 0.8                  | 3750 $\pm$ 319                  |

**Figure 4.** Bode of  $Z'$  (a) and  $Z''$  (b) vs frequency plots, measured in a range of 0.1 Hz to 100 kHz at a perturbation amplitude of 10 mV and potential 0.2 V vs Ag/AgCl(KCl<sub>sat</sub>). EIS measurements were performed in PBS, pH 7.4, while adding 2 mM of  $[\text{Fe}(\text{CN})_6]^{3-/4-}$ , signal normalised to the area of the electrode,  $A = 0.179 \text{ cm}^2$ .

from 30 to 150 nM and the affinity interaction of specific antibodies with SCov2-rS immobilised on the electrode was carried out at room temperature for 45 min (Au/SAMmix/EDC-NHS/SCov2-rS/anti-rS). After each step of incubation, the structure was rinsed with PBS solution and used further for the electrochemical measurements. The formed Au/SAMmix, Au/SAMmix/EDC-NHS, and Au/SAMmix/SCov2-rS electrodes were used in all further electrochemical experiments. The Au/SAMmix/SCov2-rS electrodes were used for the determination of specific antibodies against the SCov2-rS protein (Fig. 1, step 5).

**Electrochemical measurements.**—Electrochemical characterisation of the Au, Au/SAMmix, Au/SAMmix/EDC-NHS, and Au/SAMmix/SCov2-rS electrodes was performed using the potentiostat  $\mu\text{AUTOLAB TYPE III}$  (Metrohm, Netherland) controlled by FRA2-EIS software from ECO-Chemie (Utrecht, Netherlands). All experiments were performed in the three-electrode electrochemical cell. To bring the experiment closer to in vivo conditions, all experiments prior and after all incubation steps were performed in PBS, pH 7.4 with the addition of 2 mM of  $[\text{Fe}(\text{CN})_6]^{3-/4-}$  as a redox probe. The three-electrode system consisted of the Au-based electrode (Au, Au/SAMmix, Au/SAMmix/EDC-NHS, and Au/SAMmix/SCov2-rS) as the working electrode, platinum (Pt) wire as the counter electrode, and Ag/AgCl in saturated KCl (Ag/AgCl<sub>(KCl<sub>sat</sub>)</sub>) microelectrode (IS-AG/AGCLAQRE) as the reference electrode (ItalSens, The Netherlands). Electrochemical characterisation of bare Au, Au/SAMmix, Au/SAMmix/EDC-NHS, and Au/SAMmix/SCov2-rS electrodes at different modification steps were performed using CV and EIS methods. CV measurements were performed in the potential range from  $-0.2$  to  $+0.6$  V vs Ag/AgCl<sub>(KCl<sub>sat</sub>)</sub>, at a scan rate of  $50 \text{ mV s}^{-1}$ . For the registration of EIS spectra in the

frequency range between 0.1 Hz and 100 kHz, a perturbation amplitude of 10 mV and potential 0.2 V vs Ag/AgCl(KCl<sub>sat</sub>) were applied.

## Results and Discussion

**Electrochemical characterisation of a modified Au surface.**—Characterisation of Au, Au/SAMmix, Au/SAMmix/EDC-NHS, and Au/SAMmix/SCov2-rS electrode has been carried out by CV and EIS methods. The impact of each step of the modification of the working electrode surface on the conductivity has been analysed using a  $[\text{Fe}(\text{CN})_6]^{3-/4-}$  couple as a redox probe while analysing the oxidation/reduction peaks of the corresponding cyclic voltammogram (Fig. 2a). The 11-MUA forms a stable and compact film, in which the content of pinholes and structural defects in the monolayer is reduced, thereby enabling to observe mediated electron passage kinetics<sup>43</sup>. However, in order to facilitate access of the redox mediator to the electrode surface SAMmix consisting of 6-MCOH and 11-MUA was used<sup>44</sup>. The Au electrode shows a typical cyclic voltammogram (Fig. 2a-1), reversible reaction, characteristic of the redox couple, producing a current density peak of  $712.4 \pm 5.9 \mu\text{A cm}^{-2}$ . After modification of the Au electrode with the SAMmix (Fig. 2a-2), the peak decreased to  $504.6 \pm 19.3 \mu\text{A cm}^{-2}$ . The EDC-NHS activation (Fig. 2a-3) of the terminal  $-\text{COOH}$  groups slightly increased the current density to  $513.1 \pm 6.6 \mu\text{A cm}^{-2}$ , nevertheless, the immobilisation of SCov2-rS (Fig. 2a-4) decreased it to  $459.6 \pm 9.3 \mu\text{A cm}^{-2}$ .

EIS has been used as an efficient method for the monitoring of impedimetric characteristics and theoretical analysis of impedance properties based on the applied equivalent circuit, enabling the perception of chemical transformation and processes associated with the surface of the conductive electrode<sup>45</sup>. Figure 2b) shows the

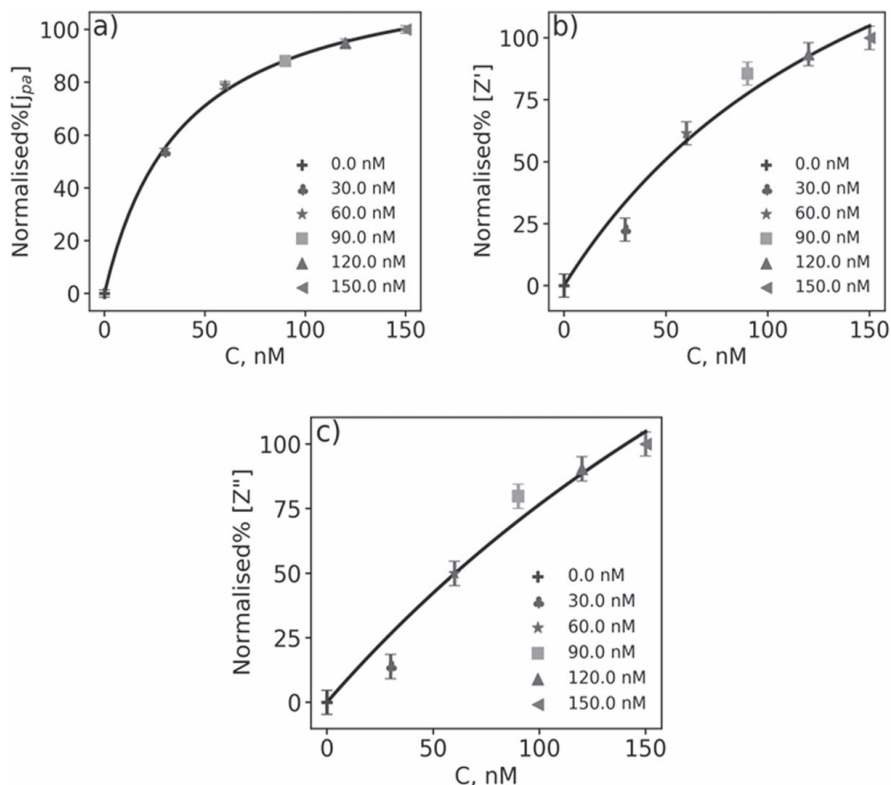


**Figure 5.** Calibration curves obtained from CV (a) and EIS spectra fitted  $R_{ct}$  (b) and EIS maximum of  $Z''$  (c). Error bars are calculated as a percentage standard error. Signal normalised to the electrode area,  $A = 0.179 \text{ cm}^2$ .

impedance responses of the  $[\text{Fe}(\text{CN})_6]^{3-/4-}$  based redox probe in PBS on the Au electrode (Fig. 2b-1), after the formation of the Au/SAMmix structure based on 11-MUA and 6-MCOH, molar ratio 1:9, respectively (Fig. 2b-2), activation of SAMmix with EDC and NHS (Fig. 2b-3), the covalent immobilisation of SCoV2-rS (Fig. 2b-4) in the frequency range from 100 kHz to 0.1 Hz.

The Nyquist coordinates are well suited to represent the electrochemical impedance, especially at the “semi-circular part” of the EIS spectra represented in Fig. 2b). It is shown that after the formation of SAMmix on the Au electrode, the diameter of the semicircle increases. Therefore, when the Au surface was modified, the electron transfer resistance  $R_{ct}$  has also increased from  $141 \pm 34 \Omega\text{-cm}^2$  to  $884 \pm 163 \Omega\text{-cm}^2$ . Then, the activation of the terminal-COOH groups with EDC-NHS forming an intermediate active ester was performed and is led to the decrease of Au/SAMmix/EDC-NHS semicircle as well  $R_{ct}$  value down to  $300 \pm 46 \Omega\text{-cm}^2$ .<sup>46</sup> This intermediate product displayed tremendous electrochemical behaviour, the increase in  $R_{ct}$  up to  $1280 \pm 237 \Omega\text{-cm}^2$  after SCoV2-rS binding can be explained by the fact that, at low frequencies, most biological molecules, including proteins, have poor electrical conductivity and therefore impede charge transfer at the interphase between the electrode and solution. For differently modified electrodes, the  $R_{ct}$  component tends to have apparent variations, which are providing the high sensitivity required for the detection of antigen-antibody complex formation by the EIS-based technique. Subsequently, after the immobilisation of SCoV2-rS, the deactivation of the remaining

activated carboxyl groups and the blocking of the free surface to avoid non-specific binding are performed using 0.5% solution of BSA.

**Electrochemical sensing of anti-rS.**—The affinity interaction of anti-rS with immobilised SCoV2-rS was performed by sequentially incubating the working surface with 30 nM of anti-rS PBS solution (the concentration range 30 nM–150 nM). CV and EIS measurements are performed in the presence of 2 mM  $[\text{Fe}(\text{CN})_6]^{3-/4-}$  in a PBS solution applying the parameters described in the previous part. The concentration range is obtained by successive dilutions of the stock solution.

The affinity interaction of anti-rS with immobilised SCoV2-rS and immune complex formation (Fig. 3a-1) continues to insulate the working electrode surface thereby reducing  $[\text{Fe}(\text{CN})_6]^{3-/4-}$  flow towards the electrode. Thus, the decrease in redox current is the stepwise flattening of the cyclic voltammograms with increasing anti-rS concentration (Fig. 3a). Partial coating of the electrode surface with the increasing concentrations of anti-rS causes a corresponding decrease of anodic ( $j_{pa}$ ) and cathodic ( $j_{pc}$ ) current density at the range of potentials from 460 mV to 600 mV and from  $-130 \text{ mV}$  to  $-200 \text{ mV}$ , respectively (Table I). The potential shift with increasing concentration of anti-rS can be explained due to hindered electron exchange at the Au electrode surface as a result of biomolecules binding, thereby, affecting the value of the redox reaction potential. Noteworthy, that for lower concentrations

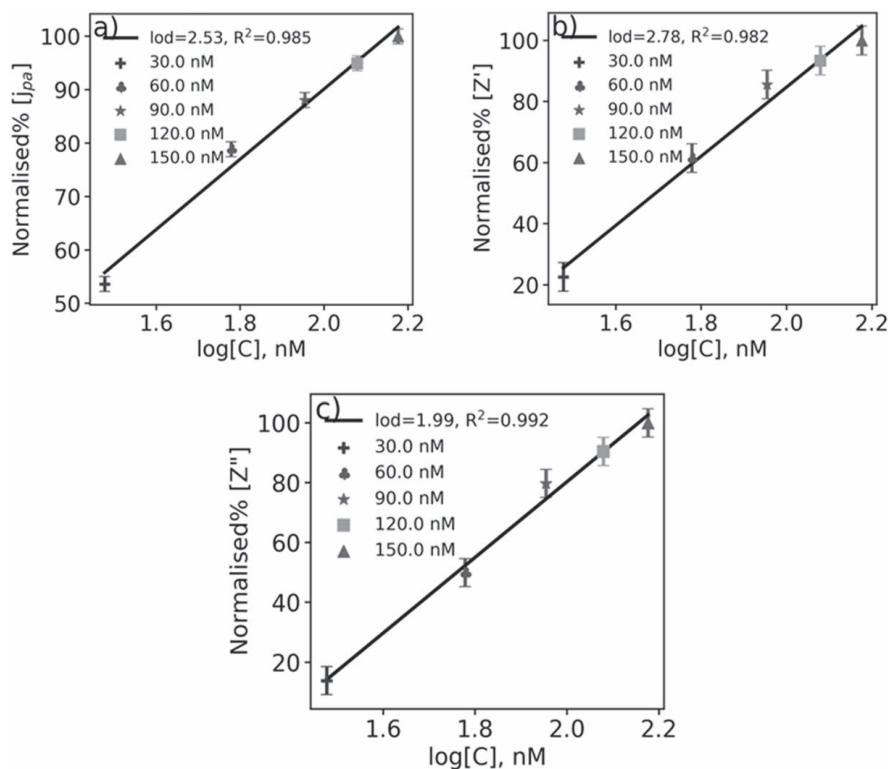


**Figure 6.** Calibration curves obtained from CV (a) and EIS fitted  $R_{ct}$  (b), EIS, maximum of  $Z''$  (c). Error bars are calculated as a percentage standard error. Signal normalised to electrode area,  $A = 0.179 \text{ cm}^2$ .

(0–90 nM) of anti-rS, the values of maximum current densities decrease faster, while for higher concentrations (90 – 150 nM) the process reaches saturation point (Figs. 4 and 5).

The same effect is accompanied by a sequential growth of the semicircle radius in the Nyquist plot (Fig. 3b). EIS reveals the broad trend for radii growth toward lower concentrations (0 – 90 nM) and a slowdown in the radii growth at high concentrations (90–150 nM). The number of non-occupied SCoV2-rS decrease with the increase of antibody concentration and obtained signal values from CV and EIS are summarised in Table 1, where the dependence of the increased  $R_{ct}$  value vs concentration tends to plateau at high content of anti-rS.

**Analytical characterisation of the immunosensor developed for the anti-rS detection.**—To evaluate the analytical characteristics of the electrochemical immunosensor, limits of detection (LODs) for sensing anti-rS were calculated from CV and EIS measurements. From CV, the highest value of the anodic current density ( $j_{pa}$ ) and the lowest value of cathodic current density ( $j_{pc}$ ) was used as the signal. From EIS, as a signal, the  $R_{ct}$  value (obtained as a maximum value of  $Z'$ ) and maximum of  $Z''$  were used.

The values of data in Table 1, were normalised using the equation:

$$z_i = (x_i - \min(x)) / (\max(x) - \min(x)) \times 100,$$

where  $z_i$  - the value of *Normalised%*,  $x_i$  - extracted electrochemical parameter ( $j_{pa}$ ,  $Z'_{\max}$ ,  $Z''_{\max}$ ) at each concentration of anti-rS;  $\min(x)$

—the minimum value in the list of each extracted electrochemical parameter;  $\max(x)$ —the maximum value of each extracted electrochemical parameter. Obtained values of the normalised signal (*Normalised%*) vs the concentration of anti-rS were plotted and shown in the Figs. 5 and 6.

The Langmuir fit was obtained by fitting the Normalised signal (as  $y$ -value) and concentration data (as  $x$ -value) to equation:

$$y = B_{\max} \times x / (K_d + x),$$

where  $B_{\max}$ —maximum value obtained during specific binding and  $K_d$ —equilibrium dissociation constant, a concentration needed to achieve a half-maximum binding at equilibrium.  $K_d$  values of 37 nM and 39 nM were obtained from parameters extracted in CV data. Similar values (19–33 nM) were reported in a previous work, where C-reactive protein was investigated.<sup>47</sup>

The equation:

$$LOD = 3\sigma / \text{slope},$$

where  $\sigma$  is the standard deviation of the  $y$ -intercept of the standard plot (*Normalised%*) vs target concentration) was used for LODs calculation.<sup>48</sup> As a result, immunosensor for anti-rS detection by the CV using  $j_{pa}$  is characterised by LOD of 2.53 nM and it was defined from the standard plot shown in Fig. 6a. For comparison, the LOD obtained from CV in the cathodic area was twice higher, giving the value of 5.85 nM, which could be explained by slower electron charge transfer in the cathodic region. LODs for EIS based method (Figs. 6b

and 6c) were calculated and compared for several methodologies of data analysis. When a plot of *Normalised%* calculated using the  $R_{ct}$  value vs concentration was used, the LOD with a value of 2.78 nM was obtained. For comparison, the LOD value obtained from the maximum of the  $Z''$  peak was 1.99 nM, which is 38% lower.

### Conclusions

In this study, the covalent immobilisation of SCoV2-rS and its affinity interaction with anti-rS were evaluated. The surface of the Au electrode was characterised by CV and EIS methods after each modification step. CVs revealed that the peak current density measured with the addition of 2 mM  $[\text{Fe}(\text{CN})_6]^{3-/4-}$  decreased after the formation of the SAMmix on the electrode surface. EIS spectra represented in Nyquist coordinates indicate evident changes in every step of Au electrode modification. The charge transfer resistance of the Au/SAMmix electrode after activation with EDC and NHS decreased compared to the electrode before activation, while the semicircle increases after immobilisation of SCoV2-rS and affinity interaction with anti-rS. The anti-rS antibodies were quantified using CV and EIS methods, giving the lowest LOD values of 2.53 nM and 1.99 nM, respectively. This allows the application of impedimetric methods to detect the formation of antigen-antibody complexes and the subsequent development of an immunosensor for the serologic diagnosis of COVID-19 and/or the determination of the success of vaccination against the SARS-CoV-2 virus.

### Acknowledgments

This research was conducted under Lithuania-Latvian-China (Taiwan) project and it has received funding according to agreement No S-LLT-21-3 with Research Council of Lithuania (LMTLT). Electrochemical impedance experiments and data acquisition was performed under the grant agreement of European Social Fund (No. 09.3.3-LMT-K-712-23-0159). Schematic illustrations were created with BioRender (<https://biorender.com>).

### ORCID

Arunas Ramanavicius  <https://orcid.org/0000-0002-0885-3556>

### References

- M. Drobysh, A. Ramanaviciene, R. Viter, and A. Ramanavicius, *Micromachines*, **12**, 390 (2021).
- S. Ramanavicius and A. Ramanavicius, *Polymers (Basel)*, **13**, 1 (2021).
- S. Ramanavicius and A. Ramanavicius, *Int. J. Mol. Sci.*, **21**, 1 (2020).
- S. Ramanavicius, A. Jagminas, and A. Ramanavicius, *Polymers (Basel)*, **13**, 1150 (2021).
- A. Ramanavicius, A. Finkelsteinas, H. Cesilius, and A. Ramanaviciene, *Bioelectrochemistry*, **79**, 11 (2010).
- I. Plikusiene, V. Maciulis, A. Ramanaviciene, Z. Balevicius, E. Buzavaite-Verteliene, E. Ciplys, R. Slibinskas, M. Simanavicius, A. Zvirbliene, and A. Ramanavicius, *J. Colloid Interface Sci.*, **594**, 195 (2021).
- F. Wu et al., *Nature*, **579**, 265 (2020).
- M. Laue, A. Kauter, T. Hoffmann, J. Michel, and A. Nitsche, *Sci Rep.*, **11**, 3515 (2021).
- R. A. Khailany, M. Safdar, and M. Ozaflan, *Gene Reports*, **19**, 100682 (2020).
- I. Astuti and Ysrafil, *Diabetes Metab. Syndr. Clin. Res.*, **14**, 407 (2020).
- Y. Peng, N. Du, Y. Lei, S. Dorje, J. Qi, T. Luo, G. F. Gao, and H. Song, *EMBO J.*, **39** (2020).
- B. W. Neuman et al., *J. Struct. Biol.*, **174**, 11 (2011).
- M. Bárcena, G. T. Oostergetel, W. Bartelink, F. G. A. Faas, A. Verkleij, P. J. M. Rottier, A. J. Koster, and B. J. Bosch, *Proc. Natl Acad. Sci. USA*, **106**, 582 (2009).
- A. C. Walls, Y. J. Park, M. A. Tortorici, A. Wall, A. T. McGuire, and D. Vesler, *Cell*, **181**, 281 (2020).
- M. Hoffmann et al., *Cell*, **181**, 271 (2020).
- J. Shang, G. Ye, K. Shi, Y. Wan, C. Luo, H. Aihara, Q. Geng, A. Auerbach, and F. Li, *Nature*, **581**, 221 (2020).
- Q. Wang et al., *Cell*, **181**, 894 (2020).
- D. Wrapp, N. Wang, K. S. Corbett, J. A. Goldsmith, C. L. Hsieh, O. Abiona, B. S. Graham, and J. S. McLellan, *Science (80-...)*, **367**, 1260 (2020).
- N. Post et al., *PLoS One*, **15**, e0244126 (2020).
- A. E. Dhamad and M. A. A. Rhida, *PeerJ*, **8**, e10180 (2020).
- Z. Li et al., *J. Med. Virol.*, **92**, 1518 (2020).
- A. Kausaite-Minkstimiene, A. Ramanavicius, J. Ruksnaite, and A. Ramanaviciene, *Anal. Methods*, **5**, 4757 (2013).
- I. Morkvenaitė-Vilkonciene, A. Ramanaviciene, A. Kisieliute, V. Bucinskas, and A. Ramanavicius, *Biosens. Bioelectron.*, **141**, 111411 (2019).
- A. Ramanaviciene and A. Ramanavicius, *Anal. Bioanal. Chem.*, **379**, 287 (2004).
- D. Plausinaitis, L. Sinkevicius, U. Samukaite-Bubniene, V. Ratautaite, and A. Ramanavicius, *Talanta*, **220** (2020).
- Z. Balevicius, A. Ramanaviciene, I. Baleviciute, A. Makaraviciute, L. Mikoliunaite, and A. Ramanavicius, *Sensors Actuators B Chem.*, **160**, 555 (2011).
- F. Cui and H. S. Zhou, *Biosens. Bioelectron.*, **165**, 112349 (2020).
- A. Raziq, A. Kidakova, R. Boroznjak, J. Reut, A. Öpik, and V. Syritski, *Biosens. Bioelectron.*, **1781**13029 (2021).
- H. Zhao et al., *Sensors Actuators B Chem.*, **327**, 128899 (2021).
- Z. S. Miripour et al., *Biosens. Bioelectron.*, **165**, 112435 (2020).
- A. Baradake, B. Jose, R. Paullikaite, and R. J. Forster, *Electrochim. Acta*, **306**, 299 (2019).
- A. Baradake, A. Santos, P. R. Bueno, and J. J. Davis, *Biosens. Bioelectron.*, **172**, 112705 (2021).
- M. H. F. Taha, H. Ashraf, and W. Caesarendra, *Appl. Syst. Innov.*, **3**, 1 (2020).
- E. B. Bahadir and M. K. Sezgentürk, *Artif. Cells. Nanomedicine Biotechnol.*, **44**, 248 (2016).
- D. Grieshaber, R. MacKenzie, J. Vörös, and E. Reimhult, *Sensors*, **8**, 1400 (2008).
- V. Ganesh, S. K. Pal, S. Kumar, and V. Lakshminarayanan, *J. Colloid Interface Sci.*, **296**, 195 (2006).
- A. Ramanaviciene and A. Ramanavicius, *Crit. Rev. Anal. Chem.*, **32**, 245 (2002).
- H. G. Hong, W. Park, and E. Yu, *J. Electroanal. Chem.*, **476**, 177 (1999).
- A. Kausaite-Minkstimiene, A. Ramanaviciene, J. Kirlyte, and A. Ramanavicius, *Anal. Chem.*, **82**, 6401 (2010).
- National Institute for Biological Standards and Control, 20/136WHO International Standard (2020), <https://www.nibsc.org/documents/ifu/20-136.pdf>.
- Immundiagnostik AG, (2021), Manual, [https://www.immundiagnostik.com/media/pages/kestkits/k-5004/e859ef5a82-1647482477/k5004\\_2021-08-10\\_idk\\_sars-cov-2-igg.pdf](https://www.immundiagnostik.com/media/pages/kestkits/k-5004/e859ef5a82-1647482477/k5004_2021-08-10_idk_sars-cov-2-igg.pdf).
- D. J. Dietzen, *Principles and Applications of Molecular Diagnostics*, ed. N. Rifai and A. R. Horvath (Elsevier, Amsterdam) p. 345 (2018).
- F. Cecchet, M. Maraccio, M. Margotti, F. Paolucci, S. Rapino, and P. Rudolf, *J. Phys. Chem. B*, **110**, 2241 (2006).
- V. Rajesh, V. K. Sharma, S. K. Tanwar, Mishra, and A. M. Biradar, *Thin Solid Films*, **519**, 1167 (2010).
- F. Patolsky, B. Filanovsky, E. Katz, and I. Willner, *J. Phys. Chem. B*, **102**, 10359 (1998).
- E. B. Bahadir and M. K. Sezgentürk, *Artif. Cells. Nanomedicine Biotechnol.*, **44**, 462 (2016).
- A. Baradake, R. Hein, X. Li, and J. J. Davis, *Anal. Chem.*, **92**, 3508 (2020).
- A. Shrivastava and V. Gupta, *Chronicles Young Sci.*, **2**, 21 (2011).

## **Paper 6**

### **Electrochemical sensor for vascular endothelial growth factor based on self-assembling DNA aptamer structure**

**V. Liustrovaite**, V. Ratautaite, A. Ramanaviciene, I. Plikusiene,  
U. Malinovskis, D. Erts, J. Sarvutiene, A. Ramanavicius

*Science of the Total Environment*, 2024, 955, 177151  
[doi.org/10.1016/j.scitotenv.2024.177151](https://doi.org/10.1016/j.scitotenv.2024.177151)





## Electrochemical sensor for vascular endothelial growth factor based on self-assembling DNA aptamer structure

Viktorija Liustrovaite<sup>a,b</sup>, Vilma Ratautaite<sup>c</sup>, Almira Ramanaviciene<sup>b</sup>, Ieva Plikusiene<sup>c</sup>, Uldis Malinovskis<sup>a,d</sup>, Donats Erts<sup>d,e</sup>, Julija Sarvutiene<sup>c</sup>, Arunas Ramanavicius<sup>a,c,\*</sup>

<sup>a</sup> Department of Physical Chemistry, Faculty of Chemistry and Geosciences, Vilnius University, Naugarduko Str. 24, Vilnius LT-03225, Lithuania

<sup>b</sup> NanoTechnas, Faculty of Chemistry and Geosciences, Vilnius University, Naugarduko Str. 24, Vilnius LT-03225, Lithuania

<sup>c</sup> Department of Nanotechnology, State Research Institute Center for Physical Sciences and Technology, Saulėtekio Av. 3, Vilnius LT-10257, Lithuania

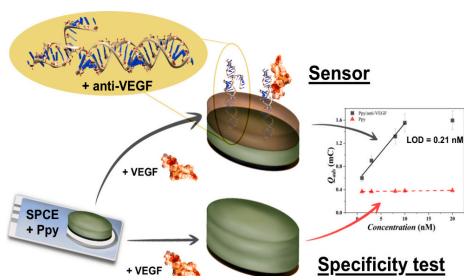
<sup>d</sup> Institute of Chemical Physics, Faculty of Science and Technology, University of Latvia, Raina Blvd. 19, Riga LV-1586, Latvia

<sup>e</sup> Department of Chemistry, Faculty of Medicine and Life Sciences, University of Latvia, Jelgavas Str. 1, Riga LV-1004, Latvia

### HIGHLIGHTS

- SPCE was modified with a thin layer of polypyrrole-supported by aptamer.
- Aptamer was self-assembled from three separated parts of single-stranded DNA.
- The modified SPCE was applied in electrochemical sensor for VEGF protein.
- VEGF proteins were detected by applying a pulsed amperometric detection method.
- The LOD of the proposed method is 0.21 nM of VEGF protein.

### GRAPHICAL ABSTRACT



### ARTICLE INFO

Editor: Damià Barceló

#### Keywords:

Vascular endothelial growth factor (VEGF)  
Polypyrrole (Ppy)  
Screen-printed carbon electrode (SPCE)  
Electrochemical sensor  
DNA aptamers  
Biosensors

### ABSTRACT

Developing vascular endothelial growth factor (VEGF) protein is essential for early cancer diagnosis and cancer treatment monitoring. This study presents the design and characterisation of an electrochemical sensor utilising a self-assembling DNA aptamer structure for the sensitive and selective detection of VEGF. The aptamer structure comprises three different parts of single-stranded DNA that are assembled prior to integration into the sensor. Polypyrrole (Ppy)-based layers were deposited onto screen-printed carbon electrodes (SPCEs) using an electrochemical deposition technique, followed by the entrapment of a self-assembled DNA aptamer structure within electrochemically formed Ppy matrix (DNA aptamer)/Ppy). The response to the sensor toward VEGF was measured by the pulsed amperometric detection (PAD), highlighting the enhanced performance of DNA aptamer/Ppy configuration compared to bare Ppy. The sensor exhibited high sensitivity, achieving a limit of detection (LOD) of 0.21 nM for VEGF. The interaction behaviour between VEGF in the solution and the immobilised DNA aptamer/Ppy-based structure was analysed using Langmuir isotherm model. The developed

\* Corresponding author at: Department of Physical Chemistry, Faculty of Chemistry and Geosciences, Vilnius University, Naugarduko Str. 24, Vilnius LT-03225, Lithuania.

E-mail address: [arunas.ramanavicius@chf.vu.lt](mailto:arunas.ramanavicius@chf.vu.lt) (A. Ramanavicius).

<https://doi.org/10.1016/j.scitotenv.2024.177151>

Received 21 September 2024; Received in revised form 19 October 2024; Accepted 20 October 2024

Available online 31 October 2024

0048-9697/© 2024 Elsevier B.V. All rights are reserved, including those for text and data mining, AI training, and similar technologies.

electrochemical biosensor is promising for in vitro applications in early cancer diagnostics and treatment monitoring, enabling rapid screening of patient samples.

## 1. Introduction

Vascular endothelial growth factor protein (VEGF) is a key signaling protein that is unregulated in response to hypoxic conditions and plays a crucial role in both physiological and pathological processes, particularly in angiogenesis and vasculogenesis. During embryogenesis, VEGF is essential for the formation of vascular system, facilitating the differentiation of endothelial cells and the development of new blood vessels. In adult organisms, the dysregulation of VEGF expression is often associated with various diseases, including cancer, where it promotes tumor growth and metastasis by enhancing blood supply to the tumor microenvironment (Rodríguez et al., 2021). The ability to accurately identify and quantify VEGF as a biomarker has significant implications for cancer diagnosis and prognosis, as it not only aids in the early identification of tumors but also serves as a critical indicator of treatment efficacy and disease progression (Kwon et al., 2021). Therefore, the development of robust and sensitive detection methods for VEGF is essential for advancing personalised medicine and improving clinical outcomes in oncology.

The VEGF protein family in mammals comprises five distinct members: VEGF-A, VEGF-B, VEGF-C, and VEGF-D (Goel and Mercurio, 2013), and placenta growth factor (PLGF) (Simons et al., 2016). VEGF-A is the most researched component and is often referred to simply as VEGF. It plays a central role in angiogenesis, especially in tumor growth and metastasis (Guyot and Pagès, 2015). VEGF-B is primarily involved in the maintaining blood vessels but does not significantly induce angiogenesis (Angelescu et al., 2013). VEGF-C and VEGF-D are key regulators of lymphangiogenesis (the formation of lymphatic vessels) and are involved in cancer metastasis to lymph nodes (Zhang et al., 2022). The most common isoform of VEGF is VEGF<sub>165</sub>, which refers to the isoform of VEGF-A containing 165 amino acids. This isoform is associated with the growth and metastasis of numerous forms of human malignancies (Ferrara et al., 2003). Additionally, human disorders, such as malignancies (Xie et al., 2018), rheumatoid arthritis (Di Stasi et al., 2023), psoriasis (Mao et al., 2023), and Alzheimer's disease (Shamsipour et al., 2021), have been linked to VEGF by blood biomarker analysis. Due to its numerous physiological and pathological functions, VEGF has attracted interest as a biomarker for analytical sensing platforms for sensing and detection.

Biosensors are generally classified according to the type of transducer or bioreceptor employed in their design, providing insights into their functionality and applications (Lu et al., 2023; Zeng et al., 2023). Bioreceptors are essential components of biosensors, as they are responsible for ensuring the specificity and sensitivity of detection methods (Qiu et al., 2019a), natural and synthetic antibodies (Yu et al., 2023a), and enzymes (Yu et al., 2023b), each offering distinct advantages for various applications. For instance, a study demonstrated the use of aptamers in a dual-channel photoelectrochemical ratiometric aptasensor that utilises up-converting nanocrystals in a custom-made 3D-printed device (Qiu et al., 2019b), which demonstrates the versatility and effectiveness of aptamers in complex detection scenarios. In contrast, the role of antibodies is highlighted in a micro-electromechanical microsystem-supported photothermal immunoassay designed for point-of-care testing of aflatoxin B1 in food products, showcasing the potential of antibodies in food safety applications (Yu et al., 2023a). Lastly, the use of enzymes is demonstrated through enzyme-encapsulated protein trap-engineered metal-organic framework-derived biomimetic probes for non-invasive prostate cancer monitoring, highlighting the effectiveness of enzymatic activity in improving detection capabilities (Yu et al., 2023b). These works collectively highlight the diverse functions of aptamers, antibodies, and

enzymes as bio-receptors in advancing biosensing technologies across various fields. While antibodies have historically served as effective bioreceptors, they have limitations such as high cost, complex purification procedures, and batch-to-batch variations (Crivianu-Gaita and Thompson, 2016). Aptamers have emerged as promising alternatives due to their DNA or RNA-based structure, which allows them to bind to specific target molecules. Two notable examples that exemplify innovative biosensing approaches are the cation exchange reaction-mediated photothermal and polarity-switchable photoelectrochemical dual-readout biosensor (Lu et al., 2023) and the photocurrent-polarity-switching photoelectrochemical biosensor for switching spatial distance electroactive tags (Zeng et al., 2023). The former utilises a cation exchange reaction to mediate photothermal effects while employing a dual-readout mechanism, enhancing sensitivity and specificity for various applications. Conversely, the latter biosensor leverages photocurrent polarity-switching techniques to detect electroactive tags based on their spatial distance, allowing for improved selectivity and control in sensing applications (Zeng et al., 2023). These examples illustrate the diversity within the biosensor field and the ongoing advancements in transducer technologies and bioreceptor designs, highlighting the potential for more sensitive and selective detection methods across various biomedical applications. Cai et al. study developed a competitive-displacement reaction strategy for sensitive photoelectrochemical aptasensing of prostate-specific antigen (PSA) using target-induced dissociation of gold nanoparticle-coated graphene nanosheets from CdS quantum dot-functionalized mesoporous titanium dioxide (Cai et al., 2018). Xu et al. study presents an ultrasensitive photoelectrochemical aptasensor for detecting 8-hydroxy-2'-deoxyguanosine (8-OHdG) using hemin/G-quadruplex photocurrent polarity switching on ultrathin ZnIn<sub>2</sub>S<sub>4</sub> nanosheets, achieving a detection limit of 0.3 pM while demonstrating high sensitivity, stability, selectivity, and accuracy in complex biological matrices (Xu et al., 2022). Aptamers, selected through the systematic evolution of ligands by the exponential enrichment (SELEX) method, exhibit high affinity and selectivity, binding non-covalently to analytes via various interactions (Qureshi et al., 2015). These characteristics enable aptamers to provide several advantages over antibodies, including higher affinity, specificity, thermal stability, and lower cost (Nourizad et al., 2023). For example, RNA aptamers isolated using SELEX demonstrated superior discrimination against similar molecules such as caffeine and theobromine compared to theophylline, with binding affinities up to 10,000 times higher (Huang and Liu, 2022). Similarly, aptamers selected for L-arginine showed a 12,000-fold preference for the target over its enantiomer (Geiger et al., 1996). Furthermore, anti-VEGF RNA aptamers strongly bind to VEGF<sub>165/164</sub>, distinguishing them from structurally similar proteins such as VEGF<sub>121</sub> (Ruckman et al., 1998). In addition, aptamers have shown the ability to differentiate target cells, even between highly similar cell types (Xie et al., 2023).

The sensor designed for VEGF detection employs a self-assembling DNA aptamer as the bioreceptor, and its electrochemical detection mechanism can be compared to the dual-readout capabilities of cation exchange reaction-mediated biosensors. This comparison highlights the capacity of the sensor to achieve high specificity and sensitivity through innovative design, akin to the methodologies used in dual-readout biosensors. Additionally, the photocurrent-polarity-switching biosensor illustrates the significance of dynamic response mechanisms in biosensing, which is relevant to the operational efficiency of the VEGF sensor. The adaptability and precision of the self-assembling DNA aptamer structure suggest a potential for enhanced interaction with the target protein, similar to the use of spatial distance and electroactive tags in other biosensors to improve detection capabilities.

Various methods have been proposed for the quantitative detection of VEGF. These include enzyme-linked immunosorbent assay (ELISA) (Hsu et al., 2016), fluorescent analysis (Al-Ameen et al., 2015), surface-enhanced Raman scattering (SERS) (Zhao et al., 2015), enzyme-linked chemiluminescence immunoassay (Wang et al., 2021), electrochemical detection (Ni et al., 2020). However, many of these techniques require intricate procedures, advanced instrumentation, and highly trained personnel. Consequently, there is considerable interest in developing VEGF sensors with high sensitivity, simple operation, and low cost. The pulsed amperometric detection (PAD) method is a rapid voltammetric detection technique used in biosensors (Ratautaite et al., 2023). Its primary advantage over other voltammetric approaches is its ability to conduct analyses without a redox probe. This greatly simplifies the experimental setup, streamlining the procedure and allowing measurements to be taken directly in the phosphate buffer solution. This capability improves efficiency and makes the method more versatile and accessible in various analytical settings. It should be noted that we specifically chose this method for our experiments because of its speed and suitability for biosensing applications.

This work focuses on developing an electrochemical sensor based on a self-assembling aptamer structure supported by electrochemically polymerised polypyrrole (Ppy), specifically designed to determine VEGF. The self-assembling aptamer structure, comprising three distinct parts of single-stranded DNA, is immobilised onto the Ppy-modified SPCE through a two-step process. Initially, the Ppy layer is electrochemically deposited onto the SPCE, providing a conductive matrix that facilitates the subsequent immobilisation of the aptamer. Following the deposition, the self-assembled DNA aptamer structure is introduced to the Ppy matrix, allowing for efficient entrapment and stabilisation of the aptamer. The pulsed amperometric detection (PAD) method was then applied to generate analytical signals in response to VEGF binding. The interaction behaviour between VEGF in solution and the immobilised DNA aptamer/Ppy structure was analysed using the Langmuir isotherm model. Overall, the developed electrochemical biosensor shows significant promise for *in vitro* applications in early cancer diagnostics and treatment monitoring, enabling rapid screening of patient samples.

## 2. Materials and methods

### 2.1. Materials

Pyrrrole 98 % (CAS# 109-97-7, Alfa Aesar, Kandel, Germany), tablets of phosphate-buffered saline (PBS), pH 7.4, (CAS# 7647-14-5, Sigma-Aldrich, Steinheim, Germany), and sulfuric acid (96 %, CAS# 7664-93-9, Lachner, Neratovice, Czech Republic) were used in the experiments. Desalted unmodified and 3'-Thiol-Modifier C6 S-S DNA oligonucleotides and DL-dithiothreitol (DTT, CAS# 3483-12-3) were obtained from Sigma-Aldrich and used without further purification. V Recombinant human VEGF<sub>165</sub> protein, expressed in HEK293 cells, was purchased from Sigma-Aldrich, Steinheim, Germany. All reagents were analytical grade, and deionised water was used to prepare all aqueous solutions.

### 2.2. Hybridization of oligonucleotides (anti-VEGF aptamer)

The underlined sequence in Table 1 denotes the previously published anti-VEGFA SL<sub>2</sub>B aptamer sequence (Kaur and Yung, 2012). Additionally, other DNA sequences form a stem (stalk) structure after oligonucleotide hybridisation (Fig. 1A). The process involves the reduction of

the thiol-modified oligonucleotide (stalkGTG) prior to aptamer assembly, wherein the disulphide bond of the 3'-thiol modifier is reduced using a standard protocol. Firstly, the thiol-modified oligonucleotide is dissolved in 125  $\mu$ L of dithiothreitol solution (100 mM DTT in 10 mM sodium phosphate buffer, pH 8.3) and incubated at room temperature for 1 h. Subsequently, any by-product is removed through a commercial Sephadex® G-25 column (NAP-10, 'Cytiva'). Following reduction, the hybridisation of oligonucleotides takes place to assemble the aptamer. This involves determining DNA concentrations via UV spectrophotometry and mixing equal volumes of normalised oligonucleotide solutions (combSL2B, stalkGTG, and r\_stalkGTG) at a concentration of 30 pM/ $\mu$ L in PBS buffer, followed by boiling in a water bath (a beaker containing 100–150 mL of water) for 5 min, then slowly cooled to room temperature.

### 2.3. Pre-treatment of working electrodes, electrochemical modification by a polymer layer, and electrochemical measurements

The electrochemical experiments were carried out using a potentiostat/galvanostat AUTOLAB TYPE III from ECO-Chemie/Metrohm (Barendrecht, The Netherlands), controlled by the FRA2-EIS software from ECO-Chemie/Metrohm, (Utrecht, The Netherlands). The initial set of electrodes consisted of DRP-110 screen-printed carbon electrodes (SPCE) obtained from Metrohm/DropSens (Oviedo, Spain). These electrodes have a working electrode with a geometric area of 0.126 cm<sup>2</sup>, a carbon-based counter electrode, and a reference electrode.

Before the electrochemical modification with Ppy, the working electrodes were electrochemically cleaned using cyclic voltammetry to ensure accurate detection in an electrochemical immunoassay (Lv et al., 2019; Zeng et al., 2022). This involved immersing the electrodes in a 0.5 M sulfuric acid solution and potential cycling for 20 cycles at a sweep rate of 0.1 V/s in the range from  $-0.1$  V to  $+1.2$  V vs. Ag/AgCl.

The polymer layer was deposited with a two-step electrochemical polymerisation procedure (Fig. 1B). Two steps were taken to deposit the Ppy-entrapped aptamer (Ppy/anti-VEGF) on the SPCE electrodes: (i) In the first step, the Ppy under-layer was electrochemically deposited from a polymerisation solution containing 0.1 M of pyrrole in 10 mM PBS, pH 7.4, and a sequence of 5 potential pulses (of  $+0.95$  V for 1 s and 0 V for 30 s) was applied; (ii) In the second step, anti-VEGF was added to the same polymerisation bulk solution, and the sequence of 5 potential pulses (of  $+0.95$  V for 1 s and 0 V for 30 s) was repeated. The anti-VEGF aptamer is embedded within the polypyrrole structure, providing support and stability to the aptamer molecule.

Pulsed amperometric detection (PAD) was used to evaluate Ppy-modified electrodes. The sequence consisted of 10 potential pulses of  $+600$  mV vs. Ag/AgCl lasting 2 s and 0 V vs. Ag/AgCl lasting 2 s.

## 3. Results and discussion

### 3.1. Electrodeposition of polypyrrole-based VEGF aptamer

Using a series of potential pulses, polymer-based layers were electrochemically deposited on the surface of SPCE. The potential pulse series profile during the application of the polypyrrole-based (Ppy) layer to SPCE is shown in Fig. 2A. According to the experimental procedures described in the experimental section, a polypyrrole-based VEGF aptamer (Ppy/anti-VEGF) layer was created on SPCEs through two steps (Fig. 2B, 2C).

**Table 1**  
DNA nucleotides.

| Oligomer   | Sequence (5'-3')                        | Modification                                   | Ln | MW    |
|------------|---|--|----|-------|
| combSL2B   | CAATTGGGCCCGTCGCGTATGTTGGGTAAGCTTGAATTC |  | 38 | 11744 |
| stalkGTG   | GTCGACCTGC6GTG/[ThiC6]                  | [ThiC6] - 3' Thiol modifier C6 S-S - on 3' end | 13 | 6763  |
| r_stalkGTG | CACGCAGGTCGACGAATCAAGCTT                |  | 25 | 7655  |

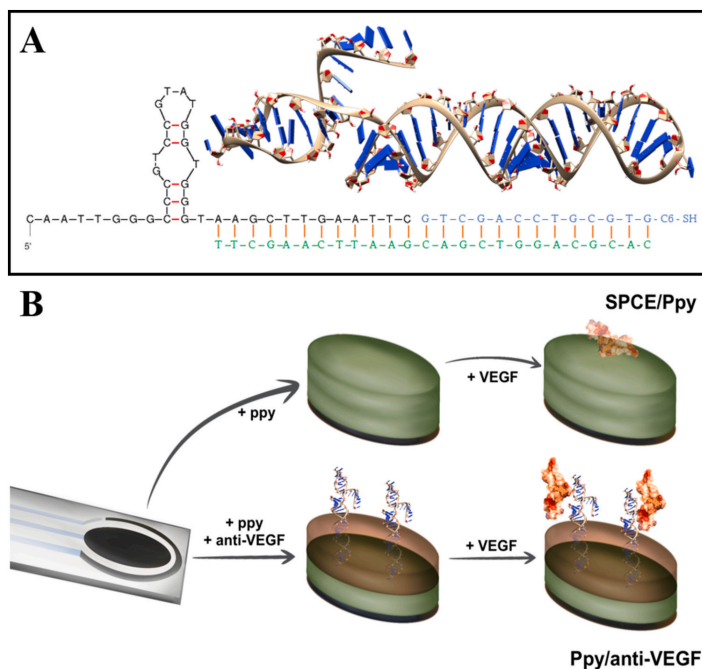


**Fig. 1.** (A) Self-assembling anti-VEGF aptamer based on the complex of three oligonucleotides. Black letters – combSI2B oligonucleotide, blue letters – stalkGTG oligonucleotide and green letters – r\_stalkGTG oligonucleotide. (B) Schematic representation of two experimental setups applied for assessment of developed aptasensor-based structures.

In the first step, a Ppy underlayer was electrochemically deposited from a solution of 0.1 M pyrrole in 10 mM PBS (pH 7.4) by applying 5 potential pulses (+0.95 V for 1 s followed by 0 V for 30 s). This thin Ppy underlayer, similar to approaches used in other studies (Balciunas et al., 2022; Ktari et al., 2015; Liustrovaite et al., 2023) was implemented to enhance the adhesion and performance of the sensing layer while minimising the direct interaction between the electrode and the target analyte. In particular, it mitigated the direct interaction of VEGF with the electrode surface, ensuring a more effective formation of the Ppy/anti-VEGF layer. In the second step, the anti-VEGF aptamer was added to the same polymerisation solution, and the sequence of 5 potential pulses was repeated. This process embeds the anti-VEGF aptamer within the Ppy structure, providing enhanced stability and support for the aptamer molecule while shielding the electrode surface. Similar to approaches seen in MIP and self-assembled monolayer (SAM) systems. This two-step process is crucial for optimising the sensing layer's adhesion and functional performance.

### 3.2. Electrochemical characterisation of polypyrrole-based aptamer layer and VEGF detection

The selection of duration in the PAD method is crucial in achieving accurate and sensitive electrochemical measurements. In this case, a series of 10 pulses of 0 V and 10 pulses of +0.6 V are utilised, each lasting for 2 s (Fig. 3A), as suggested in our previous research (Ramanaviciene and Ramanavicius, 2004). The choice of +0.6 V for detection is based on its ability to induce the desired electrochemical reactions and provide an optimal signal response. Furthermore, it was stated that at +0.65 V vs Ag/AgCl (3 M KCl), the unsubstituted Ppy starts

to overoxidise (Lewis et al., 1997). During the evaluation of the obtained current changes by application potential pulses, the drop of the current was attentively analysed at certain moments or intervals in the potential pulses of +0.6 V and 0 V. Such moments in the potential pulse were at 0.1 s, 0.2 s, 0.4 s, 0.6 s, 0.8 s, and 2.0 s (Fig. 3B). Analysing current changes at specific moments within the potential pulse allows the characterisation of different electrochemical processes. Investigating and determining different redox reactions or species exhibiting diverse kinetics or affinities toward the electrode surface becomes possible. This methodology facilitates gathering intricate and thorough insights into the electrochemical system.

Fig. 3A shows a graphical representation of the PAD method; the x-axis of the graph represents time, and the y-axis represents the electrical current. Fig. 3B depicts the pulse as two pulses, one at +0.6 V and the other at 0 V, which were applied to the electrode. Each pulse exhibits specific time points marked along the x-axis at 0.1 s intervals. Current values at 0.1 s for 0.6 V and 0 V were extracted from the graph and marked as  $\Delta I_{0.1s}$ . Similarly, data points were collected from the graph at time intervals of 0.2 s, 0.4 s, 0.6 s, and 0.8 s and were labelled as  $\Delta I_{0.2s}$ ,  $\Delta I_{0.4s}$ ,  $\Delta I_{0.6s}$ , and  $\Delta I_{0.8s}$ , respectively. These time points represent different time placements within the overall pulse duration taken for further investigation, as described in the following (Fig. 4).

### 3.3. Evaluation of analytical parameters

#### 3.3.1. Adapted Langmuir isotherm

The y-axis depicts the current response observed during that interval (Fig. 3). Fig. 3 illustrates the significance of pulse length when using the PAD method. As a result, potential pulse values of +0.6 V and 0 V were

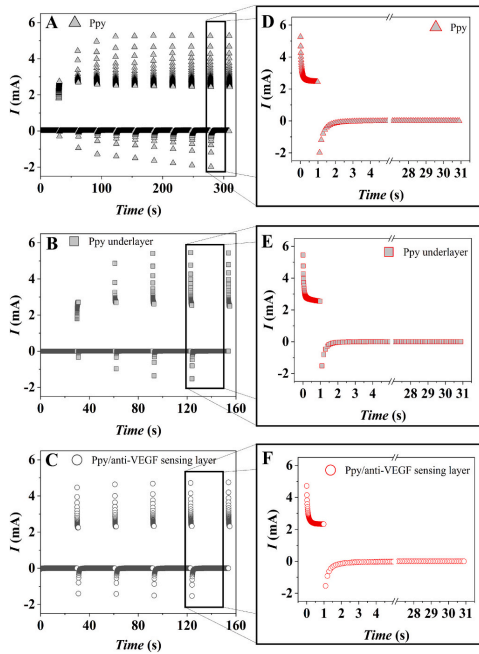


Fig. 2. Electrochemical deposition of Ppy layers: (A) on SPCE electrodes, showing the profile of the current registered during the formation of the Ppy layer from polymerisation solution without anti-VEGF. (B) Ppy underlayers on SPCE electrodes and (C) of the Ppy layers with anti-VEGF entrapped as a sensing element of the system. Inset (D–F): potential pulses for the signal analysis. Measurements were performed in 10 mM PBS solution, pH 7.4.

chosen to measure VEGF over a concentration range of 0 to 24 nM. Several specific moments in the potential pulse ( $X_s$ ) were investigated, including 0.1 s, 0.2 s, 0.4 s, 0.6 s, 0.8 s, and 2.0 s. Calibration curves (Fig. 4) were plotted using a normalised response ( $NR \Delta I_{at X_s}$ ) in current  $\Delta I_{at X_s}$  obtained from PAD measurements performed after incubating

Ppy/anti-VEGF and Ppy in the 10 mM PBS solution, pH 7.4, containing VEGF in the range of concentrations from 0 to 24 nM. The incubations were carried out for 15 min at room temperature. Ppy and Ppy/anti-VEGF electrodes were rinsed with PBS, pH 7.4, and a solution between incubating electrodes in various VEGF concentrations. To

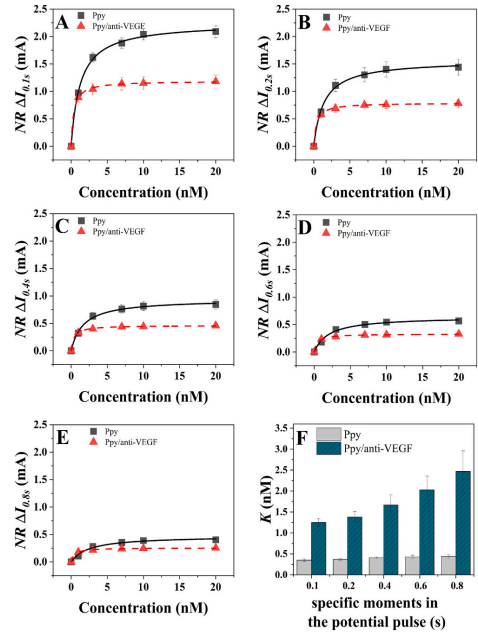


Fig. 4. Calibration curves ( $NR \Delta I_{at X_s}$ ) vs. VEGF protein concentration) obtained using modified electrodes of Ppy and Ppy/anti-VEGF modified electrodes for specific moments in the potential pulse at (A) 0.1 s, (B) 0.2 s, (C) 0.4 s, (D) 0.6 s, (E) 0.8 s. The error bars were calculated as standard deviations ( $n = 4$ ). (F) the dependence of the adapted Langmuir constant of Ppy/anti-VEGF and the corresponding Ppy-modified electrodes for specific moments in potential pulse ( $n = 4$ ) (F).

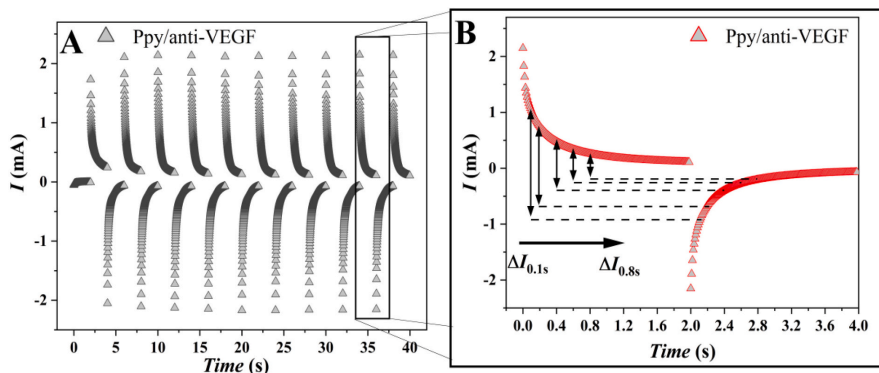


Fig. 3. (A) Pulsed amperometry-based evaluation of Ppy/anti-VEGF modified electrodes performed by the potential pulse sequence (+0.6 V and 0 V potentials) (B): the principal of the potential pulse signal analysis. Measurements were performed in 10 mM PBS solution, pH 7.4.

normalise the response of the  $\Delta I$  signals, the  $\Delta I$  at 0 nM of VEGF was set to zero (Eq. 1).

$$NR\Delta I_{at\ x_s} = \Delta I_{at\ x_s}(0\ nM\ VEGF) - \Delta I_{at\ x_s} \quad (1)$$

Understanding the interactions of binding sites with aptamers and proteins poses challenges when employing electrochemical methods. Therefore, our investigation relies heavily on the mathematical analysis of adsorption isotherms, primarily the Langmuir model. This involves fitting experimental data to the Langmuir isotherm to derive model parameters. In the study by Gonzato et al. (2021), cilostazol-extracted MIPs embedded in a polymer film were used to measure binding parameters. Experiments were performed using Freundlich, Langmuir, and Langmuir-Freundlich isotherms. The Langmuir-Freundlich isotherm best fitted the data, indicating highly homogeneous and relatively homogeneous cavities in the polymer matrix. Next, Çalik, Balci, and Özdamar (Çalik et al., 2010) conducted an equilibrium binding analysis on recombinant human growth hormone (rhGH) in liquid-phase and immobilised-aptamer phase, using the Langmuir type adsorption isotherm. Following previous research, we adapted the Langmuir isotherm (Eq. 2) and applied it to our experiments, as shown in Fig. 4.

$$\Delta I = \Delta I_{max} \times \frac{[VEGF]}{K + [VEGF]} \quad (2)$$

Where  $\Delta I_{max}$  is the maximal normalised value of current density,  $K$  – is the adapted Langmuir constant, and  $[VEGF]$  – is the concentration of VEGF.  $K$ ,  $\Delta I_{max}$ , and  $R^2$  values can be found in Table 2.

Table 2 provides a detailed summary of  $K$ ,  $\Delta I_{max}$ , and  $R^2$  values obtained from experiments calculated for specific moments in the potential pulse of +0.6 V and 0 V potential pulses at 0.1 s, 0.2 s, 0.4 s, 0.6 s, and 0.8 s (Fig. 4A-E), with the corresponding standard deviation errors. High  $R^2$  values close to 1 across different specific moments in the potential pulse indicate a strong fit of the experimental data to the adapted Langmuir model, indicating its suitability for describing the adsorption behaviour of VEGF on the sensing surface. Furthermore, the dependence of the  $K$  at specific moments in the potential pulse of Ppy/anti-VEGF and the corresponding Ppy-modified electrodes is shown in Fig. 4F. Notably, the  $K$  values tend to increase with longer specific moments in the potential pulse, indicating a positive correlation between the duration of the interaction and the affinity of VEGF for the sensing material. This observation suggests that prolonged exposure of the sensing surface to VEGF allows for more extensive binding interactions to occur, leading to a higher equilibrium constant. Longer specific moments in the potential pulse likely facilitate more significant adsorption of VEGF molecules onto the surface, resulting in enhanced sensitivity and specificity of the sensor. Increasing  $K$  values from  $1.25 \pm 0.09$  nM to  $2.47 \pm 0.49$  nM with longer specific moments in the potential pulse underscores optimising the experimental conditions to achieve the desired sensitivity and accuracy in VEGF detection. Researchers may consider adjusting the duration of the specific moments in the potential pulse to maximise the binding interactions between VEGF and the sensing surface while maintaining the dynamic range and reliability of the sensor response. It is noteworthy that  $K$  values for the Ppy layer remain relatively similar. Consequently, the  $\Delta I_{max}$  values for the Ppy/anti-VEGF layer and the Ppy layer are consistently lower for a longer specific moment in the potential

pulse compared to a shorter specific moment in the potential pulse.

### 3.3.2. Adaptation of integrated Cottrell equation

The integrated Cottrell equation (Anson plot) was employed to further analyse and discuss the results. The relation of the cumulative charge passed and time in Ppy-based electrochemical sensors obeys the integrated Cottrell equation (Eq. 3–4):

$$Q = Q_f + Q_{dl} + Q_{ads} \quad (3)$$

$$Q_f = 2nFAC\sqrt{\frac{D}{\pi}}\sqrt{t} = k\sqrt{t} \quad (4)$$

$$Q_{ads} = Fn\Gamma \quad (5)$$

where:  $Q$  – total charge (C);  $n$  – number of electrons;  $F$  – Faraday constant (96,485C/mol);  $A$  – area of the electrode ( $cm^2$ );  $C$  – concentration (M);  $D$  – diffusion coefficient ( $cm^2/s$ );  $t$  – time (s);  $Q_{dl}$  – the charge of the electrical double layer;  $Q_{ads}$  – charge induced by adsorbed ions.

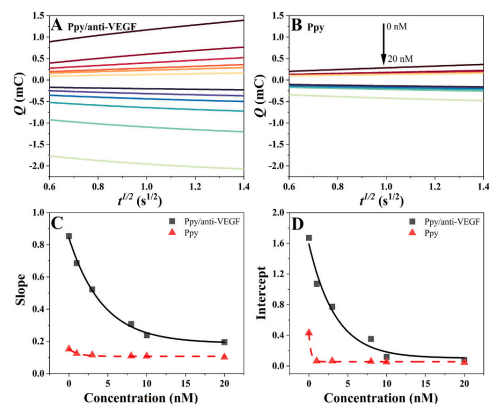
The study done by Anson et al. (Anson et al., 1967) underscored the effectiveness of a double potential step chronocoulometric technique in accurately quantifying adsorbed reactants, providing valuable insights into electrochemical processes without the need for complex models. In the integrated Cottrell equation, the total charge accumulation comprises three components: Faradaic charges ( $Q_f$ ) arising from redox activity, charges from the charging and discharging of the electrode-electrolyte double-layer capacitance ( $Q_{dl}$ ), and changes in charge due to adsorbed species ( $Q_{ads}$ ). When plotting the total charge ( $Q$ ) against the square root of time ( $t^{1/2}$ ), a linear relationship emerges, where the plot of  $Q$  versus  $t^{1/2}$  exhibits a linear correlation with the slope ( $k$ ) and the intercept corresponding to  $Q_{ads} + Q_{dl}$ . Notably, the study observed that maximum adsorption typically occurs at intermediate concentrations of specific compounds. In contrast, changes in adsorption patterns suggest specific bonding interactions between the reactants and the electrode surface. The previous study (Ratautaite et al., 2023) investigated the complex effects of electrode modification on the adsorption behaviour of analytes and reaction products. Unlike prior studies utilising plain electrodes, the study employed Pt electrodes modified with the conducting polymer Ppy, which were further imprinted or non-imprinted with glycoprotein. This modification introduced additional layers and functionalities to the electrode surface, altering the electrochemical behaviour of the system. The Ppy layer could participate in charging and discharging processes during electrochemical oxidation and reduction reactions by changing the potentials. In our study, we used the polymer-supported aptamer layer on the electrode. These insights complicate the analysis of amperograms, but it is still possible to describe them in the terms proposed by Anson.

Fig. 5A for Ppy/anti-VEGF and Fig. 5B for Ppy show the Anson plots for the data from Fig. 3 amperograms. Linear regression was used to fit the relationship between  $Q$  and  $t^{1/2}$ . Table 3 lists the parameters of the corresponding equations. The obtained  $R^2$  values indicate a linear correlation in the plot of  $Q$  vs.  $t^{1/2}$  (Table 3). The exponential dependence of the slope and the intercept on the concentration of VEGF is represented in Figs. 5C and 5D (for 0.6 V), respectively. The plots illustrate that slope and intercept values differ for Ppy/anti-VEGF and Ppy-modified

Table 2

$K$ ,  $\Delta I_{max}$ , and  $R^2$  values were calculated for specific moments in the potential pulse of +0.6 V and 0 V potential pulses at 0.2 s, 0.4 s, 0.6 s, 0.8 s, and 2 s. Errors were calculated as a standard deviation.

| Specific moments in the potential pulse, s | Ppy         |                       |       | Ppy/anti-VEGF |                       |       |
|--|-------------|-----------------------|-------|---------------|-----------------------|-------|
|  | $K$ (nM)    | $\Delta I_{max}$ (mA) | $R^2$ | $K$ (nM)      | $\Delta I_{max}$ (mA) | $R^2$ |
| 0.1  | 0.35 ± 0.03 | 1.19 ± 0.01           | 0.999 | 1.25 ± 0.09   | 2.25 ± 0.03           | 0.998 |
| 0.2  | 0.37 ± 0.02 | 0.79 ± 0.01           | 0.999 | 1.38 ± 0.14   | 1.57 ± 0.03           | 0.998 |
| 0.4  | 0.41 ± 0.03 | 0.46 ± 0.01           | 0.999 | 1.67 ± 0.24   | 0.94 ± 0.03           | 0.995 |
| 0.6  | 0.43 ± 0.04 | 0.33 ± 0.01           | 0.999 | 2.03 ± 0.33   | 0.64 ± 0.03           | 0.992 |
| 0.8  | 0.44 ± 0.04 | 0.26 ± 0.01           | 0.998 | 2.47 ± 0.49   | 0.47 ± 0.03           | 0.988 |



**Fig. 5.** A and B represent the Anson plots ( $Q$  vs.  $t^{1/2}$ ) derived from the amperometric response registered during the last (10th) potential pulse of the applied potential pulse sequence (0.6 V and 0 V) for A –Ppy/anti-VEGF modified electrode and B –Ppy modified electrode. C and D represent the slope and intercept values of the linear regression equation  $y = ax + b$  (from) vs. the concentration of VEGF protein (nM).

**Table 3**

Linear regression parameters of the Anson plot ( $Q$ , mC vs.  $t^{1/2}$ ,  $s^{1/2}$ ) (derived from the Ppy/anti-VEGF and Ppy for the last (10th) pulse of the potential pulse sequence.

| $y = ax + b$<br>C, nM | Ppy/anti-VEGF |         |                | Ppy    |        |                |
|-----------------------|---------------|---------|----------------|--------|--------|----------------|
|                       | a             | b       | R <sup>2</sup> | a      | b      | R <sup>2</sup> |
| 0                     | 0.854         | 1.672   | 0.993          | 0.1523 | 0.4314 | 0.992          |
| 1                     | 0.6859        | 1.0719  | 0.996          | 0.1242 | 0.0651 | 0.996          |
| 3                     | 0.5226        | 0.77176 | 0.994          | 0.1152 | 0.0653 | 0.999          |
| 7                     | 0.3078        | 0.35404 | 0.995          | 0.1088 | 0.0592 | 0.999          |
| 10                    | 0.2384        | 0.1197  | 0.994          | 0.1085 | 0.0524 | 0.999          |
| 20                    | 0.1951        | 0.0782  | 0.999          | 0.1017 | 0.0461 | 0.999          |

electrodes under the same experimental conditions.

The data depicted in Fig. 5C reveal a notable decrease in the slope ( $k$ ) of the Anson equation, as calculated according to equation (Eq. 4), with increasing concentrations of VEGF. The slope is associated with (i) the equivalent number of electrons ‘ $n$ ’ transferred during the electrochemical reaction; (ii) the electrochemically active area ( $A$ ); the concentration of material ( $C$ ); and the diffusion coefficient ( $D$ ). In our investigation, the observed dependence of slope ( $k$ ) on the concentration ( $C$ ) of glycoprotein suggests a decrease in the electrochemically active area ( $A$ ). This deduction is supported by the assumption that the values of parameters ( $n$ ) and ( $D$ ) remain constant across all evaluated concentrations of VEGF, owing to the consistency in the concentration of other solution components and their respective physicochemical characteristics (e.g., density and viscosity). Notably, the slope value dependency on the concentration of VEGF is more pronounced in the case of the Ppy/anti-VEGF modified electrode compared to the Ppy-modified electrode.)

In chronocoulometric experiments, the charge increases proportionally with the  $t^{1/2}$  due to the diffusion of additional reactant to the electrode surface. If some of the reactants become adsorbed at the electrode/electrolyte interface while the electrode is held at a potential of 0 V, when the potential is switched to +0.6 V, the adsorbed reactant will be reduced almost instantly, resulting in an additional burst of charge. However, after this initial response, the chronocoulometric behaviour remains unaffected by the adsorption of the reactant. In this

case, plots of  $Q$  versus  $t^{1/2}$  will have intercepts exceeding  $Q$  by an amount of charge equal to  $Q_{dl}$ . Notably, the slope remains unaffected by the presence of adsorbed reactant. The values of  $Q_{ads}$  serve as direct measures of the quantity of adsorbed reactant by Faraday’s Law (Eq. 5), where  $\Gamma$  represents the quantity of adsorbed reactant in moles. Fig. 5D depicts intercept values of the concentration of VEGF protein (nM), while the intercept corresponds to  $Q_{ads} + Q_{dl}$ . To determine  $Q_{ads}$  from the intercept of a chronocoulometric plot of  $Q$  versus  $t^{1/2}$ , it is crucial to ascertain or measure  $Q_{dl}$ . This poses no challenge when the adsorption of a reactant elicits minimal or negligible alteration in the interfacial capacitance, allowing the value obtained in a blank experiment in the absence of analyte (0 nM of VEGF) to apply to measurements conducted in the presence of the adsorbing analyte (Anson and Osteryoung, 1983).

**3.4. Determination of the limit of detection**

PAD-based electrochemical measurements were conducted to assess the limit of detection (LOD). Intercept values, which correspond to  $Q_{ads} + Q_{dl}$ , were taken from Table 3. To evaluate the  $Q_{ads}$ , a blank experiment in the absence of an analyte (0 nM of VEGF) was employed, respectively, for Ppy and Ppy/anti-VEGF as analytical signals. VEGF protein concentration linear calibration (plotted against  $\Delta Q$  (mC)) is shown in Fig. 6. The slope for the VEGF (concentration expressed in nM) registered by the Ppy electrode was 0.001 mC/nM, with  $R^2 = 0.96$ , while the linear regression slope for the VEGF onto the Ppy/anti-VEGF modified electrode was 0.1 mC/nM, with  $R^2 = 0.99$ . The LOD was calculated according to the equation:

$$LOD = \frac{3.3 \times SD}{slope} \tag{6}$$

where SD represents the standard deviation.

It was evaluated that the LOD for the modified electrode Ppy/anti-VEGF was 0.21 nM.

A comparison of electrochemical methods previously used to detect VEGF protein is shown in Table 4.

Table 4 represents various approaches to VEGF detection utilising different electrode materials, polymers, and detection techniques. The first method employs flexible silk protein matrices combined with a conducting ink containing PEDOT:PSS, showcasing a biocompatible platform suitable for antibody immobilisation. This approach demonstrates a moderate LOD of 1.03  $\mu\text{g}/\text{mL}$  and exhibits a wide linear range

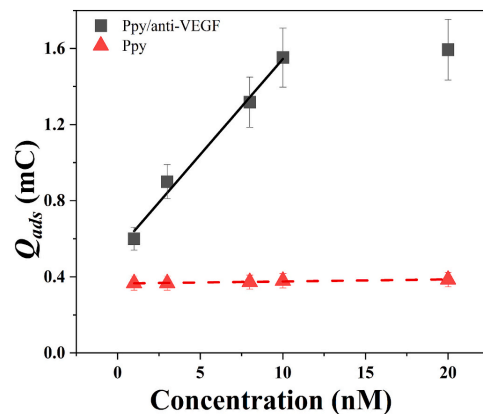


**Fig. 6.** Calibration curve  $Q_{ads}$  registered by Ppy/anti-VEGF (black line) and Ppy (red line) vs. VEGF concentration. Error bars are calculated as a standard deviation percentage ( $n = 4$ ).

**Table 4**  
Summary of the electrochemical methods previously used for the detection of VEGF protein.

| Electrode   | Polymer  | Method used | Redox mediator                           | LOD            | LR                    | Ref.                       |
|---|--|-------------|--|----------------|-----------------------|----------------------------|
| Flexible silk protein matrices with a biocompatible, antibody-containing conducting ink | PEDOT:PSS  | EIS         | –  | 1.03 pg/<br>mL | 1 pg/mL to 1<br>μg/mL | (Xu and Yadavalli, 2019)   |
| AuSPE   | dual(AA-co-MBA)-based MIP with dual-template of EGFR and VEGF. | EIS         | [Fe (CN) <sub>6</sub> ] <sup>3-/4-</sup> | 0.005<br>pg/mL | 0.01–7000 pg/<br>mL   | (Johari-Ahar et al., 2018) |
| GCE/GNRs-AuNPs  | PoPD   | DPV         | [Fe (CN) <sub>6</sub> ] <sup>3-/4-</sup> | 300 pg/<br>mL  | 0.500–500 ng/<br>mL   | (He et al., 2023)          |
| SPCE  | Ppy  | PAD         | –  | 0.21 nM        | 1.0–20 nM             | This study                 |

AA – acrylamide; AuNPs – gold nanoparticles; AuSPE – gold screen-printed electrode; DPV – differential pulse voltammetry; EGFR – epidermal growth factor receptor; EIS – electrochemical impedance spectroscopy; GCE – glassy carbon electrode; GNRs – graphene nanoribbons; LR – linear range; MBA – N,N'-methylenebis(acrylamide); PAD – pulsed amperometric detection; PEDOT – poly(3,4-ethylenedioxythiophene); PoPD – poly(*o*-phenylenediamine); PSS – polystyrene sulfonate; VEGF – vascular endothelial growth factor.

from 1 pg/mL to 1 μg/mL (Xu and Yadavalli, 2019). The second method uses a gold screen-printed electrode functionalised with a MIP, synthesised using acrylamide and *N,N*-methylenebis(acrylamide) as a monomer and crosslinker polymerised around EGFR and VEGF templates. This technique shows a LOD of 0.005 pg/mL and a wide linear range from 0.01 pg/mL to 7000 pg/mL (Johari-Ahar et al., 2018). Additionally, the biosensor demonstrates the value of using multidisciplinary approaches in protein detection. It combines MIP technology, antibody-conjugated nanoliposomes, and electrochemical detection to sensitively and selectively determine VEGF (Johari-Ahar et al., 2018). The third method, which employs poly(*o*-phenylenediamine) as the polymer matrix, uses a glassy carbon electrode modified with graphene nanoribbons (GNRs) and AuNPs. Using differential pulse voltammetry (DPV), this method yields a linear range of from 0.5 ng/mL to 500 ng/mL and a LOD of 300 pg/mL (He et al., 2023). Notably, this study significantly contributes to this field by introducing a novel PAD approach that employs the SPCE coated with Ppy. Unlike previous methods, this approach does not require the use of a redox mediator, which simplifies the detection process. The newly developed biosensor boasts an impressive LOD of 0.21 nM, enabling it to detect e VEGF within the range of 1.0–20 nM. This novel technique underscores the importance of investigating different electrode materials and detection strategies to improve the sensitivity and specificity of VEGF detection assays.

While this study did not involve the analysis of real samples, the accuracy of the developed aptasensing platform was rigorously evaluated through in vitro testing using known concentrations of VEGF protein. The use of PAD, as demonstrated by Anson et al. (Anson et al., 1967), ensured precise quantification of adsorbed reactants, allowing for accurate differentiation between Faradaic and non-Faradaic processes. The accuracy of the sensor was further validated by determining the LOD through PAD, yielding a highly sensitive detection limit of 0.21 nM with a strong linear correlation. These results suggest that the platform has strong potential for future applications involving real samples, such as clinical or environmental diagnostics. Further work will focus on real sample testing to confirm its performance in practical settings.

#### 4. Conclusions

This study represents a notable advancement in biosensing technology for cancer diagnosis and treatment monitoring. The developed electrochemical aptasensor demonstrates the potential of aptamer-based sensors for the sensitive and selective detection of disease-related proteins, specifically VEGF. The key achievements of this work include the utilisation of a self-assembling DNA aptamer structure, which offers high specificity for VEGF, and the integration of a polypyrrole (Ppy)/anti-VEGF matrix, which enhances sensitivity, resulting in a low detection limit of 0.21 nM. Moreover, adopting PAD without redox mediators simplifies the detection process, distinguishing this approach

from other more complex biosensing methods. Our development system shows great promise for point-of-care diagnostics, enabling the rapid monitoring of VEGF levels in clinical settings. Its versatility lies in the modifiability of the aptamer structure, allowing for potential adaptation to detect other disease biomarkers, thus broadening its applicability in personalised medicine. However, challenges such as aptamer stability in complex biological environments and environmental sensitivity must be addressed to optimise performance. Despite these limitations, the platform's capability for real-time biomarker monitoring paves the way for improved clinical decision-making and individualised patient care. However, the application of aptamer-based electrochemical sensors presents several challenges that must be addressed for broader clinical implementation. A key concern is the stability of DNA aptamers, particularly in complex biological environments such as blood serum, where they are prone to nuclease degradation. This degradation can significantly reduce the lifespan and effectiveness of the sensor. In addition, the sensor's performance may deteriorate if the aptamer loses its structural integrity or binding affinity for VEGF. The specificity and accuracy of VEGF detection in real-world biological samples may also be compromised by interfering substances, leading to non-specific binding or signal interference, and resulting in false-positive or false-negative readings. Furthermore, aptamer-based electrochemical sensors are sensitive to environmental variables, such as temperature and pH, which can affect aptamer folding and binding efficiency, potentially producing unreliable results. Lastly, these sensors may exhibit a limited dynamic range, which could restrict their ability to measure VEGF concentrations across the wide range observed during different stages of disease progression. Addressing these challenges is critical to fully harness the potential of aptamer-based sensors in clinical diagnostics.

#### CRedit authorship contribution statement

**Viktorija Liustrovaite:** Writing – original draft, Visualization, Methodology, Investigation, Formal analysis, Data curation, Conceptualization. **Vilma Ratautaite:** Writing – original draft, Methodology, Conceptualization. **Almira Ramanaviciene:** Writing – review & editing, Funding acquisition, Conceptualization. **Ieva Plikusiene:** Resources, Conceptualization. **Uldis Malinovskis:** Resources. **Donats Erts:** Writing – original draft, Resources. **Julija Sarvutiene:** Visualization, Writing – review & editing. **Arunas Ramanavicius:** Writing – review & editing, Supervision, Methodology, Funding acquisition, Data curation, Conceptualization.

#### Declaration of competing interest

The authors declare that they have no known competing financial interests or personal relationships that could have appeared to influence the work reported in this paper.



## Acknowledgement

Support by the Lithuanian Research council project S-MIP-24-111, "Polymer-based receptors for analytical and bioanalytical systems" is acknowledged. U.M. acknowledges Latvian Council of Science fundamental and applied research, project LZP-2020/1-0200.

## Data availability

Data will be made available on request.

## References

- Al-Ameen, M.A., Li, J., Beer, D.G., Ghosh, G., 2015. Sensitive, quantitative, and high-throughput detection of angiogenic markers using shape-coded hydrogel microparticles. *Analyst* 140. <https://doi.org/10.1039/c5an00358j>.
- Angelescu, C., Burada, F., Ioana, M., Angelescu, R., Moraru, E., Riza, A., Marchian, S., Mixich, F., Cruce, M., Saftoiu, A., 2013. VEGF-A and VEGF-B mRNA expression in gastro-oesophageal cancers. *Clin. Transl. Oncol.* 15. <https://doi.org/10.1007/s12094-012-0923-y>.
- Anson, F.C., Osteryoung, R.A., 1983. Chronocoulometry: a convenient, rapid and reliable technique for detection and determination of adsorbent reactants. *J. Chem. Educ.* 60. <https://doi.org/10.1021/ed060p293>.
- Anson, Fred C., Christie, J.H., Osteryoung, R.A., 1967. A study of the adsorption of cadmium(II) on mercury from thiocyanate solutions by double potential-step chronocoulometry. *J. Electroanal. Chem. Interfacial Electrochem.* 13, 343–353. [https://doi.org/10.1016/0022-0728\(67\)80037-8](https://doi.org/10.1016/0022-0728(67)80037-8).
- Balcianus, D., Plausinaitis, D., Ratautaitė, V., Ramanavičienė, A., Ramanavičius, A., 2022. Towards electrochemical surface plasmon resonance sensor based on the molecularly imprinted polypyrrole for glyphosate sensing. *Talanta* 241, 123252. <https://doi.org/10.1016/j.talanta.2022.123252>.
- Cai, G., Yu, Z., Ren, R., Tang, D., 2018. Exciton-Plasmon interaction between AuNPs/graphene Nanohybrids and CdS quantum dots/TiO2 for Photoelectrochemical Aptasensing of prostate-specific antigen. *ACS Sens.* 3. <https://doi.org/10.1021/acssens.7b00899>.
- Çalik, P., Balci, O., Özdamar, T.H., 2010. Human growth hormone-specific aptamer identification using improved oligonucleotide ligand evolution method. *Protein Expr. Purif.* 69. <https://doi.org/10.1016/j.pep.2009.05.015>.
- Crivianu-Gaita, V., Thompson, M., 2016. Aptamers, antibody scFv, and antibody Fab' fragments: an overview and comparison of three of the most versatile biosensor biorecognition elements. *Biosens. Bioelectron.* <https://doi.org/10.1016/j.bios.2016.04.091>.
- Di Stasi, R., De Rosa, L., D'Andrea, L.D., 2023. Structure-based Design of Peptides Targeting VEGF/VEGFRs. *Pharmaceuticals*. <https://doi.org/10.3390/ph16060851>.
- Ferrara, N., Gerber, H.P., LeCouter, J., 2003. The biology of VEGF and its receptors. *Nat. Med.* <https://doi.org/10.1038/nm0603-669>.
- Geiger, A., Burgstaller, P., Von der Eltz, H., Roeder, A., Famulok, M., 1996. RNA aptamers that bind L-arginine with sub-micromolar dissociation constants and high enantioselectivity. *Nucleic Acids Res.* 24. <https://doi.org/10.1093/nar/24.6.1029>.
- Goel, H.L., Mercurio, A.M., 2013. VEGF targets the tumour cell. *Nat. Rev. Cancer*. <https://doi.org/10.1038/nrc3627>.
- Gonzato, J.C., Żolek, T., Maciejewska, D., Kutner, A., Merlier, F., Haupt, K., Sharma, P.S., Noworyta, K.R., Kutner, W., 2021. Molecularly imprinted polymer nanoparticles-based electrochemical chemosensors for selective determination of clostazol and its pharmacologically active primary metabolite in human plasma. *Biosens. Bioelectron.* 193, 113542. <https://doi.org/10.1016/j.bios.2021.113542>.
- Guyot, M., Pagès, G., 2015. VEGF splicing and the role of VEGF splice variants: from physiological-pathological conditions to specific pre-mRNA splicing. *Methods Mol. Biol.* 1332. [https://doi.org/10.1007/978-1-4939-2917-7\\_1](https://doi.org/10.1007/978-1-4939-2917-7_1).
- He, M., Luo, P., Xie, Y., He, Y., Wang, X., Tan, L., 2023. Electrochemical determination of vascular endothelial growth factor using functional metal-polymer nanocomposites. *Colloids Surf. A Physicochem. Eng. Asp.* 677. <https://doi.org/10.1016/j.colsurfa.2023.132380>.
- Hsu, M.Y., Hung, Y.C., Hwang, D.K., Lin, S.C., Lin, K.H., Wang, C.Y., Choi, H.Y., Wang, Y. P., Cheng, C.M., 2016. Detection of aqueous VEGF concentrations before and after intravitreal injection of anti-VEGF antibody using low-volume sampling paper-based ELISA. *Sci. Rep.* 6. <https://doi.org/10.1038/srep34631>.
- Huang, P.-J., Liu, J., 2022. A DNA aptamer for theophylline with ultrahigh selectivity reminiscent of the classic RNA aptamer. *ACS Chem. Biol.* 17. <https://doi.org/10.1021/acscmbio.2c00179>.
- Johari-Ahar, M., Karami, P., Ghanei, M., Afkhami, A., Bagheri, H., 2018. Development of a molecularly imprinted polymer tailored on disposable screen-printed electrodes for dual detection of EGFR and VEGF using nano-liposomal amplification strategy. *Biosens. Bioelectron.* 107. <https://doi.org/10.1016/j.bios.2018.02.005>.
- Kaur, H., Yung, L.Y.L., 2012. Probing high affinity sequences of DNA aptamer against VEGF 165. *PLoS One* 7. <https://doi.org/10.1371/journal.pone.0031196>.
- Ktari, N., Fourati, N., Zerrouki, C., Ruan, M., Seydou, M., Barbauf, F., Nal, F., Yaakoubi, N., Chehimi, M.M., Kalfat, R., 2015. Design of a polypyrrole MIP-SAW sensor for selective detection of flumequine in aqueous media. Correlation between experimental results and DFT calculations. *RSC Adv.* 5. <https://doi.org/10.1039/c5ra16237h>.
- Kwon, Y.W., Jo, H.-S., Bae, S., Seo, Y., Song, P., Song, M., Yoon, J.H., 2021. Application of proteomics in Cancer: recent trends and approaches for biomarkers discovery. *Front. Med. (Lausanne)* 8. <https://doi.org/10.3389/fmed.2021.747333>.
- Lewis, T.W., Wallace, G.G., Kim, C.Y., Kim, D.Y., 1997. Studies of the overoxidation of polypyrrole. *Synth. Met.* 84. [https://doi.org/10.1016/s0379-6779\(97\)80803-x](https://doi.org/10.1016/s0379-6779(97)80803-x).
- Liustrovaite, V., Pogorelov, M., Boguzaitė, R., Ratautaitė, V., Ramanavičienė, A., Pilvenyte, G., Holubnycha, V., Kornienko, V., Diedkova, K., Viter, R., Ramanavičius, A., 2023. Towards electrochemical sensor based on molecularly imprinted Polypyrrole for the detection of Bacteria—*Listeria monocytogenes*. *Polymers (Basel)* 15. <https://doi.org/10.3390/polym15071597>.
- Lu, L., Zeng, R., Lin, Q., Huang, X., Tang, D., 2023. Cation exchange reaction-mediated Photothermal and polarity-switchable Photoelectrochemical dual-readout biosensor. *Anal. Chem.* 95. <https://doi.org/10.1021/acs.analchem.3c03573>.
- Lv, S., Zhang, K., Zhu, L., Tang, D., Niessner, R., Knopp, D., 2019. H2-based electrochemical biosensor with Pd nanowires@ZIF-67 molecular sieve Bilayered sensing Interface for immunoassay. *Anal. Chem.* 91, 12055–12062. <https://doi.org/10.1021/acs.analchem.9b03177>.
- Mao, Y., Ge, H., Chen, W., Wang, Y.R., Liu, H., Li, Z., Bai, Y., Wang, D., Yu, Y., Zhen, Q., Li, B., Sun, L., 2023. RasGRP1 Influences imiquimod-induced psoriatic inflammation via T-cell activation in mice. *Int. Immunopharmacol.* 122. <https://doi.org/10.1016/j.intimp.2023.110590>.
- Ni, S., Shen, Z., Zhang, P., Liu, G., 2020. Enhanced performance of an electrochemical aptasensor for real-time detection of vascular endothelial growth factor (VEGF) by nanofabrication and ratiometric measurement. *Anal. Chim. Acta* 1121. <https://doi.org/10.1016/j.aca.2020.05.003>.
- Nourizad, A., Golmohammadi, S., Aghanejad, A., Tohidkia, M.R., 2023. Recent trends in aptamer-based nanobiosensors for detection of vascular endothelial growth factors (VEGFs) biomarker: a review. *Environ. Res.* <https://doi.org/10.1016/j.envres.2023.116726>.
- Qiu, Z., Shu, J., Liu, J., Tang, D., 2019a. Dual-Channel Photoelectrochemical Ratiometric Aptasensor with up-converting nanocrystals using spatial-resolved technique on homemade 3D printed device. *Anal. Chem.* 91. <https://doi.org/10.1021/acs.analchem.8b05455>.
- Qiu, Z., Shu, J., Liu, J., Tang, D., 2019b. Dual-Channel Photoelectrochemical Ratiometric Aptasensor with up-converting nanocrystals using spatial-resolved technique on homemade 3D printed device. *Anal. Chem.* 91. <https://doi.org/10.1021/acs.analchem.8b05455>.
- Qureshi, A., Gurbuz, Y., Niazi, J.H., 2015. Capacitive aptamer-antibody based sandwich assay for the detection of VEGF cancer biomarker in serum. *Sensors Actuators B Chem.* 209. <https://doi.org/10.1016/j.snb.2014.12.040>.
- Ramanavičienė, A., Ramanavičius, A., 2004. Molecularly imprinted polypyrrole-based synthetic receptor for direct detection of bovine leukemia virus glycoproteins. *Biosens. Bioelectron.* <https://doi.org/10.1016/j.bios.2004.05.014>.
- Ratautaitė, V., Boguzaitė, R., Brazys, E., Plausinaitis, D., Ramanavičius, S., Samukaitė-Bubniene, U., Bechelany, M., Ramanavičius, A., 2023. Evaluation of the interaction between SARS-CoV-2 spike glycoproteins and the molecularly imprinted polypyrrole. *Talanta* 253. <https://doi.org/10.1016/j.talanta.2022.123981>.
- Rodriguez, D., Watts, D., Gaete, D., Sormenti, S., Wielockx, B., 2021. Hypoxia pathway proteins and their impact on the blood vasculature. *Int. J. Mol. Sci.* <https://doi.org/10.3390/ijms217919191>.
- Ruckman, J., Green, L.S., Beeson, J., Waugh, S., Gillette, W.L., Henninger, D.D., Claesson-Welsh, L., Janjic, N., 1998. 2-Fluoropyrimidine RNA-based aptamers to the 165-amino acid form of vascular endothelial growth factor (VEGF165). *J. Biol. Chem.* 273. <https://doi.org/10.1074/jbc.273.32.20556>.
- Ghanspior, S., Sharifi, G., Taghian, F., 2021. An 8-week Administration of *Bifidobacterium bifidum* and *Lactobacillus plantarum* combined with exercise training alleviates neurotoxicity of A $\beta$  and spatial learning via acetylcholine in Alzheimer rat model. *J. Mol. Neurosci.* 71. <https://doi.org/10.1007/s12031-021-01812-y>.
- Simons, M., Gordon, E., Claesson-Welsh, L., 2016. Mechanisms and regulation of endothelial VEGF receptor signalling. *Nat. Rev. Mol. Cell Biol.* <https://doi.org/10.1038/nrm.2016.87>.
- Wang, G., Yin, P., Wang, J., Ma, P., Wang, Y., Cai, Y., Qi, H., Liu, A., 2021. Specific heptapeptide screened from pIII phage display library for sensitive enzyme-linked chemiluminescence immunoassay of vascular endothelial growth factor. *Sensors Actuators B Chem.* 333. <https://doi.org/10.1016/j.snb.2021.129555>.
- Xie, C., Wan, X., Quan, H., Zheng, M., Fu, L., Li, Y., Lou, L., 2018. Preclinical characterization of antolinitab, a highly potent and selective vascular endothelial growth factor receptor-2 inhibitor. *Cancer Sci.* 109. <https://doi.org/10.1111/cas.13536>.
- Xie, S., Sun, W., Fu, T., Liu, X., Chen, P., Qiu, L., Qu, F., Tan, W., 2023. Aptamer-based targeted delivery of functional nucleic acids. *J. Am. Chem. Soc.* <https://doi.org/10.1021/jacs.3c00841>.
- Xu, J., Zhang, J., Zeng, R., Li, L., Li, M., Tang, D., 2022. Target-induced photocurrent-polarity-switching photoelectrochemical aptasensor with gold nanoparticle-ZnIn2S4 nanohybrids for the quantification of 8-hydroxy-2'-deoxyguanosine. *Sensors Actuators B Chem.* 368, 132141. <https://doi.org/10.1016/j.snb.2022.132141>.
- Xu, M., Yadvall, V.K., 2019. Flexible biosensors for the impedimetric detection of protein targets using silk-conductive polymer biocomposites. *ACS Sens.* 4. <https://doi.org/10.1021/acssens.9b00230>.
- Yu, Z., Qiu, C., Huang, L., Gao, Y., Tang, D., 2023a. Microelectromechanical microsystems-supported Photothermal immunoassay for point-of-care testing of aflatoxin B1 in foodstuff. *Anal. Chem.* 95. <https://doi.org/10.1021/acs.analchem.2c05617>.
- Yu, Z., Tang, J., Gong, H., Gao, Y., Zeng, Y., Tang, D., Liu, X., 2023b. Enzyme-Encapsulated Protein Trap Engineered Metal-Organic Framework-Derived

- Biomaterial Probes for Non-Invasive Prostate Cancer Surveillance. *Adv. Funct. Mater.* 33. <https://doi.org/10.1002/adfm.202301457>.
- Zeng, R., Qiu, M., Wan, Q., Huang, Z., Liu, X., Tang, D., Knopp, D., 2022. Smartphone-based electrochemical immunoassay for point-of-care detection of SARS-CoV-2 Nucleocapsid protein. *Anal. Chem.* 94, 15155–15161. <https://doi.org/10.1021/acs.analchem.2c03606>.
- Zeng, R., Xu, J., Liang, T., Li, M., Tang, D., 2023. Photocurrent-polarity-switching Photoelectrochemical biosensor for switching spatial distance electroactive tags. *ACS Sens.* 8. <https://doi.org/10.1021/acssensors.2c02314>.
- Zhang, L., Ye, C., Li, P., Li, C., Shu, W., Zhao, Y., Wang, X., 2022. ADSCs stimulated by VEGF-C alleviate intestinal inflammation via dual mechanisms of enhancing lymphatic drainage by a VEGF-C/VEGFR-3-dependent mechanism and inhibiting the NF- $\kappa$ B pathway by the secretome. *Stem Cell Res Ther* 13. <https://doi.org/10.1186/s13287-022-03132-3>.
- Zhao, S., Ma, W., Xu, L., Wu, X., Kuang, H., Wang, L., Xu, C., 2015. Ultrasensitive SERS detection of VEGF based on a self-assembled ag ornamented-AU pyramid superstructure. *Biosens. Bioelectron.* 68. <https://doi.org/10.1016/j.bios.2015.01.056>.

## NOTES

Vilniaus universiteto leidykla  
Saulėtekio al. 9, III rūmai, LT-10222 Vilnius  
El. p. [info@leidykla.vu.lt](mailto:info@leidykla.vu.lt), [www.leidykla.vu.lt](http://www.leidykla.vu.lt)  
[bookshop.vu.lt](http://bookshop.vu.lt), [journals.vu.lt](http://journals.vu.lt)  
Tiražas 25 egz.